# Tailoring Porous Templated Inorganic Oxide Films

Di, Andi

*Award date:*
2020

*Awarding institution:*
University of Bath

# Tailoring Porous Templated Inorganic Oxide Films

Andi Di
University of Bath


Submitted in partial fulfilment of the requirements for the degree of Doctor of Philosophy
September 2019

Supervised by
Prof. Karen J. Edler

Department of Chemistry
University of Bath
United Kingdom

# Abstract

Mesoporous materials have been widely applied in the field of separation and catalysts. Surfactant templating is one of the widely used methods for the preparation of mesoporous materials. Many methods based on surfactant templating, such as spin coating, dip coating and co-precipitation, have been developed to prepare mesoporous materials.

Free-standing film synthesis method using the surfactant templating method, which has been extensively studied by our group, enables the investigation of the change in the surface structure while the film is growing using surface sensitive techniques. Previously used silica precursors (tetramethyl orthosilicate and tetraethyl orthosilicate), produce organic species that disrupt the organisation of the micelles. Sodium silicate solution, used in this work produces water instead so is a potential precursor that could give better control of the pore size and the strength of the film. The growth of the film was followed using cutting-edge techniques: *in situ X-Ray Reflectivity* (XRR) and *in situ Grazing Incidence Small Angle X-Ray Scattering* (GISAXS), which suggest a possible growth mechanism.

Functionalisation of mesoporous materials is required to improve their catalytic properties. Novel surfactants (POM-2$C_n$, n is the carbon number of the hydrocarbon chain length, n= 12, 14, 16 and 18) were designed and were prepared through grafting double hydrocarbon chains onto a Dawson structured polyoxometalates ($[P_2W_{17}O_{61}]^{10-}$), to use these species as both templates and a source of polyoxometalate to functionalize the mesoporous materials prepared. The self-assembly of the prepared surfactants and their mixture with commercial nonionic surfactants ($C_{12}EO_6$ and $C_{12}EO_8$) in water have been studied using *Small Angle Neutron Scattering* (SANS) and *Small Angle X-Ray Scattering*(SAXS).

The pure POM-2$C_n$ molecules form less elongated micelles in water with increasing hydrophobic tail length, suggested by the SANS analysis. The micelles formed by POM-2$C_n$ were used to template titanium dioxide. The prepared materials, denoted as POM-$TiO_2$, have been proven to bear POM units well-dispersed in the porous $TiO_2$ materials using *Energy Dispersive X-Ray Analysis* (EDX). The POM-$TiO_2$ materials showed enhanced photodegradation properties for rhodamine B compared to the unfunctionalised $TiO_2$ materials. This is attributed to the charge transfer from $TiO_2$ conduction band to POM that prevent the recombination of the photo-excited holes and electrons during the photodegradation process.

The insertion of the nonionic surfactant into the POM-2$C_n$ system induces a micellar growth. The comparison of SANS studies of the two binary surfactant systems (POM-2$C_n$/$C_{12}EO_6$ and POM-$C_n$/$C_{12}EO_8$) have shown that the micellar growth caused by nonionic surfactant with a smaller polyethylene oxide group is more pronounced than that caused by that with a larger hydrophilic headgroup. The POM-2$C_n$/$C_{12}EO_8$ mixtures form *Liquid Crystal Phases* (LCP) when the total concentration is increased to 133 mM. The type of LCP formed depends on the mixing mole ratio of the POM-2$C_n$ and $C_{12}EO_8$. The POM-2$C_n$ rich mixtures form a cubic phase, while the $C_{12}EO_8$ rich mixtures form a lamellar phase. The lamellar phase formed by the mixture was then used to template long-range ordered silica. Porous silica was obtained after the organic part of the template was removed, with a relatively small surface area (ca. 313 $m^2/g$) and small pore size (1 nm - 4 nm).

This work includes several individual systematic investigations, the understanding of the growth of the silica film using sodium silicate solution, the basic understanding of surfactant behaviour of the POM-2$C_n$ surfactants and their mixtures with $C_{12}EO_m$ (m = 6 and 8). Their

applications in fabricating hybrid porous materials with enhanced properties were also studied. It is hoped that these results could give a good understanding of the surfactant behaviour of both traditional and novel surfactants and would contribute to the future study of the functionalisation of inorganic materials using a surfactant templating method.

# Acknowledgements

Foremost I would like to thank my supervisor Prof. Karen Edler for her consistent support throughout the application process prior to my arrival in the UK and for continued support, supervision and patience that have been invaluable over the past four years. I also appreciate the supervision and support from Dr. John Errington at Newcastle University.

I would also like to thank previous and current members of staff in the Department of Chemistry who have helped me learn new experimental methods and developed my theoretical understanding over the past four years. I am grateful to the members in Edler's research group Dr. Julien Schmitt, Dr. Marcelo Alves Da Silva, Dr. Iva Manasi, Naomi Elstone, Vincenzo Calabrese, and Dr. Cecilia Tognoloni who have made working in the group enjoyable socially and have helped and supported me. Great thanks to my lovely friends, Wentao Deng, Xinxing Liang, Chi Zhang, Haobo Ge, who have made Bath feel like home and helped me go through all the difficulties.

Also, I would like to thank my parents for their support both for my decision to pursue a PhD in the UK and for the decision to continue to explore abroad after my PhD. I also appreciate the help of my cousin, Chen Sun, who has helped me taking care of my parents when I am away. I am deeply grateful for the financial supports, for fees and subsistence, generously provided by the University of Bath and the China Scholarship Council, without which I would not have been able to undertake postgraduate research in the UK.

# Publication List

[1] Di, A., Schmitt, J., Elstone, N., Arnold, T., Edler, K., *In situ X-ray Reflectivity and GISAXS Study of Mesoporous Silica Films Grown from Sodium Silicate Solution Precursors.* (Draft)

[2] Di, A., Schimitt, J., da Silva, M., Mahmoudi, N., Errington, R.J., Edler, K., *Self-assembly of amphiphilic polyoxometalates for the preparation of mesoporous polyoxometalate-titania catalysts.* (Submitted to Nanoscale)

[3] Di, A., Schimitt, J., Ma, K.; da Silva, M., Elstone, N., Mahmoudi, N., Li, P., Washington, A., Wang, Z., Errington, R.J., Edler, K., *Mixed micelles of Amphiphilic Polyoxometalate and Hexaethylene Glycol Monododecyl Ether.* (Draft)

[4] Di, A., Schimitt, J., Hossain, Z., Washington, A., Errington, J.; Edler, K., *Amphiphilic Polyoxometalate Mixtures with Octaethylene Glycol Dodecyl Ether and Salt Effect on the Micellar Systems* (Draft)

# Contents

# 1 Introduction

Surfactants are molecules that comprise both hydrophilic and hydrophobic parts. The self-assembly of surfactant molecules, a process where ordered structures are formed from the pre-existing disordered components, has been widely studied. The driving forces are considered to be electrostatic and hydrophobic interactions.[1] The ordered microstructures formed by surfactants have been widely applied to the field of materials.[2,3] The surfactant-templating method, utilising the mesophases formed by traditional surfactants as templates to prepare porous materials, has allowed the generation of porous structures and different geometries in the prepared materials and are well-established. A growing amount of studies are focused on the exploration of modified synthesis methods to better control the pore size and geometry of the prepared materials for extensive applications.

In the last decades, more and more studies have explored the design of novel surfactants, such as amino acid-based surfactants[4] and inorganic material-based[5,6] surfactants. The inorganic materials-based surfactants, due to the significant properties of the inorganic molecular clusters, are very valuable systems for understanding the assembly and functionalising materials through a surfactant templating method.[7] Polyoxometalates are the most representative inorganic candidates that are applicable to the design of inorganic material-based amphiphiles, due to their solubility in polar solvents.[5] Their unique properties grant extensive applications of the designed amphiphiles.[8,9]

This thesis is focused on the better control of the structure of mesoporous materials templated by traditional surfactants and the functionalisation of porous inorganic materials through using POM-based amphiphiles as structure-directing agents. Therefore, this chapter will introduce surfactant templating from the aspects of both traditional surfactants and POM-based amphiphiles. The major goals of this work are listed below:

1. To explore the use of alternative silica sources along with the self-assembly of traditional surfactants and their application in the preparation of mesoporous films.
2. To synthesise polyoxometalate (POM)-based amphiphiles and study their novel self-assembly behaviour.
3. To use POM-based amphiphiles, alone and with nonionic surfactants, to template active porous materials, such as $TiO_2$, where synergistic effects between both species can illustrate the potential for use of POM-amphiphiles to prepare functional materials.

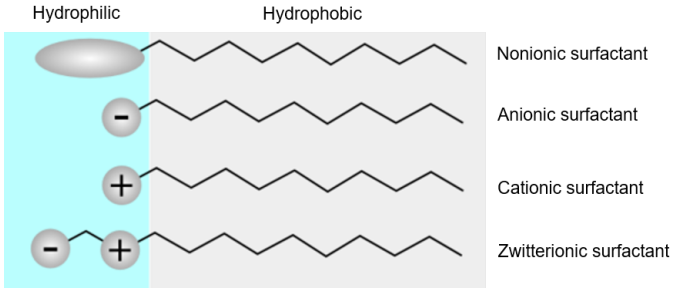


**Figure 1.1** Illustration of the four types of surfactants.

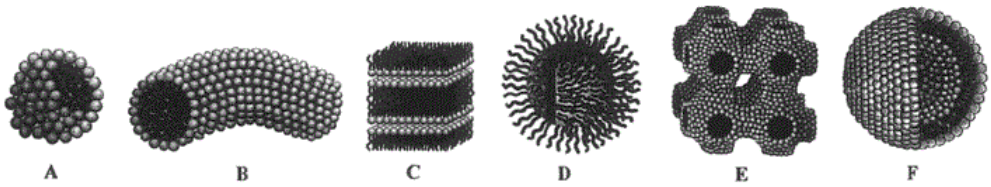


**Figure 1.2** Micellar structure (A = sphere, B = cylinder, C = bilayers, D = reverse micelles, E = bicontinuous phase, F = liposomes). Adapted with permission from [10].

## 1.1 Traditional surfactants, liquid crystal phases and ordered porous materials

Surfactants are usually organic compounds which contain both hydrophobic and hydrophilic groups. Surfactants both diffuse in a solvent and absorb at the air/liquid interface as monolayers at low concentrations. The hydrophilic group will be in contact with the aqueous solution while the hydrophobic tail will stay away from the aqueous solution. As the concentration increases and reaches the critical micelle concentration (CMC), the surfactant molecules start to assemble to form micelles. In an aqueous solution, the hydrophilic headgroups form a polar surface, while the hydrophobic tails form a nonpolar core. When forming micelles in the bulk, each micelle comprises a certain number of aggregated surfactant molecules which determines the size and the geometry of the particular micellar system.

### 1.1.1 Surfactants, micelles and liquid crystal phases

Surfactants are classified into four types according to the charge of the headgroups they possess as illustrated in Figure 1.1: anionic, cationic, zwitterionic and nonionic. Anionic and cationic surfactants are surfactants which bear a negatively charged and positively charged hydrophilic headgroup, respectively. Zwitterionic surfactants have both cationic and anionic centres that are attached to the same molecule. Nonionic surfactants have no charge in the headgroup.

The concentration where micelles start to form is called critical micelle concentration (CMC). The relationship between CMC values and the length of the surfactant can be fitted by the Traube's law:

$$log(CMC) = A - Bn_{CH_2} \tag{1.1}$$

where $n_{CH_2}$ is the number of effective methylene units, A = 1.33 and B = 0.26. Therefore, surfactants with longer hydrophobic tail length have lower CMCs.

The formation of different microstructural colloids assembled by surfactant molecules is driven by the entropic interaction and factors such as Coulombic interaction and hydrogen bonding. Typical structures of micellar systems are spheres, cylinders, bilayers, inverse spheres, bicontinuous phases and liposomes as illustrated in Figure 1.2.

The widely accepted theory used to explain and predict the self-assembly of surfactant microstructures was given by Israechvili,[11] which is based on the ratio of the surface area of the headgroup to the volume of the hydrophobic tail, namely the packing parameter ($g$). The packing parameter is calculated by:

$$g = v/a_0 l_c \tag{1.2}$$

where $v$ is the volume of the hydrophobic part, $a_0$ is the effective area per molecule of the hydrophilic part and $l_c$ is the critical tail length of the hydrophobic headgroup. For a linear single-chain surfactant with saturated hydrocarbon chain, $v$ and $l_c$ can be calculated using the Tanford equation:[12] $v = (27.4 + 26.9n)$ Å$^3$ and $l_c = (1.5 + 1.265n)$ Å (n is the number of the carbon atoms in the hydrophobic chain). As listed in Table 1.1, the micellar structure formed can be predicted by the packing parameter of the surfactant molecule.

**Table 1.1** Summary of the different micellar structures compatible with a given packing parameter.[11]

| Packing Parameter, $g$ | Micellar Structure |
|---|---|
| $g$ <1/3 | Spherical micelles |
| 1/3 <$g$ <1/2 | Cylindrical micelles |
| 1/2 <$g$ <1 | Bilayer (vesicles) |
| 1 <$g$ <2 | Bilayer (membrane) |
| 2 <$g$ <3 | Inverse cylindrical micelles |
| $g$ >3 | Inverse spherical micelles |

Liquid crystal phases (LCPs), formed at high concentrations of surfactant solutions, are considered to be ordered arrays of micelles or intermediates between the solid and liquid phase.[1] The most common LCPs are lamellar, hexagonal and cubic structure.[13–15]

The structure of the lamellar phase is illustrated in Figure 1.2C, where the surfactant molecules are organised into bilayers separated by the solvent layers. The hexagonal phase is composed of the hexagonally-packed rodlike micelles, as illustrated in Figure 1.3. Cubic phase contains more than two types of structures. Figure 1.4 shows a bicontinuous cubic structure.

### 1.1.2 Porous materials

Porous materials have been widely applied in the field of catalysis, drug delivery and separations.[17–23] Porous materials are classified by the size of the pores into micro-, meso-, macrop-

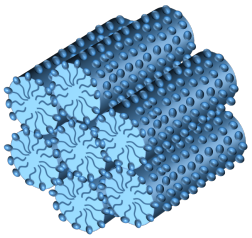

**Figure 1.3** Hexagonal phase; rodlike surfactant micelles packed hexagonally in water.

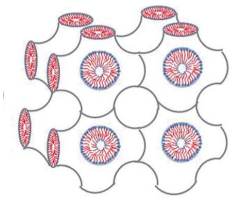

**Figure 1.4** Bicontinuous cubic phase. Adapted with the permission from [16].

orous materials.

Microporous materials are materials possessing pores that range from 0.5 to 2 nm. Typical microporous materials are zeolites which are crystalline aluminosilicates with 1D channel or 2D channels.[24] Normally, the pore size in zeolites ranges from 0.4 to 0.7 nm. Zeolites have been widely used as adsorbent and catalysts.[25,26] The small size of the pores limits the applications of zeolites, e.g., in the separation of large organic molecules.

The pore size of the macroporous materials ranges from 50 nm to 10 $\mu$m. These materials have advanced applications in the field of photonic crystals,[27,28] optical devices[29] and as potential materials for high-speed computer device packaging.[30] However, the pore size of the macroporous materials are quite large which limits their application in some fields.

Mesoporous materials are those having pores with diameters between 2 and 50 nm. These materials have many advantages due to their large surface area, medium pore size, and their potential to be modified by functional groups.[31–33] Mesoporous silica is one of the traditional mesoporous materials. Normally, the silica is condensed in an amorphous state.[34]

The preparation of the mesoporous materials has been well established. The pores could be either randomly oriented or long-range ordered. Disordered materials normally have a wide pore size distribution, which limits their application in the area of separation and catalysis. Ordered mesoporous silica materials have larger pores and narrow size distribution compared to microporous materials and disordered materials. The large pores allow the materials to be useful for applications involving large molecules. Long-range ordered mesoporous silica material prepared by surfactant templating was first synthesised by Kresge *et al.*[35] in 1992 with a 2D hexagonal structure, denoted MCM-41 (Mobil Composition of Matter). Since then, more synthesis methods have been developed and various ordered mesoporous materials have been synthesised. Well-

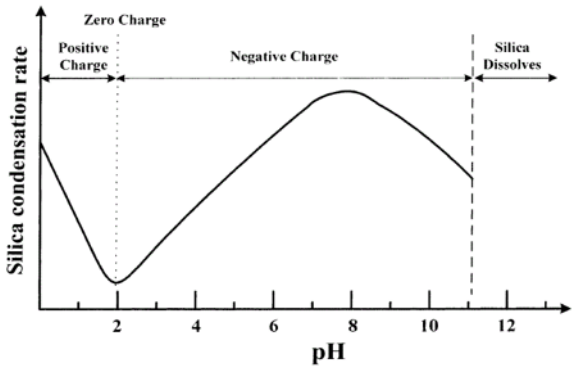


**Figure 1.5** Effects of pH value on the condensation rate and the surface charge properties of the silica species during the formation of the mesoporous silica. Reprinted (adapted) with permission from [40].

ordered silica materials with hexagonal (MCM-41, SBA-3, etc.), cubic (MCM-48, SBA-1, etc.) and lamellar (MCM-50, etc.) structure have been successfully synthesised by using arrays of surfactant molecules as the structure-directing templates in both basic and acidic solutions.[36–38] One of the most common structures is the 2D hexagonal structure with $P6mm$ symmetry.

### 1.1.3 Formation mechanism

As the organic templates can be easily removed through calcination or solvent extraction to generate pores in the as-prepared materials, the surfactant-templating method has received more and more attention.[35,39] The utilisation of a micellar surfactant solution to synthesise mesoporous materials was first proposed by Kresge and co-workers.[35] After that, the surfactant aggregates became common templates for the fabrication of ordered mesoporous materials. The assembly of the surfactant molecules and the condensation of inorganic precursors both contribute to the formation of the mesostructured materials in the syntheses. The synthesis method can be classified according to the type of the surfactant used since the interactions between the silica precursors and the surfactant micelles vary when using different types of surfactants.

Well-ordered (hexagonal, cubic, lamellar) mesoporous materials can be synthesised by using cationic surfactants as templates under both basic and acidic conditions related to different charge-matchings, one of the two dominating factors in the self-assembly. The charge-matching can be easily controlled by the pH of the solution. Take mesoporous silica material as an example, the rates of the hydrolysis and condensation of the silica precursor happen in the solution vary with pH value of the solution, more details can be found in Figure 1.5.[40] Silica species are positively charged at pH below 2, and their condensation rate increases as the pH value decreases.

For a cationic surfactant under strongly acidic conditions (pH $< 2$), the cationic parts $S^+$, mediated by the counter anions ($X^-$), interact with positively charged silica sources ($I^+$) through a weak electrostatic interaction at the surface of the micelles to form the templated species $S^+X^-I^+$ (Figure 1.6).[2,3] Interactions between the silica species and the surfactant molecules may reduce the surface area per headgroup compared to the singular surfactant system, resulting in a larger packing parameter. Referring to Figure 1.5 again,[40] the silica species are negatively charged under weak acidic and alkaline conditions. For the CTAB/sodium silicate systems in weak alkaline

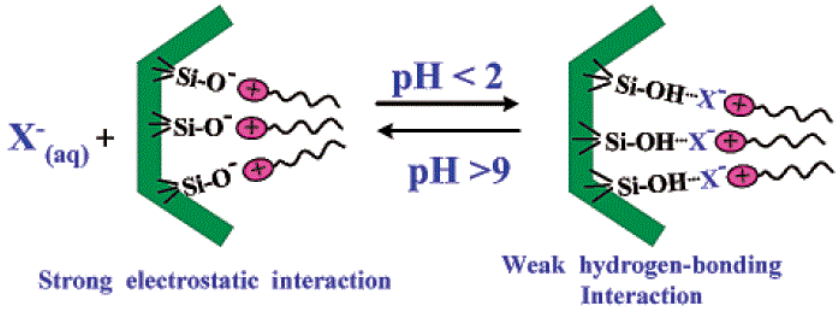


**Figure 1.6** Illustration of the variations of the interaction with the pH of the solution. Reprinted (adapted) with permission from [40].

solutions,[41] the oligomeric silica species are negatively charged instead and then exchange with the counterion $X^-$ of the surfactant to then form $S^+I^-$ through Coulombic interactions. Again, the extent of the inorganic $I^-$ binding to the cationic surfactant headgroup $S^+$ will change the packing parameter. Liu *et al.*[42] have successfully controlled the surfactant packing parameter by controlling the $SiO_2/OH^-$ ratio in the solution where silica was templated on CTAB surfactant micelles using a hydrothermal method.

The interaction for the silica oligomers with nonionic surfactants is different from that with the cationic surfactants. The nonionic surfactants $S^0$ interact with the neutral silica precursors $I^0$ by electrostatic interaction or hydrogen bonding at the surface of the micelles and subsequently form templated species $S^0I^0$.[2,43] However, the synthetic strategies used for cationic and nonionic surfactants are not applicable to anionic surfactants. Highly protonated anionic surfactants fail to interact with the positively charged silica sources in acidic solutions, and interactions between the counterions of the surfactants and the silica sources are too weak to form $S^-X^+I^-$ under basic conditions. Therefore, a mediator between anionic surfactants and silica sources is the key in these syntheses. Che *et al.*[44] have successfully used 3-aminopropyltrimethoxysilane (APS) or N-trimethoxysilylpropyl-N,N,N-trimethylammonium chloride (TMAPS) as the bridge between the anionic surfactant molecules and the silica oligomers to produce highly ordered mesoporous silica.

The exact formation mechanism of the long-range ordered mesoporous silica is still under debate. There were two early predicted mechanisms for the formation of the 2D hexagonal structure. In the first one, the surfactant molecules form an ordered liquid crystal phase (LCP) before the addition of the silica precursor. Silica species added infiltrate into the water region between adjacent micelles in the LCP structure, interact with the hydrophilic headgroup of the surfactant molecules through various driving forces as discussed above and condense around the micelles without changing the pre-existing LCP structure.[34] This mechanism is usually used to explain the synthesis methods where high concentration and viscous surfactant solution are used,[45] such as electrodeposition and casting. However, most syntheses are far too dilute for the formation of surfactant LCP at the beginning of the reaction, so this mechanism is discounted for these methods.

Another proposed mechanism suggests that the silica species interact with the surfactant

molecules and condense on the independent micelles. Then the silica coating on the micelles decreases the electrostatic double-layer repulsion between the charged micelles, allowing them to coalesce and organise into ordered mesophases. This assumption under certain conditions (surfactant concentrations are between 10 wt. % and 26 wt. % where 2D hexagonal structure often form) has been suggested by techniques such as small angle scattering, scanning electron microscopy and transmission electron microscopy.[46–48]

Other mechanisms have also been proposed. Chan *et al.*[49] reported a mechanism called a phase separation model, giving a new understanding of the process of mesostructure formation. A thermodynamically unstable oligomers/surfactant/solvent phase is produced during the growth of the inorganic oligomers. Then a liquid crystal phase rich in surfactants and silica oligomers appears as a separate phase as droplets stabilised by the electrostatic interactions. The droplets continue to adsorb surfactant molecules from the solution and provide the environment for the growth of templated species which are further stabilised by polymerisation of the oligomers. Frasch *et al.*[50] also suggested a possible mechanism. The $CTA^+X^-$ (X = Br or Cl) micelles in the solution reach an equilibrium state between the surfactant ions and the free counterions occurs. After the silica precursor is added, small amount of $X^-$ ions bonding outside the $CTA^+$ micelles by hydroxide ions or silicate ions. After a short time, siliceous prepolymers (low degree of polymerisation) form and bind the free surfactant molecules in the solution. The prepolymers gradually grow into polysilicate polymers and bind more surfactants molecules to form micelles at the expense of the pre-formed micelles. The surfactant/silica precipitates form when the complexes reach a large size and neutral state.

### 1.1.4 Ordered mesoporous silica films.

Many strategies have been applied to prepare ordered mesoporous silica materials in a powder form. Nevertheless, the powdered ordered mesoporous silica materials lack regular morphologies and a high degree of ordering. The film morphology has the potential to produce more highly ordered materials.

Evaporation induced self-assembly (EISA) is a simple and frequently used process,[51] which enables rapid production of porous layers on substrates in the form of film.[52] EISA uses largely non-aqueous solutions such as ethanol, normally with a starting surfactant concentration below its CMC. As the ethanolic solutions become concentrated while the solvents are evaporating, micelles form in the remaining small volume of the solution, and then self-organised into a periodic 2D or 3D hexagonal, cubic or lamellar mesophases.[52] Sol-gel dip coating, spin coating and casting[53–55] are the most commonly used approaches based on the EISA theory to make periodic inorganic films.

The spontaneous synthesis of films at the air/solution interface was first reported in 1996 by Yang and co-workers.[56] Later, more strategies were developed to prepare free-standing silica films at the air/solution interface.[57–60] Compared to the dip coating and spin coating methods, the growth of silica film at the air/solution interface allows insight study of the growth of the films using many advanced techniques which cannot be applied to the bulk solution, such as surface pressure, *in situ* X-ray/neutron reflectivity and *in situ* grazing incidence small angle X-ray scattering.

Our group has developed an air/solution interface method to synthesise silica film using surfactant-polyelectrolyte complexes as soft templates. The inclusion of a polymer into the templating system made the interactions between each component become more complicated but produced thicker and more robust films.[61,62] In the polyethylenimine (PEI)-CTAB-tetramethoxysline (TMOS) system, the PEI polymer which bears a small amount of positive charge in alkaline solutions are attracted to the surface of the surfactant micelles through a strong anion-mediated interaction and a dipole-cationic interaction. Amine groups are well known to cause precipitation from silica in biological systems, and thus the PEI polymer also promotes silica condensation. Upon the addition of the silica, the negatively charged silica species are able to infiltrate into the aqueous solution to interact with both the surfactant and polymer templates and form a spontaneous CTAB-PEI-silica film at the interface.[57,63]

### 1.1.5 Ordered mesoporous silica film using sodium silicate solution.

The silica source used in previous research in our group was TMOS which is expensive and environmentally unfriendly. While the TMOS ($Si(OCH_3)_4$) is condensing, methanol which has high toxicity is produced.[64] The methanol produced during the condensation will also disrupt the surfactant micelles when the concentration is high, making it difficult to control the size and the shape of the structures in the final materials. We attempted here to find an inexpensive and environmentally friendly silica source, which allows the control of the pore size and shape, to replace TMOS in the recipe for the preparation of silica films.

Sodium silicate ($Na_2SiO_3$), a common and inexpensive material, which condenses into $SiO_2$ as TMOS does, has not previously been reported to be used as a precursor to prepare free-standing silica films. While the sodium silicate is condensing, no poison is produced during the process. The polymerisation of sodium silicate in solution has been widely studied. In mild alkaline aqueous solutions, silica species appear predominantly as $Si(OH)_4^0$ neutral species.[65,66] When sodium silicate is added into highly alkaline solutions (pH >10),[66] the oligomerization of the monomers (Equation 1.3) followed by deprotonation (Equation 1.4) and polycondensation reactions govern the aqueous equilibria:[65,67–69]

$$kSi(OH)_4^0 \rightleftharpoons [Si_kO_l(OH)_{(4k-2l)}]^0 + lH_2O, 2<k<8 \tag{1.3}$$

$$[Si_kO_l(OH)_{(4k-2l)}]^0 + mOH^- + mNa^+ \rightleftharpoons [Si_{nk}O_{(n(l+m))}(OH)_{(4k-2l-m)}]^{(m-)} \cdot mNa^+ + mH_2O \tag{1.4}$$

where m is the number of singly-negatively charged oxygen anions. After that, the produced silica species (Equation 1.4) polymerize with a repetition of n, which also bear negative charges, attracting sodium ions in the solution.

There are many papers that report using sodium silicate solution to synthesise ordered silica materials in the form of powder. Edler *et al.*[70] reported synthesis methods for making an all-silica MCM-41 mesoporous silica of highly long-range order by using sodium silicate solution in 1997. Zhao *et al.*[71] successfully synthesised mesoporous manganosilicate materials (Mn-M41S) with hexagonal, cubic and lamellar structures using a low surfactant to sodium silicate ratio (0.12:1) at various temperatures and acid/base contents. Gallis *et al.*[72] reported the

use of sodium silicate to investigate the effects of the ethanol produced by tetraethoxysilane (TEOS) on the transformation to the MCM-48 structure. The results indicate that only ethanol produced by the TEOS, which is present at the interfacial region of the micelles could induce a structural transformation. Liu *et al.*[42] reported that changing the ratio of the sodium silicate and sodium hydroxide in the synthesis solution enables control of the micelle packing parameter of the surfactant molecules and therefore directing the formation of mesoporous silica with different structures. Lin *et al.*[73] successfully made MCM-41 silica materials with hierarchically structural order by using a mixture of myristyltrimethylammonium bromide, butanol (co-surfactant) and sodium silicate solution. Therefore, sodium silicate is known to be a useful silica source to make mesostructured materials. Additionally, it raises the possibility to be able to control the pore size and the shape since no extra alcohol is produced during the condensation and the polymerisation of sodium silicate.[66–69]

## 1.2 Polyoxometalate (POM), POM-based complexes and their assembly.

Inorganic-organic hybrids contain linked inorganic clusters and organic ligands through covalent bonds or electrostatic interactions form a group of novel surfactants. The hybrids are not only able to integrate the properties (redox activity,[8] catalysis,[9] magnetism[74]) of the inorganic and the organic components, but also show synergistic effects beyond an individual component. In addition, they have potential applications, such as quasi-homogeneous catalysts and templates for functionalised materials with the inorganic clusters. These advantages make them promising amphiphiles for the functionalisation of porous materials.

### 1.2.1 Polyoxometalate (POM)

Polyoxometalates (POMs) are a group of anionic metal oxide clusters[75] with structural diversities. The oxometal polyhedral $MO_x$ (x = 5, 6), are the basic construction units, where M represents early transition metals (TMs, mainly vanadium, molybdenum and tungsten). TMs are typically in their high oxidation states bridged by oxo ligands ($O^{2-}$). The TMs can be substituted by other metals, including Al, Ti, Cr, Mn, Fe, Co, Ni, Cu, Zn, Zr, etc.[76–78]

Polyoxometalates are classified into several groups depending on their composition and structure.[75,79,80] Concerning the compositions, POMs are broken down into two broad subsets:

*i)* POMs containing only one type of TM, $[M_mO_y]^{n-}$, but without an internal heteroatom, are called isopolyoxometalates (isoPOM, represented as $[M_mO_y]^{n-}$). Compared to their heteropolyoxometalate counterparts, they are much more unstable.[81] The molecular structure of an isoPOM, $[M_9O_{16}]^{2-}$, is illustrated in Figure 1.7.[82]

*ii)* Heteropolyoxometalates (heteroPOM) are a group of polyoxometalates that contain additional heteroanions such as $SO_4^{2-}$ or $PO_4^{3-}$, abbreviated as $[X_xM_mO_y]^{n-}$ (X is heteroelement, x is smaller than m). These POMs are widely studied due to their unique catalytical properties, with great emphasis on the Keggin structure ($[XM_{12}O_{40}]^{n-}$, where M represents tungsten or molybdenum) and Well-Dawson structured polyoxometalates. More structure details can be found in

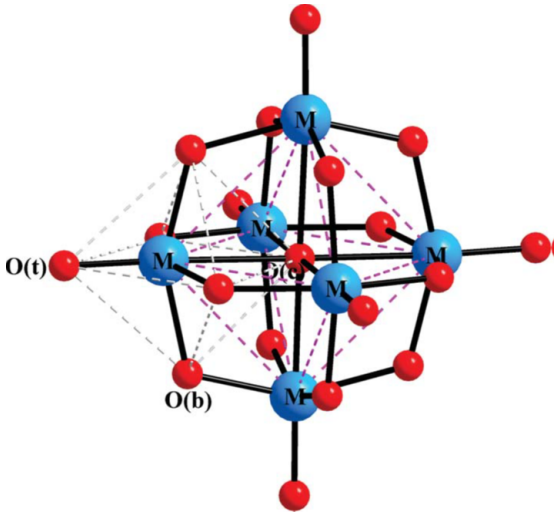


**Figure 1.7** The $[M_6O_{19}]^{2-}$. Coulour code: blue for M (transition metal) and red for oxygen. Adapted with permission from [82].

Figure 1.8, which illustrates the embedment of heteroatoms. The structure on the left represents the Dawson structure.

### The self-assembly of polyoxometalates

Due to the charge that polyoxometalates possess, they are often treated as macroionic clusters. In most cases, unlike small ions like $Na^+$, macroionic clusters spontaneously self-assemble into more stable supra-molecular structures. The self-assembled POMs are thermodynamically stable and transparent in the solution.

Polyoxometalate clusters, not limited to any specific group, [84] can self-assembled into spherical, single layer, vesicle-like, blackberry-type structures (Figure 1.9), [85] such as $Mo_{132}$, [86,87] $Mo_{176}$, [88] $[Cu_{20}Cl(OH)_{24}(H_2O)_{12}(P_8W_{48}O_{184})]^{25-}$ etc. [84] The self-assembly process normally takes several weeks at room temperature. The driving forces have been proven to have no contribution from hydrophobic interaction (as there is no hydrophobic part in the part in POMs) or van der Waals forces. [89] It has been suggested that the formation of the blackberry-type suprastructure is closely related to charge density of the macroions. [90]

### The catalytic performance of polyoxometalates

Polyoxometalates are always bulky and negatively charged. On the surface of the cage are typically abundant oxygen atoms which behave as electron donators. The metal ions in the skeleton of the POMs can accept electrons due to their unoccupied orbitals. In this way, POMs are considered as Lewis acids. [91] POMs may act as Lewis bases under a different condition. Additionally, POMs are recognised as electron reservoirs because they can release and accept electrons without any structural collapses, indicating their redox properties. [92] The high oxidation state of the transition metals, means that POMs can undergo several one-electron or two-electron reversible reductions. For example, the Dawson structure $[P_2W_{18}O_{62}]^{6-}$ undergoes four reversible (one, one, two, two electron) reductions in acidic aqueous solution. Six electrons can be added without

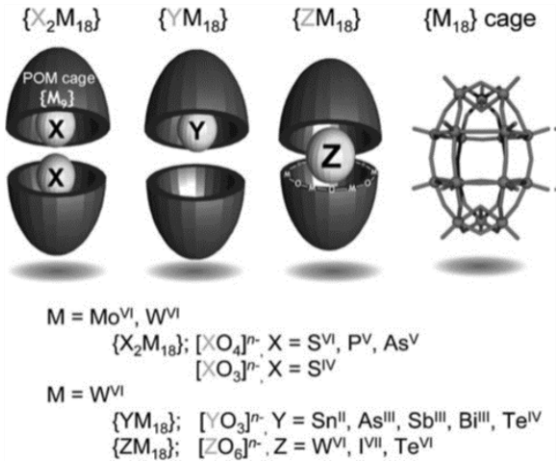


**Figure 1.8** A representation of embedding heteroatoms in POMs. The ellipsoidal $M_{18}$ cages are split open to show the heteroatoms within. The right structure is the $M_{18}O_{54}$ cage. Adapted with permission from [83].

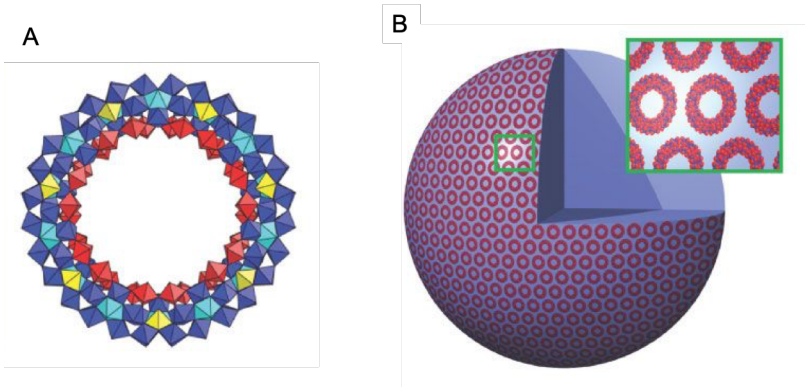


**Figure 1.9** A. $\{Mo_{154}\}$-type nanowheel. B. Schematic representatives showing the typical supramolecular blackberry-type structure formed from $\{Mo_{154}\}$-type nanowheel. Adapted with permission from [85].

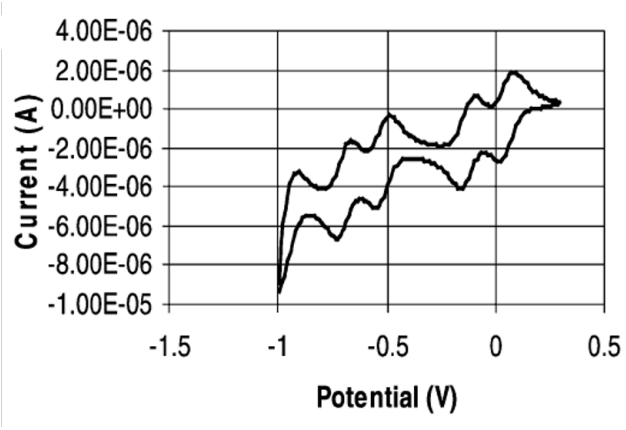


**Figure 1.10** Cyclic voltammetry spectrum of $5\times10^{-4}$ M $[P_2W_{18}O_{62}]^{6-}$ in pH = 7 buffer, scan rate 10 mM/s. Adapted with permission from [93].

decomposition and the corresponding reoxidation waves are well-defined (see Figure 1.10). The reversible redox pairs are affected significantly by the pH of the aqueous solution. In a neutral aqueous solution, $[P_2W_{18}O_{62}]^{6-}$ undergoes several one-electron reductions.[93] In 1998, Steckhan *et al.* summarised the application of POMs as electrocatalysts, a catalyst minimizes the activation energy and hence allow an electrode reaction to occur at a high current density close to the equilibrium potential or even considerably below it. Nadjo and co-workers found that mixed vanado- and molybdotungstophosphoric systems can efficiently oxidise NADH (a coenzyme) at pH = 7 without using high overpotentials which are necessary when using direct oxidation methods at the electrode surfaces.[94,95] Rong *et al.* have found the Ru-substituted heteroPOMs, $PW_{11}O_{39}Ru^{III}(H_2O)$, can be used as an electrochemical oxygen-transfer catalyst.[96]

In addition, POMs have very similar photochemical characteristics to the semiconductor photocatalysts due to the well-defined HOMO-LUMO (highest occupied molecular orbitals-lowest unoccupied molecular orbitals) gaps of POMs that is analogous to the bandgap of semiconductor metal oxides. The HOMO-LUMO gap, shares the same function as the bandgap in semiconductor, and is of vital importance from the aspect of inhibiting the recombination of holes and electrons that are generated from photoexcitation. In the process of a photocatalytic reaction, POMs are photoexcited from their ground state to an excited state by the illumination of UV or near-visible light with energy that is higher than or equals to their HOMO-LUMO bandgap energy (difference in energies between HOMO and LUMO). The nature of the excitation is the charge transfer from an oxygen atom to the $d^0$ of the transition metal.[97] Considering $[PW_{12}O_{40}]^{3-}$ as an example, charge transfer occurs from $O^{2-}$ to $W^{6+}$ during the photoexcitation to form a pair of hole centre ($O^-$) and trapped electron centre ($W^{5+}$).[98] The hole centres further react with $H_2O$ or other electron donors to generate ·OH radicals for photocatalytic reactions due to the strong oxidative ability of the holes. More specifically, the photooxidation properties can be utilised to remove organic pollutants in water,[99–103] and the photoreductive properties are useful for recovery of transition metal ions from water.[104]

### 1.2.2 POM-based molecules and composite materials

POMs usually exist in solid and crystalline states, which limit their performance in diverse systems due to their poor processability and high solubility in polar solvents.[105,106] To create more functionalities based on these intriguing POM clusters for extensive applications, a lot of studies have been conducted to modify POMs with organic groups or other functional species. The modifications are mainly classified according to the type of the bonding interactions into two main categories, non-covalent (Coulombic interactions, hydrogen bond, van der Waals forces and so forth) modification and covalent modification.[107]

#### Non-covalent modifications

It is important to note that Coulombic interactions are already well examined and are considered to be very promising in the soft supramolecular field.[108] Many kinds of organic molecules, such as typical cationic surfactants,[109–111] surfactant with functional groups[112,113] and polymers[114,115] have been employed to functionalize POMs through Coulombic interactions.

Driven by the electrostatic interactions between POMs and cationic species, the counterions in POMs are easily replaced by hydrophobic cations when the POM aqueous solution is mixed with a surfactant chloroform solution. Yang *et al.*[116] designed and prepared surface-modified POM with a cationic surfactant bearing azobenzene (Azo) groups. The Azo-containing POM complexes showed high catalytic activities and can be easily recycled through a simple photo-mediated phase transfer. Driven by Coulombic interaction, surfactant-encapsulated POM (including $[EuW_{10}O_{36}]^{9-}$, $[Eu(PW_{11}O_{39})_2]^{11-}$ and $[Eu(SiW_{11}O_{39})_2]^{13-}$) hybrids were synthesised by Wu's group.[117] The intrinsic property of the surfactant, bearing a carboxylic group at the hydrophobic end, leads to stable and reversible thermotropic liquid crystal properties of these complexes.

Besides mixing the cationic surfactant solutions and POM solutions to produce surfactant-encapsulated POM complexes through charge-charge coupling, the layer by layer (LbL) strategy is another well-known method which makes use of the Coulombic interactions (the detailed process is illustrated in Figure 1.11).[118] This method requires no specific instruments and allows easy preparation of hybrid films with arbitrary thickness and tailored properties. Especially, as most POMs are soluble in polar solvents, they are ideal for LbL techniques. Many studies have suggested that the hybrid films containing polyoxometalates prepared through the LbL approach have synergistic effects. A delicate design of graphene oxide nanosheet (GO)/$H_3PW_{12}O_{40}$ multilayers developed by Li *et al.* exploited the photocatalytic properties of $H_3PW_{12}O_{40}$ to convert GO to reduced GO (rGO) by the irradiation of UV light. The field-effect transistor fabricated using the obtained rGO/$H_3PW_{12}O_{40}$ composite film exhibits good transportation for both electrons and holes.[119] The [tetrakis (N-methylpyridyl) porphyrinato] cobalt (CoTMPyP)/$[SiW_{12}O_{40}]^{4-}$ multilayer films prepared through the LbL method have shown remarkable electrocatalytic performances for hydrogen evolution reaction (HER) in acidic media and are promising in the field of dissolved-oxygen sensors.[120]

The LbL strategy for the fabrication of POM-based composite multilayers are not limited to preparation of POM/inorganic materials. Moreover, charged polymers can accommodate POMs between their layers to afford a three-dimensional structure which presents properties that are

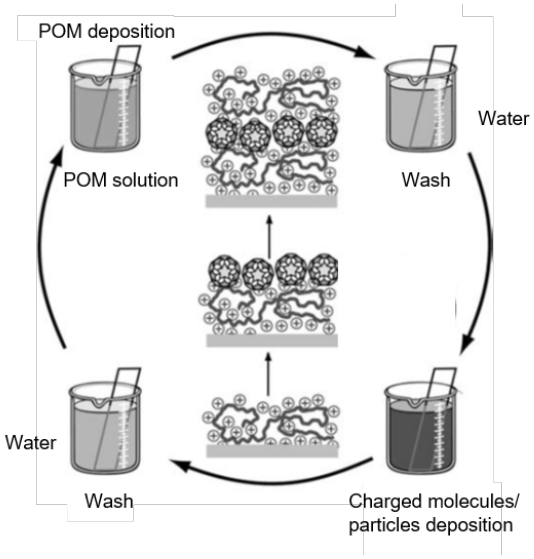


**Figure 1.11** Multilayer growth in a sequential process, in which the substrate is immersed in dilute solutions of oppositely charged species. Combinations of different components in a single film are easily put into practice. Adapted with permission from [118].

absent or less effective in a monolayer structure. Positive-charged polyethylenimine (PEI) has been one of the outstanding candidates in fabricating multilayers with POMs. There are many investigations on the incorporation of POMs, such as $H_3PMoO_{40}$,[121] $[Eu(SiW_4Mo_7O_{39})_2]^{13-}$,[122] $[Eu(SiW_{10}VO_{39})_2]^{15-}$,[123] $[NaP_5W_{30}O_{110}]^{14-}$,[124] $[SiW_{11}O_{39}]^{8-}$,[125] $[SiW_{11}Co^{II}(H_2O)O_{39}]^{6-}$,[125] into PEI layers using the LbL strategy. The Langmuir trough (LB) method also provides a synthesis route to multilayer films and the process is illustrated in Figure 1.12.[126–128]

Considering the inherent drawbacks of non-covalent modification like the inevitable leakage of toxic elements or undesired macroscopic phase separation,[116] the exploration of hybrids with a more stable connection between inorganic components and organic matrices appears to be of significant importance.

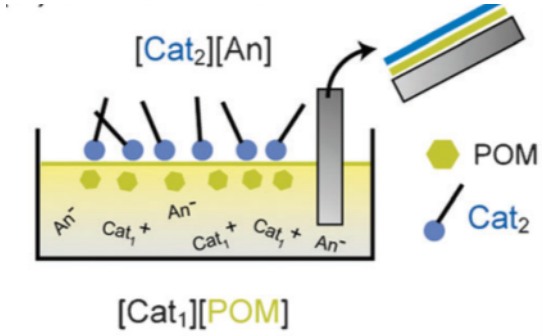


**Figure 1.12** LB film fabrication, Cat1, Cat2 and An represent the initial POM counter-cation, and organic hydrophobic cation and its counter-anion respectively. Adapted with permission from [106].

**Covalent bonding**

Covalent bonding can be achieved through an M-C bond, where M represents the metal atom within the polyoxometalate structure. Yin *et al.* reported the synthesis (see Figure 1.13C) of a single Dawson-cluster-based molecule ($((C_4H_9)_4N)_5H$-$[P_2V_3W_{15}O_{59}(OCH_2)_3CNHCOC_{15}H_{31}]$) and its surfactant properties.[129] Song *et al.* managed to graft tris(hydroxymethyl) amino methane ($[HOCH_2)_3CNH_2]$) onto hydrophilic Mn-Anderson clusters *via* the alkoxo groups. Long alkyl chains were then grafted through covalent amide bonds formed by reaction with the reactive -$NH_2$ groups on the opposite side.[130] M-C bond, when M is other transition metals (such as $Ti^{IV}$, $Zr^{IV}$, $V^{V}$ or $A^{III}$, etc.), is highly prone to nucleophilic attack.[131] In comparison, Si-$C^3_{sp}$ and Sn-$C^3_{sp}$ bonds, which can be formed using siloxane- or stannane- (tin compound with organic substituents) based precursors, are more stable and could bear the attack by nucleophilic species such as water, alcohols, hydroxylated species, etc. The precursors of these compounds are silsesquioxanes $X_3$Si-R-Si$X_3$ (X = Cl, Br or OR), organo-substituted silicic acid esters with a general formula $R_nSi(OR)_{4-n}$ and organostannanes $R_nSi(X)_{4-n}$, where R can be any organofunctional groups and n is usually 1 or 2. R may contain a simple nonhydrolysable group (e.g., alkyl chain) or any reactive group (e.g., amine[130] or methacryloyl group[132]) which can polymerise or copolymerise. The reactive group present a potential to synthesise a new type of organic-inorganic hybrid materials such as heterosilylated anions with an unsaturated terminal (general formula $[PW_9(^t BuSiO)_3(Si(CH_2)_nCH{=}CH_2)]^{3-}$, n= 0, 1 or 4) that were bridged through the Si-C bond between POMs and organic species.[133]

Addition of Si-O to bridge between M and O in the M-O bonds to form M-O-Si-$C^3_{sp}$ has been considered to enable the formation of a stable bond between the POMs and the organic ligands. $R_nSi(OR)_{4-n}$ precursors provide the potential to form M-O-Si-$C^3_{sp}$ covalent bond when grafted onto polyoxometalates. Mayer *et al.* have successfully synthesised $[\gamma$-$SiW_{10}O_{36}(RSiO)_4]^{4-}$ (R= $C_3H_6OC(O)C(Me){=}CH_2$) through four Si-O-W bridges (see Figure 1.13A).[134] The obtained inorganic-organic hybrid possesses a critical micelle concentration of 0.432 mM in water. Polymerisation with acrylamide at the end of the organic group of the hybrid allowed the formation of a gel. Negatively charged POMs in the gel network grant its application as a superabsorbent material. The same research group has also successfully functionalised $[\gamma$-$SiW_{10}O_{36}]^{8-}$ with a ligand containing a methacryloyl group to form $[\gamma$-$SiW_{10}O_{36}$ $(_2HC{=}C(Me)C(O)OPrSi)_2O]^{4-}$ (see Figure 1.13B). The copolymerisation of ethyl methacrylate within the organic component allows the formation of hybrid networks which may contribute to the swelling properties of gels.[132]

These hybrid materials combine not only the advantages of organic components and inorganic clusters, but also promote the close contact and synergistic effect between them, therefore, it is of great interest to develop such organic-inorganic hybrids through covalent functionalisation.

### 1.2.3 Self-assembly of polyoxometalate-based composite

Based on the POM-organic complexes formed through either non-covalent bonding or covalent bonding, extensive studies have been conducted to explore their applications in the materials fields. For example, the surfactant behaviour of POM-organic complexes and gelation of POM-organic complexes have been recently studied.

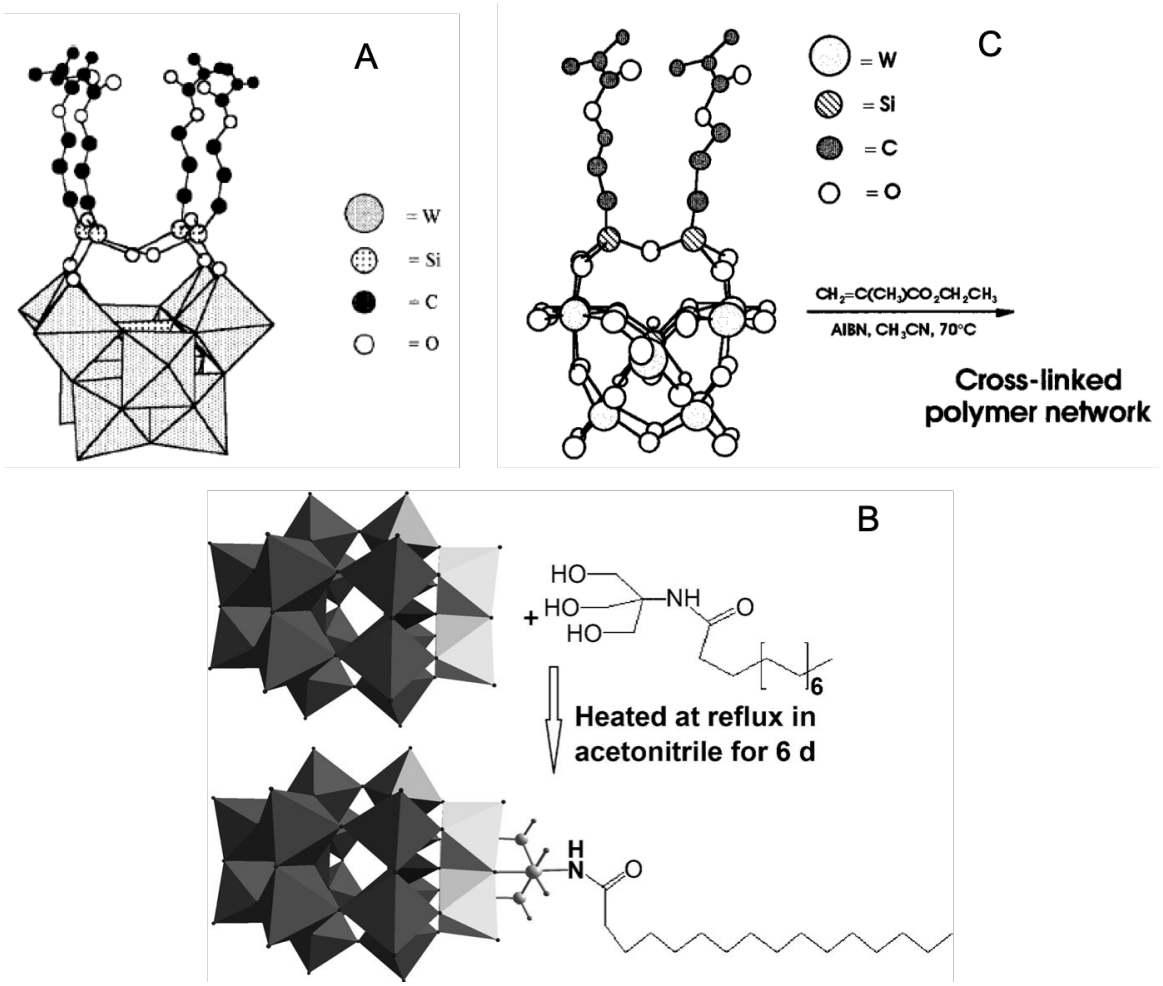


**Figure 1.13** (A)Polyhedral representative of the funtionalised polyoxometalate $[\gamma\text{-}SiW_{10}O_{36}(RSiO)_4]^{4-}$(R= $C_3H_6OC(O)C(Me)=CH_2$). Adapted with permission from [134]. (B)Representation of the functionalized polyanion, $[\gamma\text{-}SiW_{10}O_{36}(_2HCdC(Me)C(O)OPrSi)_2O]^{4-}$ copolymerised with ethyl methacrylate in acetonitrile at 70 °C in the presence of 2,2'-azobis(isobutyronitrile) (AIBN) as radical initiator. Reprinted (adapted) with permission from [132] (C) The illustration the synthesis of surfactant with Dawson-type POMs as polar headgroups. Polyhedron colour code: W=grey, P=black, V=white. Adapted with permission from [129].

### Surfactant behaviour

Many groups including Wei's, Liu's, Wang's and Polarz's research groups have reported different covalently modified POM hybrid clusters.[5,135–141] The solvophobic interaction of these amphiphilic molecules in appropriate solvents can trigger the formation of micelles, vesicles, reverse-vesicle and hexagonal structures,[6,135,136,138–140] which improves the compatibility of the POMs with organic media.

Such organic-inorganic hybrids can be treated as surfactants, and their differences/similarities compared to conventional surfactants are of great interest. The packing parameters can predict the supramolecular structures formed by traditional surfactants in selective solvents.[142] As for POM-based surfactants, the POM headgroups contains more charges than the hydrophilic headgroups of conventional surfactants, so the counterion dissociation around the headgroups strongly influences the structure of the aggregates.[7] In addition, due to the requirements for the synthesis of POM-based surfactants, using the formation of M-C or M-Si-C bond (M represents transition metals), various organic species have been used. The structure of the organic components, the properties of the organic parts and geometry of the obtained POM-based surfactant also affect the resulting supramolecular structures.[129,143,144] Moreover, counterion-mediated attractions between the POM headgroups also contribute to the geometry of the supramolecules.

The driving forces of the amphiphile assembly have also been discussed. When the grafted functional groups, such as peptides, are relatively hydrophilic compared to alkyl chains, they are unable to provide enough hydrophobic interactions for the formation of supramolecular structures.[144] Consequently, hydrogen bonding and counterion-mediated attraction dominate the self-assembly process. Some double-chained POM surfactants have one tail at each side of the POM headgroups.[129] Micelle formation in such surfactants requires a very high bending energy, therefore induces a very slow aggregation rate. When the organic groups grafted possess aromatic functional groups such as phenyl rings,[110] the competition of interaction between counterions with the anionic headgroups (electrostatic interaction) and between counterions with pyrenes in the organic group (cation-$\pi$)[145] modulated the conformation of the micelle structures.[146]

To conclude, the behaviours of such hybrid molecules in solution are predominantly controlled by the competition between the counterion-mediated attraction and other types of attractions such as hydrogen bonding, hydrophobic interaction and cation-$\pi$ interaction, which consequently determines whether they assemble in the manner of macroions or as amphiphilic surfactants.[7]

### Gelation

Gels, solid jelly-like soft materials that can have properties ranging from soft and weak to hard and tough,[147] are of interest as a result of their unique features and potential applications as new organic soft materials.[148,149] Gelation is favoured by non-covalent bonds, such as van der Waals interactions, hydrogen bonds and $\pi$ stacking interactions. Preliminary POM-based supramolecular gels were prepared by physically mixing POMs into organic gel matrices.[150] A bottom-up approach has been used to fabricate POM-containing gels by mixing with a hydro-gelator.[151] POMs are randomly dispersed in these gels. The preparation of well-organised POMs-incorporated gels is significant to tune the properties of gels.

Hydrogen bonding is found to exist between the terminal oxygen atoms of POM-containing complexes and hydrogen atoms of the organic component, which provides an alternative route to the construction of well-organised POM-based gels. He *et al.* designed a gel system based on pyridyl grafted Anderson-type POM complexes ($[MnMo_6O_{18}((OCH_2)_3CNHCOC_5H_4N)_2]^{3-}$, TBA-Py-$MnMo_6$) possessing tetrabutylammonium counterions.[152] The gel formation was assisted with carboxylic acid since bare TBA-Py-$MnMo_6$ only crystallizes from the solution. The unidirectional hydrogen bond between pyridyl groups and the carboxylic groups of dicarboxylic acid was demonstrated to be the driving force to connect TBA-Py-$MnMo_6$ with the dicarboxylic acids, resulting in the formation of polymer chains in the gels. More well-dispersed POM-containing gel systems have been prepared by utilising the hydrogen bond or van der Waals force introduced by grafting organic species onto POMs.[153–155]

## 1.3 Polyoxometalate-$TiO_2$

Some POMs have been incorporated into photoactive and inactive support materials[101,156–158] to achieve the recovery of POMs,[101,157] synergistic effect[158,159] and higher BET specific surface areas.[160] Due to the photocatalytic properties of POMs, as discussed before, POMs possess energy levels (LUMO and HOMO) corresponding to the CB and VB of semiconductors. The combination of POMs and semiconductor photocatalysts is therefore expected to enhance their photodegradation properties. $TiO_2$ material is one of the most widely studied and used photocatalysts. So far, a series of POM-$TiO_2$ hybrid materials were studied and were proven to behave more efficiently.[159,161,162] Different approaches have been exploited to fabricate POM-$TiO_2$ hybrid materials, including physical mixing, electrostatic interaction, and surface modification.

### 1.3.1 Physical mixing

POMs and $TiO_2$ are usually physically mixed well in solutions or in a sol-gel approach. The properties of the mixtures (solutions or pastes) containing $TiO_2$ and POMs, such as $[PW_{12}O_{40}]^{3-}$, $[P_2W_{18}O_{62}]^{6-}$, $[SiW_{12}O_{40}]^{4-}$, and $[W_{10}O_{32}]^{4-}$ have been investigated.[159,161,162] The effect of the variation in the amount of added POMs in the mixtures on their efficiency in photooxidizing 1,2-dichlorobenzene (DCB) was compared.[161] The rate constants of the photodegradation ($k_{rate}$) were observed to have a different maximum value for each type of POM studied. The maximum values occurred at 0.1 mM for $[PW_{12}O_{40}]^{3-}$ ($k_{rate} = 0.0318$ min$^{-1}$), 0.07 mM for $[SiW_{12}O_{40}]^{4-}$ ($k_{rate} = 0.0108$ min$^{-1}$) and 1 mM for $[W_{10}O_{32}]^{4-}$ ($k_{rate} = 0.0066$ min$^{-1}$). The distinction was explained through estimating the free energy of one electron reduction as follows: the reduction of $[W_{10}O_{32}]^{4-}$ is more endothermic than the reduction of $O_2$ under the experimental conditions compared to the reduction of the other two types of POMs which were more favourable than $O_2$ and hence kinetically favoured. Therefore, the performance improvements are predominately due to the role of POMs as an effective electron scavenger. When the POM concentration in the system reached 2 mM or more, the competition for surface sites of $TiO_2$ between POMs and DCB, and the direct reoxidation of the reduced POMs by the photo-generated holes decrease the degradation rate constant significantly.

POMs and $TiO_2$ components were also physically mixed in a paste and coated onto fluorine-doped tin oxide (FTO) to improve the photoelectrochemical properties.[159] The synergistic effect between POMs and $TiO_2$ was studied by various electrochemical analysis methods, it turned out

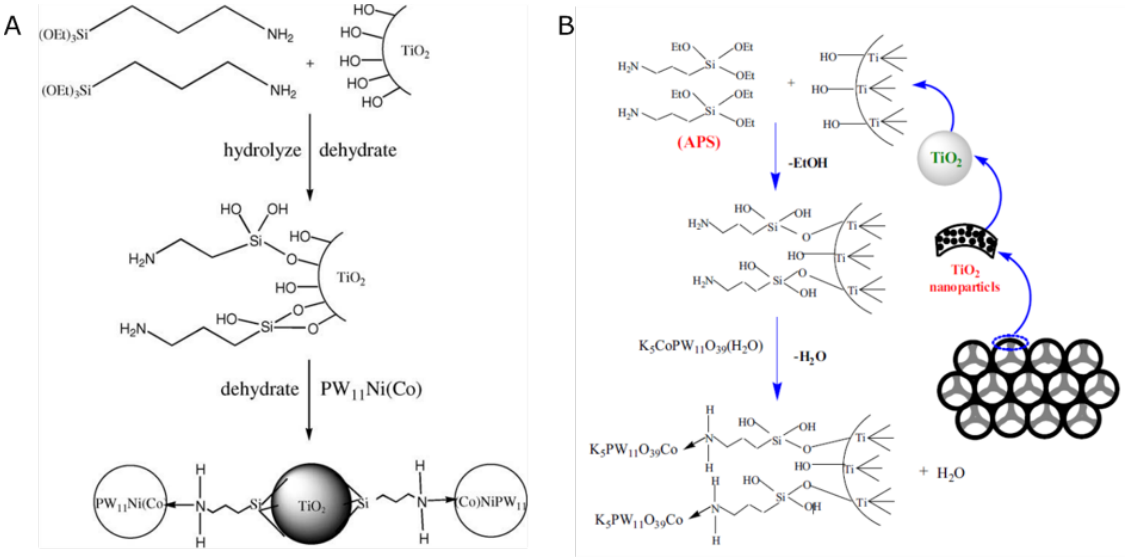


**Figure 1.14** (A) Pathway of preparation of $TiO_2$-APS-$PW_{11}M$ (M = Ni/Co). (B) Pathway for the preparation of $PW_{11}Co$-APS-$TiO_2$. Where APS stands for 3-aminopropyltriethoxysilane. $PW_{11}M$ represents transition metal (M)-monosubstituted polyoxometalates, $K_5[M(H_2O)PW_{11}O_{39}]$), where M is Ni or Co.Adapted with permission from [168,169].

that POMs are favourable in facilitating the electron transportation and suppressing the electron-hole recombination.

The physical mixing method has successfully achieved synergism, however, POMs experience difficulties in recycling due to the weak interaction between POMs and $TiO_2$ and the high solubility of POMs in most solvents. Moreover, the dispersion of POM within the system is random without any organisation.

The sol-gel method, is another method to prepare POM-dispersed within $TiO_2$ matrixes, [163–165] which not only enhance the photocatalytic efficiency due to the synergistic effect but also allows the separation and recovery of POMs from the reaction environments. However, this method limits the accessible surface area to POMs.

### 1.3.2 Electrostatic interaction and surface modification

Surface modification of $TiO_2$ using molecules containing pyridine or amine group allows the formation of coordination bond with transition-metal-substituted polyoxometalates. [166,167] A well-known method, as illustrated in Figure 1.14, utilises 3-aminopropyltriethoxysilane or ammonia as a bridge between $TiO_2$ and transition metal-substituted Keggin-structured polyoxometalates. [168–170]

Bansal's group [171–173] has reported the exploitation of electrostatic interactions between the negatively-charged POMs and the amine-modified $TiO_2$ nanoparticles or bare $TiO_2$ as a driving force. The as-prepared POM-$TiO_2$ composites exhibit more effective degradation properties and are used as a precursor to facilitate deposition of noble metals directly introduced into the system

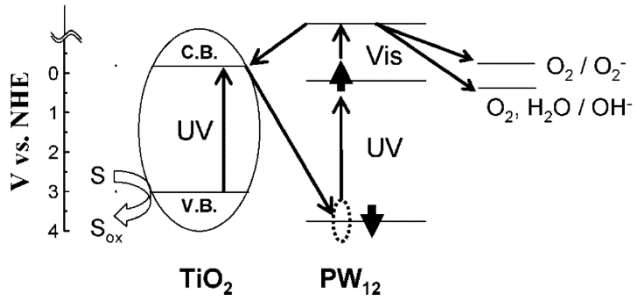


**Figure 1.15** Energy diagram of the $PW_{12}O_{40}$-$TiO_2$ system. Adapted with permission from [176].

through UV irradiation.

### 1.3.3 Synergistic effect between POMs and $TiO_2$

The synergistic effect between $TiO_2$ and polyoxometalates have been widely studied. An agreement has been achieved that the improvement in performance is attribute to enhancement of charge pair separation.[174–176] For instance, as illustrated in Figure 1.15, $[PW_{12}O_{40}]^{3-}$ ($PW_{12}$) and $TiO_2$ are excited simultaneously when irradiated by UV light. The holes in $PW_{12}$ have a very strong oxidation power and trap the electrons from the conduction band of $TiO_2$. The charge-transfer excited polyoxometalate (POM*) possesses stronger reduction power than ground-state POM, which then react with water and oxygen to produce radical species for photocatalytic reaction with the generation of ground-state POM to be reused.

## 1.4 Conclusion

This chapter has given an outline about the application of traditional surfactants in templating mesoporous silicas, and discussed polyoxometalates, POM-based surfactants and the potential application of POM-based surfactants to synthesise hybrid materials with enhanced properties. This thesis has exploited the templating of inorganic materials using both traditional surfactant (CTAB) and POM surfactant as template.

As discussed in section 1.1, the use of TMOS as the silica precursor limmited the control of structure of the prepared silica films. The 3rd chapter exploits the possibilities of using sodium silicate solution as silica precursor to better control the pore size and the morphology of the film structure. The method used is a previously developed system developed in our group,[57,59] which used a traditional organic surfatant, hexadecyltrimethylammonium bromide (CTAB) as a structure-directing agent to synthesise silica film at the air/solution interface. *In situ* X-ray reflectivity and grazing incidence small angle X-ray scattering at synchrotron were used to follow the growth of the silica films.

Traditional surfactants only behave as templates, which are burnt away to leave only tem-

plated inorganic materials. As discussed in section 1.2, many studies focused on the modification of POMs to prepare POM amphiphiles to functionalize materials simultaneously while the templating process. Therefore, novel surfactants bears inorganic polyoxometalate as the headgroup are designed and prepared.The 4th and 5th chapter of this thesis cover studies that involve the designed POM-based amphiphiles designed for the use as surfactant templates for functionalize mesoporous materals. Double hydrocarbon chains were grafted onto a Dawson structure phosphotungstate through covalent bonding, the resulting products are denoted as POM-2$C_n$ (n = 12, 14, 16 and 18). The CMCs of the prepared POM-2$C_n$ and their mixture with commercial nonionic surfactants were determined. SANS and DLS are applied to study their aggregates in water. Salt effects on these pure POM-2$C_n$ surfactant systems and the POM-2$C_n$/$C_{12}EO_8$ systems are also studied using SANS technique.

As in the extensive studies on the synergistic effect between POM and $TiO_2$ discussed in section 1.3, the POM-2$C_n$ systems were utilised to template titanium dioxides to prepared POM functionalised $TiO_2$ (POM-$TiO_2$) hybrid materials. The prepared POM-$TiO_2$ hybrid materials exhibit an enhanced property in degrading rhodamine B and are recyclable for at least 8 times.

# 2 Techniques

## 2.1 Principle of analysis

Various techniques have been used in this study. The as-prepared silica/surfactant/polymer hybrid films were characterised using a lab-based SAXSess instrument. To understand the film forming process, the formation of silica/surfactant/polymer hybrid films were investigated *in situ* using X-ray Reflectivity (XRR) and Grazing Incidence Small Angle X-ray Scattering (GISAXS) at I07 beamline at Diamond Light Source. The energy resolution is measured to be $\Delta E/E = 2.47 \times 10^{-4}$.

The self-assembly of the novel surfactants POM-2C$_n$ was studied using small angle scattering using neutrons (SANS) and X-rays (SAXS) and Dynamic Light Scattering (DLS). The prepared POM-TiO$_2$ materials were studied using a lab-based SAXSess instrument. The obtained SAXS and SANS data were analysed using Sasview software.

Thermalgravimetric analysis (TGA) was applied to study the composition ratio of the organic component in the silica/surfactant/polymer, POM-2C$_n$ materials. The porosity of the obtained porous films and powders were tested using nitrogen adsorption and desorption measurements. This chapter covers the principles underlying each of these characterisation techniques and describes relevant information about the sample environment and data processing.

### 2.1.1 X-ray and neutron basics

**X-rays**

X-rays are a form of electromagnetic radiation with wavelengths ranging from 0.1 to 100 Å corresponding to energies ranging from 100 eV to 100 keV, which makes it possible to detect much smaller structures than visible light. X-rays with wavelengths between 0.5 and 2.5 Å are normally used in material structure characterisation.

Laboratory X-rays can be generated from sealed-tubes, which are built as a vacuum-sealed metal glass cylinder, where electrons emitted from a heated tungsten filament are accelerated by a high voltage (between a tungsten filament cathode and a metal anode) and hit the metal target under vacuum conditions. The spectrum emitted consists of (1) Bremsstrahlung electromag-

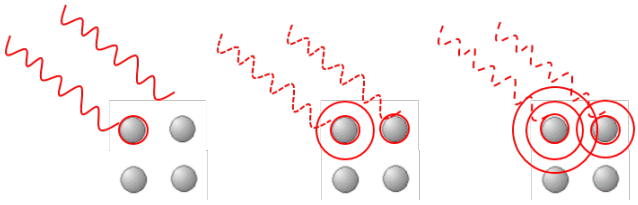

**Figure 2.1** Illustration of X-ray scattering, where grey spheres are atoms and red lines are incident X-rays and scattered X-rays.

netic radiation which is generated due to a loss of kinetic energy when electrons are slowed down through interactions with the electric field of an atomic orbital. (2) Characteristic X-rays emitted when an inner shell electron is ejected (kinetic energy exceeds the binding energy). [177] The X-ray energy limit is determined by the applied voltage between cathode and anode. Characteristic $K_\alpha$ X-rays generated from a copper target are normally used in laboratory material characterisation. A monochromator is used to select the X-rays with the specific wavelength from a broad spectrum.

At the Diamond synchrotron source, electrons are generated by an electron gun with an energy of 90 keV and then are fed into the first linear accelerator to be accelerated to 100 MeV. Before injected into the storage ring, the energy is boosted into 3 GeV. More information can be found on the Diamond light source website.

X-rays propagate and interact with matter. As shown in Figure 2.1, X-rays are scattered at the electrons of the atomic shell. During the interaction, the electron starts oscillating and sending out a dipole and a spherical wave.

There are three main interactions: photoadsorption, Compton scattering and Rayleigh scattering. Photoadsorption happens when the incident photons interact with an inner-shell electron resulting in total absorption. Compton scattering dominates at higher energies. Compton scattering (incoherent scattering) [178] happens when a photon interacts with an outer orbital electron and subsequently bounces away. Energy loss occurs during the whole process, resulting in a different wavelength compared to the incoming radiation. Rayleigh scattering (coherent scattering) [179] is produced when a photon collides with the electron, which absorbs all the energy from the photon, and emits radiation with the same frequency as the incident radiation. Since the emitted waves from neighbouring atoms oscillate synchronously, the coherent scattering can carry the information about the material structures.

Figure 2.2 is an illustration of an X-ray scattered by a single electron. A flux ($J_0$) of photons arrives along the X-axis and interacts with the single electron at the point O. A detector is put at the point P, which lies in XY plane with an angle $2\theta$ from the X-axis with a distance of R from O. The electric field vector of the incident photons, $E_0$, is in the XZ plane which is perpendicular to the Y-axis direction. The energy that reaches point P each second per area unit equals:

$$J_0(\frac{e^2}{mc^2})^2 \frac{1}{R^2} \frac{1+(\cos 2\theta)^2}{2} \tag{2.1}$$

where $J_0 = E_0^2$, m and e are the mass and the charge of an electron, respectively. $1/R$ is the solid angle between the unit area at P and O point. The $e^2/mc^2$ term is the classical radius of an

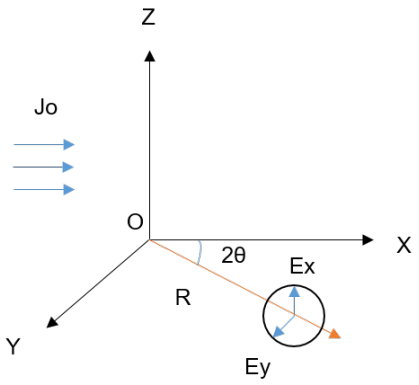


**Figure 2.2** Scattering of an unpolarized X-ray by a single free electron at the origin.

electron ($r_e$). Thus, the differential scattering cross-section of an electron for unpolarised X-rays is:

$$(\frac{\partial\sigma}{\partial\Omega})_e = r_e^2 \frac{1+(\cos 2\theta)^2}{2} \tag{2.2}$$

The scattering length of a single electron ($b_e$) from non-polarized X-rays is:

$$b_e = r_e(\frac{1+(\cos 2\theta)^2}{2})^{1/2} \tag{2.3}$$

By integrating throughout the solid angle Ω, the total scattering cross-section of an electron ($\sigma_e$) is calculated to be:

$$\sigma_e = \frac{8}{3}r_e^2 \tag{2.4}$$

Therefore, the scattering of X-rays from matter results entirely from the electrons in an atom. The X-ray scattering factor increases with the atomic number. Therefore, with X-rays, scattering from heavy atoms, such as metal atoms present in an organic molecule, can often overwhelm the scattering from the rest of the molecule. The local interaction of radiations with materials is characterised by a scattering length $b_i$ and the real space pair electron density of scatterers $\rho_i$(r):

$$\rho(r) = \sum \rho_i(r) b_i \tag{2.5}$$

X-ray scattering length densities of different materials are calculated using Equation 2.5 and are listed in Table 2.1.

To clarify the difference between some of the techniques used in this study, the geometry of X-ray techniques used here are illustrated in Figure 2.3.[183] When the incident beam has a small incident angle with respect to the sample surface, GISAXS measures the off-specular scattered intensity near the specularly reflected beam with beam stops to block the direct beam and the specularly reflected beam; XRR measures the specularly reflected beam. When the incident beam has a large incident angle, Grazing Incidence Diffraction (GID) measures the scattered intensity at a relatively large scattering angle. The techniques I used here are XRR and GISAXS. Another technique I used is Small Angle X-ray Scattering (SAXS), which applies a collimated beam on the bulk of samples, measuring scattered X-ray radiations and the transmitted intensities are recorded for analysis.

**Table 2.1** X-ray scattering length densities of a selection of materials.[a]

| Compound | Structure | Density (g/cm$^3$) | X-ray SLD ($\times 10^{-6}$ Å$^{-2}$) |
|---|---|---|---|
| CTAB headgroup | $N(CH_3)_3$ | 0.926 [180] | 9.01 |
| CTAB tail | $CH_3(CH_2)_{15}$ | 0.816 [180] | 7.94 |
| SDS headgroup | $OSO_3$ | 0.702 [181] | 5.93 |
| SDS tail | $CH_3(CH_2)_{11}$ | 0.802 [181] | 7.77 |
| TMOS | $Si(OCH_3)_4$ | 1.023[a] | 1.02 |
| Water | $H_2O$ | 0.997[a] | 9.37 |
| Silicon oxide | $SiO_2$ | 2.160 [180] | 18.20 |
| PEI | $(CH_2CH_2NH)$ | 1.080[a] | 10.20 |
| $C_{12}H_{25}$ | | 0.802 [182] | 7.44 |
| $C_{14}H_{29}$ | | 0.809[b] | 8.02 |
| $C_{16}H_{33}$ | | 0.816[b] | 8.07 |
| $C_{18}H_{37}$ | | 0.825[b] | 8.13 |

a. density obtained from MSDS form on the Aldrich website.

b. density is calculated using molecular weight and volume predicted using Tanford equation. [12]

### Neutrons

Neutron flux in a reactor neutron source, such as ILL, is produced by the fission of $^{235}$U nuclei and always contains a wide range of neutron wavelengths. Therefore, it is necessary to obtain a narrow range of neutron wavelengths using a monochromator. Alternatively, the neutron beam can be produced by an interaction between a fired proton and a heavy metal target, which is called a spallation neutron source. The ISIS Neutron Scattering Facility is a spallation source.

In structural studies, small angle neutron scattering covers the same range of spatial resolution as small angle X-ray scattering. The major difference between the techniques lies in the interaction between the probing radiation and the sample. X-rays are scattered by electrons and neutrons are scattered by nuclei. Therefore, the strength of this interaction, termed as the scattering length, is not as a function of atomic number for neutrons. The scattering length varies randomly throughout the periodic table. [184] The neutron scattering lengths of hydrogen $^1$H and deuterium $^2$H are very different. This allows the use of neutron scattering with isotopic labelling to highlight molecules or sections of molecules while studying materials.

The neutron cross-section is used to describe the amount of the neutrons that have been scattered by the scatterers. Assuming it is elastic scattering, the total scattering cross-section has the same expression as X-rays:

$$\sigma_{tot} = 4|b_n|^2 \tag{2.6}$$

where $b_n$ is the neutron scattering length. The differential cross-section for the assembly of nuclei is obtained as:

$$\frac{\partial \sigma}{\partial \Omega}(q) = \frac{1}{n}|\sum_{i}^{n} b_{n,i} \exp(iqr)|^2 \tag{2.7}$$

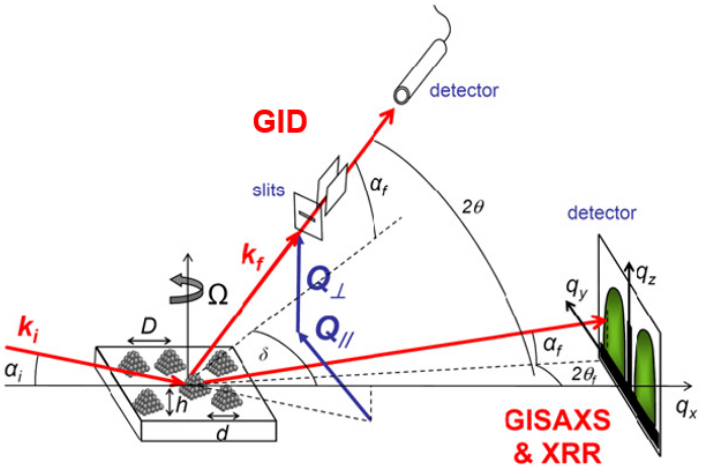


**Figure 2.3** Grazing incidence X-ray/neutron scattering geometry, at small angles (GISAXS and XRR), and relatively large angles (GID). Adapted with permission from [183].

Neutron scattering is a powerful technique to investigate the structure of materials, it has several advantages when compared to X-ray scattering.

1. Neutron scattering is radiation scattered from nuclei, and the effect of isotopic substitution is generally large.

2. Deuterium-labelling can be used to enhance scattering from parts of a system due to the fact that the scattering lengths for hydrogen and deuterium are very different.

3. Due to the weak interaction between neutrons and nuclei, neutrons are very penetrating, making it a useful technique as a bulk probe.

4. Neutrons have a magnetic moment that can couple directly to the magnetisation of materials on the atomic scale. [185]

### 2.1.2 Small Angle X-ray Scattering (SAXS)

Electromagnetic radiation can be used to obtain information about materials whose dimensions are on the same order as the wavelength of the radiation. [186] SAXS experiments generally follow the procedure as shown in Figure 2.4. A sample is irradiated by a collimated X-ray beam. The direct beam is blocked by the beam stop placed in front of the detector. Scattering patterns are caused by the interference of secondary waves that are emitted from the various structures when irradiated. Scattering of X-rays is related to the differences in electron density. The larger the diffraction angle is, the smaller the length scale probed. Wide angle X-ray scattering (WAXS) is used to determine crystal structure on the atomic length scale while SAXS is used to explore microstructure on the colloidal length scale (1 nm - 100 nm). Unlike an electron micrograph, a small angle X-ray scattering pattern does not give morphological information directly. The result of a SAXS experiment is essentially the intensity of the Fourier transform of the electron density profile within the matter and must be interpreted in order to determine the morphology. SAXS results are normally given as a function of the momentum transfer, $q$, which is related to the angle between the incident beam and wavelength of the radiation. The obtained patterns need

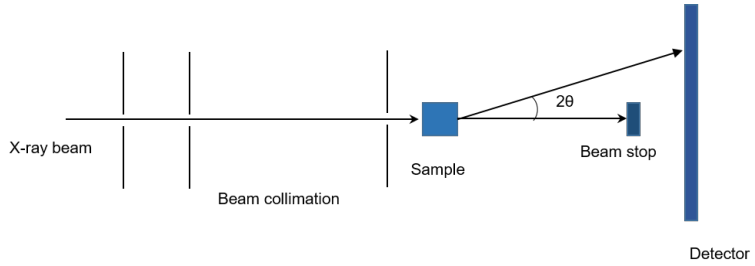


**Figure 2.4** Schematic of Small Angle X-ray scattering.

to be modelled to extract the structural information.

SAXS has been widely used to study colloidal or suspension systems, where micelles or particles of one material are dispersed in a uniform matrix of a second material. The characterisation theories are similar for these two systems. Here a particulate suspension is discussed for an example.

For a particulate suspension, when the concentration is low, e.g. in a dilute solution, there are no correlations between positions or orientations of particles. The wave scattered from each individual particle is incoherent, and the observed intensity simply becomes a sum of the individual particle scattering. In a dilute particulate system, the matrix is assumed to be devoid of any internal structure and simply presents a uniform, homogenous background. There is always a fluctuation in a real system (both solid and liquid), but as long as the scale size of such inhomogeneity is much smaller than $1/q$, the effect does not manifest itself in the $q$ range of interest here.

When X-rays of known wavelength are scattered, a momentum transfer, q, can be defined that equals $(2\pi/\lambda)(k - k_0)$ ($k$ is the scattered vector and $k_0$ is the incident vector). This definition is based on the wavelength of radiation, $\lambda$, and unit vectors in the incident and scattered X-ray directions, respectively, $k_0$ and $k$. As shown in Figure 2.4, the angle between $k_0$ and $k$ is $2\theta$. Thus the resulting momentum transfer, q, equals $(4\pi\sin\theta)/\lambda$. The scattering vector is the basis for all scattering equations. Information about the size, shape and correlations of particles within the sample can be obtained by analysing the resulting scattering pattern.

### Form factor P(q)

The form factor P(q) describes the scattering from a single particle, which strongly depends on its size and shape. The scattering intensity $I(q)$ as a function of the momentum transfer $q$ can be expressed by:

$$I(q) = \frac{\partial \sum q}{\partial \Omega} = \frac{1}{V} \left| \int_0^V \rho(r) e^{(-iqr)} dr \right|^2 \tag{2.8}$$

where $\rho$(r) is the real space pair electron density, $V$ is the illuminated volume. The scattering intensity is proportional to the square of the Fourier transform of the $\rho$(r) as seen in Equation 2.8.

For a two-phase system consisting of: $N_p$ monodispersed particles with a uniform scattering length density $\rho_p$ dispersed in a matrix, which has a scattering length density at $\rho_m$, the integral

can be separated into a uniform integral over the whole volume of the sample ($V_{total}$) and a term equal to the difference of scattering length density between the particles and the matrix ($\rho_p$ - $\rho_m$).[187] I(q) is further approximated as:

$$I(q) = \frac{\partial \sum q}{\partial \Omega} = \frac{N_p}{V_{total}}(\rho_p - \rho_m)^2 V_p^2 |\frac{1}{V_p}\int \rho(r) e^{(-iqr)} dr|^2 \tag{2.9}$$

where $V_p$ is the volume of each particle in the system. The form factor is expressed by:

$$P(q) = |\frac{1}{V_p}\int \rho(r) e^{(-iqr)} dr|^2 \tag{2.10}$$

The volume fraction of the particle ($\Phi_p$) in the system equals to $N_p V_p / V_{total}$. Then the scattering cross-section is further written as:

$$I(q) = \frac{\partial \sum q}{\partial \Omega} = (\rho_p - \rho_m)^2 V_p \Phi_p |\frac{1}{V_p}\int \rho(r) e^{(-iqr)} dr|^2 \tag{2.11}$$

Therefore, the scattering cross-section is proportional to the contrast factor, ($\rho_p$ - $\rho_m$)$^2$, the particle volume, $V_p$, the particle volume fraction, $\Phi_p$ and the form factor P(q).

The expression of the form factor depends on the shape of the particles. The simplest example of a form factor is the one for sphere which has a form factor of the equation as:[188,189]

$$P(q) = 9[\frac{\sin(qR_s) - qR\cos(qR_s)}{(qR_s)^3}]^2 \tag{2.12}$$

where $R_s$ is the radius of the sphere. The form factor of a monodispersed spherical particle with a core-shell structure is expressed as:[188,189]

$$P(q) = \frac{1}{V}[\frac{3V_c(\rho_c - \rho_s) j_1(qr_c)}{qr_c} + \frac{3V_s(\rho_s - \rho_{solv}) j_1(qr_s)}{qr_s}]^2 \tag{2.13}$$

where $j_1(x) = (\sin x - x\cos x)/x^2$; $r_s = r_c + t$ with $r_s$, $r_c$ and $t$ are the size of the total radius of the particle, radius of the core and the thickness of the shell of the particle; $V_i = (4/3)r_i^3$; $\rho_s$, $\rho_c$ and $\rho_{solv}$ are the scattering length density of the shell, the core and the solvent.

The calculated intensity of a ellipsoidal particle with core-shell structure is expressed as:

$$P(q,\alpha) = \frac{Scale}{V} F(q,\alpha) + background \tag{2.14}$$

where

$$F(q,\alpha) = f(q, R_{core}, R_{core} \times x, \alpha,) + f(q, R_{core} + t, R_{core} \times x + t, \alpha) \tag{2.15}$$

where $R_{core}$ is the radius of the core, t is the shell thickness and x is the elipticity of the core, $\alpha$ is the angle between the axis of the ellipsoid and q.

$$f(q, R_1, R_2, \alpha) = \frac{3\Delta\rho V(sin[qr(R_1, R_2, \alpha)] - cos[qr(R_1, R_2, \alpha))]}{(qr(R_1, R_2, \alpha))^3} \tag{2.16}$$

and

$$r(R_1, R_2, \alpha) = (R_1^2 sin^2\alpha + R_2^2 cos^2\alpha)^{1/2} \tag{2.17}$$

### Polydispersity

The Schulz distribution is applied when a polydispersity is required in the fitting process. The Schulz distribution is defined as:[190,191]

$$f(x) = \frac{1}{Norm}(z+1)^{(z+1)}(x/\overline{x})^{z}\frac{exp[-(z+1)x/\overline{x}]}{\overline{x}\tau(z+1)} \tag{2.18}$$

where $\overline{x}$ is the mean of the distribution, Norm is the normalisation factor which is determined during the numerical calculation. And z is a measure of the width of the distribution.

### The Guinier plot

The Guinier law[189] is widely used to determine the gyration radius of the particle only considering the size of the particles. For a dilute monodisperse spherical particle system, assuming the orientation of the particles is spatially averaged and the solution is isotropic, Equation 2.8 can be rewritten as Equation 2.19 in the low $q$ range.[192]

$$I(q) = \frac{\partial \sum q}{\partial \Omega} = \frac{1}{V}|\int_{0}^{V}\rho(r)dr|^{2}[1-\frac{R_g^2}{3}q^2+\dots] \tag{2.19}$$

where the integral corresponds to the scattering intensity at $q = 0$ ($I(0)$), the right part is approximated into an exponential form. Equation 2.19 is thus:

$$I(q) = \frac{\partial \sum q}{\partial \Omega} = I(q=0)e^{(-\frac{R_g^2}{3}q^2)} \tag{2.20}$$

The slope which equals $R_g^2/3$ is obtained through fitting the plot $ln(I(q))$ *versus* $q^2$ in Equation 2.22 at the range of $qR_g < \sqrt{3}$. ln refers to the natural logarithm.

$$ln(I(q)) = ln(I(q=0)) - \frac{R_g^2}{3}q^2 \tag{2.21}$$

For a spherical particle with a radius $R_s$:

$$R_g = \sqrt{\frac{3}{5}}R_s \tag{2.22}$$

### Structure factor S(q).

For a higher concentration where the particles in the system are interacting with each other, the calculation of the structure factor S(q) is also required.

Herein, we discuss a system with $N_s$ particles which occupy volume $V_s$ with a contrast factor $\Delta\rho^2$, and where the volume of a single particle is $n_s v_s$ ($n_s$ is the repetition segment number in the particle and $v_s$ is the volume of a singular segment). The scattering cross-section includes two parts, the intra-particle and the inter-particle components, and is given below:[193]

$$I(q) = \frac{\partial \sum q}{\partial \Omega} = \Delta\rho^2\frac{v_s^2}{V_s}[\sum_{a=b}^{N_s}\sum_{i,j}^{n_s}e^{-i\vec{q}\vec{r}_{aibj}} + \sum_{a\neq b}^{N_s}\sum_{i,j}^{n_s}e^{-i\vec{q}\vec{r}_{aibj}}] \tag{2.23}$$

in this equation, a and b indicate the two interacting particles, i and j present as different segments

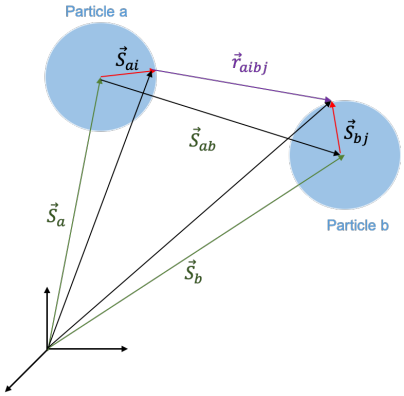


**Figure 2.5** Schematic representation of the coordinate system showing two scatterers.

in the particle a and b. The momentum transfers are illustrated in Figure 2.5. Since the particles in the dispersion are identical, therefore, the equation can be written as: [193]

$$I(q) = \frac{\partial \sum q}{\partial \Omega} = \Delta\rho^2 \frac{v_s^2}{V_s}[N_s \sum_{i,j}^{n_s} e^{-i\vec{q}\vec{r}_{aibj}} + N_s(N_s-1)\sum_{i,j}^{n_s} e^{-i\vec{q}\vec{r}_{aibj}}] \tag{2.24}$$

The distance, $\vec{r}_{aibj}$ between particle a and b can be expressed as $\vec{r}_{aibj}$ = -$\vec{S}_{ai}$+$\vec{S}_{bj}$+$\vec{S}_{ab}$ and hence the inter-particle scattering can be written as the sum of several parts: [193]

$$e^{-i\vec{q}\vec{r}_{aibj}} = \langle e^{i\vec{q}\vec{S}_{ai}}\rangle\langle e^{-i\vec{q}\vec{S}_{bj}}\rangle\langle e^{-i\vec{q}\vec{S}_{ab}}\rangle \tag{2.25}$$

Therefore, the form factor amplitude is then [193]

$$\sum_{i,j}^{n_s} e^{-i\vec{q}\vec{r}_{aibj}} = \langle e^{-i\vec{q}\vec{S}_{ab}}\rangle \sum_{i}^{n_s}\langle e^{i\vec{q}\vec{S}ai}\rangle \sum_{i}^{n_s}\langle e^{-i\vec{q}\vec{S}_{bj}}\rangle \tag{2.26}$$

Considering the definition of form factor for a single particle:

$$P(q) = \frac{1}{n_s^2}\sum_{i,j}^{n_s}\langle e^{-i\vec{q}\vec{S}_{ab}}\rangle \tag{2.27}$$

The inter-particle structure factor is defined as:

$$S(q) = \frac{1}{N_s}\sum_{a,b}^{N_s}\langle e^{-i\vec{q}\vec{S}_{ab}}\rangle \tag{2.28}$$

Therefore, the cross-section is expressed as follows:

$$\frac{\partial \sum q}{\partial \Omega} = \Delta\rho^2 \frac{n_s^2 N_s v_s^2}{V_s}[P(q) + P(q)(S(q)-1)] \tag{2.29}$$

The scattering cross-section is then:

$$\frac{\partial \sum q}{\partial \Omega} = \Delta\rho^2 \frac{n_s^2 N_s v_s^2}{V_s} P(q)S(q) \tag{2.30}$$

The volume fraction of the particle is expressed as $n_s N_s v_s / V$, denoted as $\Phi$.

$$\frac{\partial \sum q}{\partial \Omega} = n_s v_s \Phi \Delta\rho^2 P(q) S(q) \tag{2.31}$$

So information about both P(q) and S(q) in a dispersed particulate system can be extracted from modelling the experimental data using Equation 2.31.

Generally, the hard-sphere structure factor [194] is designated for un-charged particle suspensions where the particles are globular, or not very elongated. The Hayter Penfold Mean Sphere Approximation (RMSA) structure factor [195] is normally used to describe the interactions between charged particles of a spherical or a slightly ellipsoidal shape.

**Characterisation of ordered materials.**

A class of SAXS patterns is characterised by sharp peaks which are due to well-defined repeat distances in ordered materials. If several well-defined interference maxima (Bragg peaks) are seen in the SAXS pattern, the data can be evaluated in terms of basic concepts of classical crystallography, but for much larger repeat units than those of single molecules. The peaks can be assigned to a corresponding space group. The reported mesostructures and their diffraction properties are listed in Table 2.2.

**Table 2.2** Summary of the reported mesostructures and their diffraction properties.

| Crystal system | Space group | Mesoporous materials | Diffraction properties |
|---|---|---|---|
| Hexagonal | $P6mm$ | MCM-41, | $1/d^2_{hkl} = (4/3)(h^2+hk+k^2)/a^2$ |
| | (No.183) | SBA-3, | $1(100):\sqrt{3}(110) : 2(200) : \sqrt{7}(210) : 3(300)$ |
| | | SBA-15, | |
| | | FSM-16, | |
| | | TMS-1 | |
| Cubic | $Pm\bar{3}n$ | SBA-1 | $1/d^2_{hkl} = (h^2+hk+k^2)/a^2$ |
| | (No.223) | SBA-6, | $\sqrt{2}(110) : \sqrt{4}(200) : \sqrt{5}(210) : \sqrt{6}(211)$ |
| | $Im\bar{3}n$ | SBA-16, | $\sqrt{2}(110) : \sqrt{4}(200) : \sqrt{6}(211) : \sqrt{10}(310)$ |
| | (No.229) | | |
| | $Fd\bar{3}m$ | FDU-2, | $\sqrt{3}(111) : \sqrt{8}(220) : \sqrt{11}(311) : \sqrt{12}(222)$ |
| | (No.227) | | |
| | $Fm\bar{3}m$ | FDU-12, | $\sqrt{2}(110) : \sqrt{4}(200) : \sqrt{8}(220) : \sqrt{11}(311)$ |
| | (No.227) | | |
| | $Pm\bar{3}m$ | SBA-11, | $\sqrt{1}(100) : \sqrt{2}(110) : \sqrt{3}(111) : \sqrt{4}(200)$ |
| | (No.221) | | |
| Lamellar | | MCM-50 | 1(100):2(002):3(003):4(004): 5(005) |
| Wormlike | | KIT-1,MSU,HMS | One or two broad peaks |

a Numbers below the space group symbols are space group numbers (refer to website: http://it.iucr.org/A/).

### 2.1.3 Small Angle Neutron Scattering (SANS)

By integration of the scattering length density distribution across the whole sample and normalising by the sample volume, the neutron scattering cross-section is obtained and is similar to that of X-ray Equation 2.32. [196]

$$I(q) = \frac{\partial \sum q}{\partial \Omega} = \frac{1}{V} | \int_0^V \rho_n(r) e^{(-iqr)} dr | \tag{2.32}$$

where $\rho_n$(r) is the real space pair neutron scattering density, $V$ is has the same definition as for SAXS, the illuminated volume. For a dilute particulate system, in which the particles do not interact with each other, the form factor obtained is the same as Equation 2.10.

$$P(q) = |\frac{1}{V_p} \int \rho_n(r) e^{(-iqr)} dr|^2 \tag{2.33}$$

and when considering the interactions between particles, the scattering cross-section becomes:

$$\frac{\partial \sum q}{\partial \Omega} = n_s v_s \Phi \Delta \rho_n^2 P(q) S(q) \tag{2.34}$$

in the case of neutron scattering, $\rho_n$ in all the equations represents the neutron scattering length density and $\Delta\rho_n$ is the contrast factor calculated using neutron scattering length density. The other parameters, $n$, $v$, $\Phi$, $q$, $V_p$ and $V$ are the same as discussed in SAXS. Guinier analysis methods are also applicable to SANS data.

### 2.1.4 Small angle scattering modelling.

Small angle X-ray/neutron scattering data are usually analysed either by model-independent approaches or by model-dependent approaches. Both approaches require the application of the least-squares method. [197,198] The least-square method utilises the chi-square ($\chi^2$) function to measure the deviation between the experimental data and the model. The chi-square is defined as:

$$\chi^2 = \sum_{i=1}^{M} (\frac{I^{exp}(q_i) - I^{mod}(q_i)}{\sigma_{error}}) \tag{2.35}$$

$I_{exp}(q_i)$ is the scattering intensity of each data point in the experimental data, $\sigma_{error}$ is the uncertainty on the data point of $I_{exp}$(q$_i$), M is the number of the data point and $q_i$ is the momentum transfer for each data point. $I_{mod}(q_i)$ is the model intensities related to the parameters of the model $a_i$ $(i = 1, ., K)$, $K$ is the number of the parameters that are set free in the fitting model.

### 2.1.5 Grazing Incidence Small Angle X-ray Scattering (GISAXS).

GISAXS is a technique derived from small angle X-ray scattering but for detecting the surface structure or surface structure change rather than the bulk structures. Figure 2.6 and Figure 2.7 show a schematic drawing of the GISAXS measurement. During the measurement, a monochromatic beam with wave vector $K_i$ is directed onto the surface with a very small incident angle $\alpha_i$ (typically below critical angle) with respect to the sample surface to minimize the background scattering from the bulk. The beam is scattered and propagates along wave vector $K_f$ which has an in plane and out of plane angle of $2\theta_f$ and $\alpha_f$ respectively. $K_f$ is decomposed into three

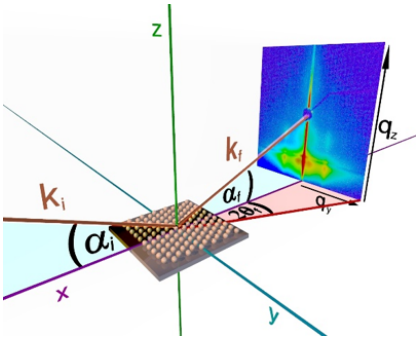


**Figure 2.6** The grazing incidence geometry. Adapted with the permission at http://www.gisaxs.de/gallery.html.

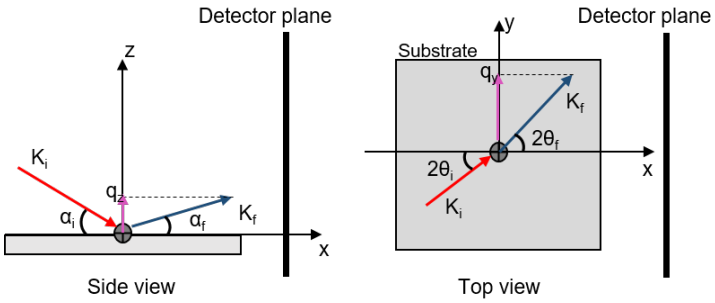


**Figure 2.7** Side view and top view corresponding to the grazing incidence geometry in Figure 2.6.

wave vectors $q_x$, $q_y$ and $q_z$ along x, y and z axes respectively. Wave vectors $q_y$ and $q_z$ carry the information of the morphology parallel to the surface (along $q_y$) and perpendicular to the surface (along $q_z$). The momentum transfer q can be expressed as

$$\begin{bmatrix} q_x \\ q_y \\ q_z \end{bmatrix} = \frac{2}{\lambda} \begin{bmatrix} \cos\alpha_f \cos\theta_f - \cos\alpha_i \cos\theta_i \\ \cos\alpha_f \sin\theta_f - \cos\alpha_i \sin\theta_i \\ \sin\alpha_f - \sin\alpha_i \end{bmatrix} \tag{2.36}$$

where $\lambda$ is the X-ray wavelength.

In general, a 2D detector is set up in a range between 1 and 4 meters away from the sample to record the intensity of the scattered X-rays. Two beam stops are set up in front of the detector to block the direct beam and the specularly reflected beam to avoid any damage caused by the saturation at the detector. GISAXS technique could provide complete structural characterisation through the collection of a 2D reciprocal image. GISAXS has been a useful technique to investigate the mesoporous silica structures. [199–201]

Herein, the detector we used relating to the measurements in the results part is a Pilatus 100k detector. [202,203] This detector is a two-dimensional single photon counting detector with a high dynamic range of 20 bits and an active area of 83.8 × 33.5 mm$^2$. The fast readout time (*ca.* 1 s) of the Pilatus 100k makes it very suitable for time-resolved measurements. [203]

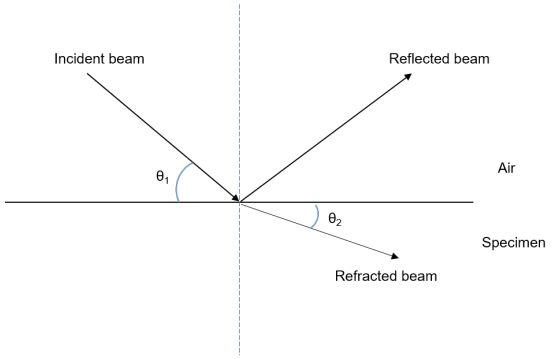


**Figure 2.8** Diagram describing the relationship between an incident beam with an incident angle at $\theta_1$ with respect to the surface. The beam is reflected with the same angle at the surface and refracted in the medium at an angle $\theta_2$.

### 2.1.6 X-ray reflectivity (XRR)

XRR is widely used for thin-layered structures, surfaces and interfaces investigation. The relationship between incident beam, reflected beam and refracted beam is illustrated in Figure 2.8. The refractive index of a specimen is approximated as: [204]

$$n = 1 - \delta_x + i\beta_x \tag{2.37}$$

where $\delta$ and $\beta$ are positive and are tabulated in the reference. [204] The imaginary component, $i\beta_x$, is due to the medium absorbance of the incident beam. For X-rays:

$$\delta_x = \frac{r_e \lambda^2}{2\pi} N_A \sum_i \frac{\rho_{x,i}}{A_i}(Z_i + f') \tag{2.38}$$

$$\beta_x = \frac{r_e \lambda^2}{2\pi} N_A \sum_i \frac{\rho_{x,i}}{A_i} f'' \tag{2.39}$$

where $N_A$ is Avogadros number, $r_e$ is the classical electron radius ($2.8 \times 10^{-5}$ Å), $\lambda$ is the wavelength of the incident radiation, $\rho_{x,i}$ is the density of element with atomic weight $A_i$ and atomic number $Z_i$, and $f'$ and $f''$ are the real and imaginary anomalous dispersion factor respectively. Equation 2.38 and Equation 2.39 can be written with respect to the electron density $\rho_{ele}$:

$$\delta_x = \frac{\rho_{ele} r_e \lambda^2}{2\pi} \tag{2.40}$$

$$\beta_x = \frac{\mu\lambda}{4\pi} \tag{2.41}$$

In most cases, the absorption factor $\beta_x$ is negligible, therefore:

$$\delta_x = \frac{r_e \lambda^2}{2\pi} N_A \sum_i \frac{\rho_{x,i}}{A_i} b_i \tag{2.42}$$

where $b_i$ is the scattering length of component i with a density $\rho_{x,i}$ and an atomic number $A_i$.

When the medium has a refractive index $n_x$ ($n_x = \cos\theta_1/\cos\theta_2$) smaller than one, a critical angle ($\theta_c$) under which total external reflection occurs can be calculated using equation

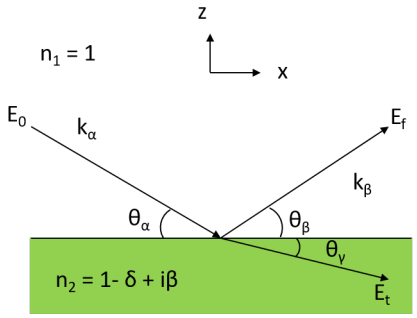


**Figure 2.9** Reflection and transmission at the surface.

$\cos\theta_c$=$\cos\theta_1$=$n_x$. Within a good approximation, the equation can be written as:[204]

$$\theta_c = (2\delta)^{1/2} \tag{2.43}$$

Considering the expression of  in Equation 2.42, the critical angle is related to the electron density, scattering electron density and the incident beam wavelength.[205] Hence, total reflection can be achieved by varying either the incident angle with fixed wavelength of the incident beam or by changing the incident beam wavelength without changing the incident angle.

In an X-ray reflectivity measurement (as illustrated in Figure 2.9, the detected angle equals to the incident angle, and the interesting component is the part that is normal to the surface. The momentum transfer along Z-axis, $q_z$, is expressed as:

$$q_z = \frac{2\pi}{\lambda}(\sin\theta_\alpha - \sin\theta_\beta) \tag{2.44}$$

The amplitude of the reflection coefficient with respect to the incident beam is written as:

$$r(q_z) = \frac{E_f}{E_0} = \frac{q_z - \sqrt{q_z^2 - q_{c,z}^2}}{q_z + \sqrt{q_z^2 - q_{c,z}^2}} \tag{2.45}$$

$$R = rr^* = |r|^2 = |\frac{E_f}{E_0}|^2 \tag{2.46}$$

For reflection in multiple layers,

$$q_{z,i} = \sqrt{q_{z,0}^2 - q_{c,z,j}^2} \tag{2.47}$$

where $q_{c,z,j}$ is the composition along Z-axis of the momentum transfer in medium $j$ at the critical incidence angle. Hence the intensity for a surface with a number of $n_l$ layers is:

$$R(q_z) = |\sum_{j=0}^{n_l} r_{j,j+1} e^{iq_{z,j}d_j}|^2 \tag{2.48}$$

where $d_j$ is the distance between adjacent layers and $r_{j,j+1}$= ($q_{z,j}$ - $q_{z,j+1}$)/($q_{z,j}$ + $q_{z,j+1}$). After approximation, $r_{j,j+1}$ can be simplified into Equation 2.49 using $q_{c,j}^2 = 16\pi r_e \rho_{r,j}$ ($r_e$ is the classical

radius of the electron, $\rho_{r,j}$ is the electron density).[204]

$$r_{j,j+1} = \frac{4\pi r_e(\rho_{r,j+1} - \rho_{r,j})}{q_z^2} \tag{2.49}$$

Equation 2.48 is further approximated as:

$$R(q_z) = |\sum_{j=0}^{n_l} r_{j,j+1} e^{iq_{z,j}\sum_{m=0}^{j} d_m}|^2 \tag{2.50}$$

Combining Equation 2.49 and Equation 2.50 gives:

$$R(q_z) = |4\pi r_e \sum_{j=0}^{n_l} \frac{(\rho_{r,j+1} - \rho_{r,j})}{q_z^2} e^{iq_{z,j}\sum_{m=0}^{j} d_m}|^2 \tag{2.51}$$

The sum over $d_m$ in the phase factor can be replaced by $Z_{j+1}$ for the layer $j, j+1$ and the equation becomes:

$$R(q_z) = |4\pi r_e \sum_{j=0}^{n_l} \frac{(\rho_{r,j+1} - \rho_{r,j})}{q_z^2} e^{iq_{z,j}\sum_{m=0}^{j} zd_z}|^2 \tag{2.52}$$

If considering the surface is covered with an infinite number of layers, the sum in the reflection coefficient in Equation 2.52 can be transformed into an integral over z:

$$R(q_z) = |\frac{4\pi r_e}{q_z^2} \int_{-\infty}^{+\infty} \frac{d\rho(z)}{dz} e^{iq_{z,j}\sum_{m=0}^{j} zd_z}|^2 \tag{2.53}$$

The Fresnel reflectivity of the substrate, $\mathrm{R}_F(\mathrm{q}_z)$, is defined as $(4\pi \mathrm{r}_e\rho_e)^2/(\mathrm{q}_z^4)$, thus,[206]

$$\frac{R(q_z)}{R_F(q_z)} = |\frac{1}{\rho_s} \int_{-\infty}^{+\infty} \frac{d\rho(z)}{dz} e^{iq_{z,j}\sum_{m=0}^{j} zd_z}|^2 \tag{2.54}$$

therefore, the reflected intensity is related to the thickness and the scattering length density of the layers. The corresponding information can be extracted from data modelling. In data modelling, according to Equation 2.54, the measured reflectivity is related to the real space pair density function $\rho$(z) perpendicular to the interface. Although $\rho$(z) is considered to be a continuously varying function, the interface layers can often be well approximated by a slab model in which a layer with a thickness $d_n$, scattering length density $\rho_n$ are placed between the super- and sub-phases. Then a refinement procedure is applied to minimize the deviation between the experimental reflectivity curves and the theoretical values through varying parameters that describe the layer.[207]

### 2.1.7 Conductivity

Electrical conductivity is the reciprocal of the electrical resistivity which expresses the ability of a material to conduct electric current. Solution conductivity is measured by submerging a conductivity meter with two plates in the solution. A potential ($E$) is applied across the two plates and the current ($I$) through the solution is measured. The A-C electric resistance[208] ($R_{resis}$) is then obtained and the solution conductivity ($\kappa$) is proportional to its reciprocal with a cell constant ($K_{cell}$) related to the distance and area of the two plates as a coefficient:

$$\kappa = K_{cell}/R_{resis} = KI/E(mS \cdot cm^{-1}) \tag{2.55}$$

The solution conductivity is facilitated by the ions in the solution, therefore $\kappa$ is proportional to the ion concentration.

Electrical conductivity can be used to measure the critical micelle concentration (CMC) of ionic surfactants in water. Below the CMC, the addition of surfactant to an aqueous solution increases the number of the charge carriers, and consequently enhances the conductivity of the solution. Above the CMC, further addition of surfactant increases the number of micelles in the solution while the monomer concentration remains approximately constant (at the CMC level). Due to the larger size of the micelles compared to the monomers, they diffuse much more slowly through solutions and perform as less efficient charge carriers. Therefore, the conductivity measurement gives two almost straight lines when the conductivity value is plotted against the concentration [208,209] with a break which indicates the point when micelles start to form, namely the CMC.

The slopes of the two straight lines can be used to assess the ion dissociation degree ($\alpha$) of the micelles in water *via* the equation:

$$\alpha = m_2/m_1 \tag{2.56}$$

where $m_1$ is the pre-CMC slope and $m_2$ is the post-CMC slope. [209]

### 2.1.8 Surface tension

In general, any interface is characterised by the free energy, which is proportional to its surface area $S_{sur}$ through the equation:

$$Free\ energy = \gamma \cdot S_{sur} \tag{2.57}$$

where $\gamma$ is the coefficient of surface tension (N/m). At equilibrium, the free energy has the smallest value. So an interface always tends to reshape to obtain minimum free energy. Therefore, the minimisation of the contact area of the interface is a spontaneous process, explaining why drops and bubbles are round.

Upon the introduction of any surface-active component, a surfactant for example, the surfactant molecules initially partition to the surface due to the hydrophobic effect. [210] It takes less energy to drive a surfactant molecule to the interface than a water molecule. Thus, a new interface is formed with a surfactant monolayer with hydrophobic tails pointing out of the water phase. The contraction tendency of the surface driven by normal surface tension gives rise to the surface pressure $\pi_{sur}$. The relationship between $\pi_{sur}$ and surface tension is defined as $\pi_{sur}$ $=\gamma_0$ - $\gamma$, where $\gamma_0$ is the surface tension of a clean air-water surface. Therefore, surface tension decreases with surface pressure. [211] At the concentration of the critical micelle concentration, the interface is almost covered by the surfactant molecules, and the surface tension reaches a minimum value. The surface tension can be measured using a Wilhelmy plate or Du Noüy ring method or by analysing the shape of a pendant drop.

The plate method was elaborated by Ludwig Wilhelmy. [212] During the measurement, a thin plate or a ring made of platinum is used. As illustrated in Figure 2.10, the plate is placed perpendicular to the air-liquid interface. The total force that is needed to detach the plate from the interface ($F_{capillary}$) equals $F_{capillary} = W_{plate} + 2l\gamma\cos(\theta)$, where $W_{plate}$ and l are the weight

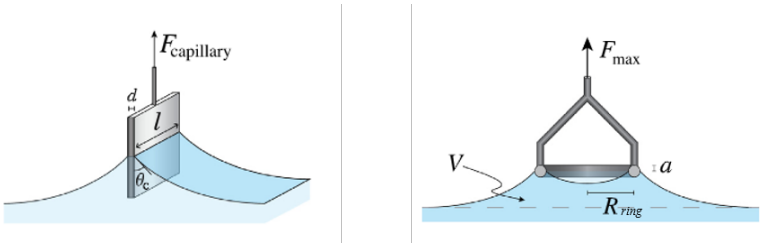


**Figure 2.10** Schematic of the Wilhelmy plate and Duo Noüy ring method to determine the surface tension.Adapted with the permission from [213]

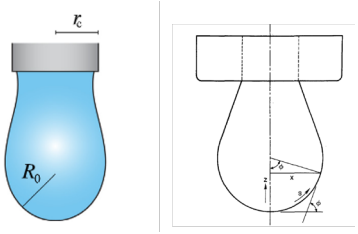


**Figure 2.11** Schematic of the pendant drop method to determine the surface tension. Adapted with permission from [213,214].

and width of the Wilhelmy plate. If the liquid completely wets the plate ($\theta = 0°$), the equation becomes $F_{capillary} = W_{plate} + 2l\gamma$. Through measuring the total force, the surface tension can be calculated through $\gamma = (W_{total}$ - $W_{plate})/(2{\cdot}l)$. A ring can be used instead of a plate, which is pulled out from the interface during measurement. The contact edge, instead of the width of the plate, is the circle of the ring. So the total force is defined $F_{max} = W_{plate} + 4_{ring}\gamma$, where $R_{ring}$ is the radius of the ring.

The pendant drop method has an advantage that only a small volume of sample is needed. The shape of the pendant drop depends on the balance between the surface tension which draws the drop to a round shape and the gravitation force which deforms the round shape of the drop. The analysis of the drop shape is based on the Young-Laplace equation:

$$\Delta\pi = \pi_{in} - \pi_{out} = \gamma(\frac{1}{R_{in}} + \frac{1}{R_{out}}) = \Delta\pi_0 - \Delta\rho_d g z \tag{2.58}$$

where $\pi_{in}$ and $\pi_{out}$ are the surface pressure inside and outside a curved air-liquid interface, $R_{in}$ and $R_{out}$ are the principle radius inside and outside a curved interface. For a pendant drop, $R_{in} = R_{out} = R_0$. The $\Delta\pi$ can also be written as the difference between the pressure at $z = 0$ ($\pi_0$) and a hydrostatic pressure $\Delta\rho_d g z$, where $\Delta\rho_d$ is the density difference of the two phases. Equation 2.58 can be expressed as three dimensionless first-order differential equations, as shown by several workers: [214–216]

$$\begin{aligned} \frac{\partial\phi}{dS} &= \frac{2}{R_{drop}} + Z\frac{\sin\phi}{X} \\ \frac{\partial X}{dS} &= \cos\phi \\ \frac{\partial Z}{dS} &= \sin\phi \end{aligned} \tag{2.59}$$

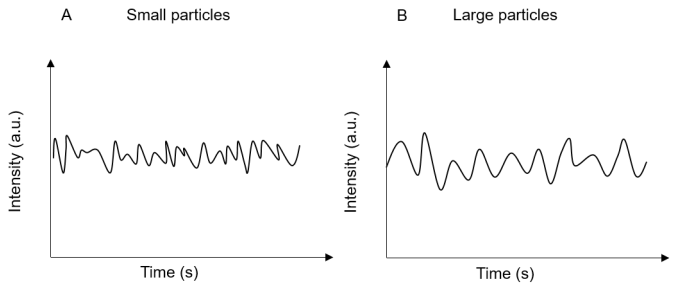


**Figure 2.12** Intensity trace of (A) small and (B) large particles.

where $\phi$ represents the angle between the horizontal axis and a tangent to the drop profile at position (x,z) as illustrated in Figure 2.11, $s$ is the contour length along the profile, $r_{drop}$ refers to the radius of curvature at the drop apex. The dimensionless reduced variables are defined as $X = x\sqrt{c}$, $Z = z\sqrt{c}$, $S = s\sqrt{c}$, and $R_{drop}$=$r_{drop}\sqrt{c}$. $R_{drop}$ is defined by

$$R_{drop} = r_{drop}\sqrt{c} = r_{drop}\frac{\Delta\rho_{drop}g}{\gamma} \tag{2.60}$$

$\Delta\rho_{drop}$ is the density difference between the drop and the surrounding medium, $g$ is the gravitational constant, $\gamma$ is the surface tension. Therefore, the surface tension can be obtained through analysing the shape of the pendant drop.

### 2.1.9 Dynamic light scattering

Dynamic light scattering (DLS) is based on the Tyndall effect (scattering) and the Brownian motion of dispersed particles. The Tyndall effect is the fact that light scattered by particles in a colloidal suspension. The intensity of the scattered light is inversely proportional to the fourth power of the wavelength of the incident beam. The Brownian motion is the random motion of particles in a well-dispersed suspension. The particles collide with the solvent molecules at all directions, randomly more colliding in a certain direction leads to a dominant force in one direction, the movement of the particles. The larger the particle, the slower the Brownian motion will be.

In a dynamic light scattering experiment, a monochromatic beam of laser light is impinged on to a sample and is scattered into a detector placed at an angle $\theta$ with respect to the transmitted beam.[217] The direct scattered intensity collected from the detector is not constant but fluctuates over time because the positions of the particles are changing constantly due to the Brownian motion. Smaller particles, as they move faster, will have a more frequent fluctuation and a smaller amplitude between highest and lowest intensity compared to larger particles, as illustrated in Figure 2.12. A correlation function ($g^2(q, \tau)$),[217] the correlation of a signal with a delayed copy of itself as a function of a time lag ($\tau$), is generated from the initial intensity trace:

$$g^2(q_{DLS}, \tau) = \frac{\langle I(t)I(t+\tau)\rangle}{\langle I(t)^2\rangle} \tag{2.61}$$

where t is time, $q_{DLS}$ is the particular wave vector and $I(t)$ is the scattered intensity at time t. The angular bracket is the expectation value. The corresponding correlation functions of the intensity

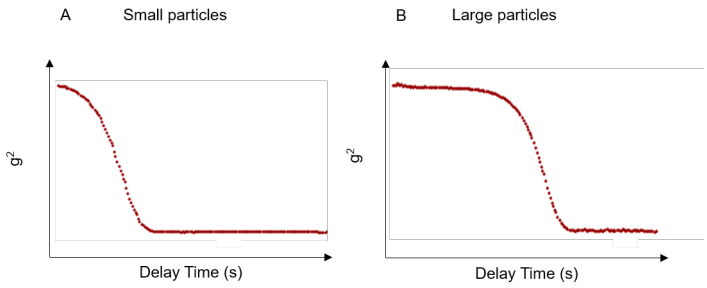


**Figure 2.13** Correlation functions of (A) small and (B) large particles.

traces in Figure 2.12 are given in Figure 2.13. At the beginning, the curve is nearly flat which indicates the particle is still in the same position as the previous moment. An exponential decay is observed in the curve when the particle is moving away from its original position. Then the curve goes flat again which is the baseline. Larger particles move with a lower velocity, therefore the decay of the curve occurs later than that of the small particles. The obtained correlation function $g^2$ ($q_{DLS}$,$\tau$) can be written in terms of the correlation function $g^{(1)}$ ($q_{DLS}$,$\tau$) according to the Siegert relation:[218]

$$g^2(q_{DLS},\tau) = 1 + \beta|g^{(1)}(q_{DLS},\tau)|^2 \tag{2.62}$$

where $g^{(1)}(q_{DLS},\tau) = exp(-T\tau)$, where $T = D \cdot q_{DLS}^2$ is the decay rate, with $D$ is the diffusion coefficient and $q_{DLS}$ is the momentum transfer which is related to the scattered angle ($\theta$) *via* $q_{DLS} = (4\pi \mathrm{n}/\lambda)sin(\theta/2)$, $\lambda$ is the wavelength of the laser under vacuum, n is the refractive index of the sample. Through fitting the decay of the correlation function, $D$ can be obtained to further calculate the hydrodynamic particle size ($R_h$) using Stokes-Einstein equation[219] $R_h = k_B\mathrm{T}/6\pi\eta\mathrm{D}$, where $k_B$ is Boltzmanns constant, T is the temperature in Kelvin, and $\eta$ is the solvent viscosity. Here in this thesis, a CONTIN method,[220] which uses a regularization techinique to seek smooth solutions, was applied to fit the decay of the curve to obtain the value of $D$.

### 2.1.10 Nitrogen adsorption/desorption.

Since 1777, when Fontana[221] found that calcined charcoal could absorb several times its own volume of gases, the measurement of adsorption of gas has been used to obtain information about surface area and pore structure of materials. The term adsorption is the enrichment of a kind of gas or liquid at the surface of a solid.[222] The adsorbed gas or vapour molecule is called the adsorbate, and the solid that adsorb the gas is called the adsorbent. The absorption between the adsorbate and adsorbent is forced by the van der Waals attraction. Physisorption can be achieved very fast without activation energy. The physisorption carried out at cryogenic temperatures has special properties.

1. Gas density at the surface is higher compared to the concentration in the bulk.

2. Compared to the higher temperature, it needs lower pressure to reach the surface coverage suitable for the analysis.

These special properties make the physisorption a suitable method to determine the specific surface area, pore volume and pore size distribution. The quantity of gas taken up by a solid

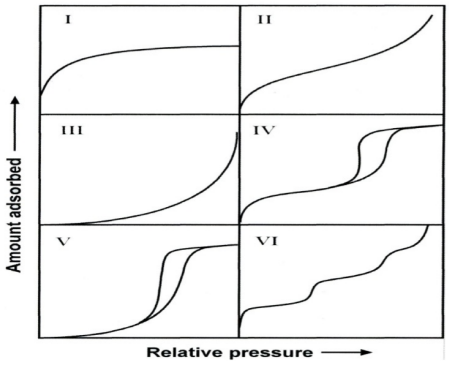


**Figure 2.14** The IUPAC classification for the sorption isotherms showing both adsorption and desorption pathways. Adapted with permission from [223].

material is affected by the mass of the sample, temperature, vapour pressure and the nature of both solid and gas.

**Sorption isotherm.**

The adsorption isotherm is plotted by measuring the amount of the gas that adsorbed over a range of partial pressures at a certain temperature. Conversely, desorption is a plot of the amount of gas removed from the solid surface as the pressure is reduced. The type of the adsorption isotherm depends on the type of intermolecular interaction between the adsorbate and the adsorbent. The six types of isotherms are given in Figure 2.14 (IUPAC classification) and describe the absorbents that are microporous (type I), nonporous or macroporous (type II, III and VI), or mesoporous (type IV and V).[224–226] The type IV and V have hysteresis between the absorption and the desorption isotherm.

**Pore size.**

The pore size generally refers to the pore width which is the distance between the two opposite walls. Pores are classified into four types according to their sizes, which are micropore ($< 2$ nm), mesopore (2 - 50 nm), macropore (50 - 7500 nm) and megapore ( $> 7500$ nm).[224] All the pores that could be accessible to gas molecules are called open pores.

**Interpretation of adsorption results**

The most commonly used model to obtain information from adsorption isotherm is the Brunauer-Emmett-Teller model,[227] a convenient form which shows the linear relation between $P/v(P^0-P)$ and $P/P^0$ in the range of $0.05 \leq P/P^0 \leq 0.35$:

$$\frac{P}{v(P^0)-P} = \frac{1}{v_m c} + \frac{c-1}{V_m c}\frac{P}{P^0} \tag{2.63}$$

where $P$ and $P^0$ are the equilibrium and the saturation pressure of the adsorbate, $v$ is the volume of the adsorbed gas, $v_m$ is the volume adsorbed in one complete unimolecular layer, $c$ is the BET constant which is related to the interaction strength between adsorbate and adsorbent and the heat of the adsorption:

$$c = e^{(\frac{E_1-E_L}{RT})} \tag{2.64}$$

where $E_1$ is the average heat of adsorption for the first layer, and $E_L$ is that for the second and more layers. It has been discussed that the value of ($E_1$ - $E_L$) is approximately constant for a given gas regardless of the type of adsorbent.[227] Furthermore, the intercept value $1/v_m c$ is proved to be small in all cases. Consequently, when the ($E_1$ - $E_L$) is known from the gas used, the value of $v_m$ can be calculated from the intercept of the plot of Equation 2.63. Therefore, the absolute value of the surface area of the adsorbent can be calculated by[227]

$$S_{total} = \frac{v_m N s}{V_{gas-molar}} \tag{2.65}$$

where $N$ is the Avogadros number, $s$ is the adsorption cross-section of the adsorbing species and $V_{gas-molar}$ is the molar volume of the adsorbate gas.

Total pore volume ($V_{total}$) equals the liquid volume that adsorbed in the pores ($V_{liq}$) (assuming pores are filled with liquid adsorbate), which is expressed as:

$$V_{liq} = \frac{P_{am} V_{ads} V_{gas-molar}}{RT} \tag{2.66}$$

where $V_{ads}$ is the amount of gas adsorbed, $V_{liq}$ is the volume of liquid nitrogen in pores, $V_{liq-molar}$ is the molar volume of liquid adsorbed, $T$ is the ambient temperature and $P_{am}$ is the ambient pressure.

Pore size distribution can also be obtained from the adsorption isotherms since the experimental nitrogen isotherm is a composite of the individual adsorption isotherms of the various sizes of pores in the adsorbent. The Kelvin equation,[228] a model that relates the pore width to the condensation pressure, is a commonly used method. The pore radius for an isolated cylindrical pore is estimated through:

$$r_k = \frac{-2\sigma_{liq} V_{liq-molar}}{RTln(P/P^0)} \tag{2.67}$$

where $\sigma_{liq}$ is the surface tension of the liquid condensate, $V_{liq-molar}$ is the molar volume of the liquid adsorbed, $R$ is the universal gas constant and T is the temperature. The Kelvin equation is valid for pore size between 10 and 250 Å. Any measured $P/P^0$ values that give a pore size that is larger than 250 Å are insufficient.

Barrett-Joyner-Halenda (BJH) algorithm[229] is also a model that is used to evaluate the full pore size distribution of a porous solid in the capillary condensation region of an isotherm. However, using either model it is difficult to tell other dimension information from the result, such as pore length.

## 2.2 Method of analysis

### 2.2.1 Small angle scattering

#### Film material characterisation

The ambient dried silica/surfactant/LPEI films and the calcined silica films were placed between two pieces of sellotape$^{TM}$. The sample was then clamped between two pieces of copper with a rectangle hole in the middle for the X-rays to go through.

Films were characterised using an Anton Paar SAXSess instrument with a PANalytical PW3830 X-ray generator at 40 kV and 50 mA, with a $CuK_\alpha$ line source which gives a q range between 0.0077 $Å^{-1}$ and 2.7 $Å^{-1}$. X-rays were detected by a reusable Europium excitation based image plate (size: 66 × 200 mm) with a 42.3 $\mu m^2$ pixel size. The image plate was subsequently read by a Perkin Elmer cyclone reader using OptiQuant software. The 1D SAXS profile was generated by using the SAXSquant program.

**Colloidal system characterisation**

The colloidal systems were investigated using small angle neutron scattering (SANS). The SANS experiments were performed on the LOQ[230] and LARMOR[231] instruments at ISIS Pulsed Neutron and Muon Facility within the Rutherford Appleton Laboratory, UK.

At LOQ beamline, the sample is around 11.1 meters away from the radiation. After the sample, there is a high-angle detector, followed by a 4 m evacuated flight path to a 64 $cm^2$ two-dimensional $^3He$ gas detector. Active area of the detector is 64 cm × 64 cm with 5 mm resolution. LOQ diffractometer uses neutrons of wavelength 2.2 - 10 Å, simultaneously by time of flight. The wavelength resolution ($\Delta\lambda/\lambda$) on LOQ is 3.8 % at 2 Å and 2.9 % at 10 Å.

The data were recorded in the q range 0.009 - 0.20 $Å^{-1}$. The samples were kept in UV-spectrophotometer grade quartz cells with a path length of 1 mm. All measurements were carried out at 25 °C. Temperature control was achieved through the use of a thermostated circulating bath pumping fluid through the base of the sample changer. Samples were measured for 40 $\mu$A and 80 $\mu$A for solution in 100% $D_2O$ and 70 mol% $D_2O$, respectively.

LARMOR beamline uses wavelengths between 1.5 and 14 Å to obtain a q-range between 0.004 and 0.6 $Å^{-1}$. The real space resolution is 1 $\times 10^{-6}$ ($\Delta$d/d, where d is defined in q=$2\pi$/d). Samples were measured for 20 meV (100% $D_2O$) and 40 meV (70 mol% $D_2O$). The raw data were corrected for sample transmission and backgrounds from the solvent, the sample cell and other instrumental background using standard workflows in the Mantid software package.[232] Scattering data were normalised against the scattering from a partially-deuterated polystyrene blend of known molecular weight converting it to the differential scattering cross-section $d\Sigma/d\Omega(q)$ (in absolute scale of $cm^{-1}$).[233] The output data are hence given in absolute scattered intensity, $I(q)$ in $cm^{-1}$, versus the momentum transfer, $q$ in $Å^{-1}$. Generic work flow for processing small angle neutron scattering includes several steps:

1. Calculating the beam center at the experimental configuration.

2. Creating mask file.

3. Calculating transmission of the sample.

4. Averaging along radial direction to give intensity as a function of q. The intensity could be the number of neutrons, a count rate per second depending on specific program.

5. Calibrating using the standard measured prior to the experiment to put the data on an absolute scale.

### 2.2.2 X-ray reflectivity

The X-ray reflectivity measurements of the films growth at the air/solution interface and the surfactant monolayers at the air/water interface were performed on I07 beamline,[234] Diamond Light Source, UK.

At beamline I07, a commercial double-crystal monochromator (DCM) is used to select X-rays with energy of 12.5 keV. The energy resolution was measured to be $\Delta E/E = 2.47\times10^{-4}$. A pair of mirrors are placed after the monochromator to focus X-rays. X-ray reflectivity measurements were measured with an incident angle ($2\theta$) up to 60°. A Pilatus 100K detector is used to collect the X-ray reflectivity data.

During the measurements, the diffuse reflection is collected and substracted from the reflectivity data. Total reflection was achieved by varying the incident angle. The obtained patterns from different incident angles are stitched together using DAWN software.[235]

### 2.2.3 Grazing incidence small angle scattering

*In situ* grazing incidence small angle scattering experiments were also measured at the I07 beamline at Diamond Light Source, UK.

In these measurements, an incident X-ray beam (energy 12.5 keV) with a size of 300 $\mu m$ 500 $\mu m$ was applied at a very shallow incidence angle (close to the critical incident angle) with respect to the air/solution interface. A vertical rod was used as a beam stop to block the direct and reflected beams.

Herein, the detector we used was a position-sensitive, single module Pilatus 100K detector.[202,236,237] Data was collected over a q range of 0.01 $Å^{-1}$ to 0.50 $Å^{-1}$. This detector is a two-dimensional single photon counting detector with a high dynamic range of 20 bits and an active area of 83.8 × 33.5 $mm^2$. The readout time around 1 s. The sample detector distance is 898 mm.

Troughs used in these experiments to hold the samples were 30 mL thin bottom Teflon troughs. A trough filled with the solution for silica hybrid film growth was placed on a metal block for temperature control using a circulating water bath. The incident angles for GISAXS measurements were 0.44, 0.08, 0.09 and 0.11 ° which correspond to a $q_z$ value at 0.1, 0.018, 0.021 and 0.024 $Å^{-1}$ respectively. The raw data were reduced and converted from pixel to momentum transfer using standard workflows in the DAWN software package, including diffraction calibration, Grazing Incidence Scattering Remapping, threshold mask and image integration.[235]

The obtained scattering data can be used to determine the surface structure in mesoscale. In this thesis, images with isotropic ring(s) are obtained. Single ring indicates a wormlike packing, double rings indicate a 2D hexagonal packing.

### 2.2.4 Nitrogen sorption

Nitrogen adsorption/desorption measurements were carried out at liquid nitrogen temperature (77 K) using a BELSORP instrument (BELSORP-mini Inc. Japan). The sample (*ca.* 0.25 grams)

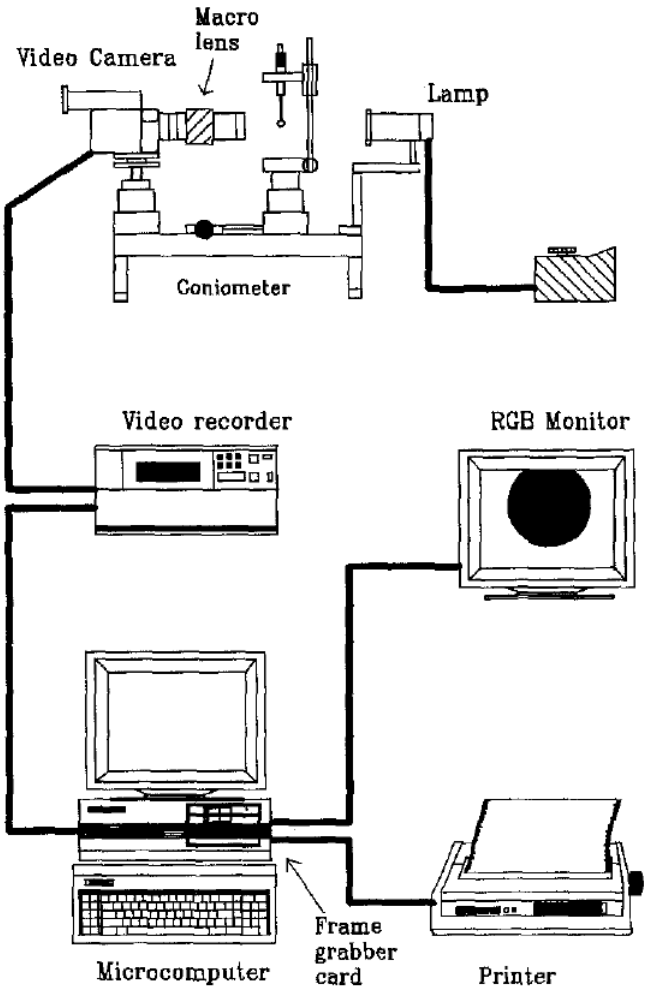


**Figure 2.15** Schematic setup of the instrument. Adapted with permission from [238].

was degassed under vacuum at 523 K for 1000 min prior to measurement. The surface area was calculated using the Brunauer-Emmett-Teller (BET) equation.

### 2.2.5 Surface tension

The surface tension values were measured using a Du Noüy Ring (Attension Sigma 701 tensiometer) or a pendant-drop method using a Kruss DSA100 to measure variation in surface tension with concentration. During the measurements, enough time was allowed to ensure that the equilibration of the surfactants at the interface was achieved prior to measurement. For Du Noüy Ring method, the force to pull the ring from the interface is measured directly for the calculation of surface tension using Nima software package. As for the pendant drop method, the set-up is illustrated in Figure 2.15. Firstly, a video camera equipped with a lens system is applied to film the pendant drop produced by using a microsyringe. Then the video is analysed by a frame grabber. The frame information from the pendant drop is input into the computer ready for analysis.

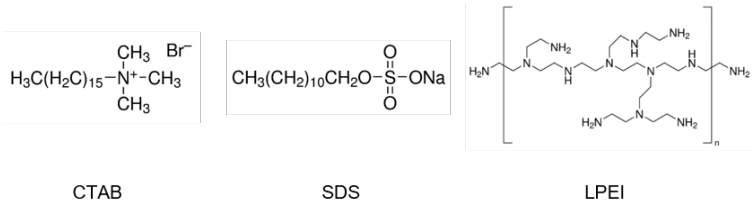


**Figure 2.16** Molecular structure of the materials used in silica film preparation.

### 2.2.6 Photocatalytic performance testing

0.015 g nPOM-$TiO_2$ (n is the carbon number in the hydrocarbon tails of the POM amphiphile that was used as the template) or sodium dodecyl sulfate templated $TiO_2$ catalyst was added to a 40 ml solution of rhodamine B (RhB) at 15 mg/L and $H_2O_2$ at 1.5 mmol/L. The mixture was exposed to a simulated solar light (illumination of natural sunlight produced by a solar simulator) under stirring for 80 min. 2 ml of solution was removed from the system every 20 min to be centrifuged. UV/vis absorption measurements (using a Perkin-Elmer Lambda 750S UV/vis spectrometer) were made on the obtained clear solutions to identify the RhB concentrations according to the major absorption intensities at 553 nm, for each degradation stage. The measured solutions were then poured back to the system at every stage to maintain the total volume. A blank experiment was carried out as follows: a 40 ml solution of RhB at 15 mg/L and $H_2O_2$ at 1.5 mmol/L was illuminated under a solar simulator without adding any photocatalyst. The change of RhB concentration with illumination time was recorded using the same method as above.

## 2.3 Material preparation

### 2.3.1 Materials

#### Materials for film preparation

Branched poly (ethylenimine) (Mw = 750 000 (denoted as LPEI, 50 w/v% in $H_2O$, analytical grade), sodium silicate solution ($(NaOH)_x(Na_2SiO_3)_yzH_2O$, 13.4 - 14.4 % NaOH, 12.0 - 13.0 % Si), sodium hydroxide (NaOH, purity > 98 %) and sodium dodecyl sulfate (SDS, purity > 98.5 %) were purchased from Sigma-Aldrich. Cetyltrimethylammonium bromide (CTAB) was purchased from ACROS Organic. All the chemicals were used as purchased. Ultra-pure Milli-Q water (18.2 MΩ·cm resistance) was used as the solvent. The molecular structure of some materials are illustrated in Figure 2.16.

#### Materials for POM amphiphile synthesis and investigation

$Na_2WO_42H_2O$ (purity > 99 %), phosphoric acid ($H_3PO_4$, 85 wt. % in water solution), $NH_4Cl$ (purity > 99.5 %), KCl (laboratory reagent grade), trichlorododecylsilane ($C_{12}H_{25}SiCl_3$, purity > 95 %), trichloroloctadecylsilane ($C_{18}H_{37}SiCl_3$, purity > 90 %), $KHCO_3$ (purity > 99.7 %), sodium dodecyl sulfate (SDS, purity > 99 %), hexaethylene glycol monododecyl ether ($C_{12}EO_6$, purity > 98 %) and $D_2O$ (99.9 atom% D) were purchased from Sigma Aldrich. N-tetradecyl trichlorosilane ($C_{14}H_{29}SiCl_3$, purity 98 %) and hexadecyltrichlorosilane ($C_{16}H_{33}SiCl_3$, purity 98 %) were purchased from Fluorochem. Octaethylene glycol monododecyl ether ($C_{12}EO_8$) was supplied by Nikko Chemical Company (Tokyo, Japan). All the chemicals are used without further

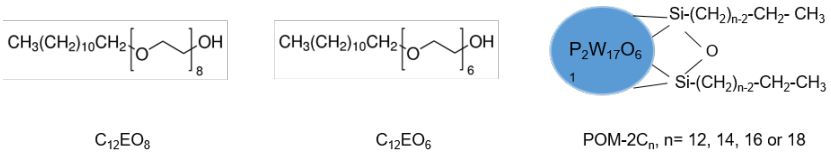


**Figure 2.17** Molecular structure of the materials used in POM amphiphile investigation.

purification. 70 mol% $D_2O$ in $H_2O$ was prepared using ultrapure water (18 MΩ·cm, from an ELGA PURELAB flex water purification system). Tail-deuterated $C_{12}EO_6$ was provided by the STFC Deuteration Facility at ISIS Neutron and Muon Facility at Didcot, and was abbreviated to d-$C_{12}EO_6$. The molecular structure of the nonionic surfactants and the POM amphiphiles are illustrated in Figure 2.17.

### 2.3.2 Film material preparation

For film material preparation, the film formation solutions (30 ml) were firstly prepared and poured into 6 cm diameter petri dishes. Then the open petri dishes with the solutions were placed on the bench at room temperature for 24 hours to allow for films to grow at the interface.

#### Silica/surfactant/LPEI films prepared from SDS/CTAB/LPEI surfactant-polyelectrolyte mixtures

To prepare the film formation solution, the surfactant-polyelectrolyte mixture was first made by blending CTAB solution, LPEI solution together, followed by the addition of SDS solution and NaOH solution. The final concentrations of these ingredients were controlled at 0.037 M, 0.003 M, 24 g/L and 0.10 M respectively in a 30 mL solution. Then a specific amount of sodium silicate solution, as the silica precursor, was added dropwise into the surfactant-polyelectrolyte mixture with stirring. The clear solution was poured into a petrie dish over a piece of plastic mesh after several minutes' stirring at ambient temperature. Subsequently, the silica film was captured by drawing the mesh out from the solution after 24 hours. The mesh was then hung on a hook to dry the film at room temperature.

#### Silica/surfactant/LPEI films prepared from CTAB/PEI surfactant-polyelectrolyte mixture

To prepare film using CTAB/PEI mixtures, CTAB solution, PEI solution and NaOH solution were mixed without adding SDS. Mesoporous silica films were prepared using the same method mentioned in the preparation of silica/surfactant/LPEI films through varying the concentrations of sodium silicate, CTAB, LPEI and alkaline conditions (NaOH concentration). Each component was controlled at different concentrations with other components kept at constant concentrations to isolate their effect on the film structure. The sodium silicate content in the solution was 10.67, 43.00, 65.00, 86.33 and 173.00 mM at a constant concentration of 0.01 M for NaOH, 0.037 M for CTAB and 24 g/L for LPEI. CTAB concentration was varied from 0.0148 M to 0.037 M at constant concentrations of LPEI (24 g/L), sodium silicate (43 mM) and NaOH (0.1 M). LPEI concentration was fixed at 12 g/L, 24 g/L, 36 g/L and 48 g/L separately with constant concentrations of 0.01 M for NaOH, 0.037 M for CTAB and 65.00 mM for sodium silicate. And

the concentration of NaOH ranged from 0.025M to 0.1M at constant concentrations of LPEI (24 g/L), sodium silicate (43 mM) and CTAB (0.037 M). A salt $NaNO_3$, as a source of $NO_3^-$, was added to the synthesis system to obtain more thermally stable mesostructures. The concentration of $NO_3^-$ was controlled between 0.012 M and 0.05 M in the final film formation solution.

**Surfactant and polymer template removal**

Ambient dried silica/surfactant/LPEI films were washed with ultrapure water to remove NaOH, followed by drying at 45 °C for 6 hrs. Films were then pre-calcined at 100 °C for 12 hrs. Mesoporous silica films without surfactant-polyelectrolyte template were obtained after calcination at 600 °C for 6 hrs.

### 2.3.3 POM surfactant preparation

**$K_6[\alpha$-$P_2W_{18}O_{62}]\cdot 14H_2O$ and $K_{10}[\alpha_2$-$P_2W_{17}O_{61}]\cdot 19H_2O$ preparation**

$K_6[\alpha$-$P_2W_{18}O_{62}]\cdot 14H_2O$ was prepared as previously described by Droege.[239] The synthesis is based on the chemical equation as follows:

$$18[WO_4]^{2-} + 32H_3PO_4 \rightarrow [P_2W_{18}O_{62}]^{6-} + 30[H_2PO_4]^- + 18H_2O$$

1. 50 grams of $Na_2WO_4\cdot 2H_2O$ was dissolved in 100 mL water, then 42 ml phosphoric acid (85 wt% in water) was added with continuous stirring. The solution was heated at reflux for 4 hours. After the reaction, the obtained solution was left to cool down before the next step. The obtained product was Dawson structured phosphotungstate with $Na^+$ as counterion.

2. 20 grams of $NH_4Cl$ was added into the solution from step 1 with stirring. The precipitate was observed once the $NH_4Cl$ was added. With 10 minutes of continuous stirring, more precipitation can be seen. The solid was filtered out from the mixture.

3. The solid obtained from step (2) was then redissolved in 120 mL water. 20 grams of $NH_4Cl$ was added into the solution with stirring. The counterion of the product was exchanged into $NH_4^+$ and was filtered out.

4. The obtained $(NH_4)_6[\alpha$-$P_2W_{18}O_{62}]\cdot 14H_2O$ was dissolved in 50 mL water at 50 ∘C and was then left to cool down to be added 8.6 grams of KCl. The precipitate was collected on a filter. This step was repeated once to make sure the $NH_4^+$ counterions were fully exchanged by $K^+$.

5. Precipitates collected from step (4) was then dissolved in water and heat with reflux for 4 hours followed by the addition of 5 grams of KCl to obtain the final product, $K_6[\alpha$-$P_2W_{18}O_{62}]\cdot 14H_2O$. The product was collected through filtration and air-dried.

$K_{10}[\alpha_2$-$P_2W_{17}O_{61}]\cdot 19H_2O$, vacant heteropolytungstate precursors, were synthesised according to the method of Finke *et al.*[240] The reaction is based on the chemical formula below:

$$7[P_2W_{18}O_{62}]^{6-} + 43HCO_3^- \rightarrow 7[P_2W_{17}O_{61}]^{10-} + [W_7O_{24}]^{6-} + 34CO_2 + 17H_2O$$

$K_6[\alpha$-$P_2W_{18}O_{62}]\cdot 14H_2O$ was dissolved in 200 mL water, and a solution of 20 grams of $KHCO_3$ in 200 mL water was added while stirring. After 1 hour, the reaction was complete. The white

precipitate was collected using a vacuum filter and was dried under suction. And then was re-dissolved in 500 mL hot water (95 °C). The snow-like crystals appeared while the solution was cooling down to room temperature, and was filtered out to be air-dried. The dried product was then used to prepare POM amphiphiles.

**POM amphiphile preparation**

1.040 mmol $K_{10}[\alpha_2\text{-}P_2W_{17}O_{61}]\cdot 19H_2O$ was dispersed in 180 mL dried MeCN for 4 hours, continuously stirred under nitrogen flow (solution 1). 4.94 mmol of trichlorosilane (either $C_{12}H_{25}SiCl_3$, $C_{14}H_{29}SiCl_3$, $C_{16}H_{33}SiCl_3$ or $C_{18}H_{37}SiCl_3$) was dissolved in 60 mL dried dichloromethane (solution 2). Then solution 2 was added dropwise into solution 1 with nitrogen flow, and the mixture was stirred with nitrogen flow for 12 hours. The obtained mixture was then filtered to remove any insoluble by-products. The filtered clear solution was rotary evaporated to dryness. Finally, the powder obtained was washed with 50 mL diethyl ether 4 times to remove the excess of trichlorosilane, followed by a vacuum-drying step to obtain the final product. The final product was characterised using FTIR, NMR and TGA techniques, which indicate a structure of $K_6[P_2W_{17}O_{61}\{SiO_2(C_nH_{2n+1})_2\}]$, denoted as POM-2$C_n$, with n = 12, 14, 16 or 18, depending on which trichlorosilane was used in the synthesis. Note that the headgroup, POM, is $[P_2W_{17}O_{61}]^{10-}$.

### 2.3.4 POM-$TiO_2$ material preparation

Synthesis of POM-$TiO_2$ was performed by mixing 9 ml of an aqueous HCl solution of 9.17 mM POM-2$C_n$ (n=12, 16 or 18) at pH = 2 and 6 ml of aqueous HCl solution (pH = 2) of 0.672 M $TiOSO_4$ to give final concentrations of 5.5 mM and 0.269 M respectively. The concentration is above the CMCs measured for all of these surfactants. The reaction was performed at 150 °C in an autoclave, via a ramping rate at 5 °C/min. And then the reaction was kept at 150 °C for 20 hours after the ramp. After the reaction, the obtained powder was then filtered out and washed with water 3 times to remove the surfactant in excess before being freeze-dried. The freeze-dried powder was calcined at 500 °C for 8 hours. The Dawson structured polyoxometalate has been shown to be stable at this temperature.[241] The calcined product was labelled nPOM-$TiO_2$ catalyst with n=12, 16 or 18 depending on the carbon number of the tails of the POM-2$C_n$ used in the synthesis. For comparison, a sample of $TiO_2$ templated using sodium dodecyl sulfate (SDS) as an anionic surfactant was synthesised according to the procedure already described in the literature which used a much higher surfactant concentration (0.26 M SDS) than that used for POM-2$C_n$ templating.[242]

# 3

# *In situ* X-ray Reflectivity and GISAXS Study of Mesoporous Silica Films Grown from Sodium Silicate Solution Precursors.

## 3.1 Introduction

Surfactants and their assembly have been widely used for the preparation of mesoporous materials.[35,243] The MCM (Mobil Composition of Matter) 41, mesoporous solid with a regularly ordered pore arrangement and narrow pore-size distribution, was discovered in 1992.[35] After that, the research interest has focused on the characterisation, the mechanism of the structural formation and the exploration of new porous materials. The characterisation on these materials was mainly conducted to understand the structural properties and provide supporting information about the formation of the structure.[244–246] It has been suggested that the formation of the inorganic-organic composite is driven by the electrostatic or counterion-mediated interaction between the surfactant micelles and silicate species.[57] Moreover, the formation of the ordered mesostructured materials is also discussed.

Mesostructured silica films have been under development since they were first reported in 1996.[56] Different synthesis methods based on the theory of evaporation induced assembly,[247] such as dip coating, spin coating, layer by layer strategy and electrochemically assisted self-assembly have been developed to prepare silica film with long-range ordered structure. These methods all require substrates to support the prepared film materials. Spontaneous silica film growth from the air-solution interface using surfactant-polymer complexes as a template has been extensively investigated in our group.[34,57,59] The film formation process requires no substrate and can be detected using various surface sensitive techniques, such as surface pressure, reflectivity and grazing incidence small angle scattering. The film formation process is suggested to be driven by the solvent-evaporation and the detailed formation route of the film structure is still under debate. Also, the developed CTAB-PEI templating approached is unique in allowing the silica film to grow from alkaline solutions. The neutron reflectivity results have suggested that the type of transformation depends on the type of polymer used for synthesis.[59] In these studies, the silica precursor used is tetramethoxysilane (TMOS), which produces methanol that is toxic and also disrupts the ordering of the micelles at higher concentrations.

Herein, a different silica source, sodium silicate, is used as the silica precursor instead of TMOS to prepare free-standing silica films. As the hydrolysation of sodium silicate produces water, it behaves as a potential candidate to improve the long-range ordering of the prepared mesoporous

silica materials. In this study, surface pressure has used to estimate the film formation time when the concentration of sodium silicate in the film formation solution is different, therefore to instruct the study on the interfacial structure using *in situ* techniques at Synchrotron. The evolution of the interfacial structure was detected using *in situ* X-ray reflectivity and grazing incidence small angle X-ray scattering (GISAXS) which give the structural information along the direction normal to the surface and the interfacial structure, respectively. The structures of the dry film are charaterised using a lab-based SAXS instrument. These results have suggested a possible formation process of the mesostructured silica film at the air-solution interface, which differs from that previously observed in a system using TMOS as silica precursor.

| This declaration concerns the article entitled: | | | | | | | | | |
|---|---|---|---|---|---|---|---|---|---|
| *In situ* X-ray Reflectivity and GISAXS Study of Mesoporous Silica Films Grown from Sodium Silicate Solution Precursors | | | | | | | | | |
| **Publication status (tick one)** | | | | | | | | | |
| **draft manuscript** | ✓ | **Submitted** | | **In review** | | **Accepted** | | **Published** | |
| **Publication details** | | | | | | | | | |
| **Candidate's contribution to the paper** | The candidate contributed to/ considerably contributed to/predominantly executed the…<br>**Formulation of ideas:**<br>The initial idea was formulated by KJE, while the proposals for beamtime were developed and written by KJE and AD (contribution 70 %).<br><br>**Design of methodology:**<br>All the measurements were designed by AD with exception of the set-up of the x-ray reflectivity and grazing incidence small angle scattering (done by TA). AD contribution 60%.<br><br>**Experimental work:**<br>Part of the preliminary data were collected by AD, NM, JS, MAS. The experimental work and data analysis (85%) was conducted by AD.<br><br>**Presentation of data in journal format:**<br>The first draft was written by AD. Subsequent draft was reworked by AD following the feedback from KJE, TA, JS and NE. (AD contribution 85%) | | | | | | | | |
| **Statement from Candidate** | This paper reports on original research I conducted during the period of my Higher Degree by Research candidature. | | | | | | | | |
| **Signed** | Andi D. | | | **Date** | 26/09/2019 | | | | |

# *In situ* X-ray Reflectivity and GISAXS Study of Mesoporous Silica Films Grown from Sodium Silicate Solution Precursors

Andi Di,[1] Julien Schmitt,[1,2] Naomi Elstone,[1] Thomas Arnold,[3] Karen J Edler[1]*

[1]Department of Chemistry, University of Bath, Claverton Down, Bath, Avon BA2 7AY, U.K.

[2]CNRS/ Saint-Gobain CREE, Saint-Gobain Research Provence, 550 avenue Alphonse Jauffret, Cavaillon, France

[3]Diamond Light Source, Harwell Campus, Didcot, OX11 0DE, U.K.

## Abstract

An environmentally friendly and inexpensive silica source, sodium silicate solution, is applied to synthesize a free-standing silica film at the air/liquid interface exploiting the co-assembly of cetyltrimethylammonium bromide and polyethylenimine. The effect of the composition of the film formation solution on the mesostructure of the as-synthesized silica films, characterized by small angle X-ray scattering (SAXS), was investigated. The film formation time was estimated by the variation of surface pressure with time. Additionally, a possible formation process of the mesostructured silica film was proposed through *in situ* grazing incidence small angle X-ray scattering (GISAXS) and X-ray reflectivity (XRR) measurements. A film with a wormlike structure formed at the interface and gradually re-organized into a 2D hexagonal structure with the long axis of the cylinders parallel to the surface, in contrast to film formation from tetramethoxysilane precursors. The 2D hexagonal structure was retained after drying. The mesostructural order was retained to some extent during calcination when nitrate ions were present in the film formation solution.

## 1. Introduction

Ordered mesostructured silica materials templated by liquid crystal phase formed by organic structure-directing agents have been extensively studied due to their potential applications in separation,[1, 2] and catalysis.[3-5] The synthesis,[6, 7] formation mechanism,[8, 9] and characterization[10] of ordered silica materials with various morphologies (powders, monoliths,

fibres *etc.*)[11-13] have been well established. However, applications in chemical sensing and separation have stimulated the exploration of the synthesis of the ordered mesoporous silica materials in thin-film geometry.[14-17]

Micellar solutions of surfactants are widely used for the preparation of mesoporous silica films since they combine large pore sizes and high surface areas in the resulting materials. Many approaches based on micellar solutions, such as evaporation-induced self-assembly (EISA)[18, 19] and electrochemically assisted self-assembly (EASA),[20, 21] have been extensively developed to synthesize mesoporous silica films on surfaces. The EASA methods normally require conducting supports to guarantee a cathodic potential.[20] The EISA methods, such as spin coating and dip coating, also need substrates for coating and are highly humidity dependent.[19, 22, 23] The free-standing film formation method, a simple process, which exploits the liquid crystalline surfactant structure for the formation of thin films at the air/solution interface, enables the detection of the surface structure *in situ* through several techniques (surface pressure, grazing incidence small angle scattering, and X-ray/neutron reflectivity). These techniques give valuable insight into the formation process but are not applicable to bulk materials. Continuous free-standing mesostructured silica films grown at the air/solution interface were initially reported by Yang *et al*[24] under acidic conditions and were proposed to form *via* the polymerization of silicates at the hydrophilic headgroup region of the surfactants in an initial surface layer, eventually forming a hexagonal mesophase.[24, 25]

Polyethylenimine (PEI), a positively charged polymer, was reported to form free-standing films when mixed with cetyltrimethylammonium bromide (CTAB) in water.[26] The aggregation of CTAB-PEI complexes are reported to be favoured by electrostatic interactions, hydrophobic interactions, and charge-dipole interactions.[27-29] The formation of CTAB-PEI films was based on the aggregation of the surfactant-polymer complex at the air-solution interface driven by evaporation,[30] and it has been applied to the successful synthesis of free-standing silica films.[31] Previous studies have also investigated free-standing CTAB-SDS-PEI films and used them as template for mesoporous silica under alkaline conditions.[32, 33] Upon completion of the

formation, the silica film templated by the CTAB-SDS-PEI complexes was pulled off from the interface onto an open mesh as a self-supporting film. These membranes are much less brittle than those containing only micelles and silica, allowing them to be more easily manipulated and calcined. Additionally, this method also allows the tunability of the as-synthesized silica films.[32] Tetramethoxysilane (TMOS), used as the silica source in this earlier work, although convenient as a model system, is not suitable for scale-up due to its toxicity and expense.[34] Moreover, methanol generated during the hydrolysis process disrupts the micelle organization, affecting the control of the mesostructure, the thickness and the strength of the prepared films. Increase of the amount of TMOS used to provide further silica to strengthen the network could not solve this problem since the amount of methanol generated dissolved the micelles. Sodium silicate solution, which produces no organic species during polymerisation, is a potential candidate to be used to avoid these drawbacks. However, for acidic systems,[35, 36] where sodium silicate solution precipitates, only alkoxysilane precursors could be used. This developed CTAB-SDS-PEI templating approach is unique in allowing the silica film to grow from alkaline solutions, permitting the use of sodium silicate solution. The use of the sodium silicate solution also has the potential to achieve better mesostructure control and stronger membranes. Therefore, we have investigated the synthesis of films using an aqueous sodium silicate solution as the silica source. In addition to the investigation of the effect of the composition of the film formation solution on the mesostructure of the silica films, we followed the film growth using *in situ* X-ray reflectivity and GISAXS to draw a possible mesostructure formation route.

## 2. Experimental section

### 2.1. Materials and Methods

Branched polyethylenimine (Mw = 750 000, denoted as LPEI, 50 w/v% in $H_2O$, analytical grade), sodium silicate solution ($(NaOH)_x(Na_2SiO_3)_y \cdot zH_2O$, 13.4-14.4 wt. % NaOH, 12.0-13.0 wt. % Si, density = 1.39 g/mL at 25 ºC), sodium hydroxide (NaOH, purity > 98%) sodium nitrate (ACS reagent, purity > 99.0%), and sodium dodecyl sulfate (SDS, purity > 98.5%) were

purchased from Sigma-Aldrich. Cetyltrimethylammonium bromide (CTAB, purity > 99.0%) was purchased from ACROS Organic. All the chemicals were used as received without further purification. Milli-Q water (18.2 MΩ·cm resistance, from an ELGA PURELAB flex water purification system) was used as the solvent.

## 2.2. Synthesis

The film synthesis procedure is a modified version of that reported earlier.[31, 32] In a standard preparation , solutions of surfactants (a singular surfactant system CTAB or binary surfactant system CTAB-SDS), LPEI and NaOH were mixed well by using a magnetic stirrer to obtain a 30 ml solution with final concentration of 0.037 M (or 0.037 M - 0.003 M for the binary surfactant system) , 24 g/L and 0.10 M, respectively. Subsequently, sodium silicate solution was added dropwise and was stirred until homogeneous. The mixture was transferred into a petri dish with a piece of plastic mesh floating on the solution surface and was left to reach a quiescent state. The growth of the mesostructured silica film was typically allowed to proceed for 24 hours under static conditions at room temperature (*ca.* 21 ºC). The film was captured by drawing the mesh out from the interface after completion of film growth. The mesh with the prepared film was then hung on a hook to dry the film at room temperature. Small pieces of films were obtained after calcination at 600 °C for 6 hrs with and without a pretreatment strategy prior to the thermal annealing. The pretreatment involved the removal of NaOH and excess structure-directing agents through washing with ultrapure water and a pre-calcination step at 100 °C for 12 hrs after the films were dried at 45 °C for 6 hrs after washing.

## 2.3. Characterization

The mesostructure of the as-prepared and calcined silica films were characterized by small angle X-ray scattering (SAXS), using an Anton Paar SAXSess instrument with a Panalytical PW3830 X-ray generator at 40 kV and 50 mM, which gives a Q range between 0.08 $Å^{-1}$ and 2.7 $Å^{-1}$. Scattered X-rays (Cu $K_\alpha$) were detected by a reusable Europium excitation based image plate (size: 66x200 mm) with a 42.3 $\mu m^2$ pixel size. The image plate was subsequently

read by a Perkin Elmer cyclone reader using OptiQuant software. SAXS profiles were generated from the 2D image using the Antor Paar SAXSquant program.

The changes of surface pressure with time were recorded by using a fibre (diameter: 0.777 mm) hung on a hook connected to a Nima surface pressure sensor. Signals from the sensor were sent to the Nima software set up in a computer to display. The sensor was zeroed when the fibre was on the hook without touching the solution. The measurement started at the point when the film formation solution was poured into the trough with sufficient height to touch the fibre.

X-ray reflectivity (XRR) and grazing incident small angle X-ray scattering (GISAXS) measurements were made using the DCD system[37] at the I07 beamline[38] at the Diamond Light Source (Didcot, Oxfordshire, UK). The X-ray energy was 12.5 keV. Teflon troughs with film formation solutions were placed on a sample holder and sealed using a plastic box with a Kapton window to allow the beam to go through. Two tubes were attached at each side of the plastic box to allow airflow through the box. The measurements were conducted at room temperature (*ca.* 21 ºC). Data were collected using a Pilatus 100 K detector using regions of interest for reflected intensity and background and reduced using the Dawn software package,[39] including a geometric footprint correction for over-illumination. The data were displayed as scattering intensity against the momentum transfer, Q. The XRR measurements are sensitive to the differences in electron density normal to the surface of the growing film, while GISAXS provides structural information of the lateral surfaces.[40]

Thermalgravimetric analysis (TGA) of the prepared silica film was performed on a SETSYS Evolution TGA 16/18 thermalgravimetric analyser (Setaram) from room temperature up to 650 °C, at a heating rate of 1 °C/min with airflow. The TGA data were displayed as the loss of weight percentage against temperature in °C.

Nitrogen sorption was measured at the liquid nitrogen temperature (77 K) using a BELSORP instrument (BELSORP-mini Inc. Japan). The samples were degassed under vacuum at 523 K

for 1000 min prior to measurements. The surface areas of the materials were derived using the Brunauer-Emmett-Teller (BET) method.

Solutions of 0.034 M CTAB water solution in the presence of different $NaNO_3$ concentrations were measured at room temperature using dynamic light scattering (DLS) in a Malvern Zetasizer Nano ZSP instrument (Malvern, UK). All samples were filtered through a 0.45 $\mu$m filter (Millex-HA) to remove any dust before the measurements. Samples were measured at a scattering angle of 173 º and a wavelength of 632.8 nm for 120 s, repeated 5 times. The size distribution, weighted in volume, was extracted using the CONTIN method.

## 3. Results and Discussion

The developed free-standing film synthesis method previously published,[31, 32] had been revealed to form mesostructured silica films using either CTAB/SDS-PEI films or CTAB-PEI films as templates. Film structure was dependent on the SDS-CTAB ratio, the molecular weight and concentration of the polyethylenimine used.[31] Here, the synthesis of silica films was attempted using the CTAB-SDS-PEI template, reported in previous work,[32] but with an alternative silica source (sodium silicate solution). Precipitation appeared with the addition of the sodium silicate solution into the CTAB-SDS-LPEI solution (pH = 10.7). Film grown at the interface was too delicate to be removed with most of the added silica precipitated at the bottom of the petri dish. Sodium hydroxide was added to the system, involving more silica in the templating interaction instead of precipitating and promoting the formation of well-ordered mesostructure,[26] increasing the pH of the solution to around 12.8. The film formed, existing as small pieces at the interface, and was characterized by SAXS after drying. The broad wide peak in the SAXS pattern (SI Fig. 1) suggests the formation of a poorly ordered mesostructure which can be understood by the polymerization and condensation processes of the sodium silicate. Sodium silicate has been reported to polymerize into anionic oligomers under alkaline conditions,[41, 42] which will be electrostatically repelled by the anionic SDS molecules in the binary SDS-CTAB system. Additionally, SDS molecules in the system also reduce the charge on the cationic micelles formed by CTAB, consequently weaken the dipole-cationic

interactions between LPEI and surfactants,[31] and compete with the anionic silica species to interact directly with the nitrogen groups in the LPEI. Considering these fact, SDS was removed from the system, resulting in the formation of a free-standing CTAB-LPEI-Silica film at the interface which was successfully removed intact on an open mesh.

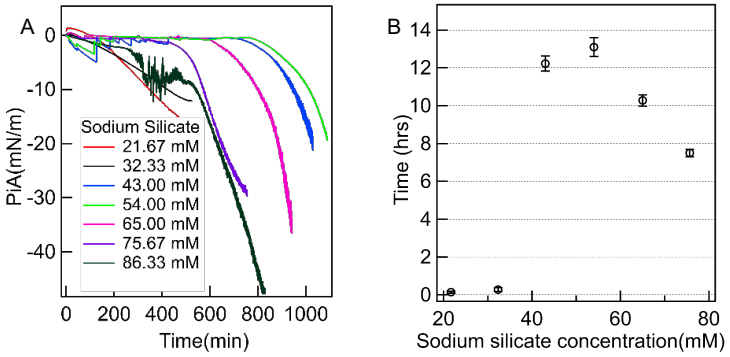


Figure 1. (A) The changes in surface pressure with time. (B) Film formation time estimated from the surface pressure change. Sodium silicate concentration was varied with CTAB, NaOH and LPEI concentration kept constant at 0.037 M, 0.1 M and 24 g/L, respectively.

In our visual observation, the film started to form at different stages when the sodium silicate concentration was changed. Film formation time can be quantified by the surface pressure changes at the air/liquid interfaces. Measurements started *ca.* 6 min after the solutions were mixed. The surface pressure change with time, as plotted in Figure 1A, was dependent on the sodium silicate concentration. The surface pressure was either measured to be constant or increase by a small amount at the beginning when using sodium silicate solution. This is very different from film growth observed using TMOS, where the surface pressure experiences a fall-off due to the lower surface tension of methanol which becomes enriched at the interface as the hydrolysis proceeds, and a decrease in height of the meniscus caused by the evaporation of the methanol from the solution.[36] This also suggests the initial surface pressure change has a close relation to the polymerisation process of the silica precursor.

For lower sodium silicate concentrations (21.67 and 32.33 mM), surface pressure went a little above 0 mN/m from the moment the measurement started, reached the maximum about 5 min later and stayed constant, followed by a decrease at about 29 min. Instead, with

concentrations lying between 43.00 and 86.33 mM, the surface pressure initially decreased and then stayed at about -0.5 mN/m for several minutes, then dropped abruptly till the end of the measurement. The point where the film solidified and attached to the glass fibre, causing a distinct decline in surface pressure due to its weight, was defined as completion of the film growth, namely film formation time (plotted in Figure 1B). Rapid film formation happened when the sodium silicate concentration was relatively low but film formation times continuously increased above a critical concentration, followed by a drop at elevated sodium silicate concentrations.

The polymerization of the sodium silicate species in the alkaline solutions is the key factor of the film formation and therefore is considered to explain the surface pressure results. In mildly alkaline aqueous solutions, silica species appears predominantly as $Si(OH)_4^0$ neutral species.[41, 42] In our condition, where sodium silicate was added into highly alkaline solutions (pH > 10),[42] the oligomerization of the monomers (Eq. 1) followed by deprotonation (Eq. 2) and polycondensation reactions governed the aqueous equilibria:[41-45]

$$kSi(OH)_4^0 \rightleftharpoons [Si_kO_l(OH)_{4k-2l}]^0 + lH_2O, 2 \leq k \leq 8 \quad (1)$$

where l denotes the number of the bridging oxygens (-Si-O-Si-).

$$[Si_kO_l(OH)_{4k-2l}]^0 + mOH^- + mNa^+ \rightleftharpoons \left[Si_{nk}O_{n(l+m)}(OH)_{4k-2l-m}\right]^{m-} \cdot mNa^+ + mH_2O \quad (2)$$

where m is the number of singly-negatively charged oxygen anions. After that, the produced silica species (Eq. 2) polymerize with a repetition of n, which also bear negative charges, attracting sodium ions in the solution. With low sodium silicate concentrations, the silica species deprotonate and polymerize fast (Eq. 2) and are driven by electrostatic interactions to condense around the positively charged CTAB-LPEI templates to form silica films. When the sodium silicate content increases but with the same NaOH concentration in the solution, the completion of the deprotonation and polycondensation of silica species require a longer time. In addition, the increased amount of water produced during the processes (Eq.1 and 2) slows

down the condensation of silica species around the templates, since the condensation process needs to repel the water molecules around the micelles. A subsequent shortening of film growth time occurs after the film formation time reaches a peak. This may be due to the higher silica oligomer to surfactant template ratio, which allows closer contact between silica species and the template, and less electrostatic repulsion between more completely silica-coated cylindrical micelles to shield the charge on the micelles while packing.[36, 46] This results in a reduction in the energy required for repelling water molecules from the micelle surfaces during the condensation process and the energy for the packing of the adjacent cylindrical micelles into a 2D hexagonal structure.[47] These changes consequently, are reflected as a drop in the film formation time.

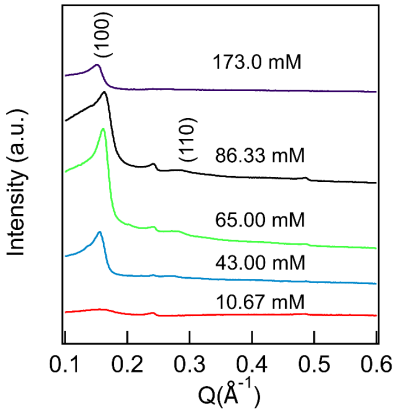


Figure 2. SAXS patterns of as-prepared silica films synthesized from CTAB(0.037 M)/LPEI(24 g/L)/NaOH(0.1 M) systems with varied sodium silicate concentration.

As illustrated in Figure 2, SAXS patterns present four diffraction peaks for silica film prepared from 43.00, 65.00 and 86.33 mM sodium silicate solution. A sharp peak appears at around 0.16 $Å^{-1}$ along with a broad peak with low intensity at around 0.28 $Å^{-1}$. These positions are in the ratio of 1.73, correlated to the (100) and (110) diffraction peaks of the 2D hexagonal structure. The second and the fourth peaks from the left at around 0.24 and 0.48 $Å^{-1}$ are indexed to the excess crystalline CTAB in the dry films.[31] At the lowest sodium silicate concentration (10.67 mM), the (100) diffraction peak was very broad and the (110) peak was absent. The TGA analysis (SI Figure 2, page 78) suggests that the silica content in the film is around 16.4 wt% which is much lower than for the film prepared from 43.00 mM sodium silicate

(30.2 wt%). So we hypothesis that the low ordering may be due to the limited amount of silica source available to form the silica scaffold around the CTAB-LPEI template and therefore restrict the packing of the adjacent micelles into a well-ordered structure. The highest silica concentration also results in a less ordered film using this method possibly due to excess silica between the micelles hindering the ordering.

The (100) peak positions are slightly different as the silica concentration changes. Recall the relationship between the position of the peak and the distance between adjacent rows of cylinders in the hexagonal structure, namely *d* spacing (d) is:[48]

$$d = \frac{2\pi}{q} \qquad \text{Equation 1}$$

where q is the position of the first peak. The calculated *d* spacings are listed in Table 1, ranging from 39.3 to 41.6 Å. The amount of sodium silicate is expected to affect the wall thickness of the silica films, resulting in different *d* spacings. However, sodium ions and hydroxide introduced along with the silica source also influence the formation of micelles and the interaction between templates and silica species. Therefore, the *d* spacing did not increase monotonically with the concentration of the silica silicate.

Table 1. (100) peak position and corresponding *d* spacings of as-prepared silica films synthesized from CTAB(0.037 M)/LPEI(24 g/L)/NaOH(0.1 M) systems with different sodium silicate concentrations.

| Conc. of sodium silicate/mM | (100) peak position /Å$^{-1}$ | *d* spacing/Å |
|---|---|---|
| 10.7 | 0.165 ± 0.050 | 38.0 ± 12.0 |
| 43.0 | 0.155 ± 0.001 | 40.5 ± 0.3 |
| 65.0 | 0.160 ± 0.001 | 39.3 ± 0.2 |
| 86.3 | 0.162 ± 0.001 | 38.8 ± 0.2 |
| 173.0 | 0.151± 0.001 | 41.6 ± 0.3 |

*In situ* XRR was conducted to follow the evolution of the surface structure at different time intervals (times labelled in Figure 3). The intensity of the reflected X-ray beam is due to the large contrast of electron densities between the soft template and the silica matrix. XRR measurements detect the interfacial structure about 20 min after the beginning of the reaction.

At early stages, the XRR patterns were similar for solutions with different sodium silicate concentrations; a broad peak at around 0.125 $Å^{-1}$ and two sharp peaks at 0.195 and 0.390 $Å^{-1}$, respectively. The two sharp peaks are assigned to an excess of surfactant forming crystals in a hydrated state due to the low Krafft point of CTAB in water (*ca.* 25 ºC).[49, 50] Measurements were carried out at 25 ºC which allowed excess surfactant, not interacting with silica or LPEI to precipitate. The broad peak is related to a wormlike structure formed at the interface,[51, 52] which had already formed at an early stage of the reaction when no film was present at the interface.

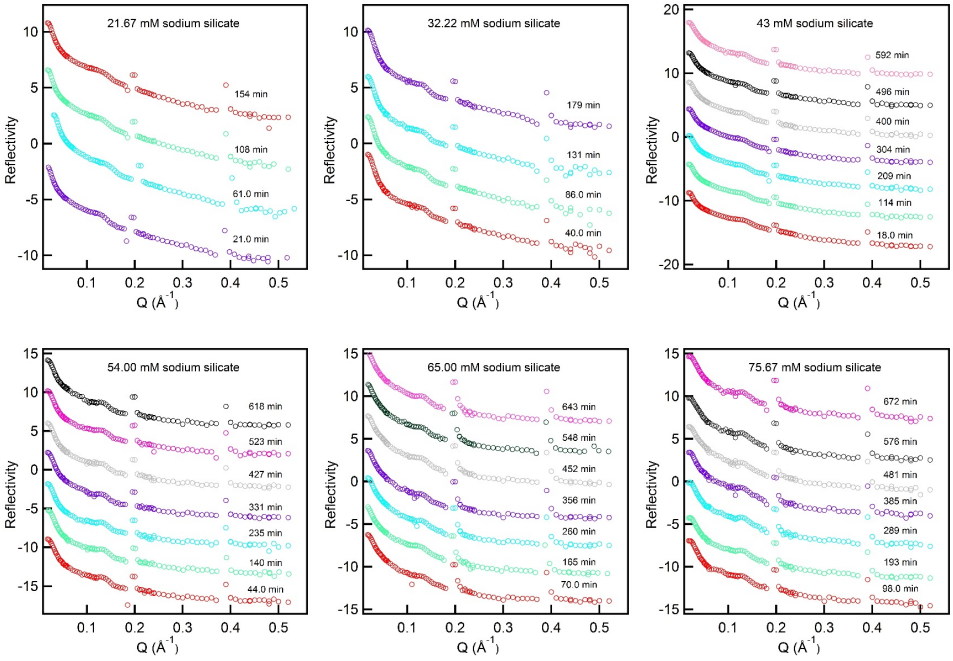


Figure 3. *In situ* XRR curves while the films were forming at the surface with different sodium silicate concentrations.

The XRR pattern did not vary significantly with time over the period measured. The peak appearing at 0.125 $Å^{-1}$ in XRR pattern corresponds to the (100) diffraction peak at higher Q (0.16 $Å^{-1}$) observed in the SAXS pattern of the dry film. This change in the (100) peak position is caused by the shrinkage of the structure that occurs due to the solvent evaporation and silica condensation upon drying. However, the (110) peak that appears in the SAXS patterns of the dry silica films is not found in the XRR patterns. We proposed that either the (110) Bragg peak supposed to occur at around 0.220 $Å^{-1}$ (estimated using the ratio of 1.732 for the 2D

hexagonal phase) was covered by the sharp peak of the crystalline surfactant at 0.195 $Å^{-1}$, or the 2D hexagonal structure of the dry film was transformed from wormlike structure in the wet silica films while drying.

Combining the XRR data with the surface pressure change, there is no observed structure change at the interface according to the time-resolved XRR patterns at the time when the surface pressure data suggest the film has formed.

The film growth and crystallization of surfactant were also observed using GISAXS measurements. The GISAXS pattern of the interfacial structure at 70 min after the reaction started, for a solution with a sodium silicate concentration at 65 mM, is displayed in Figure 4. It contains three diffraction features, with two broad but preferentially oriented peaks at around $Q_z$ = 0.18 and 0.36 $Å^{-1}$ correlated to the reflection peaks at 0.195 and 0.390 $Å^{-1}$ in the XRR data. The GISAXS data also contains an isotropic ring crossing $Q_{xy}$ and $Q_z$ at around 0.125 $Å^{-1}$, indicating the formation of wormlike mesostructures with no preferential orientation at the interface.[53] The GISAXS patterns of films grown from solutions at other sodium silicate concentrations are shown in SI Figure 3 (page 79) where surfactant crystallisation and wormlike film structures were also observed.

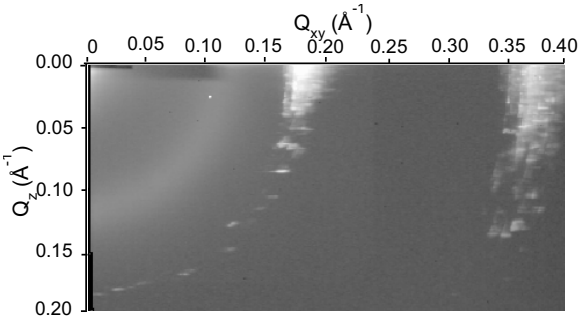


Figure 4. GISAXS pattern of the film formed at 70 min with a sodium silicate concentration at 65 mM, collected just after the first XRR pattern in Figure 3 with an incident angle of 0.1 º.

The relevant experimental parameters, the concentrations of NaOH, CTAB and LPEI in the solution, were investigated. NaOH controls the pH of the solution, without which films are not able to form. The concentrations of NaOH investigated were 0.025, 0.05, 0.075 and 0.1 M,

giving pH which values ranged between 12.3 and 12.8. SAXS patterns of the prepared films (Figure 5A) possess three peaks which are assigned, as mentioned above, to the (100) and (110) diffraction peaks of the 2D hexagonal structure plus a sharper peak at 0.24 $Å^{-1}$ due to crystalline surfactant. The positions of the primary peaks and corresponding *d* spacings are listed in SI Table 1(page 78) and are all around 40 Å. Neither the *d* spacings nor the intensity of the peak varies significantly with the NaOH concentration of the film formation solution. The third peak which can be indexed to the (110) Bragg peak is observed in these SAXS patterns, confirming the periodically ordered structure.[53] To explain the small differences in the mesostructure of the prepared silica films obtained, the both LPEI and sodium silicate solution are alkaline and thus the variation of NaOH content only allows a narrow range of the pH to be explored (12.3 – 12.8). Therefore, through this method, the alkaline degree of the subphase can be modified only over a small range, resulting in an insignificant structural difference in the mesostructured silica materials produced.

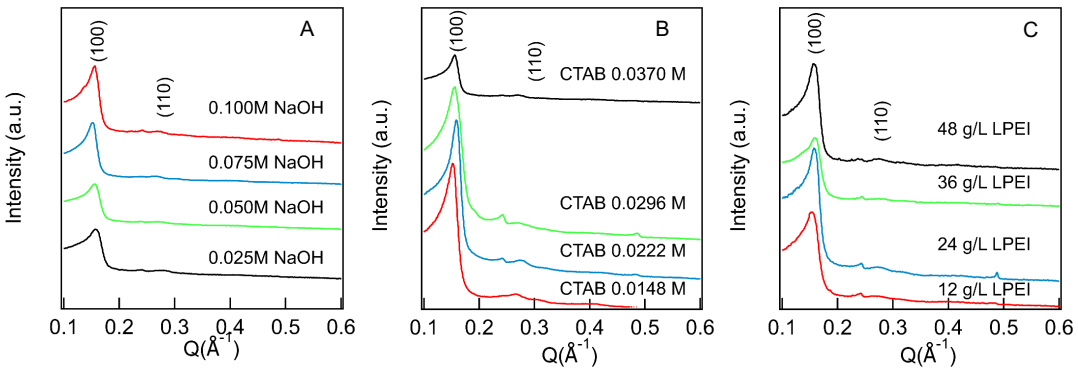


Figure 5. The SAXS patterns of as-prepared silica films synthesized from (A) sodium silicate(43mM)\CTAB(0.037M)\LPEI(24g\L) systems with different sodium hydroxide concentrations. (B) sodium silicate (43 mM)/LPEI(24 g\L) systems with different CTAB concentrations. (C) sodium silicate (43 mM)/CTAB (0.037 M) systems with different LPEI concentrations.

The concentration of CTAB, as the main part of the soft template, was also varied from 0.0148 M to 0.037 M. The intensity of the first peak becomes less distinct as the concentration of CTAB increases (refer to Figure 5B), which demonstrates a reduction of the ordering in the dry silica film. The *d* spacings of the prepared films are listed in SI Table 1 (page 78), but again little variation in peak position is observed. The adjustment of CTAB concentration would

change the template ratio between CTAB and LPEI, therefore, affects the structure of the resulting films. It turns out that a lower CTAB to LPEI ratio is conducive to the formation of well-ordered hybrid films. However, the disappearance of the peak from crystalline surfactant at the lowest CTAB concentration suggests that there may not be enough surfactant for templating since there is no sign of crystallisation from excess surfactant, this may disfavour the maintenance of the mesopores during calcination. Therefore, in the following study, we still use the highest CTAB concentration.

The effect of LPEI concentration, as a co-templating component, was studied in a sodium silicate(43 mM)/CTAB(0.037 M) system. As the LPEI concentration increases, peaks in SAXS patterns have small differences in intensity while again the peak position roughly stays in the same position (Figure 5C).

The silica films synthesised using the methods above show an ordered structure after dry at room temperature. However, they lose the ordering when during high-temperature calcination. This may occur due to the destruction of the silica mesostructure by the residual alkaline species in the structure during high-temperature annealing.

To achieve a more stable structure, nitrate ion is added to the film formation solution. Adding nitrate ions was studied previously to induce the growth of the CTAB micelles in water and so improve their effect on the ordering of templated mesostructured inorganic materials.[54-56] Herein, $NaNO_3$ was chosen as a source of nitrate ions, to study the effect of $NO_3^-$ on the structure of the silica films formed at interfaces. More than the ionic strength change in the solution that is expected, $NO_3^-$ is also known to associate with $CTA^+$ micelles much more strongly than $Br^-$. A fraction of the $Br^-$ ions are replaced by $NO_3^-$ at the micelle solvent interfaces,[55] while in general the addition of monovalent salts, also causes the solubility of ionic surfactants to decrease. The concentration of sodium nitrate was varied from 0.000M to 0.074M at fixed CTAB (0.037 M), LPEI (24 g/L) and NaOH (0.1 M) concentrations. Comparing the SAXS patterns of the prepared films in Figure 6A, the (100) diffraction peaks have roughly the same intensity with concentrations of 0.000 M and 0.012 M, and then the primary peak

fades with increasing $NaNO_3$ concentration and vanishes when the concentration reaches 0.074M as the ionic screening effects outweigh any structural enhancement due to micelle elongation.

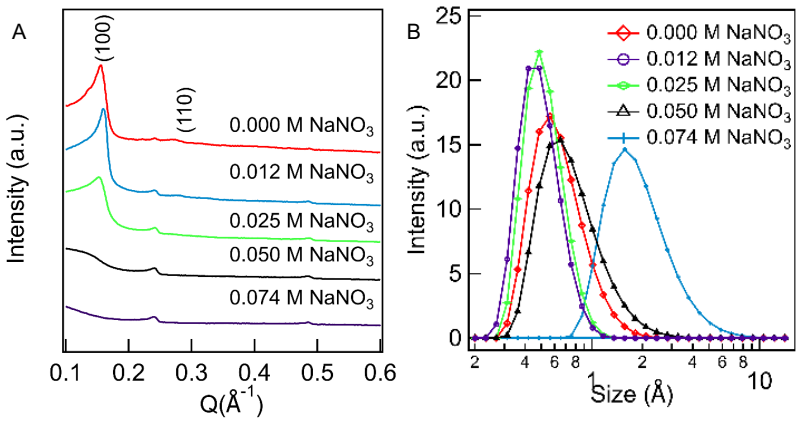


Figure 6. (A) SAXS patterns of synthesized silica films prepared from sodium silicate(65 mM)/NaOH(0.10M)/CTAB(0.037M)/LPEI(24g/L) systems, with changing $NaNO_3$ concentration. (B) The volume-weighted size distribution of $CTA^+$ micelles in the presence of different $NaNO_3$ concentrations obtained *via* the CONTIN analysis method.

The disappearance of the (100) diffraction peak at the highest $NaNO_3$ concentration may be explained by the sequence of ion-exchange constants for the $CTA^+$ micelles reported: $OH^-$ < $Cl^-$ < $B_4O_7^{2-}$ < $Br^-$ < $NO_3^-$.[57] The bidentate ligand $B_4O_7^{2-}$, which is reminiscent of oligomeric silicates,[58] binds less strongly than $NO_3^-$ or even $Br^-$ to $CTA^+$ micelles. Since the nitrate ions could bind more strongly at cationic micelle surfaces than other species in our system,[59-61] ion exchange of $Br^-$ by $NO_3^-$ on $CTA^+$ micelles occurs in the presence of $NaNO_3$.[62] The enhanced condensation of $NO_3^-$ ions may decrease the equilibrium area per molecule ($a_0$) of the $CTA^+$ headgroup due to the tighter binding of $NO_3^-$ to the micellar surface. This gives a larger packing parameter, $g = v/a_0 l_c$[63] ($v$ is the surfactant tail volume, $a_0$ is the equilibrium area per molecule and $l_c$ is the tail length), causing the elongation of the micelles and may further increase the viscosity of the solution if the degree of elongation is large enough.[61, 62] At the highest $NaNO_3$ concentration, the concentration is sufficiently large (0.074 M, which is double the concentration of CTAB at 0.037 M) to replace most of the $Br^-$ ions in CTAB. The resulting solution is of high viscosity[61] due to the elongation and the crosslinking of the micelles, which hinders the flow of the template micelles from the subphase to the interface to form films.

Therefore, the film harvested was poorly ordered. To corroborate this, 0.034 M CTAB solutions in the presence of different $NaNO_3$ concentrations were studied using dynamic light scattering (DLS). Although DLS data analysis assumes spherical objects the trends in the data confirm micellar growth as nitrate ions are added. As plotted in Figure 6B, when the $NaNO_3$ concentration was low (at 0.012 and 0.025 M), DLS results gave slightly smaller averaged micellar sizes. A micellar growth was detected using DLS when the $NaNO_3$ concentration continued to increase. Then a dramatic increase in size was observed at the highest concentration we studied. Unfortunately, the opaque solutions generated when sodium silicate solution was added to the CTAB/PEI/$NaNO_3$ solutions prevented observation of the effect of silicate anion addition on micelle size.

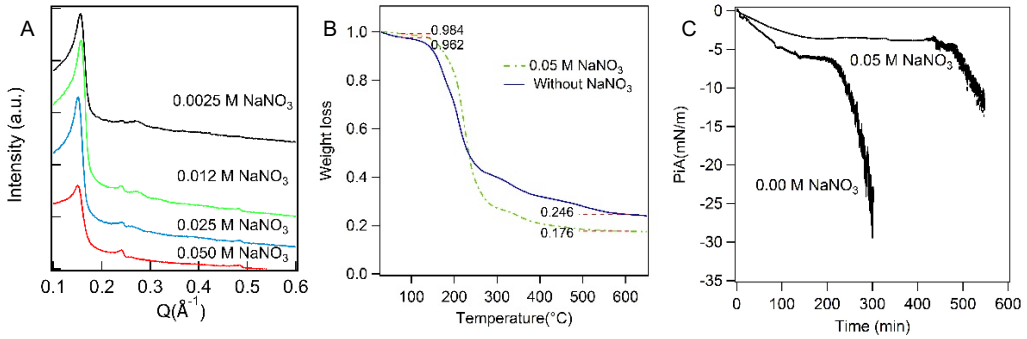


Figure 7. (A) SAXS patterns of synthesized films grown from the CTAB(0.037M)/LPEI(24g/L)/sodium silicate(65 mM)/NaOH(0.05M) systems at various $NaNO_3$ concentrations. (B) TGA of the as-prepared silica film in the presence and absence of 0.05 M $NaNO_3$. (C) Surface pressure change while the films are forming at the interface with and without 0.05 M $NaNO_3$ in the film formation solution.

The presence of NaOH is essential for the growth of the film but destroys the structure during post-synthesis calcination. Even though washing reduces the NaOH content, higher NaOH content requires long washing time, which also causes structural damage. Moreover, NaOH also increases the ionic strength of the solution to cause a high viscosity of the solution which is unfavourable to the film formation at the interfaces. Therefore, a lower NaOH concentration (0.05 M) was used in conjunction with the addition of nitrate to allow the formation of silica films and the maintenance of the mesostructural order during calcination.

When NaOH concentration was 0.10 M (see Figure 6A), the dry film synthesized from 0.074 M $NaNO_3$ lost the 2D hexagonal structure. Therefore, the studied $NaNO_3$ concentrations were between 0.0025 M and 0.050 M for 0.05 M NaOH systems. At the same $NaNO_3$ concentration of 0.050 M (Figure 7A), the (100) peak is observed in the SAXS pattern of the film prepared from 0.05 M NaOH, but not the one prepared from 0.10 M NaOH. From the observation of the prepared films (SI Figure 4, page 80), the presence of 0.05 M $NaNO_3$ allowed a more even film to form with no crystalline surfactant observed. Additionally, the thickness of the film increased from 0.142 mm to 0.162 mm and no precipitation of silica was observed in the petri dish. The clear and robust film was easily harvested from the interface and was kept in one piece until drying. Cracks occurred after drying and the film became white rather than transparent. We hypothesized that the white appearance of the dry silica film was caused by the increased thickness of the silica film. TGA results (Figure 7B) however suggested a decrease in the amount of the silica incorporated in the film from 24.6 wt% to 17.6 wt% when 0.05 M $NaNO_3$ was present. Therefore, the addition of $NaNO_3$ induced a thicker film with higher template content, but lower amounts of silica.

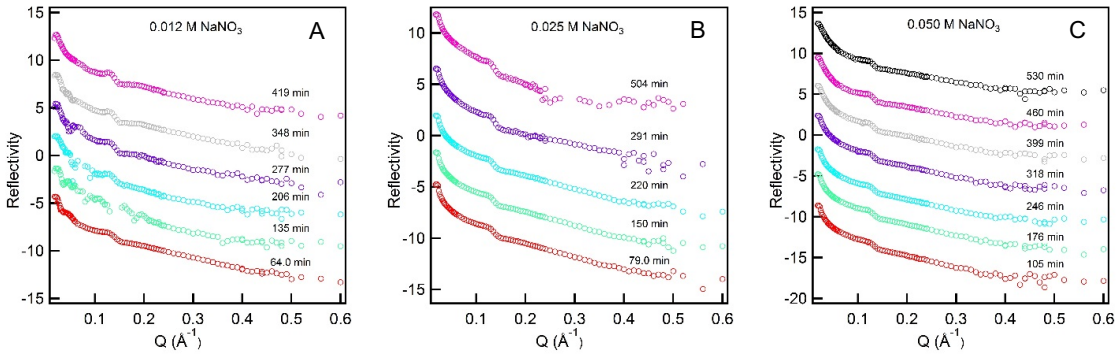


Figure 8. *In situ* XRR curves of the subphase with $NaNO_3$ concentration at (A) 0.012, (B) 0.025 and (C) 0.050 M with fixed CTAB(0.037 M), LPEI(24 g/L) and NaOH(0.05 M) concentrations.

*In situ* X-ray reflectivity was used to try to follow the film formation process (Figure 8). As observed, the (100) reflected peak stays at around 0.125 $Å^{-1}$ suggests that the ions have little effect on the *d* spacing of micelle structure normal to the surface, and no reflected peaks of crystalline surfactant were observed. The absence of the crystalline structure indicates that more surfactant remained soluble and so has the chance to template the silica film in the

presence of $NO_3^-$, which explains the TGA results. A broad (110) reflected peak is also seen in the reflectivity patterns at the end of the measurements when the $NaNO_3$ concentration is 0.012 and 0.025 M, giving evidence of the formation of a 2D hexagonal structure along the perpendicular direction to the surface. However, the rise of the (110) peak was not seen at 0.05 M $NaNO_3$ which may be due to the relatively high viscosity of this solution.

The variations of surface pressure with time while the films were forming were recorded with and without 0.05 M $NaNO_3$ in the subphase (Figure 7C). The drop of surface pressure occurred at different time, estimated as a doubling of the film formation time (450 min versus 220 min) when 0.05 M $NaNO_3$ was present in the solution. This corresponds to the longer formation time required for CTAB-PEI free-standing film when salt is present, previously reported by Edler and co-workers,[26] and may be also due to the higher solution viscosity hindering diffusion of species to the interface.

We can also see the reduction of crystallised surfactant in GISAXS patterns (Figure 9). There are two isotropic rings in the GISAXS patterns of the film formation solution in the presence of 0.12 M $NaNO_3$ (Figure 9A), of which one crosses both the y and z axes at 0.125 $Å^{-1}$ corresponding to a characteristic period of 50.2 Å. There is also a relatively indistinct ring which is related to the crystalline surfactant structure comparable to the one in Figure 4, however, this was not observed in the corresponding X-ray reflectivity patterns (Figure 8A) which may be due to the low intensity. With elevated $NaNO_3$ concentrations (0.25 and 0.5 M), the ring arising from the crystallised surfactants diminished still further, leaving a single ring in these GISAXS patterns (Figure 9B and C). Moreover, the centre of the broad ring moved progressively closer to the beam centre when more $NaNO_3$ was present. This suggests that the *d* spacing of the mesophase became larger, which is consistent with a higher CTAB content in the films, which is not neutralised completely by the silica occupying space between the micelles. Repulsion between micelles therefore increases their spacing within the films. This effect is also seen for CTAB-SPEI (polyethylenimine, Mw *ca.* 2000 Da) films in the

absence of silica where added salt resulted in an increase in the *d* spacing within the films (SI Figure 5, page 80).

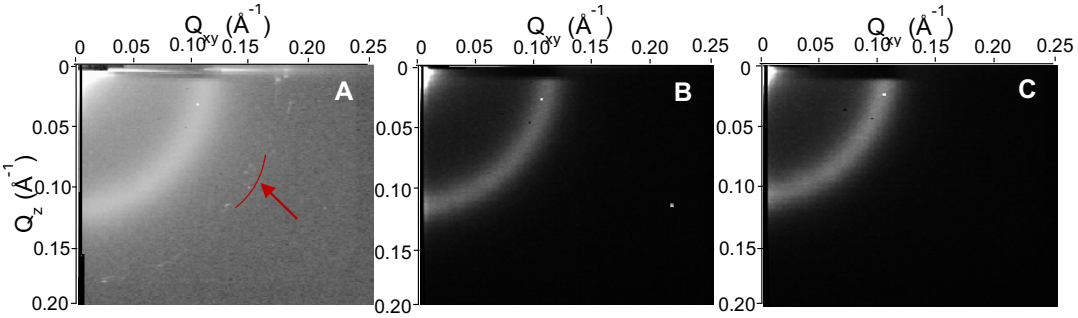


Figure 9. GISAXS patterns of subphases at an incident angle of 0.1 º at the early stage of the film formation in the presence of (A) 0.012 M $NaNO_3$ (B) 0.025 M $NaNO_3$ (C) 0.05 M $NaNO_3$.

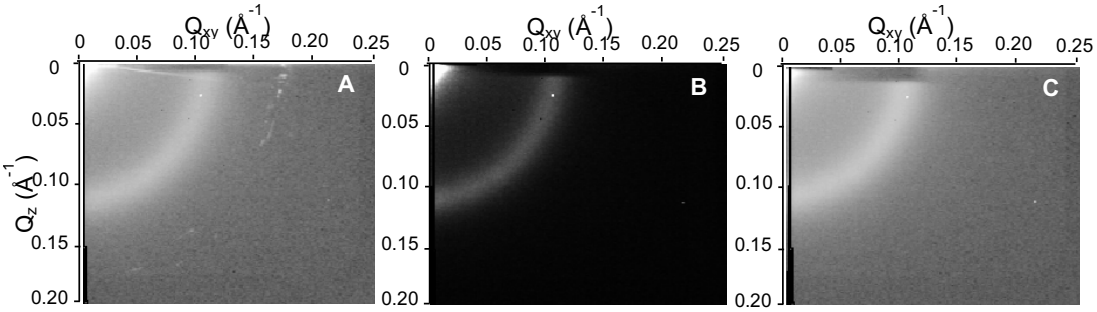


Figure 10. GISAXS patterns of subphases at an incident angle of 0.1 º at the end of the film formation in the presence of (A) 0.012 M $NaNO_3$ (B) 0.025 M $NaNO_3$ (C) 0.05 M $NaNO_3$.

The GISAXS patterns in Figure 10 suggest no (110) Bragg peaks can be seen at the end of the reaction. However, as discussed above, a broad (110) peak arises in the XRR data at the end of the measurement time (see Figure 8A). This possibly due to the difference between the two techniques, reflectivity provides depth-resolved information of the density profile normal to the surface, however, GISAXS measures the lateral surface structure of the interface, penetrating only ~100 Å into the film. The combination of XRR and GISAXS results lead to a possible structure profile, where the film at the interface displayed a wormlike structure even as a 2D hexagonal structure was gradually forming underneath in the direction normal to the surface of the subphase. The 2D hexagonal structure forms the bulk of the film and so is observed in the transmission SAXS patterns after the films are dried.

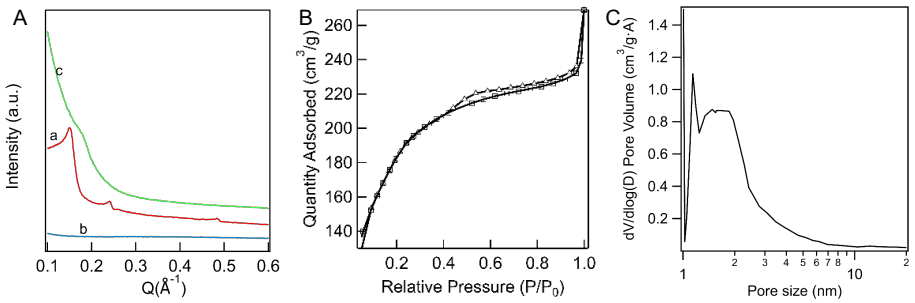


Figure 11. (A) SAXS patterns of films grown from CTAB(0.037 M)/LPEI(24 g/L)/NaOH(0.05 M)/sodium silicate(65.00 mM)/$NaNO_3$(0.050 M) solution. (a) The as-prepared film. (b) The calcined film without pretreatment and (c) with full pretreatment. (B) Nitrogen sorption isotherm for sample c in Fig.11A. (C) The pore size distribution of sample c is obtained from BJH analysis.[64]

The film grown from a subphase containing 0.5 M $NaNO_3$ was dried and calcined without and with full pretreatment described in the experimental section. When the dried film was calcined directly at 600 ºC, the flat SAXS pattern (Figure 11A, curve b) suggests the mesostructure was destroyed, ascribed to the NaOH left in the film which became concentrated during calcination and destroyed the mesostructure set by the silica. With full pretreatment, a broad diffraction peak was retained (Figure 11A, curve c), but is quite wide with relatively high intensity, indicating a relatively poor long-range order. The nitrogen sorption isotherm (Figure 11B) of sample c is a type IV isotherm with a type H4 hysteresis loop[65, 66] and gives a surface area of 660.4 $m^2/g$ and a mean pore size diameter at 2.3 nm obtained using BET method. The pore size is distributed between 1 nm and 10 nm with most of the pores under 5 nm (Figure 11C).

## 4. Conclusion

An environmentally friendly and cheap silica source, sodium silicate, was applied to synthesize mesoporous silica films at the air/solution interface. Using sodium silicate allows the formation of films containing a 2D hexagonal mesostructure, without producing any alcohol during condensation compared to TMOS. A free-standing silica film with 2D hexagonal structure can be prepared over a wide composition range using sodium silicates solution. The *in situ* GISAXS and X-ray reflectivity results show an intense reflection from excess crystallised surfactant at the interface which hindered the investigation of the film formation process. The addition of nitrate ions diminishes the crystallisation of surfactant species and also induces

the formation of a thicker film but prolongs the film formation time. *In situ* GISAXS and X-ray reflectivity suggest the surface has a wormlike liquid crystalline structure in the lateral direction with a 2D hexagonal structure gradually formed along the perpendicular direction and the 2D hexagonal structure was kept when the films are dried. Water wash treatments before calcination protect the mesostructure from collapsing during calcination, however the calcined silica films have relatively poor long-range order compared to ambient dried silica films although, it still has a relatively high surface area of 660.4 $m^2/g$.

## 5. Acknowledgement

A Di would like to thank the China Scholarship Council and the University of Bath for funding. The authors thank Diamond Light Source (UK) for the award of beam time (experiment No. SI52101-1). The authors would like to acknowledge Dr Benjamin M.D. O'Driscoll for providing the data in SI Figure 5 (page 80) and Dr Johnathan Rawle for his assistance with the reduction of GISAXS data.

## Reference

1. T.-L. Chew, A. L. Ahmad and S. Bhatia, *Adv. Colloid Interface Sci.*, 2010, **153**, 43-57.
2. B. Zornoza, C. Téllez and J. Coronas, *J. Membrane Sci.*, 2011, **368**, 100-109.
3. T. Maschmeyer, F. Rey, G. Sankar and J. M. Thomas, *Nature*, 1995, **378**, 159-162.
4. F. Jiao and H. Frei, *Angew. Chem. Int. Ed.*, 2009, **48**, 1841-1844.
5. X. Li, Y. Yang and Q. Yang, *J. Mater. Chem. A*, 2013, **1**, 1525-1535.
6. C. Kresge, M. Leonowicz, W. J. Roth, J. Vartuli and J. Beck, *Nature*, 1992, **359**, 710.
7. S. Che, Z. Liu, T. Ohsuna, K. Sakamoto, O. Terasaki and T. Tatsumi, *Nature*, 2004, **429**, 281.
8. D. Grosso, A. Balkenende, P. Albouy, A. Ayral, H. Amenitsch and F. Babonneau, *Chem. Mater.*, 2001, **13**, 1848-1856.
9. J. Patarin, B. Lebeau and R. Zana, *Curr. Opin. Colloid Interface Sci.*, 2002, **7**, 107-115.
10. M. Kruk, M. Jaroniec, C. H. Ko and R. Ryoo, *Chem. Mater.*, 2000, **12**, 1961-1968.
11. Y. Zhou, J. H. Schattka and M. Antonietti, *Nano Lett.*, 2004, **4**, 477-481.
12. P. Yang, D. Zhao, B. F. Chmelka and G. D. Stucky, *Chem. Mater.*, 1998, **10**, 2033-2036.
13. D. Zhao, J. Feng, Q. Huo, N. Melosh, G. H. Fredrickson, B. F. Chmelka and G. D. Stucky, *Science*, 1998, **279**, 548-552.
14. K.-j. Chao, P.-h. Liu and K.-y. Huang, *Comptes Rendus Chimie*, 2005, **8**, 727-739.
15. L. Nicole, C. Boissière, D. Grosso, A. Quach and C. Sanchez, *J. Mater. Chem.*, 2005, **15**, 3598-3627.
16. B. McCool, N. Hill, J. DiCarlo and W. DeSisto, *J. Membrane Sci.*, 2003, **218**, 55-67.
17. X. Lin, Q. Yang, L. Ding and B. Su, *ACS nano*, 2015, **9**, 11266-11277.
18. A. Gibaud, D. Grosso, B. Smarsly, A. Baptiste, J. Bardeau, F. Babonneau, D. Doshi, Z. Chen, C. J. Brinker and C. Sanchez, *J. Phys. Chem. B*, 2003, **107**, 6114-6118.
19. Y. Lu, R. Ganguli, C. A. Drewien, M. T. Anderson, C. J. Brinker, W. Gong, Y. Guo, H. Soyez, B. Dunn and M. H. Huang, *Nature*, 1997, **389**, 364.

20. A. Walcarius, E. Sibottier, M. Etienne and J. Ghanbaja, *Nat. Mater.*, 2007, **6**, 602.
21. A. Goux, M. Etienne, E. Aubert, C. Lecomte, J. Ghanbaja and A. Walcarius, *Chem. Mater.*, 2009, **21**, 731-741.
22. N. Nishiyama, S. Tanaka, Y. Egashira, Y. Oku and K. Ueyama, *Chem. Mater.*, 2002, **14**, 4229-4234.
23. J. Lee, J. Kim, B. J. Lee, J. Lee, H. W. Lee, M.-H. Hong, H.-H. Park, D. I. Shim, H. H. Cho and K.-H. Kwon, *Thin Solid Films*, 2018, **660**, 715-719.
24. H. Yang, N. Coombs, I. Sokolov and G. A. Ozin, *Nature*, 1996, **381**, 589.
25. K. J. Edler and S. J. Roser, *Int. Rev. Phys. Chem.*, 2001, **20**, 387-466.
26. K. J. Edler, A. Goldar, T. Brennan and S. J. Roser, *Chem. Commun.*, 2003, 1724-1725.
27. R. Klitzing and B. Kolaric, *Tenside Surfact. Det.*, 2002, **39**, 247-253.
28. D. Kudryavtsev, R. Bakeeva, L. Kudryavtseva, L. Y. Zakharova and V. Sopin, *Russ. Chem. Bull.*, 2000, **49**, 1501-1505.
29. B. M. O'Driscoll, E. Milsom, C. Fernandez-Martin, L. White, S. J. Roser and K. J. Edler, *Macromolecules*, 2005, **38**, 8785-8794.
30. B. M. O'Driscoll, C. Fernandez-Martin, R. D. Wilson, J. Knott, S. J. Roser and K. J. Edler, *Langmuir*, 2007, **23**, 4589-4598.
31. B. Yang and K. J. Edler, *Chem. Mater.*, 2009, **21**, 1221-1231.
32. B. Yang, J. A. Holdaway and K. J. Edler, *Langmuir*, 2013, **29**, 4148-4158.
33. K. J. Edler, M. J. Wasbrough, J. A. Holdaway and B. M. O'Driscoll, *Langmuir*, 2008, **25**, 4047-4055.
34. G. B. Kolesar, W. H. Siddiqui, R. G. Geil, R. M. Malczewski and E. J. Hobbs, *Toxicol.*, 1989, **13**, 285-295.
35. I. A. Alksay and M. Trau, *Science*, 1996, **273**, 892.
36. K. Edler, T. Brennan, S. Roser, S. Mann and R. Richardson, *Micropor. Mesopor. Mat.*, 2003, **62**, 165-175.
37. T. Arnold, C. Nicklin, J. Rawle, J. Sutter, T. Bates, B. Nutter, G. McIntyre and M. Burt, *J. Synchrotron Radiat.*, 2012, **19**, 408-416.
38. C. Nicklin, T. Arnold, J. Rawle and A. Warne, *J. Synchrotron Radiat.*, 2016, **23**, 1245-1253.
39. M. Basham, J. Filik, M. T. Wharmby, P. C. Chang, B. El Kassaby, M. Gerring, J. Aishima, K. Levik, B. C. Pulford and I. Sikharulidze, *J. Synchrotron Radiat.*, 2015, **22**, 853-858.
40. J. R. Levine, J. Cohen, Y. Chung and P. Georgopoulos, *J. Appl. Crystallogr.*, 1989, **22**, 528-532.
41. C. Baes and R. Mesmer, *The Hydrolysis of Cations*, John Wiley & Sons, 1976.
42. J. Šefčík and A. V. McCormick, *AIChE Journal*, 1997, **43**, 2773-2784.
43. C. T. Knight, R. J. Balec and S. D. Kinrade, *Angew. Chem. Int. Ed.*, 2007, **46**, 8148-8152.
44. J. L. Bass and G. L. Turner, *J. Phys. Chem. B*, 1997, **101**, 10638-10644.
45. D. Dimas, I. Giannopoulou and D. Panias, *J. Mater. Sci.*, 2009, **44**, 3719-3730.
46. O. Regev, *Langmuir*, 1996, **12**, 4940-4944.
47. C. Glinka, M. Nicol, G. Stucky, E. Ramli, D. Margolese, Q. Huo, J. Higgins and M. Leonowicz, *J. Porous Mater.*, 1996, **3**, 93-98.
48. P. Holmqvist, P. Alexandridis and B. Lindman, *J. Phys. Chem. B*, 1998, **102**, 1149-1158.
49. C. Vautier-Giongo and B. L. Bales, *J. Phys. Chem. B*, 2003, **107**, 5398-5403.
50. C. La Mesa, G. Ranieri and M. Terenzi, *Thermochim. Acta*, 1988, **137**, 143-150.
51. J. Esquena, C. Rodriguez, C. Solans and H. Kunieda, *Micropor. Mesopor. Mat.*, 2006, **92**, 212-219.
52. F. Michaux, N. Baccile, M. Impéror-Clerc, L. Malfatti, N. Folliet, C. Gervais, S. Manet, F. Meneau, J. S. Pedersen and F. Babonneau, *Langmuir*, 2012, **28**, 17477-17493.
53. E. K. Richman, T. Brezesinski and S. H. Tolbert, *Nat. Mater.*, 2008, **7**, 712.
54. K. J. Edler and J. W. White, *Chem. Mater.*, 1996, **9**, 1226-1233.
55. K. Kuperkar, L. Abezgauz, D. Danino, G. Verma, P. Hassan, V. Aswal, D. Varade and P. Bahadur, *J. Colloid Interface Sci.*, 2008, **323**, 403-409.

56. M. E. Helgeson, T. K. Hodgdon, E. W. Kaler and N. J. Wagner, *J. Colloid Interface Sci.*, 2010, **349**, 1-12.
57. D. Bartet, C. Gamboa and L. Sepulveda, *J. Phys. Chem.*, 1980, **84**, 272-275.
58. J. Frasch, B. Lebeau, M. Soulard, J. Patarin and R. Zana, *Langmuir*, 2000, **16**, 9049-9057.
59. E. Lissi, E. Abuin, L. Sepulveda and F. Quina, *J. Phys. Chem.*, 1984, **88**, 81-85.
60. E. Leontidis, *Curr. Opin. Colloid Interface Sci.*, 2002, **7**, 81-91.
61. C. Gamboa and L. Sepúlveda, *J. Colloid Interface Sci.*, 1986, **113**, 566-576.
62. E. Cappelaere and R. Cressely, *Colloid Polym. Sci.*, 1997, **275**, 407-418.
63. J. Israelachvili, *Intermolecular and Surface Forces*, Academic Press: San Diego, CA, 1991.
64. E. P. Barrett, L. G. Joyner and P. P. Halenda, *J. Am. Chem. Soc.*, 1951, **73**, 373-380.
65. M. Thommes, *Chem. Ing. Tech.*, 2010, **82**, 1059-1073.
66. K. S. Sing and R. T. Williams, *Adsorpt. Sci. Technol.*, 2004, **22**, 773-782.

# Supporting Information

## *In situ* X-ray Reflectivity and GISAXS Study of Mesoporous Silica Films Grown from Sodium Silicate Solution Precursors

Andi Di,[1] Julien Schmitt,[1,2] Naomi Elstone,[1] Thomas Arnold,[3] Karen J Edler[1]*

[1]Department of Chemistry, University of Bath, Claverton Down, Bath, Avon BA2 7AY, U.K.

[2]CNRS/ Saint-Gobain CREE, Saint-Gobain Research Provence, 550 avenue Alphonse Jauffret, Cavaillon, France

[3]Diamond Light Source, Harwell Campus, Didcot, OX11 0DE, U.K.

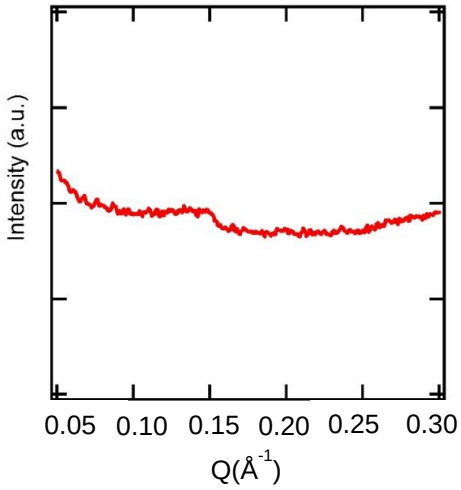


SI Figure 1. The SAXS pattern of a dried silica/CTAB/SDS/LPEI film synthesized from SDS (0.003 M)/CTAB (0.037 M)/LPEI (24 g/L) system.

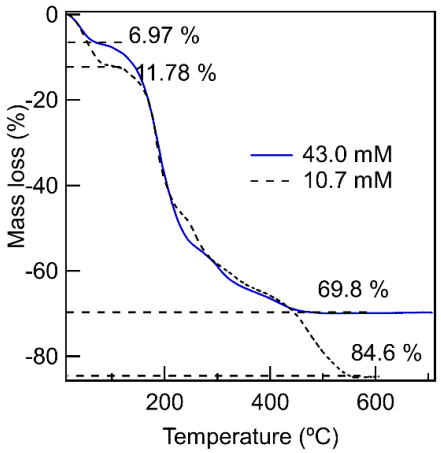


SI Figure 2. TGA analysis of an as-prepared silica film made from solutions containing 10.7 mM and 43.0 mM sodium silicate.

SI Table 1. Summary of SAXS data of the CTAB-LPEI templated silica.

| Variations | (100) peak position/Å$^{-1}$ | d-spacing/Å |
|---|---|---|
| Concentration of CTAB (M) | | |
| 0.0148 | 0.152 ± 0.001 | 41.3 ± 0.2 |
| 0.0222 | 0.158 ± 0.001 | 39.7 ± 0.2 |
| 0.0296 | 0.157 ± 0.001 | 40.0 ± 0.2 |
| 0.0370 | 0.156 ± 0.001 | 40.3 ± 0.2 |
| Concentration of PEI (g/L) | | |
| 12 | 0.153 ± 0.001 | 41.0 ± 0.2 |
| 24 | 0.157 ± 0.001 | 40.0 ± 0.2 |
| 36 | 0.159 ± 0.001 | 39.5 ± 0.2 |
| 48 | 0.158 ± 0.001 | 39.7 ± 0.2 |
| Concentration of NaOH (M) | | |
| 0.025 | 0.158 ± 0.001 | 39.7 ± 0.2 |
| 0.050 | 0.155 ± 0.001 | 41.6 ± 0.2 |
| 0.075 | 0.152± 0.001 | 41.6 ± 0.2 |
| 0.100 | 0.156 ± 0.001 | 40.3 ± 0.2 |

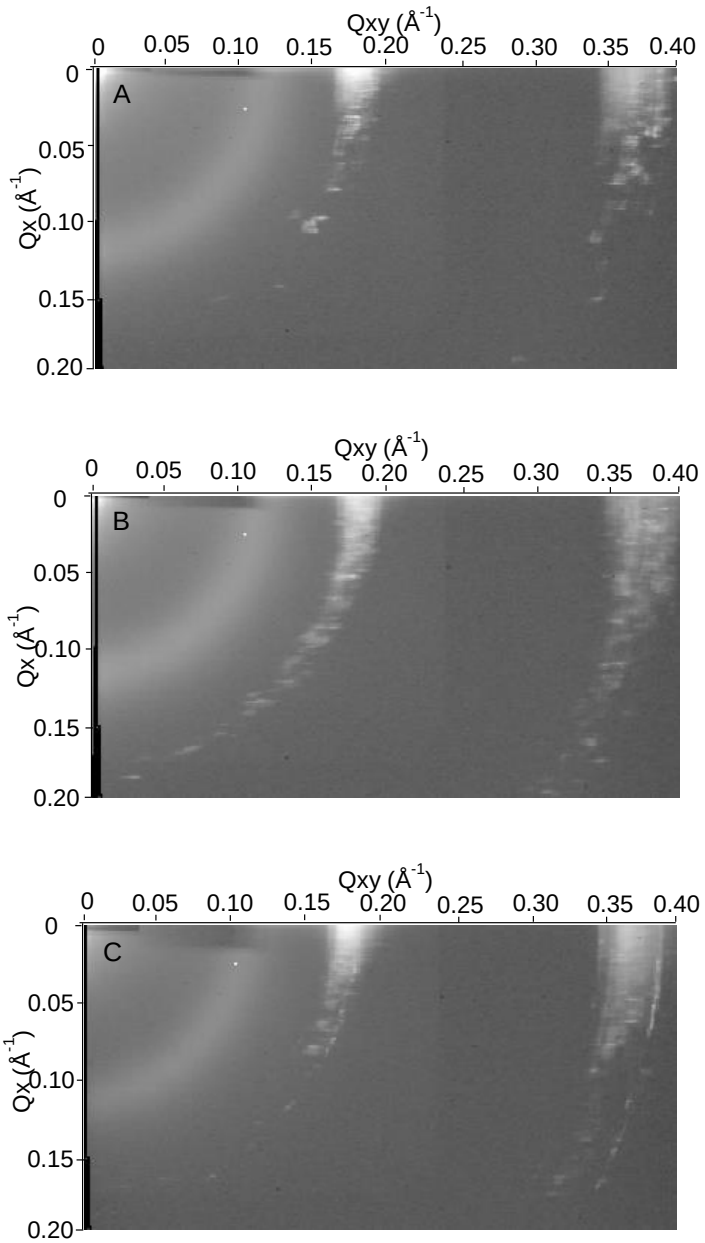


SI Figure 3. GISAXS patterns of interfacial structure on solutions with a sodium silicate concentration of (A) 43 mM (B) 54 mM and (C) 75.67 mM, collected just after the first XRR measurement in Fig. 3.

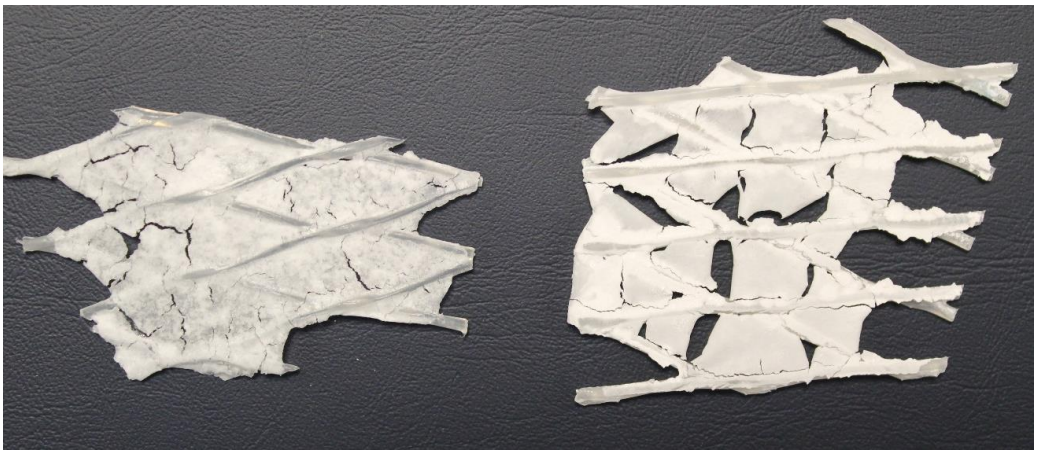

SI Figure 4.As-prepared films synthesized from solutions containing 0.037 M CTAB, 24g/L LPEI, 0.05 M NaOH and 65 mM sodium silicate. (Left) film A (thickness 0.142 mm) without $NaNO_3$ and (Right) film B with 0.05 M $NaNO_3$ (thickness 0.162 mm).

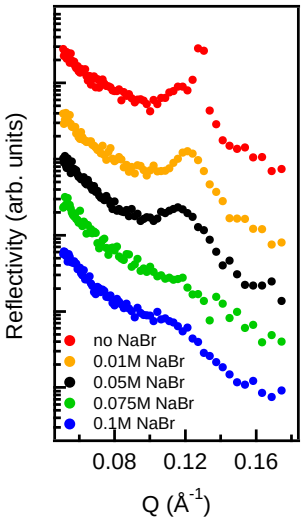


SI Figure 5: XRR from films prepared at 60 g/L SPEI with 0.037M CTAB at various NaBr concentrations demonstrating that the film ordering decreases and moves to lower Q (larger d-spacing) as the salt content in solution is increased.

## 3.2 Conclusion

In this chapter, as the first part of this project, has used the surfactant-polymer complexes as the template to synthesise free-standing silica films at the air-solution interface. This project is a follow-up study of previous work in our group, synthesising free-standing silica film using tetramethyl orthosilicate (TMOS) as the silica precursor. TMOS hydrolyses in water and produces methanol which is poisonous and will disrupt the ordering of the micelles that used as templates. Therefore, the aim of this study is to use an environmentally friendly silica source, sodium silicate, as silica precursor to synthesise silica film. Sodium silicate produces water during hydrolysation, therefore, it has the chance to template silica film with better mesostructure.

This chapter has found that the silica film prepared from sodium silicate solution has a similar mesostructure with those prepared using TMOS as the precursor. The concentration of sodium silicate in the film formation solution has been studied to investigate its effect on the film structure and the film formation time. The silica film form very fast (*ca.* 30 min) when the concentration of sodium silicate is relatively low (10.67 mM). And the film formation time prolongs with elevated concentration of sodium silicate and then decreases. The highest (173.0 mM) and lowest concentration (10.67 mM) of sodium silicate both disfavour the formation of a structure with long-range ordering. The concentrations of CTAB and LPEI have been studied to have little influence on the final structure of the dry silica film.

The thermal stability of mesostructure of the prepared silica film is quite low. Therefore, nitrate ion was added to the film formation solution to obtain silica film with a higher thermal stability. The effect of nitrate ion on the CTAB micelles has been studied using dynamic light scattering, which indicates an elongation of micelles in the presence of nitrate ions. The prepared silica film prepared when $NaNO_3$ is present in the film formation solution could maintain its mesostructure to some extent at high-temperature annealing if it is pretreated through washing with water and pre-calcination. The improvements in the thermal stability of silica film maybe attributed to the replacement of $Br^-$ by nitrate ion in the surfactant molecules, which increases the Krafft temperature of the surfactants.

In addition to the study of the influences of experimental parameters on the structure of the dry silica film. The evolution of the film structure at the air-solution interface is also studied using *in situ* GISAXS and XRR techniques. During the investigation of the film formation process when nitrate ion is absent, sharp peaks from the crystallised surfactant obstruct a clear conclusion on a detailed formation process. When nitrate is added into the system, the crystallisation of surfactant is diminished and leads to a possible film formation process: wormlike structures are formed both at the surface and along the direction normal to the surface at the beginning of the reaction (*ca.* 100 min after the reaction starts), then a 2D hexagonal packing happens along the vertical direction, the surface remains the wormlike packing till the end of the reaction.

This study even has not been able to prepare silica film with a better structure compared to previous studies, a relatively thermal stable silica film has been prepared and a possible film formation process has been concluded from the results of *in situ* techniques.

This chapter has focused on the templating method where surfactants are only used as the template and then are calcined away completely to produce the porous structure. This shines

lights on the preparation of surfactants which bear inorganic headgroup. These novel surfactants can be used not only as pore-makers but also as sources of inorganic materials to functionalise the inner pore wall of the prepared porous materials. Therefore the following chapter has focused on the preparation of inorganic material-based surfactants and the studies of their self-assembly behaviour in water using SANS and DLS techniques. As a proof of concept, the micelles they form in water are used as templates to functionalise porous materials to achieve a synergistic effect.

# 4

# Self-assembly of amphiphilic polyoxometalates for the preparation of mesoporous polyoxometalate-titania catalysts.

## 4.1 Introduction

The 3rd chapter has studied surfactant templating using organic complexes (a mixture of surfactant and polymer) to template mesoporous silica film. The surfactant template is completely burnt away to generate pores in the silica materials. In another way, surfactant templating method is also a potential method to functionalize inorganic materials within the inner wall of the generated pore in the prepared porous materials when an inorganic material is involved in the templating systems.

Polyoxometalates (POMs) are a group of inorganic metal-oxygen cluster anions, which have unique physical and chemical properties.[106,248] Polyoxometalate-based amphiphiles[110,130,139] have been widely studied and are a group of novel amphiphiles that may be applicable to material templating. This potential approach allows the decoration of POMs into the inner pore wall of non-catalytic materials (such as silica) to immobilise POM within the materials to realise the recyclability of the POM catalysts[101] and also allows the decoration of various catalysts (such as $TiO_2$, $WO_3$ etc.) materials to achieve synergistic effects for catalytic applications.[172]

Many studies have endeavoured to prepare amphiphiles that bear POMs as the hydrophilic headgroup. These methods can be classified according to the bonding type between POMs and the hydrophobic part into two types: through electrostatic interactions or chemical bonds.[110,139,249] Compared to electrostatic interactions, chemical bonds provide higher structural stability and solvent compatibility of the amphiphiles when used as soft templates.

In this chapter, double hydrocarbon chains are attached to a Dawson structured polyoxometalate ($[P_2W_{17}O_{61}]^{10-}$) to produce a final product $K_6[P_2W_{17}O_{61}\{OSi_2(C_nH_{2n+1})_2\}]$ (denoted as POM-2C$_n$, n = 12, 14, 16 and 18) through covalent bond. The POM-2C$_n$ materials are characterised using UV-vis, TGA, $^{31}$P NMR and C-H correlated NMR etc. The self-assembly of the POM-2C$_n$ in water is studied using small angle neutron scattering. Dynamic light scattering provides supporting information about the aggregation of the POM-2C$_n$ in water. The surfactant behaviour is found to be different from traditional surfactants, which normally form more elongated micelles with increasing hydrophobic tail length. The information about the micellar surface charge is also derived from SANS fitting using the rescaled Hayter-Penfold Mean Spherical

Approximation and is also studied using zeta-potential.

The micelles formed by POM-2C$_n$ in water are utilised as structure-directing agents in a hydrothermal method for the preparation of porous POM-$TiO_2$ hybrid materials. These hybrid materials show enhanced degradation properties of rhodamine B compared to unfunctionalised $TiO_2$ material. The bandgap of the resulting hybrid material is measured to be very close to that of $TiO_2$. Therefore, the improvement of the property is proposed to be attributed to the electron transfer from $TiO_2$ to POM which prevent the recombination of photo-excited electrons and holes and the electrostatic interactions between the positively-charged RhB molecules and negatively-charged POMs.

| This declaration concerns the article entitled: | | | | | | | | | |
|---|---|---|---|---|---|---|---|---|---|
| Self-assembly of amphiphilic polyoxometalates for the preparation of mesoporous polyoxometalate-titania catalysts. | | | | | | | | | |
| **Publication status (tick one)** | | | | | | | | | |
| **draft manuscript** | | **Submitted** | ✓ | **In review** | | **Accepted** | | **Published** | |
| **Publication details** | | | | | | | | | |
| **Candidate's contribution to the paper** | The candidate contributed to/ considerably contributed to/predominantly executed the…<br>**Formulation of ideas:**<br>The initial idea was formulated by KJE and RJE, while the proposals for beamtime were developed and written by KJE and AD (contribution 80 %).<br><br>**Design of methodology:**<br>All the measurements were designed by AD with exception of the set-up of small angle scattering done by NM at ISIS, with followed measurements carried out by AD. AD contribution 90%.<br><br>**Experimental work:**<br>Part of the preliminary data were collected by AD, JS, MAS and NM. AD contributed to the data analysis and the final experimental work included in the manuscript (AD contribution 70%).<br><br>**Presentation of data in journal format:**<br>The first draft was written by AD. Subsequent draft was reworked by AD following the feedback from KJE, NM, RJE, JS, MAS. (AD contribution 85%) | | | | | | | | |
| **Statement from Candidate** | This paper reports on original research I conducted during the period of my Higher Degree by Research candidature. | | | | | | | | |
| **Signed** | Andi D. | | | | **Date** | 26/09/2019 | | | |

Journal Name

ARTICLE TYPE

Cite this: DOI: 00.0000/xxxxxxxxxx

# Self-assembly of amphiphilic polyoxometalates for the preparation of mesoporous polyoxometalate-titania catalysts†

Andi Di,[a] Julien Schmitt,[a,b] Marcelo Alves Da Silva,[a] Najet Mahmoudi,[c] R. John Errington,[d] and Karen J Edler*[a]

Received Date
Accepted Date

DOI: 00.0000/xxxxxxxxxx

Amphiphilic polyoxometalate (POM) surfactants were prepared by covalently grafting double hydrophobic tails with chain lengths $C_{12}H_{25}$, $C_{14}H_{29}$, $C_{16}H_{33}$ or $C_{18}H_{37}$ onto the lacunary Wells-Dawson $\{P_2W_{17}O_{61}\}$ headgroup. The critical micelle concentrations (CMCs) of these novel surfactants in aqueous solutions were determined by conductivity, and micelle formation was studied by small angle neutron scattering (SANS). Surprisingly, the amphiphiles with longer hydrophobic tails tend to form less elongated and more globular micelles in water. The self-assembled amphiphilic polyoxometalates were used as templates in the hydrothermal synthesis of mesoporous $TiO_2$ containing dispersed, immobilised $\{P_2W_{17}O_{61}\}$ units, which showed enhanced activity for the photodegradation of rhodamine B (RhB). The catalyst was recycled eight times with no loss of efficiency, demonstrating the stability of the hybrid structure. The amphiphilic polyoxometalates, therefore have excellent potential for the synthesis of various types of catalytically active porous materials.

## Introduction

Polyoxometalates (POMs) are a class of unique nanoscale transition metal oxide clusters, formed by earth-abundant metals in their highest oxidation states.[1,2] Due to their remarkable redox and photochemical properties, they are often used as inexpensive photocatalysts for the green removal of organic pollutants or transition metals from water.[3,4] Similar to the semiconductor photocatalysts, which experience electron transfer from the valence band (VB) to the conduction band (CB) under ultraviolet irradiation, POMs undergo electron transfer from the oxygen-based highest occupied molecular orbitals (HOMO) to the lowest unoccupied molecular orbitals (LUMO) on the addenda atoms under UV irradiation,[5] resulting in a colour change to blue. The charge-transfer excited state POM (POM*) has a highly oxidizing power that is strong enough to oxidise organic species or to generate ·OH radicals.[6,7]

Amphiphilic surfactants are of great interest for their applications as templates in the formation of mesoporous materials, which typically form from mixed aqueous solutions of surfactants and inorganic precursors.[8–10] Porosity is generated in the inorganic materials after the removal of the organic components from the surfactant template. These mesoporous materials, due to their high specific surface areas and uniform mesopore size, are particularly interesting as supports for catalysts.[11,12]

The incorporation of POMs onto conventional supports, such as $SiO_2$,[13,14] $TiO_2$,[15,16] $Al_2O_3$[13] or metal-organic frameworks,[17] through direct dispersion has been investigated to increase the application of POMs for catalysis. However, it has been reported that POMs anchored onto the surface of such supports are not stable since the POMs may be leached out by water or alcohol.[18] Studies have therefore been undertaken to modify the inner walls of the support materials to improve POM adhesion: *e.g.* by grafting organic moieties such as aminosilane or imidazole, to provide strong anchoring of POMs and prevent POM leaching when applied as a catalyst in polar solvent media.[18–21] However, this method limits the applications of these materials due to the low thermal stability of the organic anchoring groups at high temperatures.[22] Alternatively, researchers have been exploring the encapsulation of POMs into aggregates formed by surfactants or polymers,[23–25] with the aim to fabricate polyoxometalate-decorated mesoporous materials *via* a one-pot synthesis.

To incorporate POMs into the matrix of inorganic mesostruc-

[a]*Department of Chemistry, University of Bath, Claverton Down, Bath, BA2 7AY, UK*
[b]*LSFC Laboratoire de Synthèse et Fonctionnalisation des Céramiques, UMR 3080 CNRS / Saint-Gobain CREE, Saint-Gobain Research Provence, 550 avenue Alphonse Jauffret, Cavaillon, France*
[c]*ISIS Neutron and Muon Source, Science and Technology Facilities Council, Rutherford Appleton Laboratory, Didcot OX11 0QX, UK*
[d]*Chemistry, School of Natural and Environmental Sciences, Newcastle University, Newcastle upon Tyne, NE1 7RU, UK*

† Electronic Supplementary Information (ESI) available: [details of any supplementary information available should be included here]. See DOI: 00.0000/00000000.

tured materials or synthesise porous hybrid materials where the POMs are accessible, a POM-based amphiphile that can be used as a templating agent is key. Self-assembly is an efficient method to synthesise materials with high surface areas and open networks, and hence the use of POM amphiphiles has the potential to organise accessible polyoxometalates directly and uniformly within the supports. There have been previous reports on the synthesis of surfactants with POMs as headgroups through covalent bonding,[26–30] to the best of our knowledge, there have been no detailed studies of the application of POM-based amphiphiles to template mesoporous POM-decorated inorganic materials.

Among various oxide semiconductor photocatalyst materials, titania is recognised as the most suitable material for widespread environmental applications due to its low cost, strong oxidizing ability and photostability.[31,32] Its performance is often reinforced through the incorporation of electron-transporting materials, such as graphene oxide[33] or graphene,[34] within the titania matrix. Also, there have been attempts to load polyoxometalates onto $TiO_2$ through a layer by layer strategy, physically mixing or electrostatic bonding.[35–37] These studies have demonstrated the synergistic effects between $TiO_2$ and polyoxometalates.

In this paper, we report the characterisation of micellar structures formed by amphiphilic $[P_2W_{17}O_{61}\{OSi_2(C_nH_{2n+1})_2\}]^{6-}$ (Wells-Dawson type POMs with double hydrocarbon tails $C_nH_{2n+1}$, denote as POM-2C$_n$, with molecular structure illustrated in Fig. 1), the influence of the tail length of the amphiphiles on the micelle shape and counterion ionisation degree, using conductivity, small angle neutron scattering (SANS), zeta-potential and dynamic light scattering (DLS).

The Wells-Dawson anion $[\alpha\text{-}P_2W_{18}O_{62}]^{6-}$ can readily accept multiple electrons without any change in the cluster geometry, and both $[\alpha\text{-}P_2W_{18}O_{62}]^{6-}$ and its lacunary derivative $[P_2W_{17}O_{61}]^{10-}$ are often used as co-catalysts for catalytic oxidation and photocatalytic reduction.[38,39] The siloxane derivatives $[P_2W_{17}O_{61}\{OSi_2(C_nH_{2n+1})_2\}]^{6-}$ are amphiphiles with redox-active metal oxide headgroups and form micelles in water. Therefore, these micelles were used directly as templating agents for the hydrothermal synthesis of POM-$TiO_2$ mesoporous materials, without the addition of any other co-templating agents. The resulting POM-$TiO_2$ hybrid materials have relatively high surface areas and better rhodamine B (RhB) photodegradation properties compared to a porous $TiO_2$ material prepared using a commercial anionic surfactant template.

## Experimental

### Materials

$Na_2WO_4{\cdot}2H_2O$ (purity > 99%), phosphoric acid (85 wt% in water solution), $NH_4Cl$ (purity > 99.5 %), KCl (laboratory reagent grade), dodecyltrichlorosilane ($C_{12}H_{25}SiCl_3$, purity > 95%), octadecyltrichlorosilane ($C_{18}H_{37}SiCl_3$, purity > 90%), $KHCO_3$ (purity > 99.7%), sodium dodecyl sulfate (SDS, purity > 99%) and $D_2O$ (99.9 atom% D) were purchased from Sigma Aldrich. Tetradecyltrichlorosilane ($C_{14}H_{29}SiCl_3$, purity 98%) and hexadecyltrichlorosilane ($C_{16}H_{33}SiCl_3$, purity 98%) were purchased from Fluorochem. All chemicals were used without further purification. 70 mol% $D_2O$ in $H_2O$ was prepared using ultrapure water (18 Ω·cm, from an ELGA PURELAB flex water purification system).

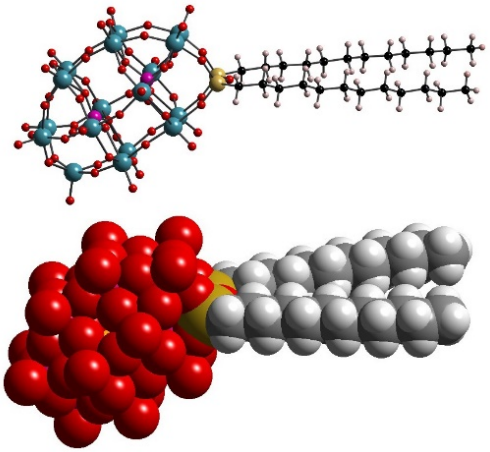

**Fig. 1** Ball-and-stick and space-filling representations of the structure of the $[P_2W_{17}O_{61}\{OSi_2(C_nH_{2n+1})_2\}]$ anion (R = $C_{12}H_{25}$) POM-2$C_{12}$. Colour code: W (blue), P (purple), O (red), Si (yellow), C (black) and H (white).

### Preparation of POM-2C$_n$

$K_6[\alpha\text{-}P_2W_{18}O_{62}]{\cdot}14H_2O$ was prepared as previously described by Droege.[40] Lacunary $K_{10}[\alpha\text{-}P_2W_{17}O_{61}]{\cdot}19H_2O$ was synthesised according to the method of Finke *et al.*,[41] and then used to prepare POM-2C$_n$. A typical reaction is as follows: $K_{10}[\alpha\text{-}P_2W_{17}O_{61}]{\cdot}19H_2O$ (1.040 mmol) was dispersed in anhydrous MeCN (180 ml) and stirred under nitrogen for 4 hours. Trichlorosilane, $RSiCl_3$ (R = $C_{12}H_{25}$, $C_{14}H_{29}$, $C_{16}H_{33}$ or $C_{18}H_{37}$, 4.94 mmol) was dissolved in anhydrous dichloromethane (60 ml), then added dropwise to POM suspension with stirring. The the obtained mixture is stirred for 12 hours to finish the reaction.

The mixture produced was filtered and the clear solution was rotary-evaporated to dryness. The powder obtained was washed four times with anhydrous diethyl ether (50 ml) to remove the excess of trichlorosilane, and was vacuum-dried to give the final product $K_6[P_2W_{17}O_{61}\{OSi_2(C_nH_{2n+1})_2\}]$, denoted as POM-2C$_n$, with n=12, 14, 16 or 18.

### Synthesis of POM-$TiO_2$

The nPOM-$TiO_2$ hybrid materials were prepared by mixing an aqueous HCl solution (pH = 2) of POM-2C$_n$ (9.17 mM, 9 ml) and an aqueous HCl solution (pH = 2) of $TiOSO_4$ (0.672 M, 6 ml) to give final POM-2C$_n$ and $TiOSO_4$ concentrations of 5.5 mM and 0.269 M respectively. The reaction was performed at 150 °C in an autoclave with a ramping rate of 5 °C/min, and then was held at 150 °C for 20 hours. The obtained powder was filtered and washed with water to remove any excess surfactant prior to freeze-drying. The freeze-dried powder was calcined at 500 °C in air for 8 hours. The hydrocarbon tails were burnt away to generate pores. And the Dawson structured polyoxometalate has been shown to be stable at this temperature.[42] The calcined

products were porous $TiO_2$ materials with functionalised POM units, and were labelled nPOM-$TiO_2$ catalyst with n= 12, 16 or 18 depending on the tail length of the POM-2$C_n$ used in the synthesis. For comparison, a sample of $TiO_2$ templated by sodium dodecyl sulfate (SDS) was synthesised according to the procedure already described in the literature which used a much higher surfactant concentration (0.26 M SDS) than that used for POM-2$C_n$ templating.[43] A higher concentration of POM-2$C_{16}$ (22.0 mM) was used to prepare POM-$TiO_2$ hybrid materials using the same method that was described above, the resulting material is labelled as 16POM-$TiO_2$-2.

The synthesised materials were characterised using transmission electron microscopy (TEM), nitrogen sorption, powder X-ray diffraction (PXRD) and energy dispersive X-ray (EDX) elemental mapping.

**Photocatalytic activity test**

0.015 g nPOM-$TiO_2$ or SDS templated $TiO_2$ catalyst was added to 30 ml of an aqueous solution of RhB (15 mg/L) and $H_2O_2$ (1.5 mmol/L). The mixture was exposed to solar light (energy equals one sun, generated by a solar simulator) under stirring for 80 min, during which time 2 ml aliquots of solution was removed from the system every 20 min and centrifuged. UV/vis absorption measurement was conducted on the clear solution obtained to determine the concentration of rhodamine B (RhB) according to the major absorption intensity at 553 nm, for each degradation stage. The measured solution was added back to the system at every stage to maintain the total volume. A blank experiment was carried out as follows: a 30 ml solution of RhB (15 mg/L) and $H_2O_2$ (1.5 mmol/L) was illuminated by solar light without adding any photocatalyst. The change of RhB concentration with illumination time was recorded using the same method as above.

**$Ag^+$ reduction**

Polyoxometalates can be reduced by organic electron donors (*e.g.*, alcohols) upon exposure to visible and ultraviolet light.[44] 0.02 g The nPOM-$TiO_2$ hybrid material (0.02 g) was dispersed in isopropanol with stirring and illuminated by solar light for about 20 min. The colour of the dispersion changed from white to blue. An aqueous $AgNO_3$ solution (0.05 M) was added dropwise into the dispersion after removal from light, causing the blue-coloured dispersion to turn to brown abruptly. The brown powder was then filtered, washed with water and air-dried for TEM and EDX elemental mapping analysis.

**Small angle neutron scattering**

**Data collection.**

Small Angle Neutron Scattering (SANS) experiments were performed on the LOQ SANS instrument[45] at the ISIS Neutron and Muon Spallation Source (Oxfordshire, UK) with a typical time-averaged flux of $2\times10^5$ $cm^{-2}s^{-1}$. The data were collected using a $^3He$-$CF_4$ filled ORDELA "area" detector. The probed q range was approximately from 0.007 to 0.20 $Å^{-1}$, where q is the momentum transfer. The samples were measured in UV-spectrophotometer grade quartz cells with a path length of 1 mm at 25 °C.

The raw spectra were corrected for the background from the solvent, sample cell and other sources using standard workflows in the Mantid software package.[46] Scattering data were normalised against the scattering from a partially-deuterated polystyrene blend of known molecular weight to put the SANS data on the absolute scale,[47] so I(q) equals the differential scattering cross section $d\Sigma/d\Omega(q)$. The output data was absolute scattered intensity, I(q) in $cm^{-1}$, versus the momentum transfer, q in $Å^{-1}$.

**Data modelling.**

The measured scattering intensity I(q) as a function of the momentum transfer q, for centrosymmetric particles, is given as:

$$I(q) = A(\Delta SLD)^2 \, P(q)S(q,\phi) \quad (1)$$

where A is the scale factor. $\phi$ is the volume fraction of particles. $\Delta$SLD corresponds to the scattering length density (SLD) contrast between particles and solvent. P(q) is the form factor, which corresponds to the orientationally averaged scattering profile of a single particle and can be computed from a structural model. $S(q,\phi)$ is the structure factor that accounts for the interactions between the particles in the solution.

For a dilute suspension, the interactions between micelles, $S(q,\phi)$, can be neglected. I(q) mainly depends on the shape and size of the particles:

$$I(q) = A(\Delta SLD)^2 \, P(q) \quad (2)$$

due to the large SLD difference between the POM-2$C_n$ headgroup ($4.42\times10^{-6}$ $Å^{-2}$) and tails ($-0.38\times10^{-6}$ $Å^{-2}$), the SANS patterns were fitted using core-shell models. For some of the scattering data, the core-shell sphere model[48] gave satisfactory fit results. However, in some circumstances, it gave an unusually large radius, which was not in accordance with the tail length of a surfactant monomer, so a core-shell ellipsoid model[49,50] was favoured and applied to get better fit results. In the modelling, the core of the micelles was assumed to only contain the hydrocarbon tails, while the shell was formed from the headgroups, a partial contribution from the tails and water. Through fitting the form factor P(q), a minimum radius of the core ($R_{min}$), a shell thickness (t), a core ellipticity ($\varepsilon$) and a shell neutron scattering length density (SLD) were obtained.

In the semi-dilute regime, where micelles are interacting, the structure factor also has to be taken into account. Since the POM-2$C_n$ micelles are charged due to the ionisable headgroups, they experience a Coulomb repulsion modelled using the Hayter Penfold Rescaled Mean Spherical Approximation (RMSA)[51] which gives the volume fraction of charged particles interacting ($\phi$) and the number of charges per micelle z (number of electrons). This model depends on the Debye screening length of interactions. This Debye length can be calculated knowing the temperature (25 °C) and the relative permittivity of the medium (72.08 for $D_2O$, 72.2 for 70 mol% $D_2O$).[52]

Scattering patterns from samples at the same concentration but

in two different solvents ($D_2O$ and 70 mol% $D_2O$) were fitted simultaneously using Sasview (version 4.2.1) in order to better constrain the fits using contrast variation. Calculated neutron SLDs of the hydrocarbon tails, the POM headgroup and the solvents used for fitting are listed in SI Table 1 (page 98).

**Other Techniques**

The electrical conductivities of the surfactant aqueous solutions were measured using a METTLER TOLEDO conductivity meter. NMR spectroscopic measurements were carried out using a 500 MHz Bruker Avance II+ spectrometer. Typical samples were made of POM-2$C_n$ surfactants dissolved in $D_2O$. The $^{31}$P NMR was measured with a relaxation time of 20 seconds. IR spectra were measured using a Bruker IR spectrometer at room temperature in a dry box. TGA was applied to measure the change of sample weight as a function of temperature. An alumina crucible with about 100 mg sample was put into a furnace, which was heated up in air at a constant heating rate 1 °C/min, while a sensitive balance was recording the loss of the sample weight. The results are displayed as the loss of mass percentage against temperature in °C. POM-2$C_n$ aqueous solutions at 5.5 mM were measured at room temperature using dynamic light scattering (DLS) in a Malvern Zetasizer Nano ZSP (Malvern, UK). All samples were filtered through a 0.45 $\mu$m filter (Millex-HA) to remove any dust before the measurements. Samples were measured at a scattering angle of 173 ° and a wavelength of 632.8 nm for 120 s, repeated 5 times. The size distribution, weighted in volume, was extracted using the CONTIN method. The zeta-potential of the micelles was also studied, at the same concentration, using the same instrument. Nitrogen sorption measurements were carried out at liquid nitrogen temperature (77.36 K) using a BELSORP instrument (BELSORP-mini Inc. Japan). The samples were degassed under vacuum at 523 K for 1000 min prior to the measurements. Surface areas were calculated using the Brunauer-Emmett-Teller (BET) equation. PXRD measurements were performed on a Stoe STADI P high-resolution system equipped with a DECTRIS Double MYTHEN 1K strip detector, and employing Cu-$K_{\alpha 1}$ radiation ($\lambda = 1.54060\times10^{-10}$ m). The samples were measured in the range of $10\,^\circ < 2\theta < 70\,^\circ$ at 2 ° per minute. The morphologies of the obtained materials were observed by TEM using a JEOL JEM-2100Plus instrument with an operating voltage at 200 kV maximum. An Oxford Instruments large area EDX detector, associated with the TEM, and Aztec analysis software were used for high-resolution elemental mapping analysis. Prepared POM-loaded mesoporous $TiO_2$ materials were characterised using an Anton Paar SAXSess instrument with a Panalytical PW3830 X-ray generator which gave a q range between 0.08 Å$^{-1}$ and 2.7 Å$^{-1}$. The line X-ray source used was a Cu $K_\alpha$ X-ray tube at 40 kV and 50 mA. X-rays were detected by a reusable Europium excitation based image plate (size: 66 × 200 mm) with a 42.3 $\mu$m$^2$ pixel size. The image plate was subsequently read by a Perkin Elmer cyclone reader using OptiQuant software. SAXS profiles were generated by using the SAXSquant program.

**Kinetics of photocatalytic degradation**

UV-vis absorption was used to follow dye degradation performed on a Perkin-Elmer Lambda 750S UV/vis spectrometer. The rate of photodegradation of rhodamine B (RhB) in the presence of photocatalysts can be calculated from a fit to the experimental data. The Langmuir-Hinshelwood model can be used to describe the kinetic of the photodegradation, and the model is further simplified if possible.[53] Here, the degradation kinetics were approximated as pseudo-first-order kinetics with respect to the concentration of RhB (C):

$$-dC/dt = k_{obs}C \tag{3}$$

where $k_{obs}$ is the rate constant. Integration of the equation (with $C_t$, $C_0$ are the RhB concentrations at time t and 0 min respectively) gives:

$$ln(C_t/C_0) = -k_{obs}t \tag{4}$$

where the values of $k_{obs}$ (unit: min$^{-1}$) can be obtained directly from the regression analysis of a linear plot of ln ($C_t/C_0$) versus time.

## Results and discussion

**Characterisation of $K_6[\alpha$-$P_2W_{18}O_{62}]\cdot14H_2O$, $K_{10}[\alpha_2$-$P_2W_{17}O_{61}]\cdot19H_2O$ and POM-2$C_n$**

The synthesis of POM-2$C_n$ surfactants with structure illustrated in Fig. 1 were prepared from $K_6[\alpha$-$P_2W_{18}O_{62}]\cdot14H_2O$, *via* the lacunary derivative $K_{10}[\alpha_2$-$P_2W_{17}O_{61}]\cdot19H_2O$ using established methods.[41]

Starting materials and POM-2$C_{12}$ were characterised by IR and $^{31}$P NMR spectroscopy (Fig. 2). In the $^{31}$P NMR spectra (Fig. 2A-C), $K_6[\alpha$-$P_2W_{18}O_{62}]\cdot14H_2O$ showed the characteristic peak at -13.03 ppm in addition to two small peaks at around -11.53 and -12.31 ppm due to the $K_6[\beta$-$P_2W_{18}O_{62}]\cdot14H_2O$ isomer, while two $^{31}$P NMR peaks were observed due to the non-equivalent phosphorus atoms in $K_{10}[\alpha_2$-$P_2W_{17}O_{61}]\cdot19H_2O$ (-7.24 and -14.38 ppm) and $K_6[P_2W_{17}O_{61}\{OSi_2(C_nH_{2n+1})_2\}]$. C-H correlated NMR further suggests the successful grafting of $C_{12}H_{25}$ hydrocarbon tails as shown in Fig. 3. The peak labelled 2 is due to diethyl ether impurities. Peaks labelled 1, 3 and 4 are correlated to the double hydrocarbon tails as illustrated in detail in Fig. 3.

In the IR spectra (Fig. 2D), only one type of $\nu$(P-O) was observed at 1087 cm$^{-1}$ for symmetric $K_6[\alpha$-$P_2W_{18}O_{62}]\cdot14H_2O$.[54,55] For $K_{10}[\alpha_2$-$P_2W_{17}O_{61}]\cdot19H_2O$, the bands of $\nu$(P-O) vibrations were observed at 1013, 1046 and 1077 cm$^{-1}$, similar to those reported in literature.[56] After the attachment of the hydrocarbon tails to form the POM-2$C_{12}$ surfactant, the three $\nu$(P-O) vibration peaks were retained with the peak at 1046 cm$^{-1}$ overlapping with the peak at 1083 cm$^{-1}$. Peaks at 2920 and 2850 cm$^{-1}$ correspond to the $\nu$(C-H) vibration, indicating the presence of both $\{P_2W_{17}O_{61}\}$ and hydrocarbon chains in the final product.

UV/vis absorbance spectra (SI Fig.1,page 98), showed a bathochromic shift in the absorption edge upon attachment of the two hydrocarbon chains, so that the POM-2$C_{12}$ derivatives ab-

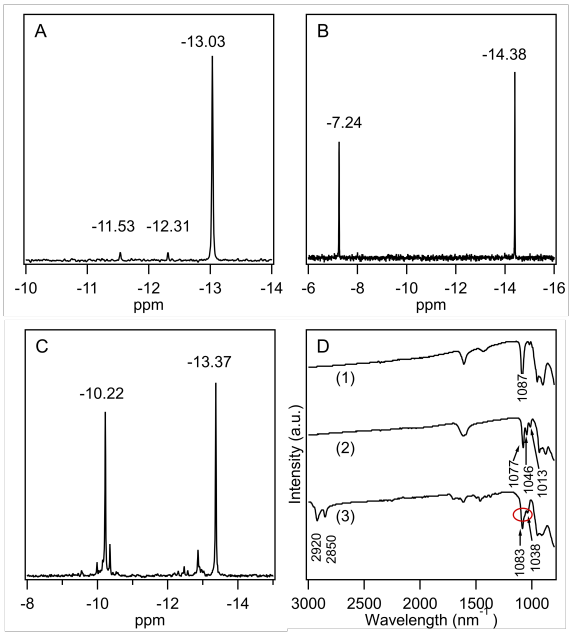


**Fig. 2** $^{31}$P NMR spectra of (A) $K_6[\alpha\text{-}P_2W_{18}O_{62}]\cdot 14H_2O$ (B) $K_{10}[\alpha_2\text{-}P_2W_{17}O_{61}]\cdot 19H_2O$ and (c) POM-2$C_{12}$. (D) IR spectra of (1) $K_6[\alpha\text{-}P_2W_{18}O_{62}]\cdot 14H_2O$ (2) $K_{10}[\alpha_2\text{-}P_2W_{17}O_{61}]\cdot 19H_2O$ and (3) POM-2$C_{12}$ (where the red circle indicates the existence of Dawson structured POM after tail grafting).

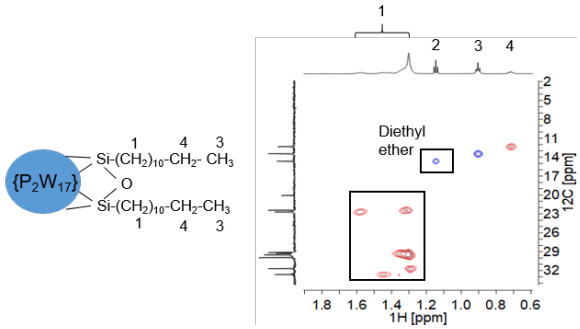


**Fig. 3** C-H correlated NMR of POM-2$C_{12}$ illustrated by the POM-2$C_{12}$ molecular structure ({$P_2W_{17}$} represents {$P_2W_{17}O_{61}$}), the square on the left of the 2D NMR graph labelled 1 is related to the 10 methylene groups labelled 1 in the POM-2$C_{12}$ molecular structure. Blue signals represent methyl groups and red for methylene groups.

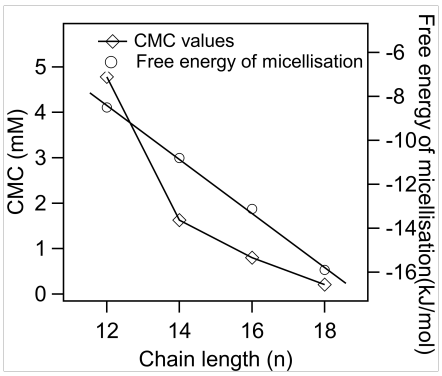


**Fig. 4** Plot of CMC and free energy of micellisation ($\Delta G^\circ_{mic}$) vs hydrocarbon chain length.

sorb light over a wider wavelength range compared to the lacunary $K_{10}[\alpha_2\text{-}P_2W_{17}O_{61}]\cdot 19H_2O$. TGA on the POM-2$C_{12}$ material (SI Fig.2, page 99), showed a mass loss of 6.7%, corresponding to the tail weight percentage in POM-2$C_{12}$ obtained (calculated mass loss is 7%). These results confirm the successful synthesis and structure of the POM-2$C_{12}$.

### Critical micelle concentrations

SI Fig.3A-D (page 99) show plots of the electrical conductivity vs the concentration of POM-2$C_n$ in water, and CMC values were determined by the intersections of the two straight lines. The CMCs of the POM-2$C_n$ surfactants versus hydrophobic chain length are plotted in Fig. 4, giving a trend similar to that observed for di-alkyl sulfosuccinate surfactants (CMCs given in SI Table 2 at page 99),[57,58] alkyl trimethylammonium bromides (abbreviated as $C_n$TAB, CMC values given in SI Table 3 at page 100)[59,60] and sodium alkyl sulfates (CMC values in SI Table 4 at page 100),[61–65] where a surfactant with longer hydrophobic tail/tails has a lower CMC compared to the one with the same headgroup but shorter hydrophobic part.

### Degree of micelle ionisation and free energy of micellisation

The percentage of bound counterions in relation to the number of surfactant ions in the micelles is the fraction of micellar charge neutralized, $\beta$, defined as counterion binding. The degree of micelle ionisation $\alpha$ equals $1-\beta$ , and can be calculated from the conductivity slope above the CMC ($m_1$) divided by that of below the CMC ($m_2$): $\alpha = m_1/m_2$.[66] The calculated $\alpha$ values are listed in Table 1. It can be seen that micelles formed by POM-2$C_n$ with longer tails have a lower counterion dissociation, therefore higher screening by the counterion. The POM-2$C_n$ surfactants show similar changing trends in $\alpha$ as seen for traditional surfactants, such as di-alkyl sulfosuccinates, $C_n$TAB and sodium alkyl sulfates (SI Table 1-3 at page 98, 99 and 100).[57,59,60,63,64,67] The counterion binding $\beta$ and the CMC are related to the free energy of micellisation *via* equation:

$$\Delta G^\circ_{mic} = (1+\beta)RTln(CMC) \quad (5)$$

the calculated free energies of micellisation are listed in Table 1 and plotted in Fig. 4. The $\Delta G^\circ_{mic}$ was calculated to be between -8.5 and -15.9 kJ·mol$^{-1}$ at room temperature. The linear relationship in the variation of $\Delta G^\circ_{mic}$ with the tail length is consistent with that observed for $C_n$TAB surfactants.[68] The value of the slope obtained from the line in Fig. 4, -1.26 $\pm$ 0.05 kJ·mol$^{-1}$, here represents the free energy increment for two $CH_2$ groups (designated as $\Delta G^\circ_t$). The $\Delta G^\circ_t$ of the POM-2$C_n$ system is much lower than that of $C_n$TAB (-3.45 $\pm$ 0.2 kJ·mol$^{-1}$) with a single hydrocarbon tail.[68]

By comparing the $\Delta G^\circ_{mic}$ values of POM-2$C_n$ with those of

di-alkyl sulfosuccinate surfactants (SI Table 2 at page 99), it is seen that the POM-2C$_n$ surfactants can form micelles more easily in water because they have longer hydrophobic tails. They also have relatively similar free energies of micellisation[60] with those of single-tailed C$_n$TAB (n= 12, 14, 16) surfactants (SI Table 3 at page 100). These results indicate that, despite the fact that POM-2C$_n$ are double-tailed surfactants, they form micelles as easily as conventional single-tailed surfactants and aggregate more efficiently compared to conventional anionic double-tailed surfactants.

**Table 1** The degree of micelle ionisation and free energy of micellisation values of POM-2C$_n$ in water, errors were calculated from those from the determination of CMCs.

| Material | CMC (mM) | $\alpha$ | $\Delta G^{\circ}_{mic}$ (kJ·mol$^{-1}$) |
|---|---|---|---|
| POM-2C$_{12}$ | 4.78 ± 0.08 | 0.53 ± 0.04 | -8.5 ± 0.2 |
| POM-2C$_{14}$ | 1.63 ± 0.05 | 0.44 ± 0.03 | -10.8 ± 0.5 |
| POM-2C$_{16}$ | 0.80 ± 0.04 | 0.29 ± 0.03 | -13.1 ± 0.9 |
| POM-2C$_{18}$ | 0.21 ± 0.02 | 0.26 ± 0.02 | -15.9 ± 0.6 |

### SANS study of POM-2C$_n$

Above CMCs, the POM-2C$_n$ surfactants assemble in water. The shape of these aggregates is expected to have important influences in the field of micellar catalysis,[69] photochemistry[70] and materials templating,[71] and is therefore interesting to investigate. We used SANS to probe the micelles formed by these surfactants in aqueous solutions.

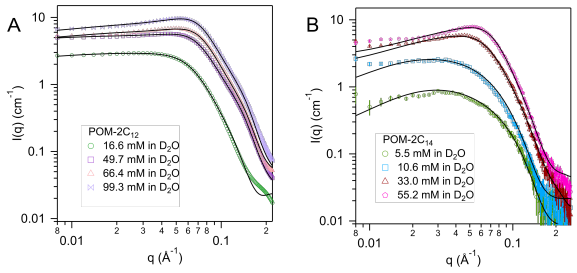


**Fig. 5** SANS patterns of (A) POM-2C$_{12}$ and (B) POM-2C$_{14}$ micelles in D$_2$O at different concentrations. The fits are given as black lines.

The best fit for the micelles formed by POM-2C$_{12}$ in water was obtained from a core-shell ellipsoidal model. The SANS patterns and their corresponding fits are plotted in Fig. 5 for the D$_2$O contrast, while the fitted parameters along with the definition of the abbreviations are listed in Table 2. The elongation of the micelles was found to be dependent on the concentration: the ellipticity, $\varepsilon$, indicating the degree of elongation, varies from 4.0 ± 0.4 to 5.1 ± 0.4. Similarly, R$_{min}$ ranges from 11 ± 1 Å to 15 ± 1 Å, slightly below the length of fully extended C$_{12}$H$_{25}$ chains according to the Tanford equation (16.7 Å).[72] Measurements of solutions prepared using 70 mo% D$_2$O as solvent (a value that was calculated to contrast match the POM-2C$_n$ headgroup) were also made (SI Fig.4A, page 100). Fitting the data at 70 mol% D$_2$O still required a shell in the model, but with a lower SLD than that calculated for both dry POM and solvent (SI Table 5 at page 101), suggesting that a portion of the hydrocarbon tail is present in the shell. The shell thickness was found to decrease with increasing concentration (from 22 ± 1 Å at 16.6 mM to 15 ± 1 Å at 99.1 mM). Except for the lowest concentration, these values (see Table 2) are in the same range as the dry {P$_2$W$_{17}$O$_{61}$} headgroup size (between 12 and 17 Å due to the ellipsoidal shape of the headgroup).[73]

With increasing concentration, a broad peak emerged at around q = 0.06 Å$^{-1}$. The peak indicates the intermicellar interactions and was fitted using the RMSA model. The fits show a moderate increase in the charge per micelle with increasing concentration. The value for the charge on the micelle (around 1 e) is surprisingly low given the potential -6 charge available to the headgroup, suggesting that although the conductivity results indicate that counterion dissociation is relatively high at the CMC, it becomes much lower above the CMC.

POM-2C$_{14}$ also forms ellipsoidal micelles in water according to the modelling of their SANS patterns given in Fig. 5B (D$_2$O contrast) and SI Fig.4B (70 mol% D$_2$O contrast given at page 100). Fit parameters associated with the form factor of POM-2C$_{14}$ micelles were found to have little dependence on the surfactant concentration (see Table 2). These micelles were less elongated compared to their POM-2C$_{12}$ counterparts, with an ellipticity of *ca.* 2.0. R$_{min}$ was found around 17 - 18 Å, again slightly smaller than the size of the fully extended C$_{14}$H$_{29}$ chain (19.2 Å) estimated by the Tanford equation.[72] The hydrated shell thicknesses were found to be 15 ±1 Å at 5.5 mM and 18 ± 1 Å for higher concentrations, which lies in the size range (12 - 17 Å) of {P$_2$W$_{17}$O$_{61}$}.[73] The difference in shell thickness between 5.5 mM and the other concentrations is probably due to the weak signal at this low concentration. Increasing concentration also results in electrostatic repulsion arising between micelles, evidenced by a broad peak in the SANS patterns, however, this time a higher micelle surface charge was seen (3.6 - 4.4 e).

For both POM-2C$_{16}$ and POM-2C$_{18}$, the fitting of the SANS patterns suggests the formation of spherical micelles in water, rather than ellipsoidal micelles (see Fig. 6 and SI Fig.5 (page 101). The radius of the spherical micelles (R) was found to be around 20

**Table 2** Fitted core-shell ellipsoidal model parameters[a] for POM-2C$_{12}$ and POM-2C$_{14}$ micelles in D$_2$O.

| Conc. (mM) (±0.1) | R (Å) (±1) | $\varepsilon$ | t (Å) (±1) | z (e) (±0.5) | SLD (×10$^{-6}$Å$^{-2}$) (±0.2) | $\phi$ (±0.005) |
|---|---|---|---|---|---|---|
| | | | POM-2C$_{12}$ | | | |
| 16.6 | 11 | 4.5 ± 0.3 | 22 | 1.0 | 5.3 | 0.096 |
| 49.7 | 12 | 4.6 ± 0.3 | 16 | 1.0 | 5.0 | 0.140 |
| 66.4 | 12 | 5.1 ± 0.4 | 15 | 1.3 | 4.6 | 0.153 |
| 99.1 | 15 | 4.0 ± 0.4 | 13 | 1.5 | 4.8 | 0.160 |
| | | | POM-2C$_{14}$ | | | |
| 5.5 | 17 | 1.9 ± 0.3 | 15 | 4.4 | 5.1 | 0.011 |
| 10.6 | 17 | 2.1 ± 0.3 | 18 | 3.7 | 5.3 | 0.034 |
| 33.0 | 18 | 2.0 ± 0.3 | 18 | 3.6 | 5.3 | 0.094 |
| 55.2 | 17 | 2.1 ± 0.2 | 18 | 4.3 | 5.0 | 0.137 |

[a] R$_{min}$, the minimum radius of the core; R$_{max}$, the maximum radius of the core; $\varepsilon$, R$_{max}$/R$_{min}$ (ellipticity); $\phi$, volume fraction; SLD, neutron scattering length density; t, shell thickness; z, micellar surface charge.

and 22 Å respectively. Shell thickness was around 18 Å for POM-$2C_{16}$, and 16 Å for POM-$2C_{18}$ (see Table 3). Similar to POM-$2C_{14}$, an increase in the concentration resulted in an increase in the intermicellar interactions, modelled by an increase in the volume fraction $\phi$. The surface charge was found around 4.2 e for POM-$2C_{16}$, and around 5.2 e for POM-$2C_{18}$. Although in general, the fit reproduced the data well, it was observed to fail to reproduce the scattering at the lowest angles for the 70 mol% $D_2O$ solution at high concentrations (see SI Fig.5 at page 101), probably caused by a small amount of large aggregates observed in these samples.

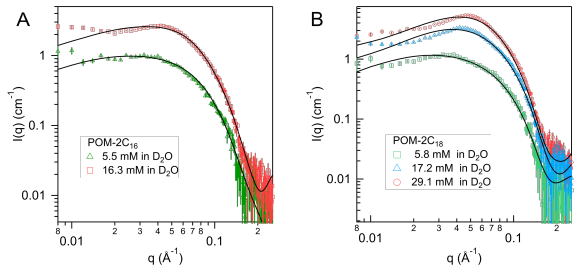


**Fig. 6** SANS patterns of (A) POM-$2C_{16}$ and (B) POM-$2C_{18}$ micelles in $D_2O$ at different concentrations. The fits are given as black lines.

**Table 3** Fitted core-shell model parameters[b] for POM-$2C_{16}$ and POM-$2C_{18}$ micelles in $D_2O$.

| Conc. (mM) (±0.1) | R (Å) (±1) | t (Å) (±1) | z (e) (±0.2) | SLD ($\times 10^{-6}$Å$^{-2}$) (±0.5) | $\phi$ (±0.005) |
|---|---|---|---|---|---|
| | | | POM-$2C_{16}$ | | |
| 5.5 | 20 | 19 | 4.2 | 5.6 | 0.019 |
| 16.3 | 22 | 19 | 4.3 | 5.7 | 0.053 |
| | | | POM-$2C_{18}$ | | |
| 5.8 | 22 | 17 | 4.9 | 5.6 | 0.015 |
| 17.2 | 22 | 17 | 5.5 | 5.5 | 0.049 |
| 29.1 | 22 | 17 | 5.2 | 5.3 | 0.077 |

[b] R, the radius of the core; $\phi$, volume fraction; SLD, neutron scattering length density; t, shell thickness; z, micellar surface charge.

From the SANS fitting, an increase in the radius of the micelles (comparing $R_{min}$ for ellipsoids and R for spheres) was observed with increase in the hydrophobicity of the surfactant, in agreement with observations made for commercial $C_n$TAB surfactants and sodium alkyl sulfates.[59,62] Moreover, the tail length strongly influences the shape of the micelles, with an obvious change from an ellipsoid to a sphere as the hydrocarbon tail length of the surfactants becomes longer. As illustrated in Fig. 7, POM-$2C_{12}$ and POM-$2C_{14}$ both form ellipsoid micelles in aqueous solutions, however, the ellipticity of POM-$2C_{14}$ (around 2) is less than half of that of POM-$2C_{12}$ (around 4.5), while both POM-$2C_{16}$ and POM-$2C_{18}$ form spherical micelles. However, commercial single-tailed surfactants, such as $C_n$TAB and sodium alkyl sulfates, undergo an increase of the micelle ellipticity with increased tail length (see the calculated ellipticity listed in SI Table 3 (page 100) and SI Table 4 (page 100) using the information provided by references).[59,62]

For the POM-$C_n$ surfactants, the theoretical packing parameters, calculated for different tail lengths but assuming the same equilibrium area per molecule (the cross-sectional area of the headgroup estimated according to the size of the headgroup,[73] 124.3 Å$^2$), lies close to the 1/3 limit between spherical and rod-like micelles, without any clear trend explaining the experimental data. This suggests that the equilibrium area per molecule may be different between them due to the difference in the repulsion between the surfactant headgroups. Considering the repulsive interactions, as listed in Table 2 and Table 3, the surface charge increases with the tail length which may induce a larger equilibrium area per molecule. Therefore the packing parameter (=v/al, where, a is the equilibrium area per molecule, v is the hydrophobic tail volume and l is the hydrophobic tail length, the volume-to-length ratio v/l of the tail is independent of the tail length for common surfactants) decreases with increased tail length, giving a value under 1/3, which predicts the formation of spherical micelles.[74] This is consistent with the SANS results where longer tailed surfactants form more globular micelles.

Dynamic light scattering (DLS) was used to detect the hydrodynamic radius distributions of the micelles, shown in Fig.8A. The singular peak in the DLS volume-weighted size distribution results suggests that there is only one population of micelles in each solution. An increase in size obtained from DLS is observed with tail length, $C_{14}H_{29}$, $C_{16}H_{33}$ and $C_{18}H_{37}$ give a hydrodynamic radius of 31 ± 5, 41 ± 5, and 48 ± 5 Å respectively, in agreement with the increase of micellar size observed from SANS fitting results. It is noted that the size of the POM-$2C_{12}$ micelles (48 ± 5 Å) probed by DLS is relatively larger compared to those of POM-$2C_{14}$ and POM-$2C_{16}$ micelles, likely due to their ellipsoidal shape, which is not taken into account in DLS analysis. The POM-$2C_n$ micelles exhibit strongly negative surface charges as evidenced by their zeta-potentials (see Fig.8B), giving similar results to the conductivity measurements (longer-tailed surfactant forms micelles with less charged surfaces), but opposite trend to the micelle charge information obtained from SANS fitting. The reason for the opposite trend between SANS results and zeta-potentials remains unclear at this stage.

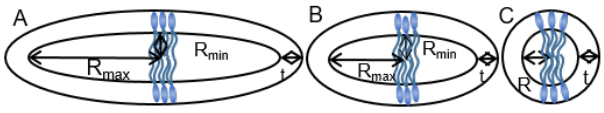


**Fig. 7** The schematic representative of the POM-$2C_n$ micelle shapes (A) POM-$2C_{12}$ (B) POM-$2C_{14}$ (C) POM-$2C_{16}$ and POM-$2C_{18}$ where t is the shell thickness, $R_{max}$ and $R_{min}$ are the maximum and minimum of core radius in an ellipsoidal micelle model, and R is the core radius of the spherical micelle.

### POM-$TiO_2$ materials synthesised using POM-$2C_n$ micelles as templates

As a proof of concept, POM-$2C_n$ micelles were utilised to template $TiO_2$ to prepare POM-$TiO_2$ hybrid catalysts. Transmission electron microscopy (TEM) image of the 12POM-$TiO_2$ material

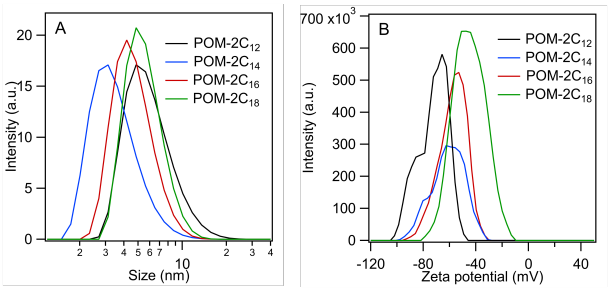


**Fig. 8** (A) Volume-weighted size distributions (obtained *via* the CONTIN method) and (B) zeta-potentials of 5.45 mM POM-2C$_n$ solutions (n= 12, 14, 16 and 18).

(Fig. 9A) shows aggregations of small spherical particles. A focus on a selected area of the 12POM-$TiO_2$ material, made *via* HRTEM (Fig. 9B), clearly shows lattice fringes which indicate an ordered crystalline structure of the $TiO_2$. $\{P_2W_{17}O_{61}\}$ units are not clearly seen which may be due to their small size and low content (Table 4).

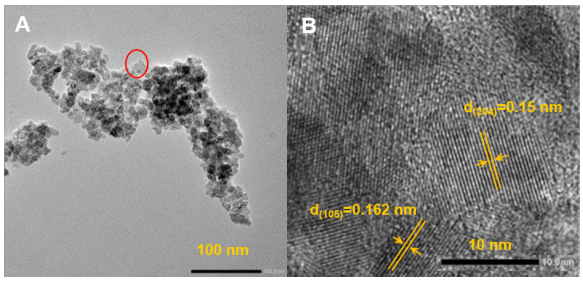


**Fig. 9** (A) TEM and (B) HRTEM images taken from the part of the 12POM-$TiO_2$ indicated with a circle in (A).

To evidence the presence of the $\{P_2W_{17}O_{61}\}$ units within the hybrid material, firstly, EDX elemental mapping analysis was applied. The element distributions of the 12POM-$TiO_2$ associated with the TEM image in Fig. 9A, are given in SI Fig.6 (page 102). It was clear that both W and Ti elements are distributed within the material, suggesting the existence of $\{P_2W_{17}O_{61}\}$ within the hybrid material.

Reduced POMs are known to reduce metal ions *in situ* to metal nanoparticles. Therefore, to corroborate the preservation of POM units within the porous $TiO_2$,[75] the photocatalytic reduction of $Ag^+$ was carried out. Experimental details can be found in the experimental section. EDX elemental mapping analysis was applied to the collected brown product, and the Ag element distribution is shown in SI Fig.7B (page 102), suggesting that Ag nanoparticles are present in the product. This indicates that POM units are present and are chemically active.

The PXRD patterns of SDS templated $TiO_2$, 12POM-$TiO_2$, 16POM-$TiO_2$ and 18POM-$TiO_2$ materials (Fig. 10) demonstrate the characteristic diffraction peaks of anatase $TiO_2$ (space group: $I41/amd$, JCPDS No. 21-1272). We found no diffraction evidence for the POM phase, since the POM with in the $TiO_2$ are dispersed but not crystallised. Small angle X-ray scattering showed no long-range ordering within the materials (see SI Fig. 8 at page 103).

All samples show a type IV nitrogen sorption isotherm (see SI

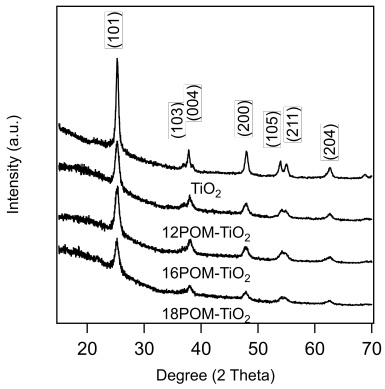


**Fig. 10** PXRD patterns of nPOM-$TiO_2$ materials (n = 12, 16 or 18)

Fig.9A at page 103). The resulting nPOM-$TiO_2$ materials have relatively high surface areas, listed in Table 4 along with their mean pore diameters (pore size distributions are illustrated in SI Fig.9B at page 103). nPOM-$TiO_2$ materials have smaller mean pore sizes compared to SDS templated $TiO_2$ due to the occupation of POMs within the pores. The mean pore diameter of 12POM-$TiO_2$ material lies between the minimum of the size ($2R_{min}$ = 2.2 nm) and the maximum of the size ($2R_{max}$ = 9.9 nm) of the POM-$2C_{12}$ micelles. The 16POM-$TiO_2$ and 18POM-$TiO_2$ materials have slightly larger mean pore sizes compared to their corresponding micellar diameter (4.0 and 4.4 nm). Larger pores (around *ca.* 60 - 100 nm) were observed in 12POM-$TiO_2$, which contribute to the largest surface area among nPOM-$TiO_2$ materials. The mean pore size of the 18POM-$TiO_2$ material is about 17.5% larger in comparison to 16POM-$TiO_2$, proves the tunability of the pore size through using larger spherical micelles as soft templates.

**Table 4** Ti: W atomic ratios obtained from EDX analysis, surface areas obtained from BET annalysis and mean pore sizes.

| Material | Ti : W | Surface area $m^2/g$ | Mean pore size (nm) |
|---|---|---|---|
| 12POM-$TiO_2$ | 122:1 | 191 ± 8 | 6.4 ± 0.5 |
| 16POM-$TiO_2$ | 154:1 | 165 ± 8 | 5.3 ± 0.6 |
| 18POM-$TiO_2$ | 169:1 | 148 ± 5 | 6.2 ± 0.4 |
| 16POM-$TiO_2$-2 | 5:1 | 179 ±5 | 5.8 ± 0.6 |
| $TiO_2$ | – | 99 ± 5 | 8.3 ± 0.4 |

**Photocatalytic properties**

Dawson structured $\{P_2W_{17}O_{61}\}$ was chosen for its photocatalytic property. The photoabsorption of 12POM-$TiO_2$ in the range of 250-800 nm shows an absorbance shoulder for wavelengths between *c.a.* 400 and 700 nm (SI Fig.10A at page 104). The

12POM-$TiO_2$ possesses a bandgap at around 3.3 eV obtained by plotting $(Ah)^2$ as a function of the energy similar to that of $TiO_2$(SI Fig.10B at page 104) .[76] The band gap does not change after the decoration of $TiO_2$ with POMs, however, the resulting material now shows absorbance in a wavelength range where $TiO_2$ normally would not absorb.[77,78] The photocatalytic properties of the nPOM-$TiO_2$ materials were tested *via* the degradation of RhB with the irradiation of solar light. Their photocatalytic behaviours were compared to SDS templated $TiO_2$ which has a surface area of *ca.* 99 $m^2/g$. The nPOM-$TiO_2$ (n = 12, 16 and 18) materials showed higher activities than that of the SDS templated $TiO_2$ (Fig. 11A). The 12POM-$TiO_2$ exhibited the best degradation performance, with almost 80% of the RhB degraded after 20 min. 16POM-$TiO_2$ and 18POM-$TiO_2$ were less effective in the first 20 min, decomposing *ca.* 65% and 45% of RhB respectively.

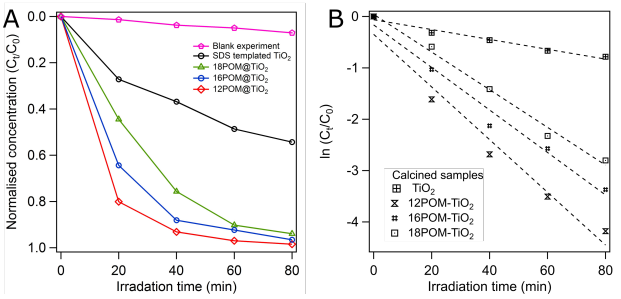


**Fig. 11** (A) Plot of normalised degraded concentration of RhB, $(1\text{-}C_t)/C_0$, in the presence of different catalysts versus irradiation time. A blank measurement was recorded for comparison. (B) Plot of ln $(C_t/C_0)$ against irradiation time, $C_t$ and $C_0$ are the RhB concentrations at time t and 0 min respectively.

The degradation rates fit a first-order model well. The slope of a linear plot of ln $(C_t/C_0)$ versus irradiation time gives the apparent degradation rate constant (Fig. 11B). The obtained fitting parameters related to the kinetics, apparent degradation rate constant $k_{obs}$ and correlation coefficient r, are listed in Table 5. There is an obvious rate enhancement of nPOM-$TiO_2$ compared to porous $TiO_2$, increasing from 0.0096 to 0.0513 $min^{-1}$. Correlation coefficients, r, are found to be between 0.9683 and 0.9910, indicating the excellent linear response in the studied range of concentrations.

The Ti to W atomic ratio in each material obtained from EDX elemental mapping analysis is listed in Table 4. The 12POM-$TiO_2$ hybrid material has a relatively higher W content compared to 16POM-$TiO_2$ and 18POM-$TiO_2$, hence the highest POM content in the material. And the value of $k_{obs}$ decreases when the less POM is present in the nPOM-$TiO_2$ materials. Therefore, besides the high surface area induced by the surfactant templating, higher POM content of the prepared 12POM-$TiO_2$ also contributes to its outstanding properties in RhB photodegradation compared to other materials studied here.

Furthermore, the RhB photodegradation activity of 12POM-$TiO_2$ is still remarkably high after eight continuous photo-catalysis cycles (see Fig. 12). The complete photodegradation of RhB is still obtained after 80 min at the 8th cycle, while there is a slight decrease of the amount of RhB degraded after 20 min (*ca.* 70% versus 80% for the 1st cycle). The PXRD pattern of 12POM-$TiO_2$ after 8 cycles indicates an anatase phase (SI Fig.11 at page 104), showing the stability of the $TiO_2$ structure.

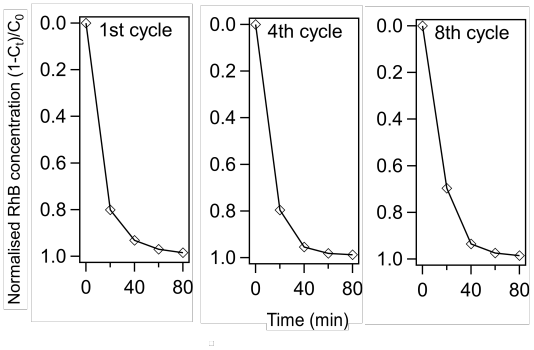


**Fig. 12** 12POM-$TiO_2$ recycling performance of RhB degradation.

The photocatalytic pathway can be summarised as follows:[36,79] (1) the electrons are excited from the valence band (VB) to the conduction band (CB) of $TiO_2$ under UV irradiation. (2) The electrons at the CB of $TiO_2$ transfer to the POMs. Furthermore, POMs are photo-excited simultaneously and the electrons from both the CB of $TiO_2$ and the photoexcitation of POMs accumulate together on the POMs to form charge-transfer excited POMs (designated as POMs*). (3) POMs* transfer electrons to oxygen in the solution to form reactive oxygen species, while photoexcited holes react with water to form ·OH radicals, and (4) these radicals are involved in the process of photodegradation. POMs have been proven to enhance the photocatalytic properties in several studies,[35,36] since they efficiently reduce the recombination rate of photoexcited holes and electrons in $TiO_2$. Therefore, step (1) is enhanced. Step (2) is accelerated due to the intimate contact between POMs and $TiO_2$ given by the synthesis method. Moreover, POMs not only behave as charge separators in the hybrid materials but also photocatalysts that contribute to the photodegradation. Furthermore, the electrostatic interaction between oppositely charged POMs and RhB molecules also reinforces step (4). Overall, the decorating POMs speed up the degradation efficiency due to their fast transportation of electrons, their ability to decrease the recombination rate of electron-hole pairs and their intrinsic photocatalytic properties, rather than by narrowing the band gap.

Chen, *et al*[36] have studied the photocatalytic degradation

**Table 5** Kinetic parameters obtained from the fitting of the experimental results in Fig. 11B.

| Material | $k_{obs}$ ($min^{-1}$) | r |
|---|---|---|
| 12POM-$TiO_2$ | $0.0513 \pm 0.0016$ | 0.9683 |
| 16POM-$TiO_2$ | $0.0414 \pm 0.0008$ | 0.9799 |
| 18POM-$TiO_2$ | $0.0367 \pm 0.0003$ | 0.9910 |
| $TiO_2$ | $0.0096 \pm 0.0003$ | 0.9708 |

of 2,4-dichlorophenol by $PW_{12}O_{40}^{3-}/TiO_2$ prepared by physically mixing, and the performance was improved by nearly 20% within the first 50 min when 0.8 mM $PW_{12}O_{40}^{3-}$ was present. This method, however, limits the recyclability of the $PW_{12}O_{40}^{3-}$ due to its solubility in water. Photodegradation of 1,2-dichlorobenzene using systems of $TiO_2$ and polyoxometalates ($PW_{12}O_{40}^{3-}$, $SiW_{12}O_{40}^{4-}$ or $W_{10}O_{32}^{4-}$) were studied by Ozer and co-workers.[80] The addition of POM anions into the $TiO_2$ suspension resulted in a significant rate enhancement, with $PW_{12}O_{40}^{3-}$ behaved most effectively. The rate constant reached a limit of 0.03 $min^{-1}$, 600% greater than pure $TiO_2$ system, when the the addition of $PW_{12}O_{40}^{3-}$ was at *ca.* 0.15 mM. In comparison to our work, the degradation rate constant of 12POM-$TiO_2$ is 0.051 $min^{-1}$, which is around 500% greater than that of $TiO_2$ materials (0.0096 $min^{-1}$), importantly our materials also provide recyclability. Pearson *et al.* conducted a series of studies on materials obtained by loading $H_3P_{12}W_{12}O_{40}$ onto $TiO_2$ nanoparticles or $TiO_2$ nanotubes as a co-catalyst.[37,81,82] The degradation of Congo red dye was improved by around 14% compared to the original $TiO_2$ within the first 30 min.[37,82] However, the recyclability of the materials was not studied.

In conclusion, our system enables an improvement in photodegradation properties as well as recycling properties with photocatalytic performance maintained for at least eight continuous photo-catalysis cycles, compared to the addition of polyoxometalates into a $TiO_2$ suspension or the previous studies discussed above. And the POM content in the POM-$TiO_2$ materials can be tuned through varying the concentration of POM amphiphiles. This synthesis method provides a stronger anchoring of polyoxometalates within the hybrid material and intimate contact between the polyoxometalates and $TiO_2$, ensuring the thermal stability, easy recovery and reuse of the materials.

## Conclusion

Novel surfactants with inorganic $\{P_2W_{17}O_{61}\}$ POM as headgroups and double-hydrocarbon chains ($C_{12}$, $C_{14}$, $C_{16}$ or $C_{18}$) were successfully synthesised. The micelle morphologies were studied using SANS to reveal core-shell structures. The shape of the micelles can be tuned by changing the length of the hydrophobic tails, such that surfactants with longer hydrophobic tails tend to form less elongated and more globular micelles. Moreover, SANS evidenced strong interactions due to Coulomb repulsion between negatively charged micelles. These data were supported by DLS and zeta-potential measurements. The micelles were used to template $TiO_2$ through a hydrothermal method to form, after calcination, nPOM-$TiO_2$ hybrid catalysts (n = 12, 16 or 18). Through this method, the $\{P_2W_{17}O_{61}\}$ units, as an excellent electron acceptor, a electron transport material and a photocatalyst, were incorporated into the porous titania materials. The photocatalytic properties of the nPOM-$TiO_2$ hybrid materials were tested by the photodegradation of aqueous RhB solution as a model reaction. The results reveal that the nPOM-$TiO_2$ photocatalysts possess enhanced photodegradation properties in comparison with SDS templated $TiO_2$, confirming their superior photocatalytic activities. The rate constants of the photodegradation extracted here were found to be almost 10 times higher for the 12POM-$TiO_2$ materials compared to porous $TiO_2$ templated by SDS. This study demonstrates the highly promising use of POM-2$C_n$ amphiphiles as templating agents in the synthesis of porous POM-$TiO_2$ hybrid catalyst, having well-dispersed polyoxometalates within a porous anatase $TiO_2$ matrix. Using the same method, it is possible to increase the polyoxometalates content in the material by using a higher concentration of the initial surfactant solution. Furthermore, other metal oxide materials loaded with polyoxometalates could be synthesised using similar methods, offering a flexible and straightforward approach to harness the functionality of polyoxometalates in porous materials for catalysis.

## Conflicts of interest

There are no conflicts to declare.

## Acknowledgements

A. Di. thanks University of Bath and China Scholarship Council for supporting her Ph.D studies. The authors would like to thank the ISIS Spallation Neutron Source for the award of beam time (experiment no. RB1720185). This work benefited from the use of the SasView application, originally developed under NSF award DMR-0520547. SasView contains code developed with funding from the European Unions Horizon 2020 research and innovation programme under the SINE2020 project, grant agreement No. 654000. The data supporting this work has been uploaded to the University of Bath Research Data Repository and is accessible at DOI: XXXXX

## Notes and references

1 Y. F. Song, D. L. Long, C. Ritchie and L. Cronin, *Chem. Rec.*, 2011, **11**, 158–171.

2 M. T. Pope and A. Müller, in *Introduction to polyoxometalate chemistry: from topology via self-assembly to applications*, Springer, 2001, pp. 1–6.

3 B. Keita, G. Zhang, A. Dolbecq, P. Mialane, F. Sécheresse, F. Miserque and L. Nadjo, *J. Phys. Chem. C*, 2007, **111**, 8145–8148.

4 S. Gao, R. Cao, J. Lü, G. Li, Y. Li and H. Yang, *J. Mater. Chem.*, 2009, **19**, 4157–4163.

5 A. Hiskia, A. Mylonas and E. Papaconstantinou, *Chem. Soc. Rev.*, 2001, **30**, 62–69.

6 S. Kim, H. Park and W. Choi, *J. Phys. Chem. B*, 2004, **108**, 6402–6411.

7 E. Bae, J. W. Lee, B. H. Hwang, J. Yeo, J. Yoon, H. J. Cha and W. Choi, *Chemosphere*, 2008, **72**, 174–181.

8 D. Zhao, J. Feng, Q. Huo, N. Melosh, G. H. Fredrickson, B. F. Chmelka and G. D. Stucky, *Science*, 1998, **279**, 548–552.

9 J. S. Beck, J. C. Vartuli, W. J. Roth, M. E. Leonowicz, C. T. Kresge, K. D. Schmitt, C. T. W. Chu, D. H. Olson, E. W. Sheppard, S. B. McCullen, J. B. Higgins and J. L. Schlenker, *J. Am. Chem. Soc*, 1992, **114**, 10834–10843.

10 Q. Huo, D. I. Margolese, U. Ciesla, P. Feng, T. E. Gier, P. Sieger, R. Leon, P. M. Petroff, F. Schüth and G. D. Stucky, *Nature*, 1994, **368**, 317.

11 T. Maschmeyer, F. Rey, G. Sankar and J. M. Thomas, *Nature*, 1995, **378**, 159.

12 C. P. Mehnert, *Chem. Commun.*, 1997, 2215–2216.

13 C. Hu, Y. Zhang, L. Xu and G. Peng, *Appl. Catal., A*, 1999, **177**, 237–244.

14 J. Zhang, A. Wang, Y. Wang, H. Wang and J. Gui, *Chem. Eng. J.*, 2014, **245**, 65–70.

15 S. Damyanova, M. Cubeiro and J. Fierro, *J. Mol. Catal. A: Chem.*, 1999, **142**, 85–100.

16 K. Lv and Y. Xu, *J. Phys. Chem. B*, 2006, **110**, 6204–6212.

17 S. Ahn, S. L. Nauert, C. T. Buru, M. Rimoldi, H. Choi, N. M. Schweitzer, J. T. Hupp, O. K. Farha and J. M. Notestein, *J. Am. Chem. Soc.*, 2018, **140**, 8535–8543.

18 H.-l. Li, N. Perkas, Q.-l. Li, Y. Gofer, Y. Koltypin and A. Gedanken, *Langmuir*, 2003, **19**, 10409–10413.

19 Z. Karimi, A. Mahjoub and F. D. Aghdam, *Inorg. Chim. Acta*, 2009, **362**, 3725–3730.

20 W. Kaleta and K. Nowiska, *Chem. Commun.*, 2001, 535–536.

21 H. Hamadi, M. Kooti, M. Afshari, Z. Ghiasifar and N. Adibpour, *J. Mol. Catal. A: Chem.*, 2013, **373**, 25–29.

22 T. Kovalchuk, H. Sfihi, L. Kostenko, V. Zaitsev and J. Fraissard, *J. Colloid Interface Sci.*, 2006, **302**, 214–229.

23 W. Qi, H. Li and L. Wu, *Adv. Mater.*, 2007, **19**, 1983–1987.

24 H. Li, H. Sun, W. Qi, M. Xu and L. Wu, *Angew. Chem., Int. Ed.*, 2007, **46**, 1300–1303.

25 D. M. Fernandes, H. M. Carapuça, C. M. Brett and A. M. Cavaleiro, *Thin Solid Films*, 2010, **518**, 5881–5888.

26 Y. Han, Y. Xiao, Z. Zhang, B. Liu, P. Zheng, S. He and W. Wang, *Macromolecules*, 2009, **42**, 6543–6548.

27 S. Landsmann, M. Luka and S. Polarz, *Nat. Commun.*, 2012, **3**, 1299.

28 S. Polarz, S. Landsmann and A. Klaiber, *Angew. Chem., Int. Ed.*, 2014, **53**, 946–954.

29 J. J. Giner-Casares, G. Brezesinski, H. Möhwald, S. Landsmann and S. Polarz, *J. Phys. Chem. Lett.*, 2012, **3**, 322–326.

30 J. Zhang, Y. Huang, G. Li and Y. Wei, *Coordination Chemistry Reviews*, 2019, **378**, 395–414.

31 D. Y. Leung, X. Fu, C. Wang, M. Ni, M. K. Leung, X. Wang and X. Fu, *ChemSusChem*, 2010, **3**, 681–694.

32 H. Guan, L. Zhu, H. Zhou and H. Tang, *Anal. Chim. Acta*, 2008, **608**, 73–78.

33 J. Du, X. Lai, N. Yang, J. Zhai, D. Kisailus, F. Su, D. Wang and L. Jiang, *ACS nano*, 2010, **5**, 590–596.

34 H. Zhang, X. Lv, Y. Li, Y. Wang and J. Li, *ACS nano*, 2009, **4**, 380–386.

35 Z. Sun, L. Xu, W. Guo, B. Xu, S. Liu and F. Li, *J. Phys. Chem. C*, 2010, **114**, 5211–5216.

36 C. Chen, P. Lei, H. Ji, W. Ma, J. Zhao, H. Hidaka and N. Serpone, *Environ. Sci. Technol.*, 2004, **38**, 329–337.

37 A. Pearson, H. Jani, K. Kalantar-Zadeh, S. K. Bhargava and V. Bansal, *Langmuir*, 2011, **27**, 6661–6667.

38 Y. Guo and C. Hu, *J. Mol. Catal. A: Chem.*, 2007, **262**, 136–148.

39 N. Fu and G. Lu, *Chem. Commun.*, 2009, 3591–3593.

40 M. W. Droege, *Ph.D Dissertation*, University of Oregon, 1984.

41 R. G. Finke, M. W. Droege and P. J. Domaille, *Inorg. Chem.*, 1987, **26**, 3886–3896.

42 C. Comuzzi, G. Dolcetti, A. Trovarelli, F. Cavani, F. Trifirò, J. Llorca and R. G. Finke, *Catal. Lett.*, 1996, **36**, 75–79.

43 B. Sun, G. Zhou, C. Shao, B. Jiang, J. Pang and Y. Zhang, *Powder Technol.*, 2014, **256**, 118–125.

44 E. Papaconstantinou, *J. Chem. Soc., Chem. Commun.*, 1982, 12–13.

45 P. Seeger and R. Hjelm, *J. Appl. Crystallogr.*, 1991, **24**, 467–478.

46 O. Arnold, J.-C. Bilheux, J. Borreguero, A. Buts, S. I. Campbell, L. Chapon, M. Doucet, N. Draper, R. F. Leal and M. Gigg, *Nucl. Instrum. Methods A*, 2014, **764**, 156–166.

47 G. T. Wignall and F. Bates, *J. Appl. Crystallogr.*, 1987, **20**, 28–40.

48 A. Guinier, G. Fournet and K. L. Yudowitch, *Small Angle Scattering of X-rays*, John Wiley Sons, Inc., New York, 1955.

49 M. Kotlarchyk and S. Chen, *J. Chem. phys.*, 1983, **79**, 2461–2469.

50 S. Berr, *J. Phys. Chem.*, 1987, **91**, 4760–4765.

51 J.-P. Hansen and J. B. Hayter, *Mol. Phys.*, 1982, **46**, 651–656.

52 K. R. Srinivasan and R. L. Kay, *J. Chem. Phys.*, 1974, **60**, 3645–3648.

53 K. V. Kumar, K. Porkodi and F. Rocha, *Catal. Commun.*, 2008, **9**, 82–84.

54 N. Fay, E. Dempsey, A. Kennedy and T. McCormac, *J. Electroanal. Chem.*, 2003, **556**, 63–74.

55 C. Kato, S. Nishihara, R. Tsunashima, Y. Tatewaki, S. Okada, X.-M. Ren, K. Inoue, D.-L. Long and L. Cronin, *Dalton Trans.*, 2013, **42**, 11363–11366.

56 M. N. Sokolov, N. V. Izarova, E. V. Peresypkina, D. A. Mainichev and V. P. Fedin, *Inorg. Chim. Acta*, 2009, **362**, 3756–3762.

57 L. Magid, K. Daus, P. Butler and R. Quincy, *J. Phys. Chem.*, 1983, **87**, 5472–5478.

58 M. Karaman, B. Ninham and R. Pashley, *J. Phys. Chem.*, 1994, **98**, 11512–11518.

59 J. Joshi, V. Aswal and P. Goyal, *J. Macromol. Sci. Phys.*, 2008, **47**, 338–347.

60 G. B. Ray, I. Chakraborty, S. Ghosh, S. Moulik and R. Palepu, *Langmuir*, 2005, **21**, 10958–10967.

61 P. Mukerjee and K. J. Mysels, *Critical micelle concentrations of aqueous surfactant systems*, National Bureau of Standard, NSRDS-NBS 36, US Goverment Printing Office, Washingtong D. C., pp. 66–67.

62 S. Vass, T. Gilanyi and S. Borbely, *J. Phys. Chem. B*, 2000, **104**, 2073–2081.

63 K. J. Mysels and R. J. Otter, *J. Colloid Sci.*, 1961, **16**, 462–473.

64 H. Gharibi and A. Rafati, *Langmuir*, 1998, **14**, 2191–2196.

65 H. Nakamura, A. Sano and K. Matsuura, *Anal. Sci.*, 1998, **14**, 379–382.

66 A. Dominguez, A. Fernandez, N. Gonzalez, E. Iglesias and

L. Montenegro, *J. Chem. Educ.*, 1997, **74**, 1227–1231.
67 R. Zana, *J. Colloid Interface Sci.*, 1980, **78**, 330–337.
68 R. Zana, *Langmuir*, 1996, **12**, 1208–1211.
69 M. N. Khan, *Micellar catalysis*, CRC Press, 2006.
70 T. Wolff and B. Klaussner, *Adv. Colloid Interface Sci.*, 1995, **59**, 31–94.
71 Y. Liu, J. Goebl and Y. Yin, *Chem. Soc. Rev.*, 2013, **42**, 2610–2653.
72 C. Tanford, *J. Phys. Chem.*, 1974, **78**, 2469–2479.
73 S. G. Mitchell and M. Jesús, *J. Mater. Chem.*, 2012, **22**, 18091–18100.
74 R. Nagarajan, *Langmuir*, 2002, **18**, 31–38.
75 A. Troupis, A. Hiskia and E. Papaconstantinou, *Appl. Catal. B: Environ.*, 2003, **42**, 305–315.
76 K. M. Reddy, C. G. Reddy and S. Manorama, *J. Solid State Chem.*, 2001, **158**, 180–186.
77 T. Tachikawa, S. Tojo, K. Kawai, M. Endo, M. Fujitsuka, T. Ohno, K. Nishijima, Z. Miyamoto and T. Majima, *J. Phys. Chem. B*, 2004, **108**, 19299–19306.
78 K. M. Reddy, S. V. Manorama and A. R. Reddy, *Mater. Chem. Phys.*, 2003, **78**, 239–245.
79 S. Yanagida, A. Nakajima, T. Sasaki, Y. Kameshima and K. Okada, *Chem. Mater.*, 2008, **20**, 3757–3764.
80 R. R. Ozer and J. L. Ferry, *Environ. Sci. Technol.*, 2001, **35**, 3242–3246.
81 A. Pearson, S. K. Bhargava and V. Bansal, *Langmuir*, 2011, **27**, 9245–9252.
82 A. Pearson, H. Zheng, K. Kalantar-zadeh, S. K. Bhargava and V. Bansal, *Langmuir*, 2012, **28**, 14470–14475.

# Supporting Information

## Self-assembly of amphiphilic polyoxometalates for the preparation of mesoporous polyoxometalate-titania catalysts

Andi Di,[1] Julien Schmitt,[1,2] Marcelo Alves Da Silva,[1] Najet Mahmoudi,[3] R. John Errington,[4] and Karen J Edler[1*]

1. Department of Chemistry, University of Bath, Claverton Down, Bath, BA2 7AY, UK

2. LSFC – Laboratoire de Synthèse et Fonctionnalisation des Céramiques, UMR 3080 CNRS / Saint-Gobain CREE, Saint-Gobain Research Provence, 550 avenue Alphonse Jauffret, Cavaillon, France

3. ISIS Neutron and Muon Source, Science and Technology Facilities Council, Rutherford Appleton Laboratory, Didcot OX11 0QX, UK

4. Chemistry, School of Natural and Environmental Sciences, Newcastle University, Newcastle upon Tyne, NE1 7RU, UK

SI Table 1. Calculated SLDs, given in $Å^{-2}$, used for SANS fitting.

| Fit parameters | $D_2O$ | 70 mol% $D_2O$ | $C_{12}H_{25}$ | $C_{14}H_{29}$ | $C_{16}H_{33}$ | $C_{18}H_{37}$ |
|---|---|---|---|---|---|---|
| | $6.35 \times 10^{-6}$ | $4.27 \times 10^{-6}$ | $-0.38 \times 10^{-6}$ | $-0.37 \times 10^{-6}$ | $-0.36 \times 10^{-6}$ | $-0.35 \times 10^{-6}$ |

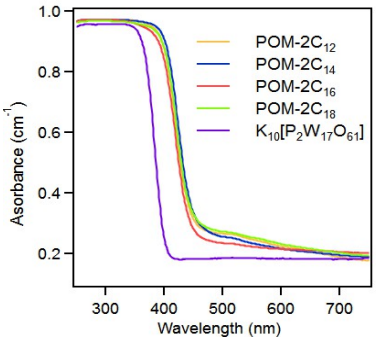


SI Fig. 1 UV–Vis absorbance spectra of $K_{10}[\alpha_2\text{-}P_2W_{17}O_{61}]\cdot 19H_2O$ and POM-$2C_n$ surfactants (n = 12, 14, 16 or 18).

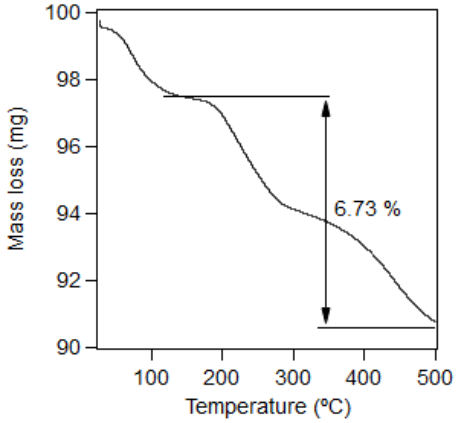


SI Fig. 2 Thermogravimetric analysis (TGA) of POM-2$C_{12}$.

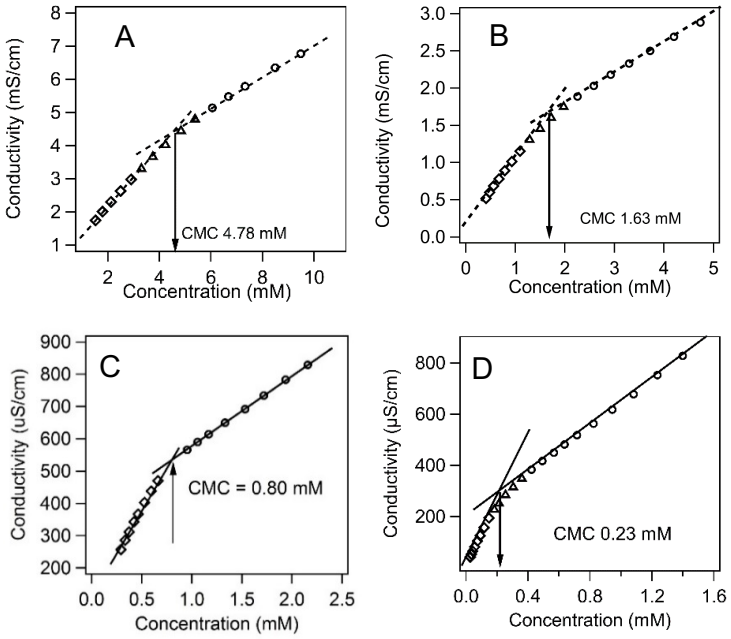


SI Fig. 3 Electrical conductivity measurements with concentration of (A) POM-2$C_{12}$, (B) POM-2$C_{14}$, (C) POM-2$C_{16}$ and (D) POM-2$C_{18}$ in aqueous solution.

SI Table 2. List of CMCs, degrees of micelle ionisation (α) and free energies of micellisation of traditional anionic surfactants.[1]

| di-n-alkyl sulfosuccinates | CMC (mM) | α | $\Delta G^{\circ}_{mic}$ (kJ·mol$^{-1}$) |
|---|---|---|---|
| di-$C_6H_{13}$ | 120.0 ± 2.4 | 0.59 ± 0.06 | -3.2 |
| di-$C_8H_{17}$ | 1.14 ± 0.02 | 0.38 ± 0.08 | -1.2 |

SI Table 3. List of CMCs, degrees of micelle ionisation and free energies of micellisation of $C_nTAB$.[2-4]

| $C_nTAB$ | CMC (mM) | α | ε | $\Delta G^{\circ}_{mic}$ (kJ·mol$^{-1}$) |
|---|---|---|---|---|
| 12 | 15.7 ± 0.3 | 0.26 ± 0.01 | 1.7 ± 0.2 | -7.8 |
| 14 | 3.94 ± 0.08 | 0.21 ± 0.02 | 1.9 ± 0.1 | -10.7 |
| 16 | 0.92 ± 0.02 | 0.14 ± 0.02 | 2.5 ± 0.2 | -14.0 |

SI Table 4. List of CMCs and ellipticities of micelles at 40 °C, degrees of micelle ionisation at 25 °C of sodium alkyl sulfates.

| Chain length | CMC (mM)[5] | α | ε[6] |
|---|---|---|---|
| 10 | 33 ± 0.7 | 0.55 ± 0.01[7] | 1.07 ± 0.04 |
| 12 | 8.4 ± 0.2 | 0.35 ± 0.01[8] | 1.53 ± 0.09 |
| 14 | 2.2 ± 0.1 | 0.26 ± 0.01[9] | 1.61 ± 0.07 |
| 16 | 0.6 ± 0.1 | -- | 5.00 ± 0.04 |

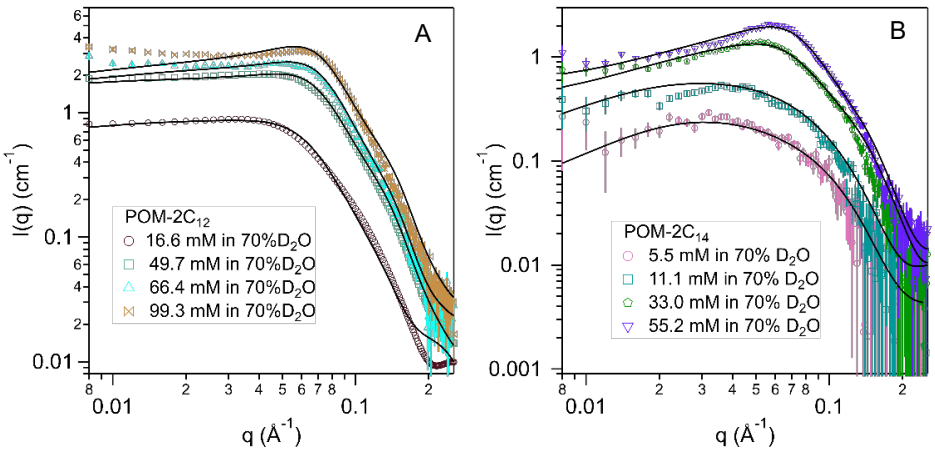


SI Fig. 4 SANS patterns of (A) POM-2$C_{12}$ and (B) POM-2$C_{14}$ micelles in 70 mol% $D_2O$ at different concentrations. The fits are given as black lines.

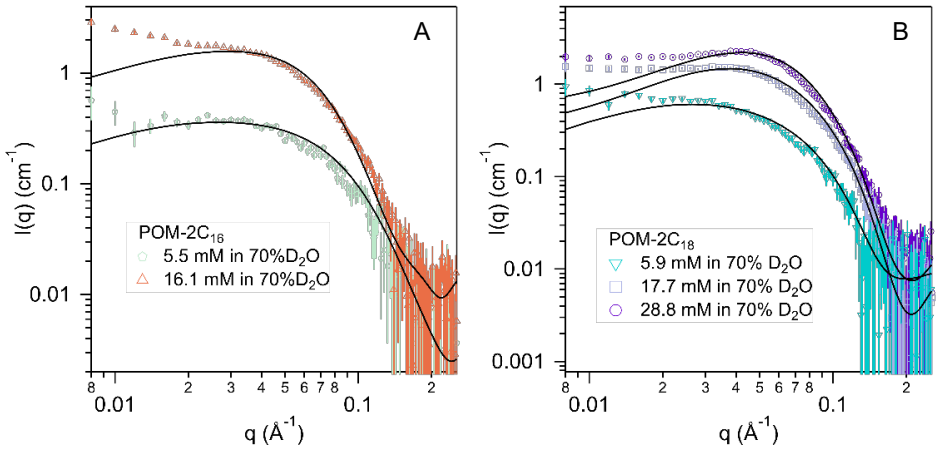


SI Fig. 5 SANS patterns of (A) POM-2C$_{16}$ and (B) POM-2C$_{18}$ micelles in 70 mol% $D_2O$ at different concentrations. The fits are given as black lines.

SI Table 5. Fitted core-shell ellipsoidal model parameters[a] for POM-2C$_{12}$ and POM-2C$_{14}$ micelles in 70 mol% $D_2O$.

| Conc. (mM) (± 0.1) | $R_{min}$ (Å) (±1) | ε | t (Å) (±1) | z (e) (±0.5) | Shell SLD ($\times10^{-6}$ Å$^{-2}$) (±0.2) | φ (±0.005) |
|---|---|---|---|---|---|---|
| POM-2C$_{12}$ | | | | | | |
| 16.7 | 11 | 4.5 ± 0.3 | 22 | 1.0 | 3.8 | 0.096 |
| 49.7 | 12 | 5.3 ± 0.3 | 16 | 1.0 | 3.6 | 0.140 |
| 66.4 | 12 | 5.1 ± 0.4 | 15 | 1.3 | 3.4 | 0.153 |
| 99.1 | 15 | 4.0 ± 0.4 | 13 | 1.5 | 3.7 | 0.160 |
| POM-2C$_{14}$ | | | | | | |
| 5.5 | 17 | 1.9 ± 0.3 | 15 | 5.4 | 3.9 | 0.011 |
| 10.6 | 17 | 2.1 ± 0.3 | 18 | 3.7 | 4.1 | 0.034 |
| 33.0 | 18 | 2.0 ± 0.3 | 18 | 3.6 | 4.2 | 0.094 |
| 55.2 | 17 | 2.1 ± 0.2 | 18 | 4.7 | 4.0 | 0.137 |

[a] $R_{min}$, the minimum radius of the core; $R_{max}$, the maximum radius of the core; ε, $R_{max}/R_{min}$ (ellipticity); φ, volume fraction; SLD, Neutron scattering length density; t, Shell thickness.

SI Table 6. Fitted core-shell sphere model parameters[b] for POM-2C$_{16}$ and POM-2C$_{18}$ micelles in 70 mol% $D_2O$.

| Conc. (mM) (± 0.1) | R = $R_{min}$ (Å) (±1) | t (Å) (±1) | z (e) (±0.5) | Shell SLD ($\times10^{-6}$ Å$^{-2}$) (±0.2) | φ (±0.005) |
|---|---|---|---|---|---|
| POM-2C$_{16}$ | | | | | |
| 5.5 | 20 | 19 | 6.2 | 3.9 | 0.019 |
| 16.3 | 22 | 22 | 6.0 | 3.6 | 0.053 |
| POM-2C$_{18}$ | | | | | |
| 5.9 | 23 | 17 | 4.9 | 3.5 | 0.015 |
| 17.7 | 22 | 17 | 5.5 | 3.7 | 0.049 |
| 28.8 | 22 | 17 | 5.1 | 3.7 | 0.077 |

[b] R, the radius of the core; φ, volume fraction; SLD, Neutron scattering length density; t, Shell thickness.

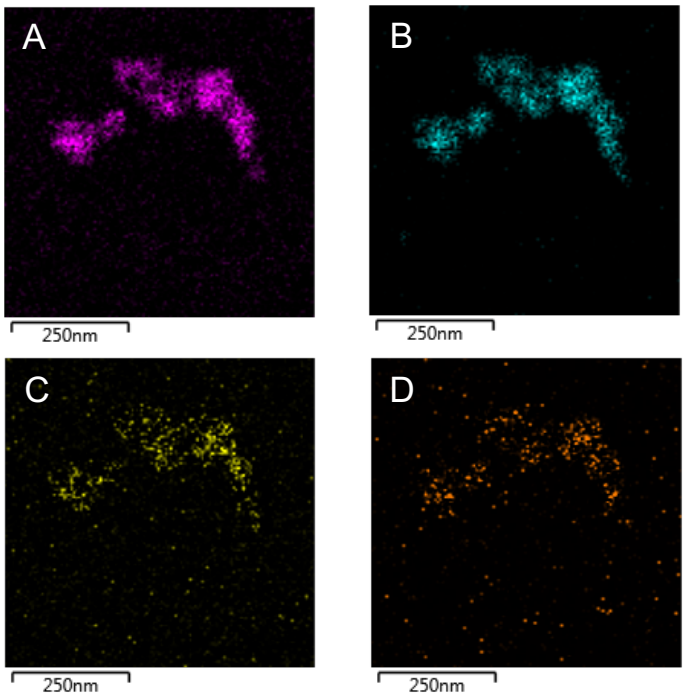


SI Fig. 6 EDX elemental mapping analysis of element distributions (A) oxygen (B) titanium (C) tungsten (D) phosphorous of the 12POM-$TiO_2$ material.

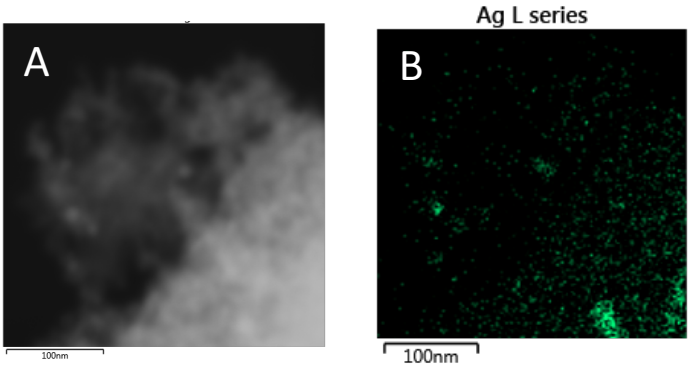


SI Fig. 7 (A) SEM image and (B) Ag elemental mapping analysis of product: 12POM@$TiO_2$ after Ag reduction reaction.

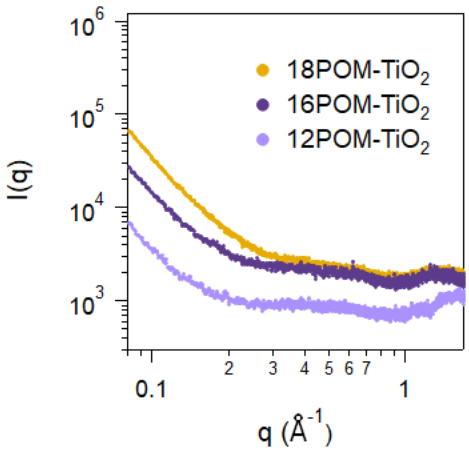


SI Fig. 8 SAXS patterns from nPOM-$TiO_2$ materials.

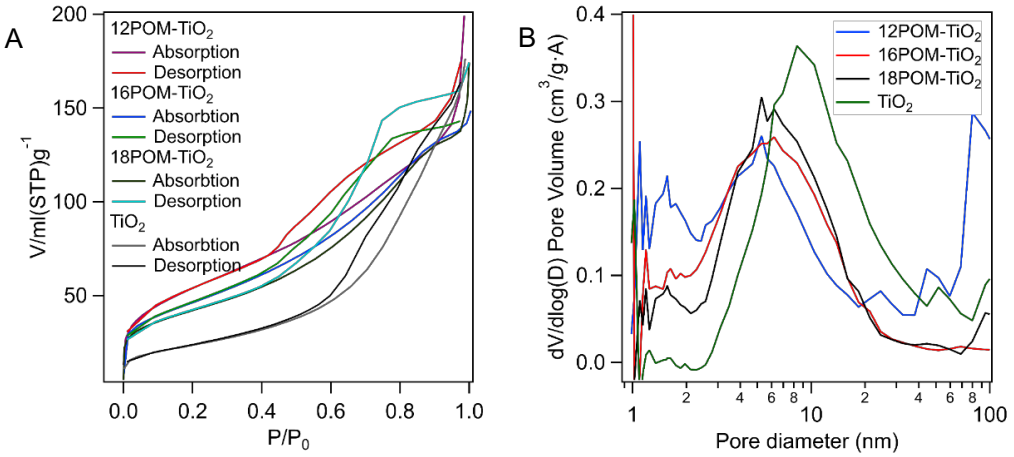


SI Fig. 9 (A) $N_2$ sorption isotherms (B) pore diameter distributions of the nPOM-$TiO_2$ and $TiO_2$ materials.

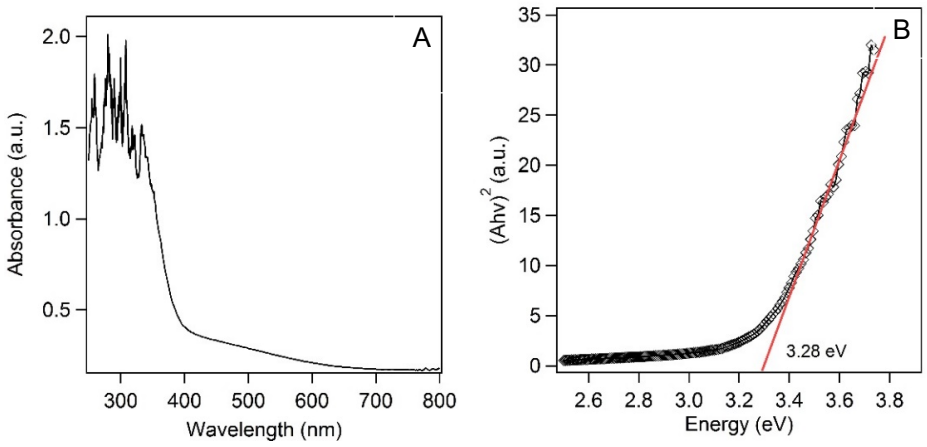


SI Fig. 10 (A) Steady-state diffuse reflectance spectrum observed for 12POM-$TiO_2$ material. (B) Plot of $(Ahv)^2$ vs Energy. Bandgap $E_g$ is obtained by the extrapolation to $(Ahv)^2 = 0$ of the linear fit of the signal at high energy.

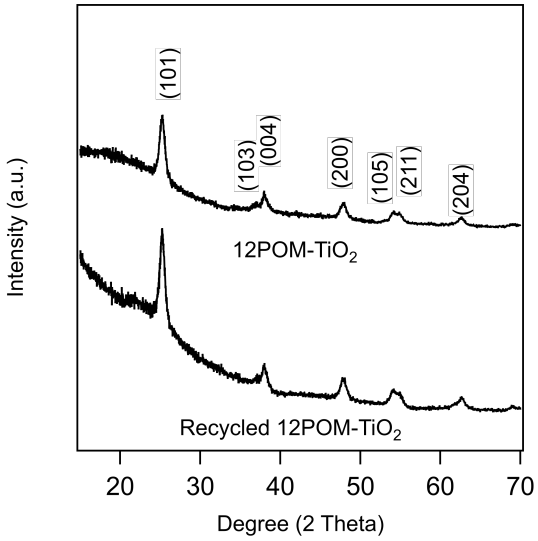


SI Fig. 11 PXRD patterns of 12POM-$TiO_2$ materials before and after recycling for eight times.

## References


1. L. Magid, K. Daus, P. Butler and R. Quincy, *J. Phys. Chem.*, 1983, **87**, 5472-5478.
2. J. Joshi, V. Aswal and P. Goyal, *J. Macromol. Sci., Phys.*, 2008, **47**, 338-347.
3. G. B. Ray, I. Chakraborty, S. Ghosh, S. Moulik and R. Palepu, *Langmuir*, 2005, **21**, 10958-10967.
4. R. Zana, *J. Colloid Interface Sci.*, 1980, **78**, 330-337.
5. P. Mukerjee and K. J. Mysels, *Critical micelle concentrations of aqueous surfactant systems*, National Standard reference data system, 1971.
6. S. Vass, T. Gilanyi and S. Borbely, *J. Phys. Chem. B*, 2000, **104**, 2073-2081.
7. K. J. Mysels and R. J. Otter, *J. Colloid Sci.*, 1961, **16**, 462-473.
8. A. Domínguez, A. Fernández, N. González, E. Iglesias and L. Montenegro, *J. Chem. Educ.*, 1997, **74**, 1227.
9. H. Gharibi and A. Rafati, *Langmuir*, 1998, **14**, 2191-2196.

## 4.2 Conclusion

This chapter focuses on the studies of surfactants with inorganic polyoxometalate (POM) as the hydrophilic headgroup (POM-2C$_n$). Compared to the traditional organic surfactant, these surfactants not only behave as the pore maker in the synthesis process but also decorate their POM headgroup in the resulting material when they are used as structure-directing agents.

In this chapter, POM amphiphiles with different hydrophobic tail lengths are prepared and studied. The structure of the synthesised POM amphiphiles are confirmed using TGA and $^{31}$P NMR and C-H correlated NMR techniques. The self-assembly behaviour of these surfactants in water is studied using SANS technique. The obtained SANS patterns are modelled using either a core-shell spherical model or a core-shell ellipsoidal model. The interactions between the micelles are modelled using rescaled Hayer-penfold Mean Spherical Approximation. The shape-dependant modelling suggests that the POM-2C$_n$ with longer hydrophobic tails form more globular micelles in water. The trend of micellar charge when the hydrophobic tail length in the molecule structure becomes longer are studied. The results derived from the structure factor modelling of the SANS patterns are opposite to those obtained from zeta-potential measurements. The contradiction may be due to the fact that the micellar charge obtained from SANS fitting is a rescaled value instead of the actual value.

As POM is a photocatalyst, the micelles formed by POM-2C$_n$ in water are used to template $TiO_2$ through a hydrothermal method. The hydrocarbon tails are burnt away to generate pores, the thermally stable POMs are then left over within the porous materials, the resulting material is denoted as nPOM-$TiO_2$ (n is the number of carbon in the hydrophobic tails of the surfactant used for templating). The $TiO_2$ in the hybrid materials has an anatase phase according to XRD characterisation. BET analysis of nitrogen absorption and desorption gives a surface area at *ca.* 160 m$^2$/g. Elemental scanning measurements suggest a well-distribution of P and W elements, indicating the presence of POM units in the prepared materials. The photocatalytic property of the nPOM-$TiO_2$ materials are tested through Rhodamine B (RhB) photodegradation. Their photocatalytic properties are improved compared to unfunctionalised porous $TiO_2$ material. The bandgap of the 12POM-$TiO_2$ hybrid material is measured to be very close that of $TiO_2$ material. Therefore, the improvements of photocatalytic property are proposed to be: the redox property of the POMs that prevent the recombination of photo-generated electrons and holes, the electrostatic interactions between the negatively-charged POMs and positively-charged RhB molecules.

Additionally, the photocatalytic properties of nPOM-$TiO_2$ materials are different. The 12POM-$TiO_2$ behaves the best in RhB degradation. The elemental scanning and BET characterisation suggest that 12POM-$TiO_2$ has the highest POM content and highest surface area. The large surface area has the contribution from large pores that may be attributed to the elongated POM-2C$_{12}$ micelles that used to template $TiO_2$.

Based on the studies in this chapter, a follow-up study is proposed. Since the POM content has been proven to affect the photocatalytic property of the prepared hybrid materials. A method can be developed to tune the POM content in the resulting hybrid materials. So in the next chapter, mixtures of POM-2C$_n$ and hexaethylene glycol monododecyl ether ($C_{12}EO_6$) with three different mixing ratios (1:3, 1:1 and 3:1) are studied. Critical micelle concentrations (CMCs) of these studied mixtures in water are obtained through measuring either the conductivity or the surface

tension. The interaction parameters are calculated using the CMCs of the mixtures and pure surfactants. Additionally, the morphologies of the mixed micelles are studied using SANS. Due to the non-ideal mixing of the two surfactants, the more fraction of each surfactant in the micelles are estimated through a calculation using the obtained interaction parameters. The mole fraction of surfactants in the micelles are also obtained by taking advantage of the deuterium-labelling in SANS technique. The mixing ratios obtained from the two methods are also compared and discussed.

# 5

# Mixed micelles of Amphiphilic Polyoxometalate and Hexaethylene Glycol Monododecyl Ether.

## 5.1 Introduction

Mixed micelles are of great interest in terms of their non-ideal behaviour compared to singular surfactant systems.[250,251] The mixed surfactant systems are important for the enhancement and the adjustment of the interactions between the silica precursor and the organic template,[59] adjustment of the structure and the pore dimension of the prepared porous silica,[252] and the use of cost-effective approaches by replacing the expensive or self-prepared surfactants by the commercially available surfactants.

As discussed in Chapter 4, surfactants with POM as the hydrophilic headgroup are prepared. POM-2C$_n$ form micelles in water and their self-assembly behaviour in water are studied using SANS technique. It has suggested that the surfactant with longer hydrophobic tails forms more globular micelles. The morphology of the micelles can be explained by the micellar charge. The micellar charges are also studied using zeta-potential, which gives an opposite trend to the those obtained from SANS fitting. The micelles formed by POM-2C$_n$ are used to template $TiO_2$ materials to produce POM-$TiO_2$ hybrid materials through a hydrothermal method. The POM-$TiO_2$ hybrid materials show synergistic effects in photodegradation of RhB. The catalytic property test has suggested that the POM content within the hybrid materials affects their photocatalytic property. This study has proven that the introduction of POMs into the $TiO_2$ systems could improve its photocatalytic properties.

Moreover, as reported previously,[161] the efficiencies of the POM-$TiO_2$ mixtures with increasing POM percentage experience a drop after they reach the maxima. Therefore, it is interesting to explore a method which could control the amount of POMs in the resulting materials. Mixed micelles containing POM-2C$_n$ is a potential method. The amount of POM units that are functionalised within the porous materials can be controlled through using mixed micelles as templates.

With this aim, the POM-2C$_n$ are mixed with other commercial surfactants to form mixed micelles to be used as templates for the preparation of POM-functionalised materials. The POM content in the templated hybrid materials can be tuned through using micelles with different mole fractions of POM-2C$_n$ surfactant. Additionally, the mixed micelles are also important to

generate pores with higher volume in the templated materials compared to those produced by the pure POM-2C$_n$ system since the large POM headgroups are spaced out by the organic headgroup of the commercial surfactant in the micelles.

For these reasons, the mixtures of POM-2C$_n$ (n = 12, 14, 16 or 18) and hexaethylene glycol monododecyl ether ($C_{12}EO_6$) are studied in this chapter. The critical micelle concentrations of the mixtures are measured using conductivity or surface tension. The morphology and the surface charge of the mixed micelles formed are studied through fitting the SANS patterns. The modelling results indicate a formation of either core-shell spherical micelles or core-shell spherical/ellipsoidal micelles. Additionally, an isotopic-labelling method was used to investigate the mole fraction of the POM-2C$_n$ component within the mixed micelles, from which the results are consistent with those obtained from the CMC results.

<table>
<tr><td colspan="9">This declaration concerns the article entitled:</td></tr>
<tr><td colspan="9">Mixed micelles of Amphiphilic Polyoxometalate and Hexaethylene Glycol Monododecyl Ether</td></tr>
<tr><td colspan="9">Publication status (tick one)</td></tr>
<tr><td>draft manuscript</td><td>✓</td><td>Submitted</td><td></td><td>In review</td><td></td><td>Accepted</td><td></td><td>Published</td></tr>
<tr><td>Publication details</td><td colspan="8"></td></tr>
<tr><td>Candidate's contribution to the paper</td><td colspan="8">The candidate contributed to/ considerably contributed to/predominantly executed the…<br>Formulation of ideas:<br>The initial idea and the proposals for beamtime were formulated by KJE and AD, (AD, contribution 70 %).<br><br>Design of methodology:<br>All the measurements were designed by AD with exception of the set-up of small angle neutron scattering done by NM and AW at ISIS, with followed measurements carried out by AD. AD contribution 90%.<br><br>Experimental work:<br>Part of the preliminary data were collected by AD, JS, MAS, AW and NM. AD contributed to the data analysis and the final experimental work included in the manuscript (AD contribution 70%).<br><br>Presentation of data in journal format:<br>The first draft was written by AD. Subsequent draft was reworked by AD following the feedback from KJE, NM, RJE, JS, MAS, NE, KM, ZW and AW. (AD contribution 85%)</td></tr>
<tr><td>Statement from Candidate</td><td colspan="8">This paper reports on original research I conducted during the period of my Higher Degree by Research candidature.</td></tr>
<tr><td>Signed</td><td colspan="4">Andi D.</td><td>Date</td><td colspan="3">26/09/2019</td></tr>
</table>

# Mixed micelles of Amphiphilic Polyoxometalate and Hexaethylene Glycol Monododecyl Ether

Andi Di,[1] Julien Schmitt,[1,2] Kun Ma,[3] Marcelo Da Silva,[1] Naomi Elstone,[1] Najet Mahmoudi,[3] Peixun Li,[3] Adam Washington,[3] Zi Wang,[3] R. John Errington,[5] Karen J Edler[1*]

[1]Department of Chemistry, University of Bath, Bath, BA2 7AY, UK

[2]LSFC - Laboratoire de Synthèse et Fonctionnalisation des Céramiques, UMR 3080 CNRS / Saint-Gobain CREE, Saint-Gobain Research Provence, 550 avenue Alphose Jauffret, Cavaillon, France

[3]ISIS Neutron and Muon Source, Science and Technology Facilities Council, Rutherford Appleton Laboratory, Didcot OX11 0QX, UK

[4]Chemistry, School of Natural and Environmental Sciences, Newcastle University, Newcastle upon Tyne, NE1 7RU, UK

## Abstract

Polyoxometalates (POMs) are metal oxygen clusters with a range of interesting magnetic and catalytic properties. However, they are limited by processability and recoverability, factors which could be alleviated by supporting them on mesoporous hosts using micelle templating to create porosity. As a preliminary study, we have therefore investigated the self-assembly of POM-amphiphiles ($P_2W_{17}$-$2C_n$), obtained by grafting double hydrocarbon chains on to the $[P_2W_{17}O_{61}]^{10-}$ (denoted as $P_2W_{17}$) "headgroup", in mixed micelles with hexaethylene glycol monododecyl ether ($C_{12}EO_6$) relevant to the synthesis of POM-functionalised micelle-templated porous materials. The mixing of these two surfactants is not ideal and unusually suggests unfavourable interactions between the two species, despite evidence of the mixed micellisation. The interaction parameters for $P_2W_{17}$-$2C_n$/$C_{12}EO_6$ systems were calculated from experimental CMC values and applied to predict the micellar compositions. The tail length of $P_2W_{17}$-$2C_n$ surfactants was varied (n= 12, 14, 16 and 18) to evaluate its effect on the mixed micellisation and intermicellar interactions. Small angle neutron scattering (SANS) was used

to study the micellisation of the mixed $P_2W_{17}$-$2C_n$/$C_{12}EO_6$ systems in water, which suggests the inserted $C_{12}EO_8$ molecules induce an elongation of the mixed micelles. Micellar compositions obtained from SANS modelling were in good accordance with those predicted using averaged interaction parameters for $P_2W_{17}$-$2C_n$/$C_{12}EO_6$ (n = 12 and 14).

## Introduction

Polyoxometalates (POMs), inorganic metal-oxygen cluster anions, are fascinating nanomaterials due to their diverse magnetic,[1] catalytic,[2] chemical,[3] and electronic[4] properties. However, their applications are somewhat limited due to their poor processability, and so practical polyoxometalate-based devices are rare.[5] The synergism between polyoxometalates and organic/inorganic matrix makes the resulting hybrid materials of great interest in the field of the fabrication of electronic devices and catalysis.[6-8]

In our previous work, we investigated the use of $P_2W_{17}$-headed surfactants, produced by attaching double hydrocarbon chains onto a Dawson-type polyoxometalate, $[P_2W_{17}O_{61}]^{10-}$ ions ($P_2W_{17}$), as templates for the preparation of P2W17 functionalised $TiO_2$ (abbreviated as $P_2W_{17}$-$TiO_2$). The recyclable $P_2W_{17}$-$TiO_2$ catalysts displayed outstanding performance for photodegrading rhodamine B compared to porous $TiO_2$ templated by sodium dodecyl sulfate (SDS).[9] The incorporation of POMs into surfactant micelle templates directed POMs onto the pore surfaces and integrated their functionality into the templated materials, resulting in a significant improvement in performance.

Binary surfactant mixtures are a natural extension of this work, as they allow the concentration of POM units in the microstructure to be tuned. This approach is also more cost-effective, since a lower concentration, higher cost $P_2W_{17}$-$2C_n$ surfactant is required. This motivates our investigation of mixed systems of our $P_2W_{17}$-$2C_n$ surfactants with commercial surfactants. The high negative charge of the $P_2W_{17}$-$2C_n$ headgroups, are expected to cause large repulsive interactions or co-precipitation when these $P_2W_{17}$-$2C_n$ surfactants are mixed with an anionic or a cationic surfactant. We have therefore chosen to investigate mixtures of the $P_2W_{17}$-$2C_n$

surfactants with a nonionic surfactant, $C_{12}EO_6$, as a co-template. Such mixtures may also enable the synthesis of functional hybrid materials with variable amounts of $P_2W_{17}$.

In this paper, we present the measured critical micelle concentration (CMC) values of the mixed systems, alongside small angle neutron scattering (SANS) measurements on mixed micelles of $P_2W_{17}$-$2C_n$ with $C_{12}EO_6$. For these experiments, the surfactant composition of the solutions were varied at a fixed overall surfactant concentration. By fitting the SANS data, we derived the geometries and the aggregation numbers ($N_{agg}$) of the mixed micelles. The mole fractions of $C_{12}EO_6$ in the micelles were determined by isotopic substitution and were found to be consistent with the micellar compositions predicted by the micellar interaction parameters derived from the experimental CMC values, based on the regular solution theory (RST).[10]

## Experimental Methods

**Materials.** Fully hydrogenated hexaethylene glycol monododecyl ether (h-$C_{12}EO_6$, purity > 98%) and $D_2O$ (99.9 atom% D) were purchased from Sigma Aldrich and were used as supplied. $K_6[P_2W_{17}O\{Si_2(C_nH_{2n+1})_2\}]$ ($P_2W_{17}$-$2C_n$, n = 12, 14, 16 and 18) were synthesised according to a published protocol.[9] All the $P_2W_{17}$-$2C_n$ materials used in this paper were tail-hydrogenated. Tail-deuterated $C_{12}EO_6$ (98 atom D%, abbreviated to d-$C_{12}EO_6$) was provided by the STFC Deuteration Facility at ISIS Neutron and Muon Facility at Didcot.

$P_2W_{17}$-$2C_n$ surfactants were used as synthesised without further purification for SANS measurements. All hydrogenated surfactant solutions were prepared in either $D_2O$ or 70 mol% $D_2O$, prepared by diluting $D_2O$ was ultrapure water (18.2 MΩ·cm, from an ELGA PURELAB flex water purification system). $P_2W_{17}$-$2C_n$/d-$C_{12}EO_6$ mixtures were prepared in $D_2O$.

**Critical Micelle Concentration (CMC) measurement.** We have previously reported the CMCs of the pure $P_2W_{17}$-$2C_n$ surfactants (n = 12, 14, 16 and 18).[9] The CMC of the $C_{12}EO_6$ in water was measured using a Du Noüy Ring (Attension Sigma 701 Tensiometer). The CMCs of the binary systems were measured by either conductivity using a METTLER TOLEDO conductivity meter or a pendant-drop method using a Kruss DSA100 in lab 51 at Diamond

Light Source. For $P_2W_{17}$-$2C_n$-rich mixtures, electrical conductivity measurements should give CMC values with more accuracy, whereas surface tension measurements provide more accurate results of $C_{12}EO_6$-rich mixtures. Enough time was allowed to ensure that the equilibrium at the interface was achieved prior to measurement.

**SANS Data collection.** SANS experiments were performed on the LOQ[11] and LARMOR[12] instruments on Target Station I and II, respectively at the ISIS Neutron and Muon Spallation Source, Oxfordshire, UK.

The samples were measured in 1 mm path-length optical quartz cells at 25 °C, using a thermostat-controlled circulating bath. Samples were measured for 40 μA ($D_2O$) and 80 μA (70 mol% $D_2O$) on LOQ instrument. For experiments on LARMOR, mixtures containing $P_2W_{17}$-$2C_n$ with d-$C_{12}EO_6$ in $D_2O$ were measured for 20 μA.

The raw data were corrected for sample transmission and backgrounds from the solvent, the sample cell and other instrumental background using standard workflows in the Mantid software package.[13] Scattering data were normalised against the scattering from a partially-deuterated polystyrene blend of known molecular weight converting it to the differential scattering cross section $d\sum/d\Omega(q)$ (in absolute scale of $cm^{-1}$).[14] The output data are hence given in absolute scattered intensity, I(q) in $cm^{-1}$, *versus* the momentum transfer, q in $Å^{-1}$.

Data from all samples measured were labelled with the molar ratio between the two surfactants X≡ $[P_2W_{17}$-$2C_n]/ [C_{12}EO_6]$ = 3:1, 1:1 and 1:3, with the overall surfactant concentrations $[P_2W_{17}$-$2C_n]$ + $[C_{12}EO_6]$ of 8 and 16 mM in aqueous solutions. The corresponding mole fractions of $P_2W_{17}$-$2C_n$ are 0.75, 0.5 and 0.25, corresponding to a molar ratio value at 3:1, 1:1 and 1:3 respectively. For $P_2W_{17}$-$2C_n$/$C_{12}EO_6$ (n = 12 and 14) systems, measurements were made with both surfactants fully hydrogenated and tail-deuterated $C_{12}EO_6$ mixed with hydrogenated $P_2W_{17}$-$2C_n$.

**SANS Data analysis.** SANS scattering patterns were modelled by shape-dependent approaches, either a core-shell sphere model[15] or core-shell ellipsoid model,[16, 17] using the

Sasview software (version 4.2.1). Polydispersity was not accounted for since good fits were obtained for monodisperse models. Both models used here assume that the thickness of the shell is constant at all points around the sphere or the ellipsoid. A structure factor, the Hayter-Penfold Rescaled Mean Spherical Approximation (RMSA),[18] was used to account for the intermicellar interactions. RMSA is appropriate for dilute solutions of charged spherical and ellipsoidal micelles with a small aspect ratio[19, 20] and gives a good fit to the data obtained.

SANS fitting was carried out through a simultaneous approach at two different solvent contrasts, $D_2O$ and 70 mol% $D_2O$. The molar composition of the solvent is known, and the solvent neutron scattering length densities (SLD) were calculated to be $6.35\times10^{-6}$ Å$^{-2}$ for $D_2O$ and $4.27\times10^{-6}$ Å$^{-2}$ for 70 mol% $D_2O$ accordingly. Hence the solvent SLDs were always fixed in the fitting process. Similarly, during the fitting of systems with hydrogenated surfactant mixtures, the core SLDs (refer to the values given in SI Table 1 at page 132), temperature (298 K) and dielectric constant of solvent (78 for $D_2O$ and 78.2 for 70 mol% $D_2O$)[21] were all held at the known values. The minimum radius of the core of the micelles ($R_{min}$), the shell thickness (t), the micellar charge ($Z_m$), the shell SLD, the ellipticity ($\varepsilon$, for ellipsoids) and the volume fraction of micelles ($\varphi$) were the fitting parameters.

$P_2W_{17}$-$C_n$/d-$C_{12}EO_6$ systems were treated differently while fitting. The parameters which were known from the experimental details (SLD of solvent) and parameters ($R_{min}$, $\varepsilon$, t and $\varphi$) obtained from the modelling results of the equivalent fully hydrogenated $P_2W_{17}$-$2C_n$/$C_{12}EO_6$ system were fixed. The core SLD values were extracted from the fitting.

Experimental data were in good accordance with either the core-shell spherical model or core-shell ellipsoidal model with a core composed of the hydrophobic tails of the surfactant and a shell due mostly to the hydrophilic headgroups. $R_{min}$ was always left free to vary during the fitting procedure while the core SLD was fixed to the value expected for saturated hydrocarbon chains for the fully hydrogenated binary surfactant systems during the data analysis process. Consequently, the shell can be formed only the solvated $P_2W_{17}$ headgroups but also any counterions associated with the micelles and possibly part of the hydrocarbon chains due to

the roughness of the shell-core interface. Due to the complexity of potential components in the shells, we did not attempt to evaluate the hydration of the shell in the analysis.

## Results and Discussion

**CMC Determination.** The CMCs of the $P_2W_{17}$-$2C_n$ surfactants have been reported previously by our group and are presented in SI Table 2 (page 134).[9] The CMC value of $C_{12}EO_6$ obtained from surface tension measurements (SI Figure 1, page 132) was found to be 0.085 ± 0.05 mM, which is consistent with the value reported in the literature.[22] The CMCs of the $P_2W_{17}$-$2C_n$/$C_{12}EO_6$ systems with various compositions were measured and plotted in Figure 1. The surface tension and conductivity data used to determine these values can be found in the supplementary information (see SI Figures 2, 3 and 4 at page 133). CMCs of $P_2W_{17}$-$2C_{18}$/$C_{12}EO_6$ could not be accurately determined and are not reported since either the electrical conductivities of the surfactant solutions were too low or the surface tension values were very close to the water surface tension due to the low CMCs. The surface tension measurements suggest the presence of small amounts of impurities in these $P_2W_{17}$-$2C_n$ surfactants, causing a slight dip below the average final surface tension at the point of the CMC (for example, $P_2W_{17}$-$2C_{12}$/$C_{12}EO_6$ with X ≡ 1:1, see SI Figure 2b at page 133). The impurities may come from the excess of unreacted long-chain trichlorosilane molecules which were not completely washed out during the post-synthesis steps.

Table 1. $P_2W_{17}$-$2C_n$ dissociation degree in $P_2W_{17}$-$2C_n$:$C_{12}EO_6$ = 3:1 mixtures and pure $P_2W_{17}$-$2C_n$ systems (n=12, 14 and 16)

| Dissociation degree | 3:1 $P_2W_{17}$-$2C_n$:$C_{12}EO_6$ | $P_2W_{17}$-$2C_n$[9] |
|---|---|---|
| n=12 | 0.61 ± 0.05 | 0.53 ± 0.04 |
| n=14 | 0.45 ± 0.05 | 0.44 ± 0.03 |
| n=16 | 0.40 ± 0.04 | 0.29 ± 0.03 |

The ionisation degree of the $P_2W_{17}$-$2C_n$ molecules in the $P_2W_{17}$-$2C_n$-rich mixtures were calculated using conductivity data[23] and are listed in Table 1. These are higher than those of pure $P_2W_{17}$-$2C_n$ systems.[9] We hypothesise that for the mixed systems, the insertion of nonionic surfactant molecules between the $P_2W_{17}$-$2C_n$ molecules in the micelles increases the distance between anionic $P_2W_{17}$ headgroups, reducing the electrostatic repulsion between

them. Consequently, more counterions are able to dissociate from the surfactant headgroups compared to the pure $P_2W_{17}$-$2C_n$ systems.

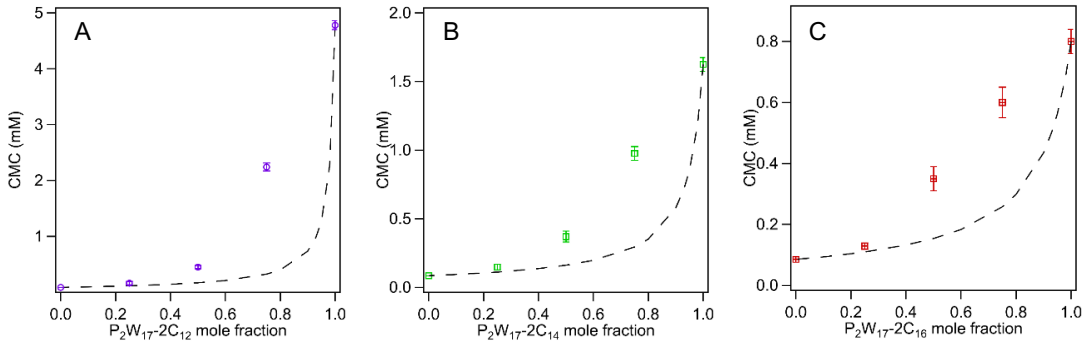


Figure 1. CMC values for mixtures (A) $P_2W_{17}$-$2C_{12}$/$C_{12}EO_6$ (B) $P_2W_{17}$-$2C_{14}$/$C_{12}EO_6$ (C) $P_2W_{17}$-$2C_{16}$/$C_{12}EO_6$ as a function of $P_2W_{17}$-$2C_n$ mole fraction in the mixture. The dashed line is the calculated CMCs in the case of ideal mixing using equation (1).

The experimental CMC values of the mixtures with three different compositions are summarised in SI Table 2 (page 134) and Figure 1. The CMC values decrease as the solution composition becomes increasingly nonionic-rich. This is consistent with trends seen in anionic-nonionic commercial surfactant mixtures that have been reported by others.[24] Mixtures containing longer-chain $P_2W_{17}$-$2C_n$ also have lower CMCs compared to their shorter-chains counterparts with the same mixing ratio.[25]

The experimental CMCs of the mixtures, plotted as a function of $P_2W_{17}$-$2C_n$ mole fraction in Figure 1, are compared to the dependence of the CMCs predicted for ideal mixing (dashed line). Comparison of the experimental results and the CMCs estimated if the two surfactants are demixing are displayed in SI Figure 5 (page 134). The experimental results follow neither the ideal mixing nor the demixing behaviour. The deviations from ideal mixing in mixed systems can be understood by using regular solution theory (RST),[10, 26] expressed in terms of a single intermicellar interaction parameter β. The value of β is related to the CMC of a mixed surfactant solution ($CMC_{mix}$) *via*:

$$\frac{1}{CMC_{mix}} = \frac{x_1}{f_1 CMC_1} + \frac{1-x_1}{f_2 CMC_2} \qquad (1)$$

where $x_1$ is the mole fraction of surfactant 1, and $CMC_1$ and $CMC_2$ are the critical micelle concentrations of surfactant 1 and surfactant 2 separately. The activity coefficient $f_1$ and $f_2$ are expressed as a function of β, $f_1 = \exp[\beta(1-x_1)^2]$ and $f_2 = \exp[\beta(x_1)^2]$. β was calculated from the $CMC_{mix}$ for each mixture using equation (1). The obtained β value for each given composition and the averaged value $\overline{\beta}$ for each specified system are listed in Table 2. The positive β values imply an unfavourable interaction occurs while mixing. The calculated β values, considering the errors, are roughly constant over the range of compositions studied for each mixed system, which is consistent with the report on mixtures within the regular solution approximation.[27] Additionally, the mixed micelles were probed using SANS, combined with the isotopic substitution method to determine the micelle composition for comparison with that predicted from the mixing parameters.

Table 2. The calculated interaction parameters β for the systems studied (uncertainties derived from the errors in the CMC values).

| $P_2W_{17}$-2$C_n$:$C_{12}EO_6$ | β (n=12) | $\bar{\beta}$ (n=12) | β (n=14) | $\bar{\beta}$ (n=14) | β (n=16) | $\bar{\beta}$ (n=16) |
|---|---|---|---|---|---|---|
| 3:1 | 3.92 ± 0.9 | 4.43 ± 0.8 | 2.56 ± 1.0 | 3.74 ± 0.8 | 2.21 ± 0.6 | 3.02 ± 0.6 |
| 1:1 | 3.96 ± 0.8 | | 4.36 ± 0.8 | | 3.29 ± 0.5 | |
| 1:3 | 5.42 ± 0.6 | | 4.30 ± 0.5 | | 3.55 ± 0.6 | |

**SANS structural characterisation.** SANS data modelling gives information about the microstructure of these micellar systems. Figure 2 and Figure 3 show the SANS data and their fits for the h-$P_2W_{17}$-2$C_n$/h-$C_{12}EO_6$ mixtures in $D_2O$ at a total surfactant concentration of 8 mM and 16 mM and with three mixing compositions. The same samples in 70 mol% $D_2O$ were also measured as another contrast to constrain the structure fitting. The SANS data and the corresponding fits for the h-$P_2W_{17}$-2$C_n$/d-$C_{12}EO_6$ mixtures are given in SI Figure 6 and 7 (page 134 and 135). The fits are in give good agreement with the experimental data collected.

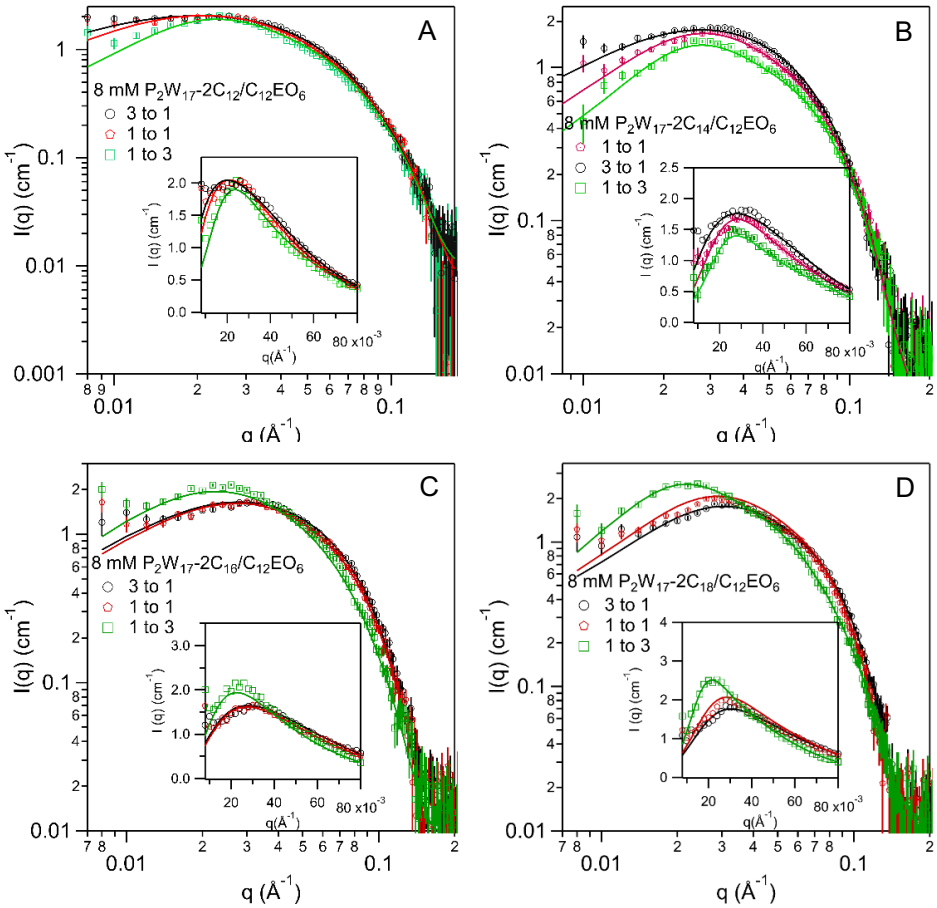


Figure 2. SANS data (I(q) versus q) and fits for h-$P_2W_{17}$-$2C_n$/h-$C_{12}EO_6$ with n= (A) 12 (B) 14 (C) 16 and (D) 18 at a total concentration of 8 mM in $D_2O$, given on a log-log scale. The insets corresponds to the scattering data plotted in linear scale.

These graphs show plots of SANS data on both a linear (inset) and log-log scale. The use of a linear scale on x-axis highlights the scattering caused by intermicellar interactions. After comparing the three patterns in each of the sub-graphs in Figure 2 (B) (C) (D) and Figure 3 (A) (B) (C) (D), a peak arises in the linear scattering patterns at a position between q = 0.025 and 0.35 $Å^{-1}$, accounting for the interactions between micelles. This peak shifts to lower q values and becomes sharper for solutions progressively richer in the nonionic surfactant. This indicates a greater micellar repulsion is present in solutions with a higher $C_{12}EO_6$ composition. This is further demonstrated by the micellar surface charge parameter $Z_m$ extracted from data fitting listed in Table 3. This effect becomes more prominent as the hydrophobic tails of $P_2W_{17}$-$2C_n$ become longer. For $P_2W_{17}$-$2C_{12}$/$C_{12}EO_6$ mixtures at 8 mM (Figure 2A), there is no significant increase in the peak intensity or shift in the scattering pattern (nonetheless the trend

is still observed from the values extracted from the fits). However, this becomes more pronounced for $P_2W_{17}$-$2C_{18}/C_{12}EO_6$ mixtures (Figure 2D).

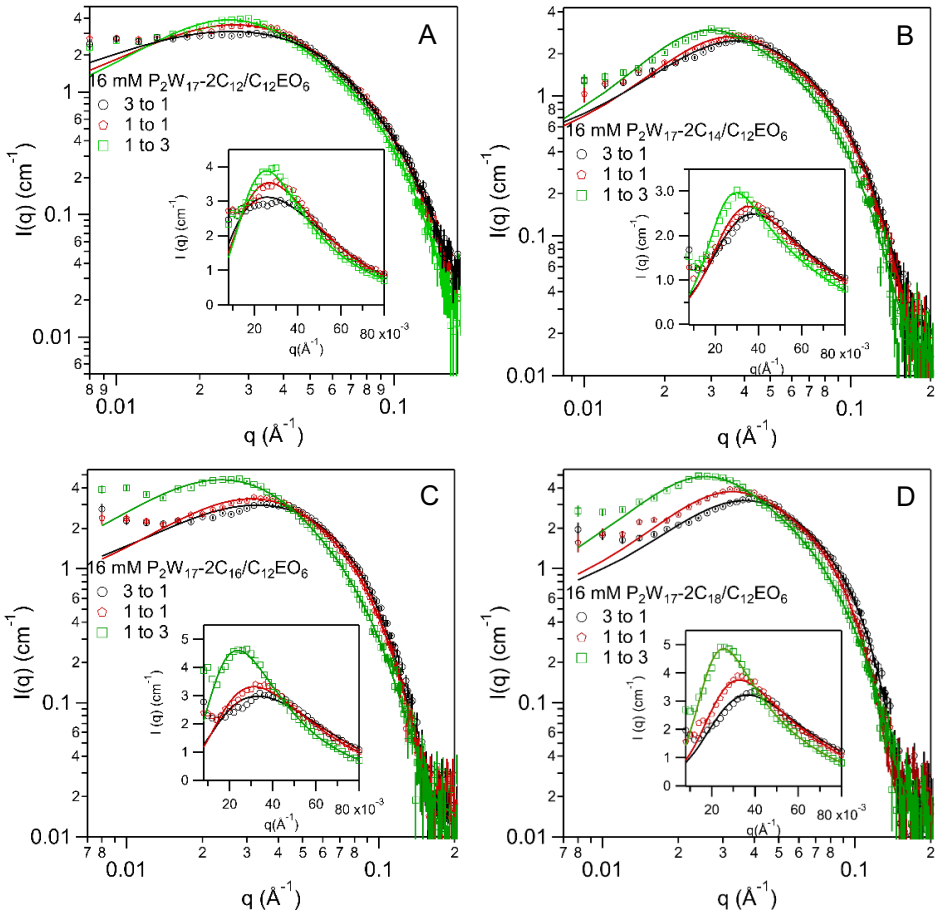


Figure 3. SANS data (I(q) versus q) and fits for $P_2W_{17}$-$2C_n/C_{12}EO_6$ with n= (A) 12 (B) 14 (C) 16 and (D) 18 at a total concentration of 16 mM in $D_2O$, given on a log-log scale. The insets corresponds scattering data plotted on linear scale.

Fitted model parameters are given in Table 3. As seen from Table 3, the volume fraction, φ values obtained for the 1:3 solutions are lower than those found for the 3:1 solutions, but $N_{agg}$ increases (except for the $P_2W_{17}$-$2C_{14}/C_{12}EO_6$ mixtures which have a very small variation in $N_{agg}$ among 3 ratios). The volume fraction differences are supported by the fact that the single-tailed nonionic surfactant has a smaller molecular volume compared to $P_2W_{17}$-$2C_n$. It is also seen that the ellipticity (ε) of the micelles increases with the $C_{12}EO_6$ content in these mixtures at a given concentration. The fitted shell thickness (t) varies between 12 and 17 Å which are comparable to the dry $P_2W_{17}$ headgroup size which lies in the range of 12-18 Å.[28]

The aggregation numbers, $N_{agg}$, were calculated from the volume of the core divided by the corresponding tail volume per surfactant ($V_{tail}$). $V_{tail}$ can be calculated using the equation:

$$V_{tail} = V_{2Cn} \times [P_2W_{17}\text{-}2C_n]_{cor} + V_{C12} \times [C_{12}EO_6]_{cor} \quad (2)$$

where $[P_2W_{17}\text{-}2C_n]_{cor}$ and $[C_{12}EO_6]_{cor}$ are corrected mole fractions of $P_2W_{17}\text{-}2C_n$ and $C_{12}EO_6$ in the micelles respectively (calculated in the Micellar Composition section below), $V_{2Cn}$ and $V_{C12}$ are the estimated volume of each surfactant, therefore are the volume of the double-$C_nH_{2n+1}$ tails and $C_{12}H_{25}$ tail estimated *via* Tanford equation.[29] Consequently, the charge number of each $P_2W_{17}\text{-}2C_n$ molecule, $Z_p$, was calculated according to the obtained aggregation numbers and corrected $P_2W_{17}\text{-}2C_n$ mole fractions. Values of $Z_p$ (refer to Table 3) increase with rising nonionic species present in the mixtures.

The micellar surface charge ($Z_m$) of our systems are found to be smaller than those found in SDS/$C_{12}EO_6$ systems (which range between 8 and 21e)[30] even if the POM headgroups could be highly charged (monovalent *versus* hexavalent). The RMSA, structure factor used for fitting, utilises the pair potential between two spherical colloids within a linearization approximation taking the Debye–Hückel form. This method, however, becomes inadequate to describe highly charged objects for which the electrostatic energy of a micro-ion near the colloid surface largely exceeds $k_BT$ (thermal energy).[31] The obtained "surface charge" $Z_m$, in that case, is the charge at a surface far from the actual surface of the micelles, therefore the bare surface charge is replaced by an effective or re-normalised quantity.[31] This explains the relatively low surface charge in our systems given by SANS modelling.

However, the re-normalised charge obtained still can be compared for discussion. With a given mixture containing $P_2W_{17}\text{-}2C_{12}$ or $P_2W_{17}\text{-}2C_{14}$, the charge per $P_2W_{17}\text{-}2C_n$ surfactant molecule ($Z_p$) becomes larger when more $C_{12}EO_6$ molecules are present in the mixtures, suggesting the $P_2W_{17}\text{-}2C_n$ molecules become more ionised as they are diluted by the $C_{12}EO_6$ molecules within the micelles. This is consistent with the discussion above on the ionisation degree values obtained from conductivity measurements. For longer-tailed counterpart, $P_2W_{17}\text{-}C_{16}$, the trend is not as obvious. Comparing the absolute ionisation values among different $P_2W_{17}\text{-}2C_n$ surfactants in the given mixtures, longer-tailed $P_2W_{17}\text{-}2C_n$ ionised less. This is similar to what

has been observed for the singular $P_2W_{17}$-$2C_n$ surfactant systems, and also for single tail quaternary ammonium surfactants and sodium alkyl sulfates[9, 32, 33]

When the total concentration of surfactant in solution was increased to 16 mM without changing the mole fractions, the micelles elongate slightly compared to those formed at 8 mM (see the micellar ellipticities listed in Table 3).

Table 3. Fitted model parameters[a] for $P_2W_{17}$-$2C_n$/$C_{12}EO_6$ mixed micelles at concentrations of 8 mM and 16 mM.

| $P_2W_{17}$-$2C_n$: $C_{12}EO_6$ | $N_{agg}$ (± 3) | $Z_m$ (e) (± 1) | $Z_p$ (e) (±25% ) | $R_{min}$ (Å)(± 1) | ε (±0.3) | φ (±0.002) | A(Å$^2$) (±5) | t (Å) (±1) |
|---|---|---|---|---|---|---|---|---|
| 8 mM $P_2W_{17}$-$2C_{12}$/$C_{12}EO_6$ mixtures | | | | | | | | |
| 3:1 | 94 | 4 | 0.07 | 16 | 2.9 | 0.011 | 80 | 15 |
| 1:1 | 125 | 6 | 0.23 | 15 | 3.6 | 0.007 | 64 | 13 |
| 1:3 | 148 | 9 | 1.93 | 15 | 3.8 | 0.008 | 54 | 14 |
| 16 mM $P_2W_{17}$-$2C_{12}$/$C_{12}EO_6$ mixtures | | | | | | | | |
| 3:1 | 88 | 4 | 0.13 | 16 | 3.0 | 0.035 | 86 | 16 |
| 1:1 | 92 | 4 | 0.21 | 14 | 3.3 | 0.026 | 73 | 14 |
| 1:3 | 139 | 9 | 1.09 | 17 | 4.5 | 0.020 | 59 | 15 |
| 8 mM $P_2W_{17}$-$2C_{14}$/$C_{12}EO_6$ mixtures | | | | | | | | |
| 3:1 | 49 | 5 | 0.14 | 16 | 1.7 | 0.016 | 109 | 16 |
| 1:1 | 74 | 9 | 0.23 | 18 | 1.9 | 0.010 | 84 | 13 |
| 1:3 | 69 | 11 | 1.15 | 15 | 2.1 | 0.007 | 74 | 13 |
| 16 mM $P_2W_{17}$-$2C_{14}$/$C_{12}EO_6$ mixtures | | | | | | | | |
| 3:1 | 28 | 8 | 0.40 | 14 | 2.1 | 0.021 | 128 | 12 |
| 1:1 | 64 | 9 | 0.34 | 17 | 1.9 | 0.014 | 86 | 11 |
| 1:3 | 61 | 11 | 2.02 | 14 | 2.9 | 0.012 | 77 | 13 |
| 8 mM $P_2W_{17}$-$2C_{16}$/$C_{12}EO_6$ mixtures | | | | | | | | |
| 3:1 | 51 | 5 | 0.13 | 21 | 1 | 0.011 | 112 | 14 |
| 1:1 | 51 | 6 | 0.26 | 17 | 1.7 | 0.008 | 101 | 13 |
| 1:3 | 110 | 8 | 0.37 | 17 | 2.7 | 0.007 | 70 | 14 |
| 16 mM $P_2W_{17}$-$2C_{16}$/$C_{12}EO_6$ mixtures | | | | | | | | |
| 3:1 | 61 | 5 | 0.14 | 21 | 1 | 0.035 | 113 | 17 |
| 1:1 | 63 | 5 | 0.19 | 16 | 2.2 | 0.017 | 104 | 13 |
| 1:3 | 108 | 4 | 0.11 | 16 | 3.4 | 0.022 | 69 | 16 |
| 8 mM $P_2W_{17}$-$2C_{18}$/$C_{12}EO_6$ mixtures | | | | | | | | |
| 3:1 | 55 | 8 | -- | 21 | 1 | 0.011 | -- | 14 |
| 1:1 | 72 | 9 | -- | 22 | 1 | 0.0096 | -- | 14 |
| 1:3 | 129 | 12 | -- | 18 | 3.1 | 0.0074 | -- | 13 |
| 16 mM $P_2W_{17}$-$2C_{18}$/$C_{12}EO_6$ mixtures | | | | | | | | |
| 3:1 | 72 | 8 | -- | 23 | 1 | 0.025 | -- | 13 |
| 1:1 | 94 | 9 | -- | 24 | 1 | 0.017 | -- | 12 |
| 1:3 | 132 | 11 | -- | 18 | 3.3 | 0.014 | -- | 12 |

[a] $R_{min}$, the minimum radius of core; $R_{max}$, the maximum radius of core; ε, $R_{max}/R_{min}$ (ellipticity); φ, volume fraction; SLD, neutron scattering length density; t, shell thickness; $N_{agg}$, aggregation number; $Z_m$, charge per micelle; $Z_p$, charge per $P_2W_{17}$-$2C_n$ molecule; A, averaged area per molecule.

The averaged area per molecule (A) values are listed in Table 3, estimated using the surface area of the mixed micelle divided by its corresponding aggregation number. The dry $P_2W_{17}$ headgroup has a cross-sectional area ($A_{P2W17}$) at around 120 Å$^2$, and the cross-sectional area

for $EO_6$ group ($A_{EO6}$) lies in the range of 46 to 58 Å$^2$.[34] Estimated area per molecule values ($A_{cor}$) are listed in SI Table 3 (page 135), calculated using the corrected mole fraction of each component:

$$A_{cor} = A_{P2W17} \times [P_2W_{17}\text{-}2C_n]_{cor} + A_{EO6} \times [C_{12}EO_6]_{cor} \quad (3)$$

A and $A_{cor}$ give similar results if the uncertainties are included. It is also seen these values decrease with the $C_{12}EO_6$ component, giving larger packing parameters,[35, 36] which contributes to the formation of more elongated micelles. This is also reflected by the increasing ellipticity values obtained from SANS fitting.

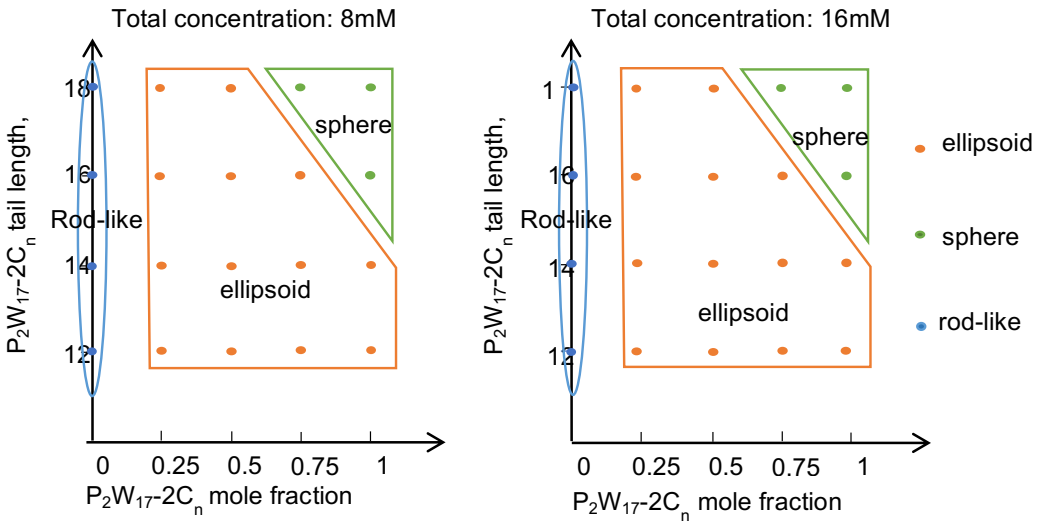


Figure 4. Phase diagram of binary $P_2W_{17}$-$2C_n$/$C_{12}EO_6$ mixtures at two dilute concentrations, n, the carbon atom number in the hydrophobic $P_2W_{17}$-$2C_n$ tails is given on the y-axis and the x-axis corresponds to the $P_2W_{17}$-$2C_n$ mole fraction.

A phase diagram concerning the shapes of the micelles compared to their compositions was obtained from the SANS modelling results and is given in Figure 4. $C_{12}EO_6$ forms rod-like micelles in water, measured using three different techniques reported in the literature.[37] Once mixed with $P_2W_{17}$-$2C_n$, the micelle shape depends on the mixing ratio and the hydrophobic tail length of $P_2W_{17}$-$2C_n$. For compositions rich in $P_2W_{17}$-$2C_{18}$ or $P_2W_{17}$-$2C_{16}$, more globular micelles were formed. For nonionic-surfactant rich compositions, more elongated ellipsoidal micelles were favoured.

**Micellar composition.** The interaction parameters, β, calculated from the experimental CMC values, indicate antagonism in mixed micelle formation. In the analysis of SANS data

from the h-$P_2W_{17}$-2$C_n$/h-$C_{12}EO_6$ systems, the composition of the micelles cannot be calculated from the shell SLD obtained by the fitting of the SANS patterns, due to the complexity of shell composition discussed before.

To evaluate the mixing mole fractions of the two surfactants in the micelles and the departures from ideal mixing, the fully hydrogenated $C_{12}EO_6$ was replaced by d-$C_{12}EO_6$ in the mixtures without changing the mole fractions or total surfactant molar concentrations. Through the fitted core SLD in the partially deuterated mixtures, the micellar compositions in these systems were calculated. The SANS data and their fits are given in SI Figure 8 and 9 (page 136). Results of the SANS-derived $C_{12}EO_6$ mole fractions in $P_2W_{17}$-2$C_n$/$C_{12}EO_6$ (n = 12 and 14) systems obtained at both concentrations with three mixing ratios are shown in Figure 5 and Figure 6 respectively (markers) and are compared to the theoretical curves for ideal (solid line) and non-ideal (dashed line) mixing. The micellar compositions at non-ideal mixing conditions were calculated using $\bar{\beta}$ listed in Table 2 according to the pseudo-phase-separation model based on regular solution theory.[27, 38] The relationship between the micellar composition and the total surfactant concentration was proposed by Clint[38] and is given as:

$$x_1 = \frac{-(C-\Delta)+\left((C-\Delta)^2+4Cx_1\Delta\right)^{1/2}}{2\Delta} \qquad (4)$$

where $\Delta = f_2CMC_2 - f_1CMC_1$ in the case of non-ideal mixing. $x_1$ is the mole fraction of surfactant 1, $f_1$ and $f_2$ are activity coefficients which are expressed as discussed above. C is the overall concentration of the surfactants.

As seen in Figure 5 and Figure 6, at these mixing ratios studied for the two systems, positive deviations from ideal mixing are observed in SANS fitted results (markers), as expected from the positive β values. They are much closer to agreement with the results obtained from the non-ideal mixing with the given interaction parameters. The nonionic-rich mixtures represent the smallest departure from the non-ideal mixing. When the two surfactants have equivalent mole fractions, the SANS fitted micellar compositions show the largest deviation from the non-

ideal mixing conditions in both systems. The standard deviations of the micellar compositions are small but increase when the nonionic surfactant ratio increases.

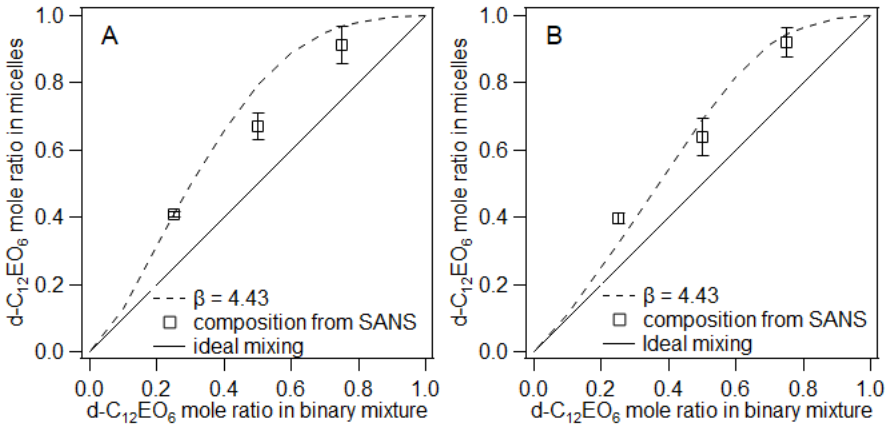


Figure 5. d-$C_{12}EO_6$ micellar mole fraction extracted from SANS fitting (markers), ideal mixing (solid line) and non-ideal mixing with β = 4.43 (dashed line) for the $C_{12}EO_6/P_2W_{17}$-$2C_{12}$ system at a total surfactant molar concentration of (A) 8 mM and (B) 16 mM

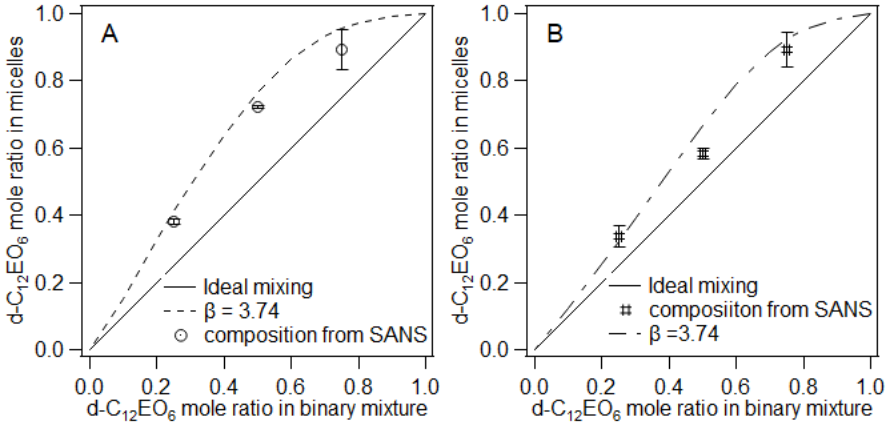


Figure 6. d-$C_{12}EO_6$ micellar mole fraction extracted from SANS fitting (markers), ideal mixing (solid line) and non-ideal mixing with β = 3.74 (dashed line) for the $C_{12}EO_6$/ $P_2W_{17}$-$2C_{14}$ system at a total surfactant molar concentration of (A) 8 mM and (B) 16 mM

The differences that are found between the micellar compositions between SANS fitting and the ones calculated from the non-ideal mixing theory using the β values from the CMC data can be explained by taking into account of the errors in the SANS fitting on one side, and the uncertainties in the measurements of the CMC values used to extract $\bar{\beta}$ on the other. Moreover, as illustrated in Figure 5 and Figure 6, the composition of the micelles is found to differ with the overall surfactant concentration.

$P_2W_{17}$-$2C_{16}$/d-$C_{12}EO_6$ and $P_2W_{17}$-$2C_{18}$/d-$C_{12}EO_6$ systems were not measured using SANS. However, the results discussed above have shown that the interaction parameter can be used to predict the micellar composition. Therefore, the averaged interaction parameter ($\bar{\beta}$ = 3.02) for the $P_2W_{17}$-$2C_{16}$/$C_{12}EO_6$ system was used to predict the micellar compositions for the $P_2W_{17}$-$2C_{16}$/$C_{12}EO_6$ mixtures (see Table 4). It could not be calculated for $P_2W_{17}$-$2C_{18}$/$C_{12}EO_6$ systems using interaction parameters as the CMCs were not measured. The obtained mole fractions considering the unfavourable interactions are called corrected mole fractions in the following discussion and are labelled as $[M]_{cor}$ (M represents for $P_2W_{17}$-$2C_n$ or $C_{12}EO_6$).

Table 4. $[C_{12}EO_6]_{cor}$ of $P_2W_{17}$-$2C_{16}$:$C_{12}EO_6$ mixtures at three molar ratios.

| $P_2W_{17}$-$2C_{16}$:$C_{12}EO_6$ | 3:1 | 1:1 | 1:3 |
|---|---|---|---|
| 8 mM | 0.265 | 0.550 | 0.804 |
| 16 mM | 0.257 | 0.525 | 0.779 |

## General discussion

The experimental CMC values of binary mixtures are found to be higher than those calculated for ideal mixing which implies that non-ideal mixing is present for these systems, and are found to decrease rapidly with an increase of the nonionic surfactant concentration in the mixture because the CMC of $P_2W_{17}$-$2C_n$ component is much higher than that of the $C_{12}EO_6$.[9, 22] Positive β values were obtained, indicating an unfavourable interaction between the two types of surfactant molecules. These interactions are different from those reported for other anionic/nonionic binary surfactant systems where normally attractive interactions between surfactants were found.[24, 27, 39-42]

For anionic/nonionic binary surfactant systems, in general it has been suggested that the insertion of nonionic surfactant molecules between the ionic surfactant molecules reduces the electrostatic repulsion between the ionic headgroups allowing the formation of micelles at a lower concentration.[42] Furthermore, for mixtures of an anionic surfactant with $C_mEO_n$ nonionic surfactant (m: the number of methylene groups, n: the number of ethylene oxide groups), the negatively charged headgroups interact with the slightly positively charged ether oxygen atoms,[39-41] i.e. oxonium ions, present in the polyoxyethylene groups at several points on the

micelle surface. For example, a synergistic effect between surfactant molecules have been reported for sodium bis(2-ethyl hexyl) sulfosuccinate/$C_{12}EO_4$ and SDS/$C_{10}EO_5$mixtures.[24, 27] In both systems, the experimental CMC values are lower than those expected in the case of ideal mixing. NaDS/$C_{12}EO_{12}$ and $Mg(DS)_2$/$C_{12}EO_{12}$ have also been reported to have attractive interaction between surfactant molecules.[42] The $Mg(DS)_2$ turned out to have weaker interactions with nonionic surfactants in comparison to NaDS due to strong condensation of the $Mg^{2+}$ counterions onto the micelles.

Reports of an unfavourable interaction between anionic surfactants and nonionic surfactants in mixtures are uncommon. Our mixed systems were found to exhibit antagonistic behaviour. The highest antagonistic interactions were obtained between $P_2W_{17}$-$2C_{12}$ and $C_{12}EO_6$ (averaged β value: $\bar{\beta}$ = 4.43). The interaction becomes less prominent when the $P_2W_{17}$-$2C_n$ component bears a longer hydrocarbon chain length. The smallest $\bar{\beta}$ was found in $P_2W_{17}$-$2C_{16}$/$C_{12}EO_6$ mixtures to be 3.02, giving the smallest absolute deviations between the measured CMC values and those predicted for ideal mixing, compared to $P_2W_{17}$-$2C_n$/$C_{12}EO_6$ (n = 12 or 14) systems. A similar phenomenon of the effect of tail length on the interaction has also been reported for a mixture of $C_{12}EO_{23}$ and alkanediyl-α-ω-bis (alkyldimethyl ammonium) dibromide which also has double alkyl chains. The antagonistic interaction parameters of that system decreased from 3.584 to 0.087 when the number of carbons in the chain of the cationic surfactant increased from 12 to 16.[43]

The principal interactions in the surfactant mixing are:[44] (1) electrostatic interactions between headgroups, (2) ion-dipole attractions between ionic and nonionic headgroups, (3) steric interactions between bulky groups, (4) van der Waals interactions between hydrophobic groups, and (5) hydrogen bonding among constituent surfactant molecules.

In an anionic-nonionic surfactant mixed system, the micelles are stabilized primarily through the contact of hydrocarbon chains of both surfactants, termed hydrophobic interactions. It is apparent that when our $P_2W_{17}$-$2C_n$ is present with the nonionic surfactant, the unfavourable interactions between the two kinds of molecules are strong, despite the hydrophobic interactions, therefore giving a positive β value. Several effects may induce unfavourable

interactions: first and foremost, bare POMs are known to self-assemble in solutions driven by counterion-mediated electrostatic interaction.[45, 46] The tendency of the $P_2W_{17}$ headgroups to assemble possibly hinders the aggregation of the two kinds of surfactant molecules to some extent. Secondly, $K^+$ ions, are termed as "structure makers", which means that water molecules surrounding them are more organised compared to pure water.[47] The water molecules around the $P_2W_{17}$ headgroups are well-organised due to the existence of $K^+$ counterions and are driven towards $P_2W_{17}$ headgroups due to the electrostatic interactions, and this could result in lower hydration of the $EO_6$ group fitted between $P_2W_{17}$-$2C_n$ molecules. The reduced hydration in $EO_6$ group may contribute to the antagonistic mixing behaviour of the two components in the micelles. Moreover, unfavourable mixing behaviour is also considered from the aspect of the structures of the two hydrophilic headgroups. Ethylene oxide chains usually behave as a Gaussian coil[34, 39, 48] and keep a characteristic size unperturbed in a saturated adsorption layer instead of forming extended chains in the solutions. The energetically favourable coil configuration is smaller (10.29 Å, calculated from the equation in reference[34, 49]) than the $P_2W_{17}$ headgroup (around 12-18 Å).[28] In this case, the $EO_6$ groups may be forced to take on a configuration away from their most energetically favourable conformation. The combination of these factors lead to the observed antagonistic effect.

β value differs among systems containing $P_2W_{17}$-$2C_n$ with different alkyl chain lengths. The variations can be attributed to the effects of alkyl chain symmetry and asymmetry, which has been studied for cationic and anionic surfactant mixed systems.[50] In the case of a system with high alkyl chain symmetry ($P_2W_{17}$-$2C_{12}$/$C_{12}EO_6$), packing of the surfactants tails is favoured and therefore, strong unfavourable interactions between headgroups prevails. For two surfactants with different alkyl tail lengths, a dense packing is sterically unfavourable. Therefore, β decreases with the difference between tail lengths. This is corroborated by the larger $A_{cor}$ values for $P_2W_{17}$-$2C_{14}$/$C_{12}EO_6$ and $P_2W_{17}$-$2C_{16}$/$C_{12}EO_6$ systems compared to those of the mixtures containing $P_2W_{17}$-$2C_{12}$.

The phase behaviour of the individual di-alkyl chain surfactants, $P_2W_{17}$-$2C_n$ have been previously reported by us[9] and the nonionic surfactant, $C_{12}EO_6$, is well established.[37] $P_2W_{17}$-

$2C_n$ surfactants have a relatively large headgroup (12-18 Å in length with an area per molecule around 120 $Å^2$),[28] which favours the formation of spherical micelles. These surfactants have been shown to form globular or ellipsoidal micelles in water depending on the tail length. The addition of the nonionic surfactant $C_{12}EO_6$, which tends to form rod-like micelles in water, into the $P_2W_{17}$-$2C_n$ system induces the elongation of the mixed micelles. On addition of $C_{12}EO_6$ to the solution of $P_2W_{17}$-$2C_{12}$, the nonionic surfactant molecules incorporate into the ionic surfactant micelles, leading to a modest increase of the elliptical ratio from 2.9 to 3.8. However, the micelles also grow considerably in size, and aggregation number and the resulting increase in total micelle charge lead to an obvious peak shift in the scattering pattern as the nonionic content increases.

The phase behaviour and the microstructure of ionic and nonionic molecules mixtures have been studied in the literature.[24, 30] Most of them report on the growth of micelles upon addition of nonionic surfactant to charged surfactant molecules in solutions. The shift of the micelle interaction peak has also been reported for SDS/$C_{12}EO_6$ and SDS/ $C_{12}EO_8$ mixtures which have been studied by Penfold[30] *et al*. For SDS/$C_{12}EO_6$ mixtures, the elliptical ratio increased from 1.3 to 2.4 when the $C_{12}EO_6$ mole percent increased from 20% to 90%. Sodium bis(2-ethyl hexyl)sulfosuccinate (AOT), a anionic surfactant which is double-tailed that is similar to $P_2W_{17}$-$2C_n$ surfactants, was also mixed with $C_{12}EO_6$ and shows favourable aggregation.[24] Similarly, more elongated micelles were formed in the nonionic rich mixtures. The differences in interaction type between the AOT/$C_{12}EO_6$ system and our systems cannot be explained in terms of molecular geometry since both of them are double-tailed (although the branched tails in AOT are much shorter than the linear chains in the $P_2W_{17}$-$2C_n$) as monomers. Consequently, the counterion-mediated electrostatic interactions and counterion condensation onto the micelles must play a crucial role in the aggregation of molecules at equilibrium in our systems. As reported in Table 3, there is an increase in the micellar surface charge with the increase of the nonionic surfactant mole fraction. This appears to occur because the $P_2W_{17}$-$2C_n$ molecules ionise more when more nonionic surfactant molecules are inserted into the micelles. This is also suggested by the calculated $Z_p$ values. The modest increase in surface charge observed

for our system is the opposite to the results that have been found in SDS/ $C_{12}EO_8$, SDS/ $C_{12}EO_6$ [30] and sodium bis(2-ethyl hexyl) sulfosuccinate/$C_{12}EO_4$ mixtures,[24] which give a decrease in surface charge with the increase of nonionic surfactant ratio. This may be due to the fact that the $P_2W_{17}$ headgroups bear more ionisable counterions when $C_{12}EO_6$ is mixed into the micelles, than SDS which has only one counterion per molecule. Additional interactions, counterion-mediated electrostatic interactions, which does not usually exist in other systems, may also affect the overall micellar charges.

## Conclusion

The structures and CMC values for mixed surfactant systems consisting of $P_2W_{17}$-$2C_n$ with different tail lengths and $C_{12}EO_8$ at three mixing ratios and two concentrations have been studied. Conductivity and surface tension measurements were applied to measure their CMCs. Based on the experimental CMCs, the interaction parameters for the different mixtures were calculated and found to be positive, which implies an antagonistic interaction between the two components in the mixtures, despite the formation of mixed micelles. Accordingly, the compositions of micelles for various mixtures are predicted using the averaged interaction parameters. The $C_{12}EO_6$ mole fractions in the mixed $P_2W_{17}$-$2C_{12}$/$C_{12}EO_6$ and $P_2W_{17}$-$2C_{14}$/$C_{12}EO_6$ micelles were obtained by SANS modelling and compared with those values calculated using averaged interaction parameters. Small deviations were observed, showing that the interaction parameters predicted values for micellar composition are valid with only a small error. The $C_{12}EO_6$ ratios in $P_2W_{17}$-$2C_{16}$/$C_{12}EO_6$ mixed micelles at three mixing ratios were calculated. The micellar morphology information obtained from SANS modelling allows a phase diagram at two dilute concentrations to be drawn.

The study shows that the $C_{12}EO_6$ and $P_2W_{17}$-$2C_n$ molecules successfully form mixed micelles. The morphology of these mixed micelles depends on the ratio between the two surfactants which shows the potential of these mixed surfactant solutions to control the polyoxometalate content of soft matter templates.

## Acknowledgement

A. Di. thanks University of Bath and China Scholarship Council for supporting her PhD studies. The authors would like to thank the ISIS Neutron and Muon Spallation Source for the award of beam time on beamline LARMOR and LOQ (experiment nos. 1810278 and 1720185) that contributed to the results presented here. The raw SANS data can be found at DOI: 10.5286/ISIS.E.RB1810278 and 10.5286/ISIS.E.RB1720185, while the CMC data and reduced SANS data supporting this paper can be found in the University of Bath Research Data Archive, 2019 DOI: 10.15125/BATH-00XXX. This work benefited from the use of the SasView application, originally developed under NSF Award DMR-0520547. SasView also contains code developed with funding from the EU Horizon 2020 programme under the SINE2020 project Grant 654000.

## Reference

1. J. Lehmann, A. Gaita-Arino, E. Coronado and D. Loss, *Nat. Nanotechnol.*, 2007, **2**, 312.
2. B. Yue, Y. Zhou, J. Xu, Z. Wu, X. Zhang, Y. Zou and S. Jin, *Environmental science & technology*, 2002, **36**, 1325-1329.
3. M. Sadakane and E. Steckhan, *Chem. Rev.*, 1998, **98**, 219-238.
4. X. López, C. Bo and J. M. Poblet, *J. Am. Chem. Soc.*, 2002, **124**, 12574-12582.
5. Y. Han, Y. Xiao, Z. Zhang, B. Liu, P. Zheng, S. He and W. Wang, *Macromolecules*, 2009, **42**, 6543-6548.
6. H. Li, S. Pang, S. Wu, X. Feng, K. Müllen and C. Bubeck, *J. Am. Chem. Soc.*, 2011, **133**, 9423-9429.
7. Y. Kim and S. Shanmugam, *ACS Appl. Mater. Interfaces*, 2013, **5**, 12197-12204.
8. W. Qi and L. Wu, *Polym. Int.*, 2009, **58**, 1217-1225.
9. A. Di, J. Schimitt, M. da Silva, J. Errington and K. Edler, unpublished work.
10. D. Rubingh and K. Mittal, *Solution chemistry of surfactants*, Plenum, New York, 1979.
11. R. Heenan and S. King, *Development of small-angle diffractometer LOQ at the ISIS pulsed neutron source*, Joint Institute for Nuclear Research, Dubna, 1993.
12. S. M. Bennington, *Nucl. Instrum. Methods Phys. Res., Sect. A*, 2009, **600**, 32-34.
13. O. Arnold, J.-C. Bilheux, J. Borreguero, A. Buts, S. I. Campbell, L. Chapon, M. Doucet, N. Draper, R. F. Leal and M. Gigg, *Nucl. Instrum. Methods Phys. Res., Sect. A*, 2014, **764**, 156-166.
14. G. T. Wignall and F. Bates, *J. Appl. Crystallogr.*, 1987, **20**, 28-40.
15. A. Guiner, G. Fournet, C. Walker and K. Yudowitch, *Small-Angle Scattering of X-rays*, John Wiley and Sons, New York, 1955.
16. M. Kotlarchyk and S. H. Chen, *J. Chem. Phys.*, 1983, **79**, 2461-2469.
17. S. Berr, *J. Phys. Chem.*, 1987, **91**, 4760-4765.
18. J.-P. Hansen and J. B. Hayter, *Mol. Phys.*, 1982, **46**, 651-656.
19. H. Pilsl, H. Hoffmann, S. Hofmann, J. Kalus, A. Kencono, P. Lindner and W. Ulbricht, *J. Phys. Chem.*, 1993, **97**, 2745-2754.
20. P. Griffiths, M. Whatton, R. Abbott, W. Kwan, A. Pitt, A. Howe, S. King and R. Heenan, *J. Colloid Interface Sci.*, 1999, **215**, 114-123.
21. K. Srinivasan and R. L. Kay, *J. Chem. Phys.*, 1974, **60**, 3645-3648.
22. D. McDermott, J. Lu, E. Lee, R. Thomas and A. Rennie, *Langmuir*, 1992, **8**, 1204-1210.

23. A. Domínguez, A. Fernández, N. González, E. Iglesias and L. Montenegro, *J. Chem. Educ.*, 1997, **74**, 1227.
24. I. Grillo and J. Penfold, *Langmuir*, 2011, **27**, 7453-7463.
25. M. S. Bakshi, J. Singh, K. Singh and G. Kaur, *Colloids Surf., A*, 2004, **234**, 77-84.
26. P. M. Holland and D. N. Rubingh, *Cationic surfactants: physical chemistry*, Marcel Dekker, New York, 1991.
27. A.-M. Misselyn-Bauduin, A. Thibaut, J. Grandjean, G. Broze and R. Jérôme, *Langmuir*, 2000, **16**, 4430-4435.
28. S. G. Mitchell and M. Jesús, *J. Mater. Chem.*, 2012, **22**, 18091-18100.
29. C. Tanford, *J. Phys. Chem.*, 1974, **78**, 2469-2479.
30. J. Penfold, I. Tucker, R. Thomas, E. Staples and R. Schuermann, *J. Phys. Chem. B*, 2005, **109**, 10760-10770.
31. L. Bocquet, E. Trizac and M. Aubouy, *J. Chem. Phys.*, 2002, **117**, 8138-8152.
32. S. A. Buckingham, C. J. Garvey and G. G. Warr, *J. Phys. Chem.*, 1993, **97**, 10236-10244.
33. N. V. Lebedeva, A. Shahine and B. L. Bales, *J. Phys. Chem. B*, 2005, **109**, 19806-19816.
34. R. Sedev, *Langmuir*, 2001, **17**, 562-564.
35. J. N. Israelachvili, D. J. Mitchell and B. W. Ninham, *J. Chem. Soc. Faraday Trans. II*, 1976, **72**, 1525-1568.
36. R. Nagarajan, *Langmuir*, 2002, **18**, 31-38.
37. J. Gapinski, J. Szymanski, A. Wilk, J. Kohlbrecher, A. Patkowski and R. Hołyst, *Langmuir*, 2010, **26**, 9304-9314.
38. J. H. Clint, *J. Chem. Soc. Faraday Trans. I*, 1975, **71**, 1327-1334.
39. M. Schick, *J. Colloid Sci.*, 1962, **17**, 801-813.
40. L. Hsiao, H. Dunning and P. Lorenz, *J. Phys. Chem.*, 1956, **60**, 657-660.
41. P. Becher, *J. Colloid Sci.*, 1962, **17**, 325-333.
42. T. Joshi, J. Mata and P. Bahadur, *Colloids Surf., A*, 2005, **260**, 209-215.
43. H. Akbaş, M. Boz and A. Dinç, presented in part at the International Conference on Chemical, Environment & Biological Sciences, Kuala Lumpur (Malaysia), 2014.
44. M. S. Sheikh and A. A. Dar, *J. Colloid Interface Sci.*, 2009, **333**, 605-612.
45. P. Yin, D. Li and T. Liu, *Chem. Soc. Rev.*, 2012, **41**, 7368-7383.
46. J. Luo and T. Liu, *Langmuir*, 2019, **35**, 7603-7616.
47. C. Holtzscherer and F. Candau, *J. Colloid Interface Sci.*, 1988, **125**, 97-110.
48. N. Nishikido, *J. Colloid Interface Sci.*, 1977, **60**, 242-251.
49. Y. Nikas, S. Puvvada and D. Blankschtein, *Langmuir*, 1992, **8**, 2680-2689.
50. O. Regev and A. Khan, *J. Colloid Interface Sci.*, 1996, **182**, 95-109.

# Supporting Information

## Mixed micelles of Amphiphilic Polyoxometalate and Hexaethylene Glycol Monododecyl Ether

Andi Di,[1] Julien Schmitt,[1,2] Kun Ma,[3] Marcelo Da Silva,[1] Naomi Elstone,[1] Najet Mahmoudi,[3] Peixun Li,[3] Adam Washington,[3] Zi Wang,[3] R. John Errington,[5] Karen J Edler[1*]

[1]Department of Chemistry, University of Bath, Bath, BA2 7AY, UK

[2]LSFC - Laboratoire de Synthèse et Fonctionnalisation des Céramiques, UMR 3080 CNRS / Saint-Gobain CREE, Saint-Gobain Research Provence, 550 avenue Alphose Jauffret, Cavaillon, France

[3]ISIS Neutron and Muon Source, Science and Technology Facilities Council, Rutherford Appleton Laboratory, Didcot OX11 0QX, UK

[4]Chemistry, School of Natural and Environmental Sciences, Newcastle University, Newcastle upon Tyne, NE1 7RU, UK

SI Table 1. Neutron scattering length density (SLD) of the nonpolar parts of the surfactants.

| | $C_{12}D_{25}$ | $C_{14}D_{29}$ | $C_{12}H_{25}$ | $C_{14}H_{29}$ | $C_{16}H_{33}$ | $C_{18}H_{37}$ |
|---|---|---|---|---|---|---|
| SLD ($Å^{-2}$) | $6.78\times10^{-6}$ | $6.84\times10^{-6}$ | $-0.378\times10^{-6}$ | $-0.367\times10^{-6}$ | $-0.360\times10^{-6}$ | $-0.353\times10^{-6}$ |

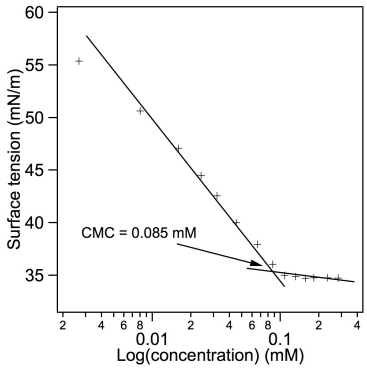


SI Figure 1. Surface tension ($\gamma$) *versus* log (C) plot for pure $C_{12}EO_6$ surfactant at room temperature.

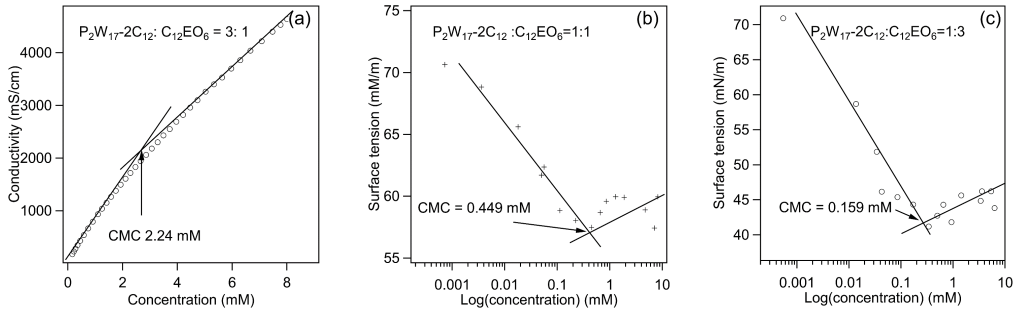


SI Figure 2. (a) Conductivity measurements at molar ratio of $P_2W_{17}$-$2C_{12}$: $C_{12}EO_6$ = 3:1; Surface tension measurements *versus* log (concentration) of aqueous solutions with a composition of (b) $P_2W_{17}$-$2C_{12}$: $C_{12}EO_6$ = 1:1 and (c) $P_2W_{17}$-$2C_{12}$: $C_{12}EO_6$ = 1:3.

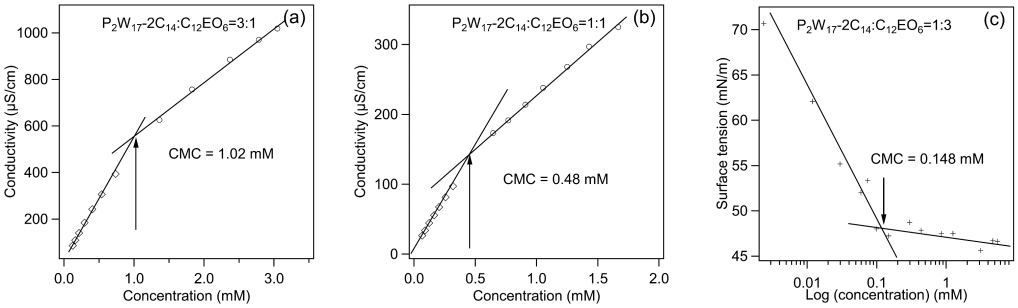


SI Figure 3. Conductivity measurements with concentration of aqueous solutions with a composition of (a) $P_2W_{17}$-$2C_{14}$: $C_{12}EO_6$ = 3:1 and (b) $P_2W_{17}$-$2C_{14}$: $C_{12}EO_6$ = 1:1; (c) Surface tension measurements *versus* log(concentration) of aqueous solutions with a composition of $P_2W_{17}$-$2C_{14}$: $C_{12}EO_6$ = 1:3.

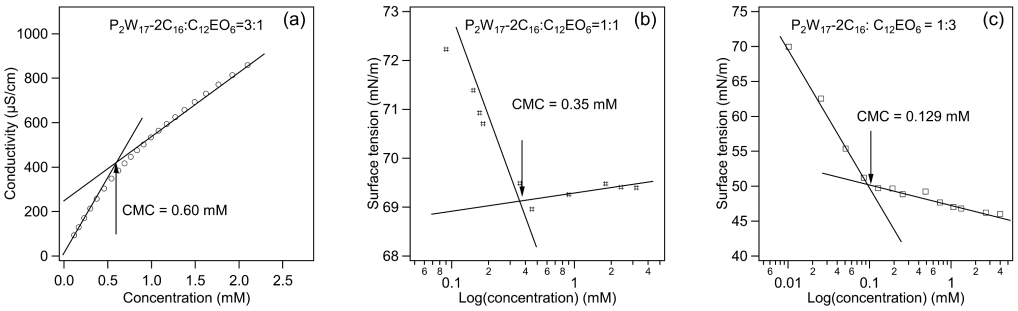


SI Figure 4. (a) Conductivity measurements *versus* concentration of aqueous solutions with a composition of $P_2W_{17}$-$2C_{16}$: $C_{12}EO_6$ = 3:1; Surface tension measurements *versus* log(concentration) of aqueous solutions with a composition of (b) $P_2W_{17}$-$2C_{16}$: $C_{12}EO_6$ = 1:1 and (c) $P_2W_{17}$-$2C_{16}$: $C_{12}EO_6$ = 1:3.

SI Table 2. CMC values of the binary systems at three mixing ratios in water.

| $P_2W_{17}$-2$C_n$:$C_{12}EO_6$ | 1:0 | 3:1 | 1:1 | 1:3 |
|---|---|---|---|---|
| $P_2W_{17}$-2$C_{12}$ (mM) | 4.78 ± 0.08 | 2.24 ± 0.07 | 0.45 ± 0.03 | 0.16 ± 0.03 |
| $P_2W_{17}$-2$C_{14}$ (mM) | 1.63 ± 0.05 | 1.02 ± 0.05 | 0.48 ± 0.04 | 0.15 ± 0.02 |
| $P_2W_{17}$-2$C_{16}$ (mM) | 0.80 ± 0.04 | 0.60 ± 0.06 | 0.35 ± 0.05 | 0.13 ± 0.02 |

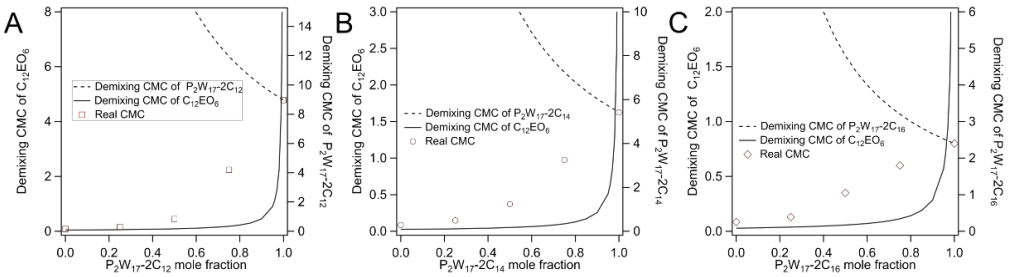


SI Figure 5. Estimated CMC when demixing. The dashed line is the CMC of $P_2W_{17}$-2$C_n$ component and solid line is that of $C_{12}EO_6$. All these results were estimated under extreme conditions: the other component does not form micelles.

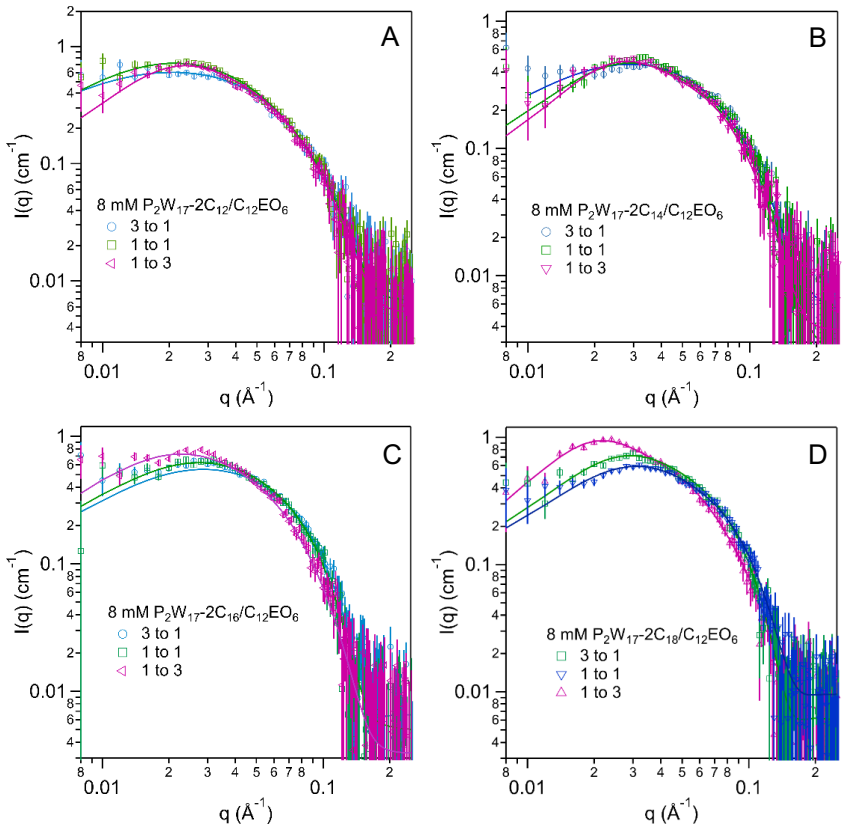


SI Figure 6. SANS data (I(q) versus q) and fits for $P_2W_{17}$-2$C_n$/$C_{12}EO_6$ at 8 mM in 70 mol% $D_2O$ (A) $P_2W_{17}$-2$C_{12}$/$C_{12}EO_6$ (B) $P_2W_{17}$-2$C_{14}$/$C_{12}EO_6$ (C) $P_2W_{17}$-2$C_{16}$/$C_{12}EO_6$ (D) $P_2W_{17}$-2$C_{18}$/$C_{12}EO_6$ on a log-log scale.

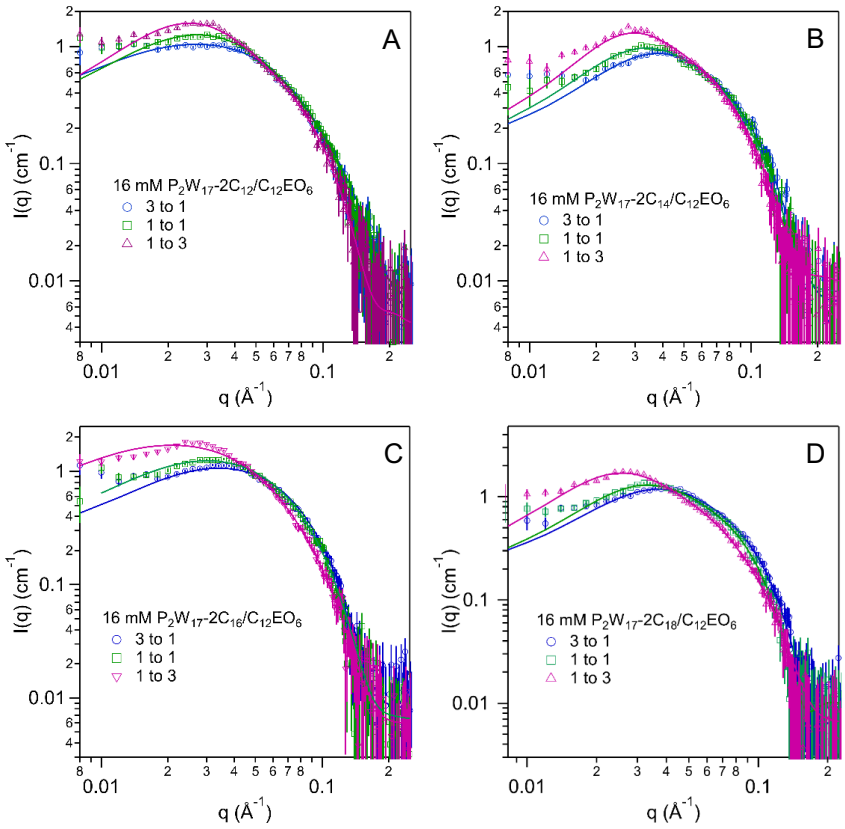


SI Figure 7. SANS data (I(q) versus q) and fits for $P_2W_{17}$-2$C_n$/$C_{12}EO_6$ at 16 mM in 70 mol% $D_2O$ (A) $P_2W_{17}$-2$C_{12}$/$C_{12}EO_6$ (B) $P_2W_{17}$-2$C_{14}$/$C_{12}EO_6$ (C) $P_2W_{17}$-2$C_{16}$/$C_{12}EO_6$ (D) $P_2W_{17}$-2$C_{18}$/$C_{12}EO_6$ on a log-log scale.

SI Table 3. The calculated area per molecule, $A_{cor}$, using corrected surfactant mole fractions.

| $P_2W_{17}$-2$C_n$:$C_{12}EO_6$ | $A_{cor}$ (Å$^2$) (n=12) | $A_{cor}$ (Å$^2$) (n=14) | $A_{cor}$ (Å$^2$) (n=16) |
|---|---|---|---|
| 8 mM | | | |
| 3:1 | 95 ± 5 | 105 ± 5 | 106 ± 5 |
| 1:1 | 68 ± 4 | 85 ± 4 | 85 ± 4 |
| 1:3 | 56 ± 4 | 64 ± 4 | 67 ± 4 |
| 16 mM | | | |
| 3:1 | 102 ± 5 | 104 ± 5 | 106 ± 5 |
| 1:1 | 76 ± 4 | 81 ± 4 | 87 ± 4 |
| 1:3 | 56 ± 4 | 62 ± 4 | 69 ± 4 |

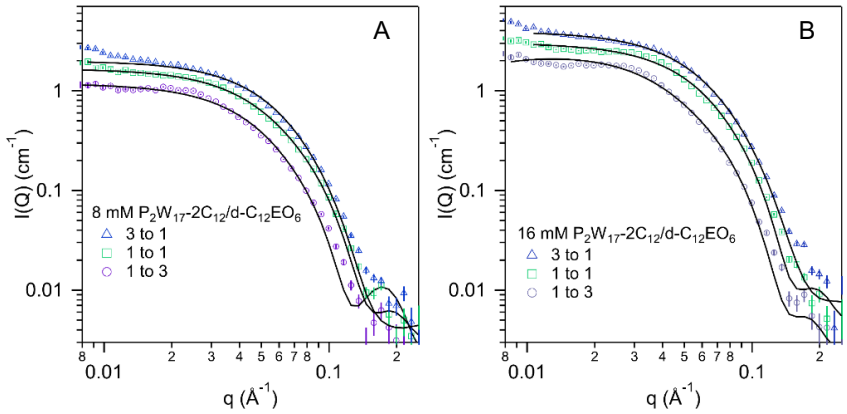


SI Figure 8. SANS data (I(q) versus q) and fits for $P_2W_{17}$-2$C_{12}$/d-$C_{12}EO_6$ at (A) 8 mM and (B) 16 mM on a log-log scale.

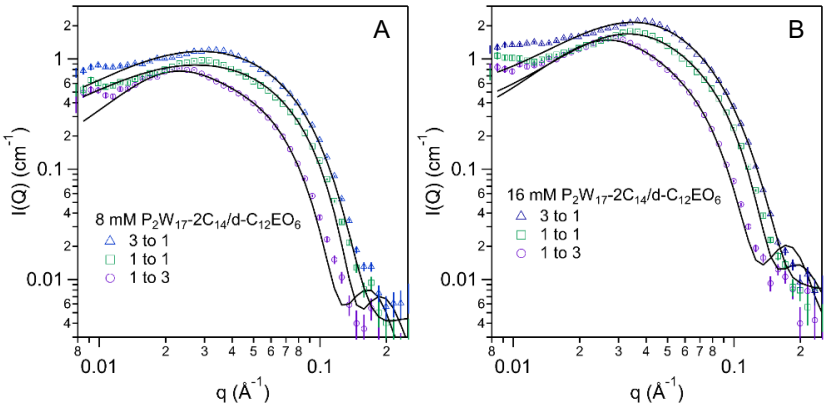


SI Figure 9. SANS data (I(q) versus q) and fits for $P_2W_{17}$-2$C_{14}$/d-$C_{12}EO_6$ at (A) 8 mM and (B) 16 mM on a log-log scale.

## 5.2 Conclusion

The chapter studied the mixture of POM-2$C_n$ and $C_{12}EO_6$ with three mixng ratios, C[POM-2$C_n$]:C[$C_{12}EO_6$] = 3:1, 1:1 and 1:3 at a total concentration of 8 and 16 mM. The mixing behaviour of the two molecules in water are unfavourable indicated by the measured CMCs of the mixtures. The interaction parameters ($\beta$) between the two molecules are calculated using the experimental CMC values of the mixtures, pure POM-2$C_n$ and pure $C_{12}EO_6$ surfactants. The $\beta$ values calculated from mixtures with different mixing ratios are constant when considering the errors. The unfavrourable interaction becomes lower when the tail length of POM-2$C_n$ becomes longer. The strong unfavourable interactions between POM-2$C_{12}$ and $C_{12}EO_6$ compared to other systems may be due to the close packing of the two surfactants since they have the same hydrophobic tail length. And the interaction becomes smaller when the difference of the tail length between the two molecules becomes larger.

The mixed micelles formed in water are studied using SANS. The form factor used for fitting the SANS patterns are core-shell spherical/ellipsoidal models. The comparison of the micelle morphology derived from the shape-dependent fitting between different mixing ratios indicates that the insertion of the $C_{12}EO_6$ molecules induces the elongation of the micelles. Interactions between the micelles are modelled using a rescaled Hayter Penfold Mean Spherical Approximation structure factor, this gives the surface charge of the micelles. Therefore, the charge that each POM-2$C_n$ molecule in the micelles carries is calculated. As the ratio of the $C_{12}EO_6$ in the solution increases the POM-2$C_n$ molecules in the mixed micelles are able to dissociate more counterions.

As it shows an unfavourable mixing, the mole fractions of the surfactant in the mixture is different from those in the mix micelles. Therefore, the compositions of the mixed micelles of POM-2$C_{12}$/$C_{12}EO_6$ and POM-2$C_{14}$/$C_{12}EO_6$ systems are calculated using the interaction parameters and are investigated through deuterium-labelling combined with SANS technique. Results obtained from the two methods are much closer to agreement. The compositions of micelles in POM-2$C_{16}$/$C_{12}EO_6$ system are also estimated using interaction parameters.

The interactions between the two molecules are discussed to be a combination of different forces and are related to the configuration of the headgroup of $C_{12}EO_6$. The unfavourable iteractions are concluded to have a close relation to the counterion-mediated interactions that occur between the POM headgroups. This study has suggested the formation of micelles in water by POM-2$C_n$ and $C_{12}EO_6$ surfactant molecules. The mixing ratio of the mixed micelles can be tuned and therefore can be used as templates to tun the POM content in the hybrid materials.

In the next chapter, a study of surfactant mixture of POM-2$C_n$ and $C_{12}EO_8$ has been conducted. The aim of this study is to compare with the POM-2$C_n$/$C_{12}EO_6$ mixtures. These two surfactant are chosen is because they have the same hydrophobic tail length and the same type of headgroup (polyethylene oxide) but different repetition of ethylene oxide group. These mixtures are studied with two total surfactant concentrations (8 and 16 mM), same as concentrations studied in POM-2$C_n$/$C_{12}EO_6$ mixtures. The mixed micelles are also studied using SANS. Apart from the study of the mixed systems, the effect of adding KCl on the change of micellar morphologies are also studied. The salt effect on both the pure surfactant and mixed surfactant systems are studied. Additionally, higher concentration (133 mM) is studied for these mixtures. The small

angle X-ray scattering (SAXS) data suggest that liquid crytal phase may form at 133 mM in water. The nonionic surfactant rich mixtures are used to template silica. The SAXS pattern of the prepared silica materials has two broad peaks which may suggest a lamellar structure.

# 6

# Amphiphilic Polyoxometalate Mixtures with Octaethylene Glycol Dodecyl Ether and Salt Effect on the Micellar Systems.

## 6.1 Introduction

As discussed in Chapter 5, the mixing of POM-2$C_n$ and $C_{12}EO_6$ in water is unfavourable. The interactions of the mixed POM-2$C_n$/$C_{12}EO_6$ systems have a close relationship with the counterion mediated interactions between the POM headgroups. The modelling of SANS data indicates that the insertion of the $C_{12}EO_6$ molecules between the POM-2$C_n$ molecules in the micelles elongate the micelles along one axis of the micelles with the other axis restricted by the tail length of the surfactant molecules. The introduction of the nonionic surfactant into the pure POM-2$C_n$ systems are of vital importance in terms of cost-effective applications. For example, the tunability of the POM amount in the POM-containing hybrid materials prepared using a mixed-surfactant system as a template to achieve the best efficiency by using the least amount of POM-2$C_n$ surfactants, which are relatively expensive and require a long process to synthesise.

To compare to the mixtures of POM-2$C_n$ and $C_{12}EO_6$ studied in Chapter 4, this chapter studies the mixtures of POM-2$C_n$ and $C_{12}EO_8$ surfactants. The $C_{12}EO_8$ molecule bears a larger and more water-soluble hydrophilic headgroup but the same hydrophobic tail compared to $C_{12}EO_6$ molecule. The mixed micelles formed in the solution of mixed surfactants with a mole ratio at 3:1, 1:1 or 1:3 at a total concentration of 8 or 16 mM are studied using SANS. The best fits of the SANS data suggest these mixtures form either spherical or ellipsoidal micelles composed of POM-2$C_n$ and $C_{12}EO_8$ molecules.

The comparison of the mixed micelles form in POM-2$C_n$/$C_{12}EO_6$ and POM-2$C_n$/$C_{12}EO_8$ systems shows that the polyethylene oxide surfactant ($C_{12}EO_m$) with a larger hydrophilic headgroup is less effective in inducing the elongation of the mixed micelles. The effect of adding KCl on these mixed micelles is of interest because of the available high charge of the POM-2$C_n$ (hexavalent) molecules. In this chapter, the effect of KCl on both the pure POM-2$C_n$ micelles and mixed POM-2$C_n$/$C_{12}EO_8$ micelles formed in their aqueous solutions are studied using SANS in this chapter. The concentration of KCl is varied between 0.10 and 0.75 M.

Studies at the low concentrations (8 and 16 mM) have suggested the formation of micelles in the mixed surfactant systems. Therefore, a total surfactant concentration of 133 mM is also studied for POM-2$C_n$/$C_{12}EO_8$ (n = 12, 14 and 16) mixtures to explore their potential to form liquid

crystal phases (LCPs) in water at high concentrations. The LCPs formed may find applications in templating POM-functionalised materials with long-range ordering. The SAXS patterns of the mixtures at the concentration of 133 mM suggest the formation of different types of LCPs when the mixing ratio of the two surfactants is different. The lamellar phase formed in the 133 mM POM-2$C_n$/$C_{12}EO_8$ mixture with 1:3 mole ratio was used to template porous silica with long-range ordering. The prepared silica material was measured using SAXS to prove the concept of synthesising POM-functionalised silica with long-range ordering using the mixed POM-2$C_{12}$/$C_{12}EO_8$ systems.

| This declaration concerns the article entitled: | | | | | | | | | |
|---|---|---|---|---|---|---|---|---|---|
| Amphiphilic Polyoxometalate Mixtures with Octaethylene Glycol Dodecyl Ether and Salt Effect on the Micellar Systems | | | | | | | | | |
| **Publication status (tick one)** | | | | | | | | | |
| **draft manuscript** | ✓ | **Submitted** | | **In review** | | **Accepted** | | **Published** | |
| **Publication details** | | | | | | | | | |
| **Candidate's contribution to the paper** | The candidate contributed to/ considerably contributed to/predominantly executed the…<br>**Formulation of ideas:**<br>The initial idea was formulated by KJE and AD, and the proposals for beamtime were developed and written by KJE and AD (contribution 80 %).<br><br>**Design of methodology:**<br>All the measurements were designed by AD with exception of the set-up of small angle scattering done by NM at ISIS, with followed measurements carried out by AD. AD contribution 90%.<br><br>**Experimental work:**<br>Part of the preliminary data were collected by AD, JS, MAS and NM. AD contributed to the data analysis and the final experimental work included in the manuscript (AD contribution 70%).<br><br>**Presentation of data in journal format:**<br>The first draft was written by AD. Subsequent draft was reworked by AD following the feedback from KJE, JS and ZH. (AD contribution 85%) | | | | | | | | |
| **Statement from Candidate** | This paper reports on original research I conducted during the period of my Higher Degree by Research candidature. | | | | | | | | |
| **Signed** | Andi D. | | | **Date** | 26/09/2019 | | | | |

# Amphiphilic Polyoxometalate Mixtures with Octaethylene Glycol Dodecyl Ether and Salt Effect on the Micellar Systems

Andi Di,[1] Julien Schmitt,[1,2] Zakir Hossain,[1] Adam Washington,[3] R. John Errington,[4] Karen J Edler[1*]

[1]Department of Chemistry, University of Bath, Claverton Down, Bath, BA2 7AY, UK

[2]LSFC – Laboratoire de Synthèse et Fonctionnalisation des Céramiques, UMR 3080 CNRS / Saint-Gobain CREE, Saint-Gobain Research Provence, 550 avenue Alphonse Jauffret, Cavaillon, France

[3]ISIS Neutron and Muon Source, Science and Technology Facilities Council, Rutherford Appleton Laboratory, Didcot OX11 0QX, UK

[4]School of Chemistry, Newcastle University upon tyne, Newcastle, NE1 7RU, UK

## Abstract

Micellar solutions of the mixture of $K_6[P_2W_{17}O_{61}\{OSi_2(C_nH_{2n+1})_2\}]$ (POM-2$C_n$, n = 12, 14 and 16) and octaethylene glycol dodecyl ether ($C_{12}EO_8$) surfactant with three compositions were studied using small angle neutron scattering (SANS). It was found that the morphology of the mixed micelles is mainly dominated by the ionic component. Measurements of pure POM-2$C_n$ and mixed POM-2$C_n$/$C_{12}EO_8$ micelles in the presence of KCl for different equimolar surfactant to salt concentrations were also investigated. It was found that the addition of $K^+$ ion induces micellar growth along one axis for the pure POM-2$C_n$ systems, while the influence of KCl is relatively more pronounced in the POM-2$C_n$/$C_{12}EO_8$ (n = 12 or 14) mixtures. These mixed micelles are also potentially useful to template POM-encapsulated materials.

## 1. Introduction

The study of mixed surfactants systems is of great interest for both theoretical and practical reasons as they behave non-ideally when mixed and hence often provide changes in performance compared to single-surfactant systems.[1-3] In mixed surfactant systems, the molecular structure of the surfactant (tails and headgroups),[4, 5] the additives (such as salt)[6] and the experimental variables (concentration, pH and temperature)[4, 7, 8] can be manipulated to change the intra and intermicellar forces and therefore change the micellar behaviour. Specifically, reduction of the electrostatic repulsion between the ionic surfactant headgroups, induced by the addition of inorganic salts, is a key factor that influences the morphology of

aggregates that contain ionic surfactants. For traditional single-chain ionic surfactants, such as sodium dodecyl sulfate (SDS) and alkyl trimethylammonium bromides ($C_n$TAB) surfactants, adding salt causes a micellar shape transition from globular to rod-like or wormlike.[9-12] There are at least two factors responsible for causing such a transition of micellar shape. One is the change in the electrostatic repulsion between ionic headgroups induced by the counterions added with the introduction of salt,[10, 12, 13] and the other is the hydrophobic interaction between surfactant molecules or ions caused by the change in the hydrogen-bonded structure of water.[14]

Previously, we have reported the synthesis of surfactants with phosphotungstate units as the headgroup - $K_6[P_2W_{17}Si_2O_{61}\{O(C_nH_{2n+1})_2\}]$, POM-2$C_n$, where n = 12, 14 and 16 - and their aggregation behaviour in water.[15] These surfactants ionize in aqueous solution and form anionic micelles with $K^+$ as counterions binding at the micellar surfaces. We have also studied their mixtures with hexaethylene glycol dodecyl ether ($C_{12}EO_6$) and found the insertion of the $C_{12}EO_6$ surfactant molecules in between the POM-2$C_n$ molecules in the micelles induces elongation of the micelles.[16]

Herein, we have used SANS to determine the structure of the micelles formed by mixed POM-2$C_n$ and $C_{12}EO_8$ surfactants to compare with the previously reported mixtures with $C_{12}EO_6$ that bears a smaller headgroup to probe the significance of headgroup interactions on the self-assembly behaviour.[15, 16] These systems were also studied in the presence of KCl to investigate its effect on the mixed micelles. The pure POM-2$C_n$ surfactants in KCl aqueous solutions were studied at the same surfactant concentration for comparison. By comparing the sizes of the micelles from the SANS modelling results, we relate the aggregation behaviour to the surfactant mixing ratio and the addition of KCl and discuss the effects of nonionic surfactant headgroup size, by comparison with previously reported POM-2$C_n$/$C_{12}EO_6$ mixtures. These mixed micelles are also useful to encapsulate the POM units and control the POM content in the as-prepared hybrid materials if used as templates for synthesising inorganic materials. Therefore, a high concentration (133 mM) was studied and was found to

form different liquid crystal phases when the mixing mole ratio is different, and the lamellar LCP phase formed by 1:3 POM-2$C_{12}$/$C_{12}EO_8$ mixture was applied to functionalize silica.

## 2. Experimental Section

**Materials.** Octaethylene glycol dodecyl ether ($C_{12}EO_8$) was supplied by Nikko Chemical Company (Tokyo, Japan). $Na_2WO_4 \cdot 2H_2O$ (purity > 99%), phosphoric acid (85 wt. % in water solution), $NH_4Cl$ (purity > 99.5%), KCl (laboratory reagent grade), trichlorododecylsilane ($C_{12}H_{25}SiCl_3$, purity > 95%), trichloroloctadecylsilane ($C_{18}H_{37}SiCl_3$, purity > 90%), $KHCO_3$ (purity > 99.7%) and $D_2O$ (99.9 atom% D) were purchased from Sigma Aldrich. Tetradecyltrichlorosilane ($C_{14}H_{29}SiCl_3$, purity 98%) and hexadecyltrichlorosilane ($C_{16}H_{33}SiCl_3$, purity 98%) and were purchased from Fluorochem. All the chemicals were used as supplied. 70 mol% $D_2O$ in $H_2O$ solution was prepared using Milli Q water (18.2 MΩ·cm) was obtained from an ELGA PURELAB flex water purification system.

**SANS/SAXS experiments.** SANS measurements were performed on LARMOR diffractometer[17] at the ISIS Spallation Neutron Source, Oxfordshire, UK. The samples for SANS experiments were prepared by dissolving surfactants in $D_2O$ or 70 mol% $D_2O$. The use of $D_2O$ and 70 mol% $D_2O$ as solvents to substitute $H_2O$ allows better contrast in neutron scattering experiments.

SANS measurements were carried out on micellar solutions of POM-2$C_n$ in the presence of varying concentrations (0 - 0.75 M) of KCl and mixed POM-2$C_n$/$C_{12}EO_8$ micellar solutions at three mixing mole ratios (3:1, 1:1 and 1:3) in the presence and absence of 0.25 M KCl. Samples were held in quartz cells of 1 mm thickness. The temperature was kept constant at 25 °C for all measurements.

The raw data were corrected of the background from the solvent, sample cell and other sources using a standard workflow in the Mantid software package.[18] Scattering data were normalised against the scattering from a partially-deuterated polystyrene blend of known molecular weight to put them on an absolute scale,[19] so *I(q)* equals the differential scattering

cross-section $d\Sigma/d\Omega\ (q)$. The output data was absolute scattered intensity, *I(q)* in $cm^{-1}$, versus the momentum transfer, *q* in $Å^{-1}$.

SAXS measurements were conducted on a Nano-inXider SAXS/WAXS system from Xenocs. Samples were prepared by dissolving the surfactant powder in $H_2O$. Surfactant solutions were sealed in glass capillaries that were then placed on the sample holder prior to the measurements. The background from the capillary and the solvent ($H_2O$) was measured and was subtracted from the obtained SAXS patterns.

Data from all samples measured were labelled using the molar ratio of the two surfactants X ≡ [POM-2$C_n$]/[$C_{12}EO_8$] = 3:1, 1:1 and 1:3 and the overall surfactant concentrations [SF] ≡ [POM-2$C_n$] + [$C_{12}EO_6$] set at 8 and 16 mM in aqueous solutions. The corresponding mole fractions of POM-2$C_n$ are 0.75, 0.5 and 0.25.

**Silica preparation.** The silica was prepared by adding 2 grams of tetramethoxysilicate into 133 mM POM-2$C_{12}$/$C_{12}EO_8$ solution in HCl (pH = 2). Methanol was removed by vacuum. The resulting solution was sealed and placed at room temperature until solidified. The obtained solid was refluxed in ethanol for 4 hrs followed by calcination at 500 °C for 4 hrs.

**SANS/SAXS data analysis.**

**Guinier analysis.** The Guinier approximation was used to determine the radius of gyration ($R_g$) of micelles without taking the shape of the micelles into consideration. This method allows the estimation of the sizes of the aggregates by analysing the data within the intermediate q range. The data were plotted as *ln(I(q)) versus* $q^2$. The $R_g$ values were obtained by fitting the low angle data to the form of the equation given below:

$$\ln\big(I(q)\big) = \ln\big(I(0)\big) - \frac{R_g^2}{3}\,q^2 \qquad (1)$$

where *I(q)* is the scattering intensity and *q* is the momentum transfer.

**Shape dependence analysis.** To provide better information about the micellar structure, the SANS patterns were fitted to shape-dependent models. The SANS data for the same sample at two contrasts ($D_2O$ and 70 mol% $D_2O$) were fitted simultaneously using Sasview (version 4.2.1) in order to better constrain the fits using contrast variation. Data fitting was done using

least-square fitting procedures, minimising $\chi^2 = \sum_{i=1}^{N} \left(\frac{I_{exp}(q_i) - I_{theo}(q_i)}{\sigma_i}\right)^2$, with $I_{exp}(q_i)$ the intensity found experimentally at the q vector qi, $I_{theo}(q_i)$ the intensity from the fit and $\sigma_i$ the uncertainty on $I_{exp}(q_i)$.

For the systems that were studied in this work, either a core-shell sphere model[20] or a core-shell ellipsoid model[21, 22] was applied in the modelling. The core-shell sphere model provides the form factor for a spherical particle of a radius (R) with a shell thickness (t).[20] The core-shell ellipsoid model describes an ellipsoidal particle with a minimum radius ($R_{min}$) and a core ellipticity (ε , $R_{max}/R_{min}$ the maximum radius of the core radius divided by the minimum radius of the core) and a shell thickness (t).[23, 24] In both models, the core contains predominantly the hydrocarbon chains, and the shell is composed of the hydrophilic headgroups of the surfactant molecules with associated water molecules and counterions.

The rescaled mean spherical approximation (RMSA)[25] was used to parameterise the intermicellar interactions and was applied when an obvious interaction peak is seen in the SANS patterns. Data collected from systems in the presence of KCl did not require a structure factor due to charge screening of interactions between the micelles at this high salt concentration. The aggregation number was calculated by the relationship $N_{agg} = 4\pi R_{max} R_{min}^2 / v$, where $v$ is the surfactant tail volume estimated using the Tanford equation.[26]

The SAXS data in this work were also fitted using either the core-shell model or core-shell ellipsoidal model. A polydispersity in R and $R_{min}$ using a Schultz size distribution is included for core-shell sphere and ellipsoid model, respectively.

## 3. Results and discussion

**POM-2$C_n$/$C_{12}EO_8$ (n = 12, 14 and 16) binary systems.** $C_{12}EO_8$ forms spherical micelles with a 16 ± 1 Å core radius and a 17 ± 1 Å shell thickness in water at concentrations of 8 mM and 16 mM, indicated by the fit of the SANS data (SI Figure 1, page 160), which is consistent with the data from the literature.[27] The aggregation behaviour of the pure POM-2$C_n$ systems

studied previously suggested the formation of less elongated micelles with longer hydrocarbon chains.[15] SANS data from POM-2$C_n$/$C_{12}EO_8$ (n = 12, 14 or 16) mixtures were fitted (see the SANS patterns and fits in Figure 1) and the related micellar parameters are listed in Table 1 for n = 12 and 14, fitted using the core-shell ellipsoid model and Table 2 for n = 16 fitted using the core-shell sphere model. It is clearly observed that the fitted volume fraction decreases with increased $C_{12}EO_8$ mole fraction in a given system, indicating a higher volume fraction of micelles in the solution, which may be due to the smaller volume that $C_{12}EO_8$ molecules have compared to that of POM-2$C_n$ molecules. Additionally, higher $C_{12}EO_8$ mole fraction induces the formation of larger aggregates, reflected as an increase in the aggregation number. These facts indicate that with increased nonionic surfactant mole fraction, less but more elongated micelles are formed. The similar phenomenon was also observed in the SDS/$C_{12}EO_3$ systems[28] and sodium dioxyethylene monododecyl sulfate/$C_{12}EO_8$ systems[29] where the aggregation number of the mixed micelles increases upon addition of the nonionic component.

In the POM-2$C_{12}$/$C_{12}EO_8$ system where both components have the same hydrophobic tail length, SANS data analysis evidences that ellipsoidal micelles are formed in aqueous solutions for the three mixing ratios studied (Figure 1A, D for $D_2O$ contrast and SI Figure 2 (page 160) for 70 mol% $D_2O$ contrast, fitted parameters are listed in Table 1). This indicates that the micellar geometry is dominated by the POM-2$C_{12}$ surfactant which forms ellipsoidal micelles in water due to the lower micellar surface charge despite the large apparent headgroup size.[15] The ellipticity value (ε) increases slightly with increasing total surfactant concentration and $C_{12}EO_8$ mole fraction. Higher concentration and the higher nonionic composition both lead to a closer pack (the equilibrium surface area, $a_0$) which is another way increase the packing parameter ($p = v/a_0 l_c$), consequently cause the formation of larger aggregates.

According to the fits of the SANS data (Figure 1B, E for $D_2O$ contrast, SI Figure 3 for 70 mol% $D_2O$ contrast at page 161), POM-2$C_{14}$/$C_{12}EO_8$ systems at 8 mM form spherical micelles when the mixture is ionic surfactant-rich, but form ellipsoidal micelles at the other two mixing ratios.

When the total surfactant concentration increases to 16 mM, a broad peak emerged at around q=0.045 $Å^{-1}$, which suggests the appearance of micellar repulsion. The micelles formed are also ellipsoidal (parameters listed in Table 1). The POM-$2C_{14}$ micelles in water are less elongated than the ones formed by POM-$2C_{12}$ (see Table 3). Similarly, the ellipticity of the POM-$2C_{14}$/$C_{12}EO_8$ micelles is less than half of the one for POM-$2C_{12}$/$C_{12}EO_8$ solutions at 16 mM and with the same mixing ratio and total surfactant concentration.

Table 1. Fitted micellar parameters[a] from SANS analysis of POM-$2C_n$/$C_{12}EO_8$ (with n = 12 and 14) solutions with three mole ratios using the core-shell ellipsoid model.

| POM-$2C_n$/$C_{12}EO_8$ | $R_{min}$(Å) (± 1) | ε (± 0.2) | Shell-SLD (± 0.2) (×$10^{-6}$ $Å^{-2}$) | t (Å)(± 1) | $N_{agg}$ (± 5) | φ (± 0.002) |
|---|---|---|---|---|---|---|
| | 8 mM POM-$2C_{12}$/$C_{12}EO_8$ | | | | | |
| 1:3 | 15 | 3.9 | 4.0 | 17 | 126 | 0.003 |
| 1:1 | 16 | 3.4 | 4.8 | 15 | 111 | 0.007 |
| 3:1 | 17 | 3.2 | 5.1 | 19 | 107 | 0.013 |
| | 16 mM POM-$2C_{12}$/$C_{12}EO_8$ | | | | | |
| 1:3 | 13 | 4.7 | 3.2 | 15 | 98 | 0.005 |
| 1:1 | 13 | 4.4 | 5.0 | 19 | 77 | 0.024 |
| 3:1 | 13 | 3.9 | 5.3 | 20 | 59 | 0.040 |
| | 8 mM POM-$2C_{14}$/$C_{12}EO_8$ | | | | | |
| 1:3 | 15 | 1.7 | 4.0 | 15 | 75 | 0.004 |
| 1:1 | 15 | 1.3 | 4.3 | 15 | 46 | 0.008 |
| 3:1 | 17 | 1.0 | 4.5 | 15 | 30 | 0.013 |
| | 16 mM POM-$2C_{14}$/$C_{12}EO_8$ | | | | | |
| 1:3 | 16 | 1.9 | 3.8 | 12 | 70 | 0.006 |
| 1:1 | 16 | 1.7 | 4.9 | 15 | 53 | 0.018 |
| 3:1 | 15 | 1.5 | 5.1 | 16 | 31 | 0.031 |

[a] $R_{min}$, the minimum radius of the core; $R_{max}$, the maximum radius of the core; ε, $R_{max}/R_{min}$ (ellipticity); φ, volume fraction; SLD, neutron scattering length density; t, shell thickness.

However, the SANS data from POM-$2C_{16}$/$C_{12}EO_8$ aqueous solutions were well described by the core-shell sphere model (Figure 1 C and F), with the fit parameters listed in Table 2. As previously reported, the POM-$2C_{16}$ form spherical micelles in water due to the larger equilibrium surface area caused by the higher surface charge compared to those with shorter hydrocarbon chains.[15] More counterions ionize from the POM-$2C_{16}$ molecules in the mixed micelles when $C_{12}EO_8$ molecules are added. In a traditional system, the addition of nonionic molecules shields the repulsion between anionic POM-$2C_{16}$ molecules and causes one dimensional growth of micelles,[28, 30, 31] this effect is less effective due to its competition with the counterion-mediated attractive forces occurs between POM headgroups.[32, 33] At different

concentrations, 8 mM and 16 mM, the morphology of the micelles remains constant while the volume fraction doubles. At a fixed total surfactant concentration, similar to the mixtures with POM-2$C_{12}$ and POM-2$C_{14}$, the fitted volume fraction becomes larger, while the SLD of the shell also increases, when the mixtures compose more POM-2$C_{16}$ molecules compared to $C_{12}EO_8$.

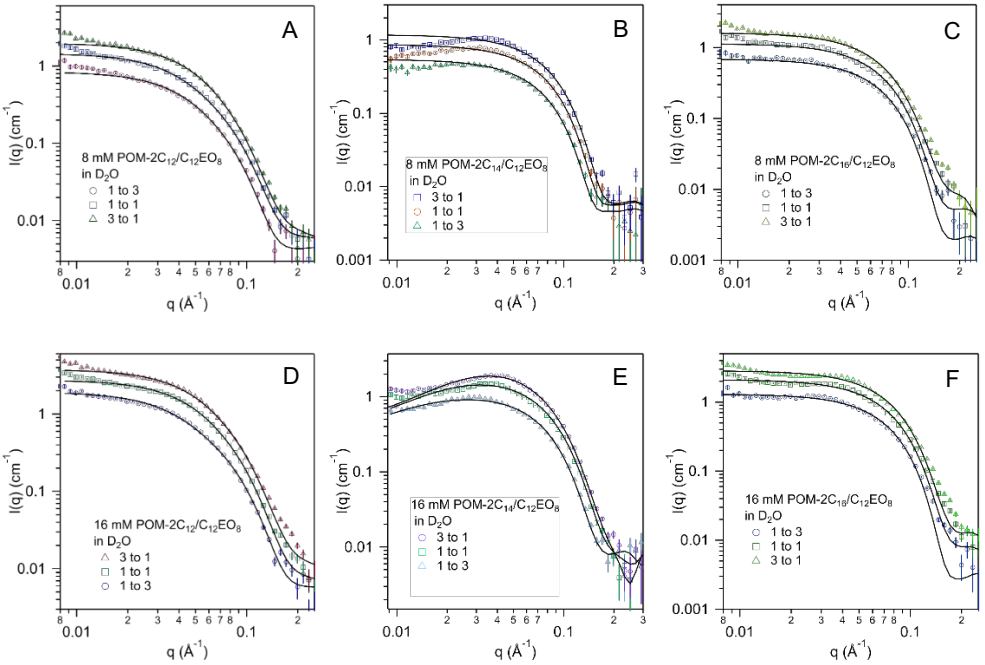


Figure 1. SANS patterns of (A) 8 mM POM-2$C_{12}$/$C_{12}EO_8$, (B) 8 mM POM-2$C_{14}$/$C_{12}EO_8$, (C) 8 mM POM-2$C_{16}$/$C_{12}EO_8$, (D) 16 mM POM-2$C_{16}$/$C_{12}EO_8$, (E) 16 mM POM-2$C_{14}$/$C_{12}EO_8$ and (F) 16 mM POM-2$C_{16}$/$C_{12}EO_8$ in $D_2O$. Fits are given as black lines.

POM-2$C_n$/$C_{12}EO_8$ (n = 12 and 14) systems form ellipsoidal aggregates in water, similarly to POM-2$C_n$ systems (n= 12 and 14), with a less elongated behaviour with increasing value of n. Additionally, both POM-2$C_{16}$/$C_{12}EO_8$ and POM-2$C_{16}$ systems form spheres.[15] Therefore, the morphologies of POM-2$C_n$/$C_{12}EO_8$ systems, as discussed above, are dominated by the ionic component.

The POM-2$C_{12}$/$C_{12}EO_6$ systems experience an increase in micellar ellipticity by 50% when the mole fraction of $C_{12}EO_6$ increased from 0.25 to 0.75,[16] while that of the POM-2$C_{12}$/$C_{12}EO_8$ systems is around 20% when the $C_{12}EO_8$ mole fraction change from 0.25 to 0.75. Therefore,

the extent of influencing the micellar size has been reported to drop with a large polyoxyethylene moiety.[28] This may be explained in terms of the solubility of the nonionic part in the mixture. When $C_{12}EO_6$ molecules with a smaller and so less soluble headgroup tend to solubilize in the inner core region, then induce a micellar growth. Longer oxyethylene chains stabilize itself in the aqueous solution, i.e. in the micelle shells, rather than in the hydrophobic core.

Table 2. Micellar parameters[b] from SANS analysis of POM-2$C_{16}$/$C_{12}EO_8$ solutions with different mixing ratios using core-shell sphere model.

| POM-2$C_{16}$/$C_{12}EO_8$ | R (Å) (± 1) | Shell-SLD (± 0.2) (×$10^{-6}$ Å$^{-2}$) | t (Å) (± 1) | $N_{agg}$ (± 5) | φ (± 0.002) |
|---|---|---|---|---|---|
| | 16 mM POM-2$C_{16}$/$C_{12}EO_8$ | | | | |
| 1:3 | 18 | 4.3 | 16 | 50 | 0.010 |
| 1:1 | 18 | 4.8 | 17 | 40 | 0.022 |
| 3:1 | 17 | 4.9 | 17 | 27 | 0.038 |
| | 8.0 mM POM-2$C_{16}$/$C_{12}EO_8$ | | | | |
| 1:3 | 19 | 4.5 | 17 | 58 | 0.005 |
| 1:1 | 19 | 4.8 | 18 | 45 | 0.011 |
| 3:1 | 18 | 5.2 | 20 | 32 | 0.022 |

[b] R, the core radius of spherical micelles; φ, volume fraction; SLD, neutron scattering length density; t, shell thickness.

### Salt effect on pure POM-2$C_n$ system.

Salt effect on both pure POM-2$C_n$ and mixed POM-2$C_n$/$C_{12}EO_8$ micelles were investigated, using KCl. The POM-2$C_n$ surfactants have $K^+$ counterions, so the addition of KCl does not alter the nature of the counterions present, but only their total concentration. Figure 2 shows the SANS data from 16 mM POM-2$C_n$ (n= 12, 14 and 16) $D_2O$ solutions in the presence of different concentrations of KCl. The corresponding SANS patterns obtained in 70 mol% $D_2O$ solutions are given in SI Figure 4 (page 161). The micellar parameters of these systems derived from the fitting are given in Table 3.

The KCl concentration in 16 mM POM-2$C_n$ systems was progressively increased from 0.00 M to 0.75 M. For n = 12, with increasing concentration of KCl up to 0.5 M, the micelles become more elongated, as reflected in the increase of the ellipticity listed in Table 3. $R_{min}$ is restricted by the hydrophobic tail length. This occurs to avoid any empty space or water penetration inside the hydrophobic core which is energetically unfavourable.[34, 35] Similarly, the POM-2$C_{14}$

and POM-2$C_{16}$ micellar solution also experienced a growth in micellar size upon addition of KCl, with a change from spherical micelles to ellipsoidal micelles for the latter. The presence of 0.5 M KCl causes a micellar growth of POM-2$C_{12}$ micelles by 25%, while those of POM-2$C_{14}$ and POM-2$C_{16}$ are 16% and 50%, respectively. Salt also induced a small growth (*ca.* 1.4%) of micelle when 0.1 M of KCl was present in 0.1 M cetyltrimethylammonium chloride surfactant (CTAC) solution.[36] The presence of 0.1 M NaBr induced an increase of 15% in the ellipticity of the sodium dodecyl sulfate micelles in a 0.5 wt. % aqueous solution.[37] A more pronounced salt effect was seen in the alkyltrimethylammounium bromide systems ($C_n$TAB).[38] The growth of micellar ellipticity upon addition of 40 mM KBr was of 10%, 13% and 50% for $C_{12}$TAB, $C_{14}$TAB and $C_{16}$TAB surfactant solution, respectively. This was explained by the lower sensitivity of the fractional charge on the $C_n$TAB micelles that are formed by molecules with shorter hydrocarbon chains, supported by the SANS data.[38] Additionally, the micellar aggregation number increases as more salt are present in the POM-2$C_n$ solution, which is also seen in the $C_n$TAB systems in the presence of KBr.[38]

Table 3. Micellar parameters[c] from SANS analysis of 16 mM POM-2$C_{12}$, POM-2$C_{14}$ and POM-2$C_{16}$ solutions with different KCl concentrations.[15]

| KCl conc. (M) | $R_{min}$(Å) (± 1) | ε (± 0.2) | t (Å) (± 1) | Shell SLD (± 0.2) (×$10^{-6}$ Å$^{-2}$) | $N_{agg}$ (± 4) | φ(± 0.002) |
|---|---|---|---|---|---|---|
| | | POM-2$C_{12}$ | | | | |
| 0.00 | 10 | 4.1 | 19 | 5.4 | 25 | 0.069 |
| 0.10 | 10 | 4.5 | 19 | 5.0 | 27 | 0.065 |
| 0.25 | 10 | 4.9 | 18 | 4.8 | 29 | 0.060 |
| 0.50 | 10 | 5.1 | 19 | 4.8 | 31 | 0.051 |
| 0.75 | 10 | 2.7 | 16 | 4.8 | 16 | 0.017 |
| | | POM-2$C_{14}$ | | | | |
| 0.00 | 15 | 1.8 | 18 | 5.2 | 33 | 0.050 |
| 0.10 | 15 | 2.0 | 14 | 4.6 | 35 | 0.030 |
| 0.25 | 15 | 2.0 | 14 | 4.8 | 35 | 0.028 |
| 0.50 | 15 | 2.2 | 15 | 4.4 | 38 | 0.034 |
| | | POM-2$C_{16}$ | | | | |
| 0.00 | 18 | 1.0 | 20 | 5.3 | 27 | 0.086 |
| 0.10 | 18 | 1.0 | 19 | 5.2 | 27 | 0.059 |
| 0.25 | 18 | 1.1 | 19 | 5.1 | 29 | 0.053 |
| 0.50 | 18 | 1.5 | 19 | 4.8 | 40 | 0.046 |
| 0.75 | 18 | 1.3 | 19 | 5.2 | 35 | 0.022 |

[c] $R_{min}$, the minimum radius of the core; $R_{max}$, the maximum radius of the core; ε, $R_{max}/R_{min}$ (ellipticity); φ, volume fraction; SLD, neutron scattering length density; t, shell thickness, $N_{agg}$, aggregation number.

The trend is not followed for the highest KCl concentration (0.75 M KCl). Indeed, the POM-2$C_{12}$ micelles see their electrostatic repulsion completely shielded by the amount of $K^+$ ions added and experience salting-out effect suggested by the sudden drop in volume fraction (φ = 0.069 to 0.017 between 0.5 and 0.75 M KCl, see Table 3) and by macroscopically observable precipitates. In addition, the fitted ellipticity value drops to 2.7 and the estimated aggregation number ($N_{agg}$) is nearly half of those with lower KCl concentrations. Salting-out effect was also observed in the 16 mM POM-2$C_{16}$ systems when the KCl concentration is 0.75 M, while it is not studied for the POM-2$C_{14}$ sample.

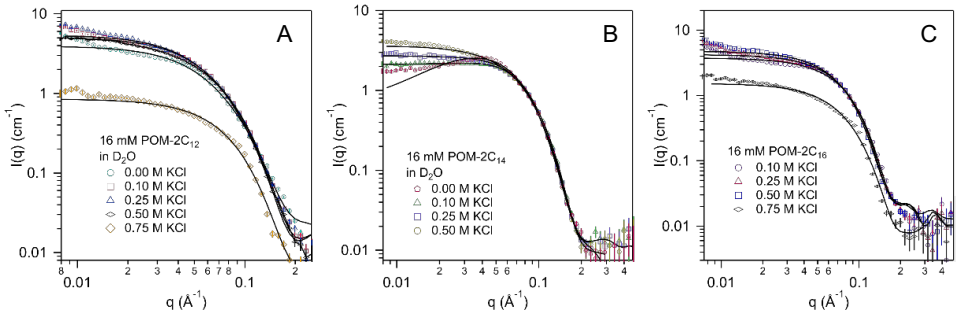


Figure 2. SANS data of 16 mM (A) POM-2$C_{12}$, (B) POM-2$C_{14}$ and (C) POM-2$C_{16}$ micellar $D_2O$ solutions in the presence of different KCl concentrations. The fits are given as black lines.

In these POM-2$C_n$ systems, it can be seen that the aggregation number ($N_{agg}$) increases gradually with elevated salt concentration until salting-out phenomenon emerges. This is in good agreement with reports on $C_n$TAB (n = 12, 14 and 16), CATC and SDS/$C_{12}EO_4$ systems.[28, 38, 39] This can be understood from the aspect of charge neutralisation at the shells that consequently reduced the electrostatic repulsion between headgroups, resulting in an increased number of aggregated surfactant molecules induced by the hydrophobic interactions.[28]

### Salt effect on POM-2$C_n$/$C_{12}EO_8$ (n = 12, 14 and 16) systems.

Salt effect on the binary mixed systems was also studied. The total concentration for these mixtures was fixed at 16 mM, which is the same as the studied individual surfactant solutions. The studied KCl concentration was 0.25 M chosen as it is below the salting-out effect for each

surfactant. SANS data are given in Figure 3 and Figure 4, the fitted parameters are listed in Table 4 and Table 5. To the exception of the POM-2$C_{12}$/$C_{12}EO_8$ mixture with a POM-2$C_{12}$ mole fraction at 0.25, all samples evidence a distinction increase of $N_{agg}$ upon addition of KCl.

The POM-2$C_{12}$/$C_{12}EO_8$ mixtures form ellipsoidal micelles at 16 mM in the presence and absence of 0.25 M KCl. Due to the limitation during SANS beamtime, the mixture with a mole fraction of POM-2$C_{12}$ at 0.25 was measured using small angle X-ray scattering (SAXS), the fit of the SAXS data is given in Figure 3B. The volume fraction was not extracted for this mixture since its SAXS data is not given in absolute scale.

In these investigated compositions for 16 mM POM-2$C_{12}$/$C_{12}EO_8$ systems, the SANS data analysis results suggest that addition of salt results in a micelle size growth by *ca.* 2 %, 18 % and 31 % for mixtures containing 25 mol%, 50 mol% and 75 mol% POM-2$C_{12}$, respectively. The elongation of the 3:1 POM-2$C_{12}$/$C_{12}EO_8$ system experiences an even more distinct increase compared to the pure 16 mM POM-2$C_{12}$ system (*ca.* 20%).

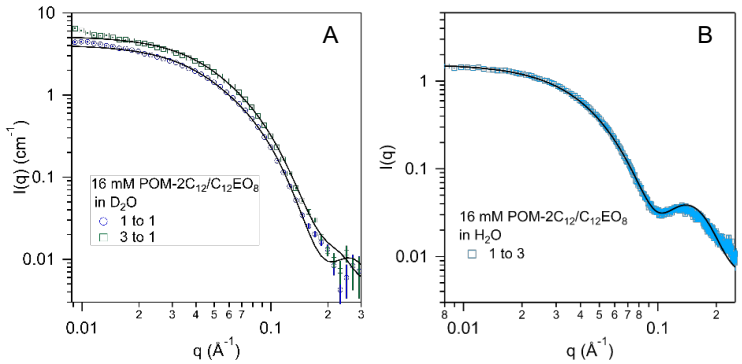


Figure 3. (A) SANS of POM-2$C_{12}$/$C_{12}EO_8$ system in $D_2O$ (mole ratio 1:1 and 3:1) and (B) SAXS pattern of 1:3 POM-2$C_{12}$/$C_{12}EO_8$ mixture in $H_2O$, in the presence of 0.25 M KCl.

The addition of KCl salt induces the formation of slightly elongated micelles in POM-2$C_{14}$/$C_{12}EO_8$ mixture compared the equimolar counterpart without salt. The radii of gyration of these mixed POM-2$C_{14}$/$C_{12}EO_8$ micelles were initially predicted through the Guinier analysis (shape-independent analysis)[40] (see SI Figure 5 at page 161), suggesting the nonionic rich micelles have the largest size (the obtained $R_g$ can be found in SI Figure 5 at page 161). The micelles become smaller as the composition of the mixture progressively moves to the ionic-

rich component. Shape-dependent analyses of SANS (Figure 4A) and SAXS (Figure 4B) data agree with the Guinier analyses, ionic-rich mixed micelles have the largest ellipticity value (see Table 4), providing supportive structural evidence. The ellipticity rises by 11%, 12% and 13% for 0.25, 0.5 and 0.75 POM-2$C_{14}$ of POM-2$C_{14}$, respectively, giving a similar result than the pure POM-2$C_{14}$ system (*ca.* 11%) in the presence of 0.25 M KCl.

Table 4. Micellar parameters from SANS/SAXS analysis of 16 mM POM-2$C_n$/$C_{12}EO_8$ (n = 12 and 14) mixtures at a constant KCl concentration (0.25 M).

| POM-2$C_n$/$C_{12}EO_8$ | $R_{min}$(Å) (± 1) | ε (± 0.2) | t (Å) (± 1) | Shell-SLD (± 0.2) (×$10^{-6}$ Å$^{-2}$) | $N_{agg}$ (± 5) | φ(± 0.002) |
|---|---|---|---|---|---|---|
| | | POM-2$C_{12}$/$C_{12}EO_8$ mixtures | | | | |
| 1:3 | 12 | 4.8 | 20 | 11.1* | 79 | -- |
| 1:1 | 12 | 5.8 | 18 | 4.6 | 80 | 0.025 |
| 3:1 | 13 | 5.1 | 18 | 4.9 | 77 | 0.036 |
| | | POM-2$C_{14}$/$C_{12}EO_8$ mixtures | | | | |
| 1:3 | 17 | 2.1 | 18 | 4.4 | 93 | 0.010 |
| 1:1 | 16 | 1.9 | 15 | 4.5 | 56 | 0.017 |
| 3:1 | 17 | 1.7 | 15 | 4.8 | 50 | 0.026 |
| | | POM-2$C_{14}$/$C_{12}EO_8$ mixtures | | | | |
| 1:3 | 17 | 2.1 | 18 | 12.8* | 93 | -- |
| 1:1 | 17 | 1.9 | 15 | 13.5* | 67 | -- |
| 3:1 | 18 | 1.8 | 12 | 17.4* | 70 | -- |

$R_{min}$, the minimum radius of the core; $R_{max}$, the maximum radius of the core; ε, $R_{max}/R_{min}$ (ellipticity); φ, volume fraction; SLD, Neutron/X-ray scattering length density; t, shell thickness, $N_{agg}$, aggregation number.
* This represents the corresponding parameters were from the analysis of SAXS data and the SLD is an X-ray scattering length density value.

The POM-2$C_{16}$/$C_{12}EO_8$ systems form spherical micelles with and without 0.25 M KCl in the solutions. The SANS patterns are plotted in Figure 4C and the fit parameters are listed in Table 5. As illustrated, no obvious growth in micellar size was seen compared to that of the POM-2$C_{16}$/$C_{12}EO_8$ system without KCl. This is very similar to the effect seen in the 16 mM POM-2$C_{16}$ system, which experiences a very small growth (*ca.* 10%) in the micellar size and has larger micellar aggregation numbers after the addition of 0.25 M KCl. As previously reported, the fractional charge on the pure POM-2$C_{16}$ micelles is quite low compared to the ones formed by surfactant with shorter chains,[15] therefore, the counterion condensation is less sensitive to the addition of KCl, consequently experience smaller micellar growth.

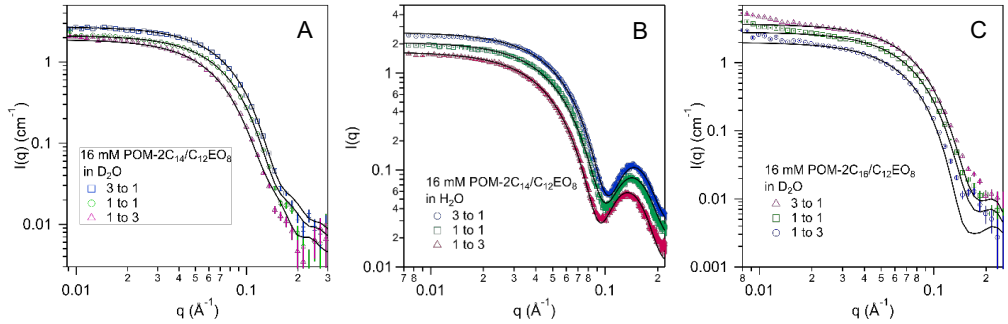


Figure 4. (A) SANS and (B) SAXS patterns of POM-2$C_{14}$/$C_{12}EO_8$ mixtures in $D_2O$ and $H_2O$, respectively, in the presence of 0.25 M KCl. (C) SANS data on 16 mM POM-2$C_{16}$/$C_{12}EO_6$ mixed micellar $D_2O$ solutions with the addition of 0.25 M KCl. The fits are given as black lines.

Table 5. Micellar parameters[d] from SANS analyses of 16 mM POM-2$C_{16}$/$C_{12}EO_8$ mixtures at a constant KCl concentration (0.25 M).

| POM-2$C_{16}$/$C_{12}EO_8$ | R (Å) (± 1) | Shell-SLD (± 0.2) (×$10^{-6}$ Å$^{-2}$) | t (Å) (± 1) | $N_{agg}$ (± 5) | φ (± 0.002) |
|---|---|---|---|---|---|
| 1:3 | 20 | 4.3 | 18 | 68 | 0.011 |
| 1:1 | 19 | 4.8 | 19 | 45 | 0.027 |
| 3:1 | 18 | 4.9 | 19 | 32 | 0.043 |

[d] R, the core radius of spherical micelles; φ, volume fraction; SLD, neutron scattering length density; t, shell thickness; $N_{agg}$, aggregation number.

It is seen that the effect of the charge neutralisation by the addition of KCl is less pronounced on the POM-2$C_{16}$/$C_{12}EO_8$ micelles when comparing with POM-2$C_{12}$/$C_{12}EO_8$ and POM-2$C_{14}$/$C_{12}EO_8$ micelles. This agrees with what has been observed in the pure POM-2$C_n$ systems. This may be due to the higher degree of ionisation of the POM-2$C_{12}$ and POM-2$C_{14}$ in aqueous solutions compared to POM-2$C_{16}$, therefore are more sensitive to the change of the ionic strength in the solutions.[15]

**POM-2$C_n$/$C_{12}EO_8$ (n = 12, 14 and 16) binary systems at a total concentration of 133 mM.**

As discussed, the mixed micelles were studied in the absence and presence of KCl. And these micelles are potentially useful to be used as structure-directing agents for the synthesis of inorganic materials with POM units decorated. Different mixing ratios are applicable to control the POM content in the resulting hybrid materials. In order to explore the possibility of exploiting these micelles to template long-range ordered materials, a higher concentration (133 mM) was studied. As illustrated in Figure 5, diffraction peaks are seen in the SAXS patterns. The positions of the diffraction peaks of the SAXS patterns from the 3:1 mixtures are

listed in Table 6. The liquid crystal phases (LCP) formed by the POM-2$C_{12}$/$C_{12}EO_8$ and POM-2$C_{14}$/$C_{12}EO_8$ only display two peaks in the SAXS measurements, which can be predicted as a cubic phase with two possible space groups ($Pm\bar{3}n$ or $Im\bar{3}m$ space group). The one formed by POM-2$C_{16}$/$C_{12}EO_8$ shows three diffraction peaks, which is indexed as a cubic phase with an $Im\bar{3}m$ space group. The increase in d spacing (=2π/q, q, the position of the main peak) of the resulting LCP occurs with increasing tail length of POM-2$C_n$. The SAXS pattern of POM-2$C_{12}$/$C_{12}EO_8$ mixtures with the mole ratio of 1:1 are contributed by the scattering from micelles as seen in Figure 5, and those of POM-2$C_{14}$/$C_{12}EO_8$ and POM-2$C_{16}$/$C_{12}EO_8$ mixtures have a small diffraction peak and are mostly contributed by the micelles. A lamellar phase is seen in the 1:3 POM-2$C_{12}$/$C_{12}EO_8$ mixture, however, other mixtures with 1:3 mole ratio do not form long-range ordered micelles.

Table 6. Diffraction peak position obtained from SAXS data of 133 mM POM-2$C_n$/$C_{12}EO_8$ mixtures at a mole ratio of 3:1.

| POM-2$C_n$/$C_{12}EO_8$ | Main peak ($Å^{-1}$) (± 0.002) | Secondary peak ($Å^{-1}$) (± 0.002) | Third peak ($Å^{-1}$) (± 0.002) |
|---|---|---|---|
| n = 12 | 0.011 | 0.017 | -- |
| n = 14 | 0.016 | 0.022 | -- |
| n = 16 | 0.017 | 0.023 | 0.026 |

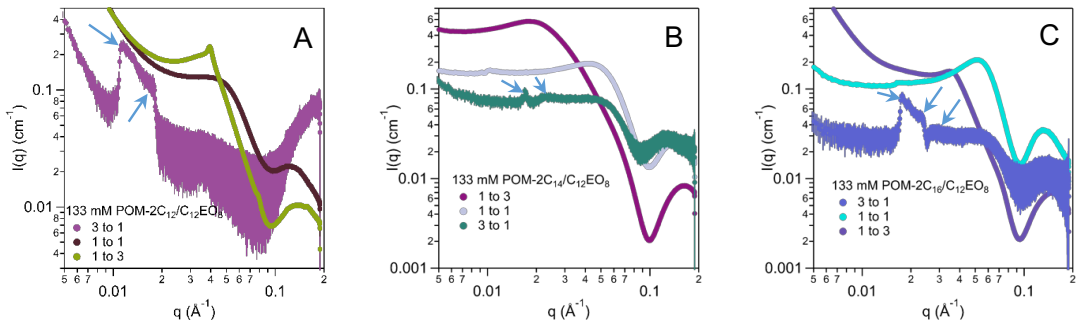


Figure 5. SAXS patterns of (A) POM-2$C_{12}$/$C_{12}EO_8$ (B) POM-2$C_{14}$/$C_{12}EO_8$ (C) POM-2$C_{16}$/$C_{12}EO_8$ mixtures at concentration of 133 mM with three mixing mole ratios.

**The preparation of silica.**

As a proof of concept, the lamellar phase formed by 133 mM 1:3 POM-2$C_{12}$/$C_{12}EO_8$ mixture was used to template silica. The SAXS pattern of the prepared silica has two broad peaks,

which may correspond to a lamellar phase. The two diffraction peaks were maintained after calcination as seen in Figure 6 (A). The calcined sample possesses a type IV isotherm with a type H4 hysteresis loop (see Figure 6B),[41, 42] and a surface area of 313 $m^2/g$. The inserted pore size distribution in Figure 6B suggests that the pore size in the calcined porous silica mostly distributes between 1 nm and 4 nm.

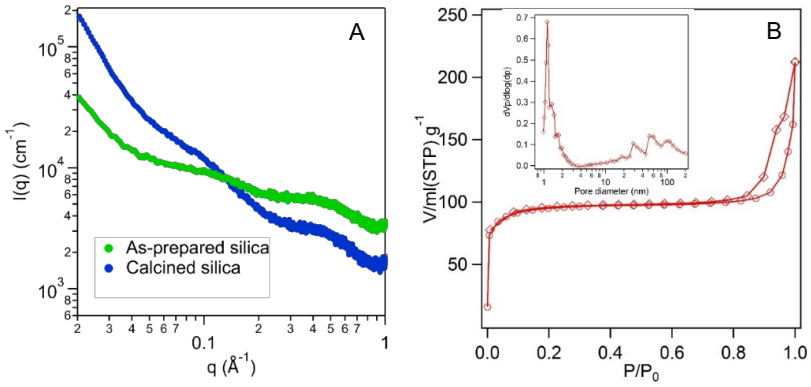


Figure 6. (A) SAXS patterns of the prepared silica and the calcined silica. (B) Nitrogen adsorption-desorption isotherm and pore size distribution of the calcined silica.

## Conclusion

The aggregation behaviours of mixed anionic POM-2$C_n$ and nonionic $C_{12}EO_8$ surfactants in water were studied by small angle neutron scattering. The SANS analysis results indicate that morphologies of the mixed micelles are dominated heavily by the ionic part even though in the case of the POM-2$C_{16}$ the degree of counterion binding to the surface of the micelle is high, meaning this surfactant bears very little charge when it is in the micelles. We employed KCl, which contains the same counterion as the POM-2$C_n$ headgroup, as a modulator of the ionic strength in the micellar solutions. Effects of KCl addition on both the pure POM-2$C_n$ system and their binary mixture with $C_{12}EO_8$ were studied at a fixed surfactant molar concentration (16 mM) using SANS. The investigation of the salt effect on the pure POM-2$C_n$ systems is carried out by continuously increasing the KCl concentration at a fixed surfactant total concentration from 0 M to 0.75 M where a salting-out effect is observed. For increasing ionic strength, growth in the micellar size is evidenced by the SANS analysis. The addition of KCl also induced an increase in the micellar size of the mixed POM-2$C_n$/$C_{12}EO_8$ micelles. The

elongation effect induced by salt addition is more effective when the ionic part in the mixture bears shorter hydrophobic chains, this is attributed to the higher ionisation degree of these surfactants. These mixtures form LCP at high concentration (133 mM), and the LCP structure can be transformed into silica materials through surfactant templating method. The results in this paper have studied the mixing of POM-2$C_n$ and $C_{12}EO_8$, both at low concentration and high concentration. The feasibility of transforming the LCP structure formed by POM-2$C_n$/$C_{12}EO_8$ mixture has also been proven.


## Acknowledgement

A. Di. thanks University of Bath and China Scholarship Council for supporting her PhD. The authors would like to thank ISIS spallation neutron source for the award of beam time (experiment no. 1810278). The raw SANS data can be found at DOI: 10.5286/ISIS.E.RB1810278, while the CMC data and reduced SANS data supporting this paper can be found in the University of Bath Research Data Archive, 2019 DOI: 10.15125/BATH-00XXX. This work benefited from the use of the SasView application, originally developed under NSF Award DMR-0520547. SasView also contains code developed with funding from the EU Horizon 2020 programme under the SINE2020 project Grant 654000. The authors would like to thank Dr. Gavin Stenning and Dr. Daniel Nye for their assistance in collecting SAXS data on Xenocs instrument.


## Reference


1. A. Khan and E. F. Marques, *Curr. Opin. Colloid Interface Sci.*, 1999, **4**, 402-410.
2. K. Ogino and M. Abe, *Mixed surfactant systems*, CRC Press, 1992.
3. A. Shiloach and D. Blankschtein, *Langmuir*, 1998, **14**, 7166-7182.
4. T. Goloub, R. Pugh and B. Zhmud, *J. Colloid Interface Sci.*, 2000, **229**, 72-81.
5. M. J. Suárez and V. Mosquera, *Phys. Chem. Chem. Phys.*, 1999, **1**, 3583-3587.
6. S. Prévost and M. Gradzielski, *J. Colloid Interface Sci.*, 2009, **337**, 472-484.
7. K. Singh and D. G. Marangoni, *J. Colloid Interface Sci.*, 2007, **315**, 620-626.
8. J. C. Amante, J. F. Scamehorn and J. H. Harwell, *J. Colloid Interface Sci.*, 1991, **144**, 243-253.
9. M. Almgren, J. Gimel, K. Wang, G. Karlsson, K. Edwards, W. Brown and K. Mortensen, *J. Colloid Interface Sci.*, 1998, **202**, 222-231.
10. S. Ozeki and S. Ikeda, *J. Colloid Interface Sci.*, 1982, **87**, 424-435.
11. G. V. Jensen, R. Lund, J. Gummel, T. Narayanan and J. S. Pedersen, *Angew. Chem., Int. Ed.*, 2014, **53**, 11524-11528.
12. M. Cates and S. Candau, *J. Phys.: Condens. Matter*, 1990, **2**, 6869-6892.

13. N. Vlachy, M. Drechsler, J.-M. Verbavatz, D. Touraud and W. Kunz, *J. Colloid Interface Sci.*, 2008, **319**, 542-548.
14. L. Jiang, K. Wang, M. Deng, Y. Wang and J. Huang, *Langmuir*, 2008, **24**, 4600-4606.
15. A. Di, J. Schmitt, M. A. Da Silva, N. Mahmoudi, R. J. Errington and K. Edler, unpublished work.
16. A. Di, J. Schmitt, K. Ma, M. A. Da Silva, N. Elstone, N. Mahmoudi, P. Li, A. Washingtong, Z. Wang, R. J. Errington and K. Edler, unpublished work.
17. S. M. Bennington, *Nucl. Instrum. Methods Phys. Res., Sect. A*, 2009, **600**, 32-34.
18. O. Arnold, J.-C. Bilheux, J. Borreguero, A. Buts, S. I. Campbell, L. Chapon, M. Doucet, N. Draper, R. F. Leal and M. Gigg, *Nucl. Instrum. Methods Phys. Res., Sect. A*, 2014, **764**, 156-166.
19. G. T. Wignall and F. Bates, *J. Appl. Crystallogr.*, 1987, **20**, 28-40.
20. A. Guinier, G. Fournet and K. L. Yudowitch, *Small-angle scattering of X-rays*, John Wiley and Sons, New York, 1955.
21. M. Kotlarchyk and S. H. Chen, *J. Chem. Phys.*, 1983, **79**, 2461-2469.
22. S. Berr, *J. Phys. Chem.* , 1987, **91**, 4760-4765.
23. M. Kotlarchyk and S. H. Chen, *J. Chem. Phys.*, 1983, **79**, 2461-2469.
24. S. Berr, *J. Phys. Chem.*, 1987, **91**, 4760-4765.
25. J.-P. Hansen and J. B. Hayter, *Mol. Phys.*, 1982, **46**, 651-656.
26. C. Tanford, *J. Phys. Chem.*, 1974, **78**, 2469-2479.
27. J. Penfold, E. Staples, I. Tucker and P. Cummins, *J. Colloid Interface Sci.*, 1997, **185**, 424-431.
28. T. Patel, G. Ghosh, V. Aswal and P. Bahadur, *Colloid Polym. Sci.*, 2009, **287**, 1175-1181.
29. J. Liley, J. Penfold, R. Thomas, I. Tucker, J. Petkov, P. Stevenson, I. Banat, R. Marchant, M. Rudden and A. Terry, *J. Colloid Interface Sci.*, 2017, **487**, 493-503.
30. J. Penfold, E. Staples, L. Thompson, I. Tucker, J. Hines, R. Thomas, J. Lu and N. Warren, *J. Phys. Chem. B*, 1999, **103**, 5204-5211.
31. C. Han, Y. Guo, X. Chen, M. Yao, Y. Zhang, Q. Zhang and X. Wei, *Soft Matter*, 2017, **13**, 1171-1181.
32. J. Luo and T. Liu, *Langmuir*, 2019, **35**, 7603-7616.
33. J. M. Pigga, M. L. Kistler, C. Y. Shew, M. R. Antonio and T. Liu, *Angew. Chem., Int. Ed.*, 2009, **48**, 6538-6542.
34. Y. Chevalier and T. Zemb, *Rep. Prog. Phys.*, 1990, **53**, 279-371.
35. J. Israelachvili, *Intermolecular and surface forces*, Academic Press, 1992.
36. V. Aswal and P. Goyal, *Phys. Rev. E*, 2003, **67**, 051401.
37. M. Bergström and J. S. Pedersen, *Phys. Chem. Chem. Phys.*, 1999, **1**, 4437-4446.
38. V. Aswal and P. Goyal, *Chem. Phys. Lett.*, 2002, **364**, 44-50.
39. V. Aswal and P. Goyal, *Phys. Rev. E*, 2000, **61**, 2947-2953.
40. B. Hammouda, *J. Appl. Crystallogr.*, 2010, **43**, 716-719.
41. M. Thommes, *Chem. Ing. Tech.*, 2010, **82**, 1059-1073.
42. K. S. Sing and R. T. Williams, *Adsorpt. Sci. Technol.*, 2004, **22**, 773-782.

# Supporting Information

## Amphiphilic Polyoxometalate Mixtures with Octaethylene Glycol Dodecyl Ether and Salts Effect on the Micellar Systems

Andi Di,[1] Julien Schmitt,[1,2] Zakir Hossain,[1] Adam Washington,[3] R. John Errington,[4] Karen J Edler[1*]

[1]Department of Chemistry, University of Bath, Claverton Down, Bath, BA2 7AY, UK

[2]LSFC – Laboratoire de Synthèse et Fonctionnalisation des Céramiques, UMR 3080 CNRS / Saint-Gobain CREE, Saint-Gobain Research Provence, 550 avenue Alphonse Jauffret, Cavaillon, France

[3]ISIS Neutron and Muon Source, Science and Technology Facilities Council, Rutherford Appleton Laboratory, Didcot OX11 0QX, UK

[4]School of Chemistry, Newcastle University upon tyne, Newcastle, NE1 7RU, UK

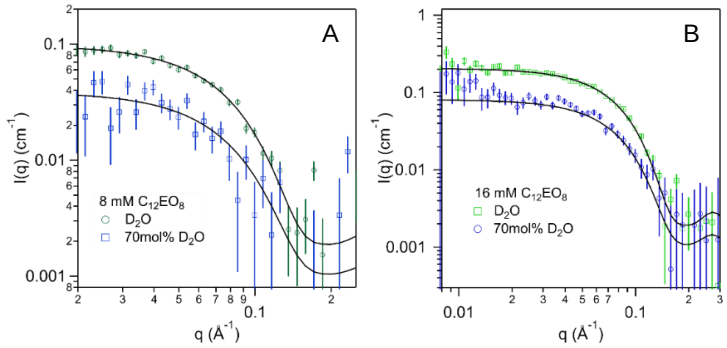


SI Figure 1. SANS patterns and fits of $C_{12}EO_8$ aqueous solutions (A) 8 mM and (B) 16 mM. Fits are made using the core-shell sphere model and are given as black lines.

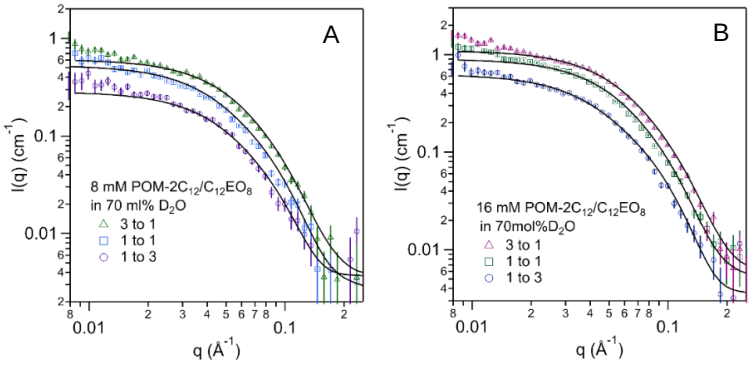


SI Figure 2. SANS patterns and their corresponding fits of POM-$2C_{12}$/$C_{12}EO_8$ systems with three mixing mole ratios at a total concentration of (A) 8 mM and (B) 16 mM in 70 mol% $D_2O$. Fits are made using the core-shell ellipsoid model and are given as black lines.

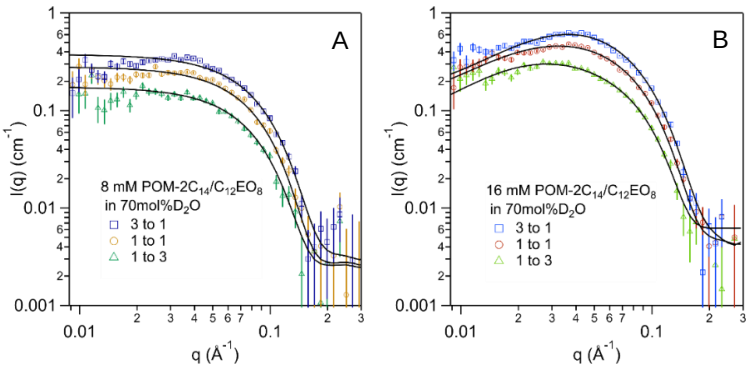


SI Figure 3. SANS patterns and their corresponding fits of POM-2C$_{14}$/C$_{12}$EO$_8$ systems with three mixing mole ratios at a total concentration of (A) 8 mM and (B) 16 mM in 70 mol% D$_2$O. Fits are made using the core-shell ellipsoid model and are given as black lines.

.

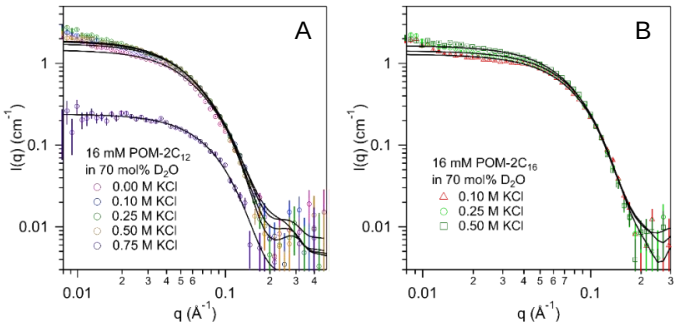


SI Figure 4. SAXS patterns and fits of (A) 16 mM POM-2C$_{12}$ and (B) 16 mM POM-2C$_{14}$ in 70 mol% D$_2$O, in the presence of different KCl concentrations.

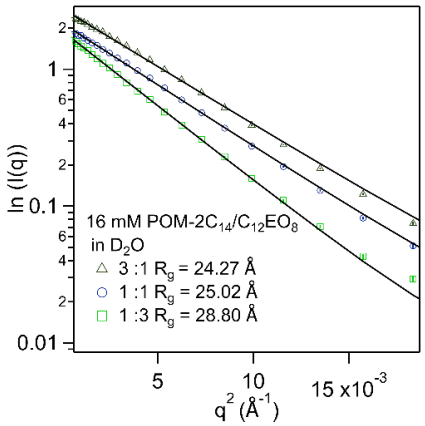


SI Figure 5. The Guinier plot of ln (I (q)) versus q$^2$ for 16 mM POM-2C$_{14}$/C$_{12}$EO$_8$ mixtures with the addition of 0.25 M KCl.

## 6.2 Conclusion

In this chapter the mixture of POM-2$C_n$/$C_{12}EO_8$ at both low concentrations (8 and 16 mM) and a high concentration (133 mM) are studied. The mixed systems POM-2$C_n$/$C_{12}EO_6$ and POM-2$C_n$/$C_{12}EO_8$ are both studied using SANS technique for comparison to find out how the headgroup of the nonionic surfactant in the mixed systems affects the shape of the mixed micelles. The fitting of the obtained SANS data suggest that when the nonionic surfactant has a less soluble headgroup, it induces a more obvious elongation along one direction of the micelles if involved in the POM-2$C_n$ systems.

Additionally, when KCl salt is added into the pure POM-2$C_n$ systems, the surfactant molecules form more elongated micelles in water due to the shield of repulsive interactions between the POM headgroups caused by the appearance of the $K^+$ ions. The salt effect is more obvious when the POM-2$C_n$ in the mixtures has shorter tail lengths (n = 12 and 14). And the mixed micelles in 16 mM mixed surfactant solutions are studied in the presence of 0.25 M KCl. The elongation of the 3:1 POM-2$C_{12}$/$C_{12}EO_8$ system experiences an even more distinct increase compared to the pure 16 mM POM-2$C_{12}$ system (*ca.* 20%). This is explained from the aspect of fractal charge that POM-2$C_{12}$ molecules bear in the micelles: in the mixed micelles, the POM-2$C_{12}$ molecules are able to dissociate more counterions due to the insertion of $C_{12}EO_8$ molecules, therefore, is more sensitive to the change of the ionic strength in the solutions.

The micellar structures of the mixed surfactant systems at a high concentration (total surfactant concentration 133 mM) with the three same mixing ratios are also studied. The SAXS patterns of the 3:1 POM-2$C_n$/$C_{12}EO_8$ (n = 12, 14 and 16) mixtures have very obvious noise which maybe caused by the large aggregates formed at this high concentration. The SAXS patterns of 1:1 POM-2$C_n$/$C_{12}EO_8$ (n = 14 and 16) mixtures have a small peak which are difficult to define their orderings. The 1:3 POM-2$C_n$/$C_{12}EO_8$ (n = 12) mixtures clearly show two peaks which maybe related to a lamellar liquid crystal phase. The 133 mM POM-2$C_{12}$/$C_{12}EO_8$ mixture with the mole ratio at 1:3 is then used to template silica materials. The resulting silica material gives two broad peaks that could indicate a lamellar structure. And BET analysis of the nitrogen absorption line indicates a surface area of *ca.* 313 $m^2$/g. And the BJH analysis suggests the pore size in the structure lies in the range of 1 nm and 4 nm. The small pore size may be due to the contraction of the pore structure during high-temperature annealing. Since the peaks in the SAXS patterns from the silica material before and after calcination are very broad, it is difficult to compare the change in d-spacing caused by high-temperature annealing.

This study has proven the concept of using the mixed surfactant systems, which contain the novel POM-2$C_n$ surfactants, to template POM-functionalised materials. The resulting materials also have a porous structure in a mesoscale which increases the active surface area that is available to catalytic reactions. This study inspires future studies on loading the POM units on to long-range ordered porous catalysts to achieve a structure with POM units well-aligned in the inner pore wall. This structure not only increases the active surface area but also may grant a synergistic effect in catalytic properties between POM and the templated materials.

Additionally, the well-mixing of POM-2$C_n$ and $C_{12}EO_m$ also suggest the compatibility of POM-2$C_n$ with commercial surfactants. This could extend the application of POM-2$C_n$ surfactants into other areas. For example, to crosslink with other polymers to produce gels. The pre-

pared gels are proposed to have well-dispersed POM units in their structures, therefore they can be used as superabsorbents or to be three-dimensionally printed into devices with well-dispersed POM units.

# 7 Conclusion and Future work

## 7.1 Conclusion

This thesis has focused on the preparation of porous inorganic materials through a surfactant templating method. The templating systems used in Chapter 3 were formed by a traditional surfactant (hexadecyltrimethylammonium bromide, CTAB). In order to functionalize the prepared inorganic materials, novel surfactants that possess Dawson structured polyoxometalate as the hydrophilic headgroup (POM-2$C_n$, n = 12, 14, 16 and 18) were designed and prepared. Chapters 4, 5 and 6 focused on the aggregation behaviour of the pure POM-2$C_n$ as well as mixed POM-2$C_n$/$C_{12}EO_m$ (m = 6 and 8) systems, and their applications in functionalising $TiO_2$ and $SiO_2$.

### 7.1.1 Preparation of silica films using traditional CTAB surfactant in the presence of LPEI and NaOH.

The preparation of silica using organic materials has been well established, including the synthesis methods, the formation mechanisms and applications. Silica materials of a film geometry are of importance in the field of catalysis and separations. The surfactant-polymer mixtures have allowed the preparation of robust and free-standing silica films, and were widely studied by our group. Here, with the aim to better control the pore size of the prepared silica films with controllable mesostructures, an alternative silica precursor, sodium silicate solution, was used in the preparation. The variations in the composition of the film growth solutions, such as the concentrations of sodium silicate, CTAB, LPEI and NaOH, were studied and were found to have little effect on the type of the mesostructure of the as-synthesised silica films. The growth of the silica films was followed by using *in situ* X-ray reflectivity (XRR) and grazing incidence small angle X-ray scattering (GISAXS). The results have shown that the wormlike mesophase is already formed at the surface at the early stage of the film growth process. However, the diffraction peaks from the crystallised surfactants may hinder the possibility to discern the secondary peak that is important to determine the detailed evolution of the interfacial structure. The addition of $NaNO_3$ salt, as a source of $NO_3^-$, allowed the diminishment of the crystallisation of the surfactants in the system, and hence allowed the detection of the secondary peak. *In situ* XRR and GISAXS results indicated the formation of 2D hexagonal structure normal to the surface and the lateral interface retained the wormlike structure during the film growth process. However overall the ordering in the sodium silicate derived films was poor compared to that achieved with tetramethoxysilane precursors.

### 7.1.2 The micellar phase of pure POM-2C$_n$ surfactants and their application in material templating.

POM-headed surfactants were designed to functionalize materials through the surfactant templating method. These surfactants were prepared by grafting double hydrocarbon chains to a Dawson structured polyoxometalate ($[P_2W_{17}O_{61}]^{10-}$), abbreviated as POM-2C$_n$. The lengths of the hydrophobic chains were 12, 14, 16 and 18. These POM-2C$_n$ surfactants are soluble in water and their CMCs in water have been determined using conductivity measurements. Their surfactant behaviours were studied using SANS and were seen to be different compared to the traditional surfactants (C$_n$TAB), which form more globular micelles with increasing hydrophobic tail length. Based on the previously reported synergism between POM and $TiO_2$, these micelles were used to template $TiO_2$. The resulted hybrid POM-$TiO_2$ materials have different pore-size distributions and values of surface area, which may be due to the different morphologies of the POM-2C$_n$ micelles used for templating. The hybrid materials possess enhanced degradation properties for rhodamine B compared to unfunctionalised $TiO_2$ material. This chapter has proven the feasibility of the application of POM-2C$_n$ surfactants as templates for supporting POM onto templated materials.

### 7.1.3 The micellar phase of POM-2C$_n$/C$_{12}$EO$_6$ mixtures.

The mixtures of POM-2C$_n$ with C$_{12}$EO$_6$ with three different mixing ratios were studied to investigate their use in tuning the POM content in the resulting hybrid template materials. As seen for other anionic surfactants (for instance sodium dodecyl sulfate, SDS), the insertion of C$_{12}$EO$_6$ molecules induces elongation of the micelles. The mole fractions of the POM-2C$_n$ in the mixed micelles were determined through analysing the SANS data. Similar results were found using the CMCs of the mixed systems. demonstrating antagonistic non-ideal mixing. Despite this unfavourable interaction between the nonionic and POM-surfactants formation of mixed micelles does still occur and could assist in control of micelle properties. These results are useful to estimate the POM content in the resulting hybrid materials which could be synthesised using these mixtures.

### 7.1.4 The micellar phase of POM-2C$_n$/C$_{12}$EO$_8$ mixtures and applications.

The mixtures of POM-2C$_n$ with C$_{12}$EO$_8$ with three mixing ratios were studied. The C$_{12}$EO$_8$ surfactant was chosen since it has the same tail geometry and the same type of hydrophilic headgroup (polyethylene oxide) as C$_{12}$EO$_6$, but has a larger headgroup (eight repeated ethylene oxide units *versus* six in C$_{12}$EO$_6$). The comparison between the micellar phases formed by POM-2C$_n$/C$_{12}$EO$_6$ and POM-2C$_n$/C$_{12}$EO$_8$ suggested that the larger headgroup in the nonionic surfactant structure reduces their abilities to elongate the mixed micelles when mixed with POM-2C$_n$ surfactants due to the reduced packing parameter arising from larger average headgroup size. The effect of salt addition on the micellar phase structures is of interest given the fact that POM-2C$_n$ are hexavalent surfactants, therefore this was studied and was found to induce the growth of the micelles along one direction of the micelles with the other two axes remaining nearly constant. These micelles are potentially useful to template porous materials with spherical pore walls, in a cubic or 3D hexagonal close packed geometry, similar to those seen in surfactant templated silicas, but including POM units functionalised within the inner pores. Different liquid crystal phases were formed when the total surfactant concentration was increased to 133 mM at different

mixing mole ratios. The lamellar phase formed by 1: 3 POM-2$C_{12}$/$C_{12}EO_8$ mixture was applied to synthesise silica. The resulting silica material may show two diffraction peaks that could indicate a lamellar structure. The surface area however is relatively small (*ca.* 313 $m^2$/g) with most pores lying in the size range between 1 nm and 4 nm.

## 7.2 Future work.

The outlook for the future work can be separated into two parts, which are proposed from the aspect of functionalised inorganic materials and gel systems.

### 7.2.1 Functionalised inorganic materials.

As listed above, the pure POM-2$C_n$ systems have been used to template POM-functionalised $TiO_2$ (Chapter 4). This has proven the feasibility of utilisation of the micelles for material preparation although further work would be needed to find conditions under which materials with a high degree of long-range ordering could be prepared, if such ordering is required. Most applications simply require high surface area and accessible porosity so in this sense control over POM loading and pore connectivity are more important goals. Since the SANS studies of the mixtures (in Chapter 5 and Chapter 6) demonstrate that the POM-2$C_n$ surfactants mix well with the polyethylene oxide surfactants, these mixed micelles have potential advantages in tuning the amount of POM on the micelle surface. Such mixtures can also allow the formation of pores with larger volume in the resulting materials after the nonionic component is calcined away. Therefore, it is worth studying in more detail the properties of hybrid materials prepared by templating using the mixed micelles to study the change in amount of POM loaded into the materials and the effect this has on their photocatalytic efficiency. In addition, liquid crystal phases formed by the POM-2$C_n$/$C_{12}EO_8$ mixtures at high concentrations can be exploited to synthesise long-range ordered materials with POM units well aligned in the inner pores.

This method is applicable to functionalised materials varying from non-catalytic materials to various catalysts. For non-catalytic materials, such as silica, the prepared POM-functionalised materials are potentially useful as super absorbents [253] due to the high charge of the POMs, and are also useful in redox and photodegradation reactions due to the catalytic properties of the POMs. For catalytic materials, in addition to the $TiO_2$ materials studied in Chapter 4, other photocatalysts ($WO_3$ etc.) [175] and electrocatalysts (NiO, $Co_3O_4$ etc.) [254,255] can also be functionalised with POMs to achieve synergistic effects using this method.

The ideas proposed above are based on the preparation of POM-functionalised materials in the form of powders. The study of silica film preparation in Chapter 3 has investigated a feasible method to prepare spontaneous free-standing films. This work could also be extended by mixing the POM-2$C_n$ surfactant into the templating systems to prepare the POM-functionalised silica films or other metal oxide materials in a film geometry for membrane catalysis.

Future studies would contribute to the effective design of POM-functionalised materials in the form of both powders and films, and to the cost-effective design and economic application for industrial use.

### 7.2.2 Functionalised gels.

POM-2C$_n$ molecules contain simple alkyl chains which have a tendency to gel with various organic solvents through van der Waals interactions.[256] Moreover, the high charge possessed by the headgroup of POM-2C$_n$ surfactants also allows them to crosslink in the presence of other polymers through electrostatic interactions, thus to form gels. Therefore, the hydrocarbon chain modified POMs are potential candidates for the preparation of POM-functionalised gel systems, which unmodified POMs do not favour due to the non-directional electrostatic interactions they possess. The negatively charged POMs offer the potential application as superabsorbent materials for removal and separation of ionic dyes.[253] Additionally, soft systems containing well-dispersed POM are also a potential candidate for designing new organic soft materials.

To conclude but not finalise, the applications of the POM-based amphiphiles are not limited to the design of inorganic materials and organic networks (gels). There are many more possibilities to be explored. Moreover, the synthesis method of the POM amphiphiles used in this thesis may also apply to other types of POM, which may contribute to even broader outlook in the fundamental studies and applications of these novel materials.

# References


[1] G. J. Tiddy, *Surfactant-water liquid crystal phases*, Phys. Rep., **57**, pp. 1–46 (1980).

[2] Q. Huo, D. I. Margolese, P. Feng, T. Gier, and P. Sieger, *Generalized syntheses of periodic surfactant/inorganic composite materials*, Nature, **368**, pp. 317–321 (1994).

[3] Q. Huo, D. I. Margolese, U. Ciesla, D. G. Demuth, P. Feng, T. E. Gier, P. Sieger, A. Firouzi, and B. F. Chmelka, *Organization of organic molecules with inorganic molecular species into nanocomposite biphase arrays*, Chem. Mater., **6**, pp. 1176–1191 (1994).

[4] M. C. Morán, A. Pinazo, L. Pérez, P. Clapés, M. Angelet, M. T. García, M. P. Vinardell, and M. R. Infante, *Green amino acid-based surfactants*, Green Chem., **6**, pp. 233–240 (2004).

[5] J. Zhang, Y.-F. Song, L. Cronin, and T. Liu, *Self-assembly of organic inorganic hybrid amphiphilic surfactants with large polyoxometalates as polar head groups*, J. Am. Chem. Soc., **130**, pp. 14408–14409 (2008).

[6] J. Zhang, Y. Song, L. Cronin, and T. Liu, *ReverseVesicle Formation of OrganicInorganic PolyoxometalateContaining Hybrid Surfactants with Tunable Sizes*, Chem. Eur. J., **16**, pp. 11320–11324 (2010).

[7] J. Luo and T. Liu, *Competition and Cooperation among Different Attractive Forces in Solutions of InorganicOrganic Hybrids Containing Macroionic Clusters*, Langmuir, **35**, pp. 7603–7616 (2019).

[8] C. Ritchie, C. Streb, J. Thiel, S. G. Mitchell, H. N. Miras, D.-L. Long, T. Boyd, R. D. Peacock, T. McGlone, and L. Cronin, *Reversible redox reactions in an extended polyoxometalate framework solid*, Angew. Chem., Int. Ed., **47**, pp. 6881–6884 (2008).

[9] S.-S. Wang and G.-Y. Yang, *Recent advances in polyoxometalate-catalyzed reactions*, Chem. Rev., **115**, pp. 4893–4962 (2015).

[10] D. F. Evans and H. Wennerstrom, *Colloidal domain*, Wiley-Vch (1999).

[11] J. Israelachvili, *Intermolecular and Surface Forces*, Academic Press: San Diego, CA (1991).

[12] C. Tanford, *The hydrophobic effect: formation of micelles and biological membranes*, WileyInterscience, New York (1980).

[13] P. Ekwall, *Advances in liquid crystals*, Brown, GH, Ed, p. 1 (1975).

[14] P. Winsor, *Binary and multicomponent solutions of amphiphilic compounds. Solubilization and the formation, structure, and theoretical significance of liquid crystalline solutions*, Chem. Rev., **68**, pp. 1–40 (1968).

[15] P. A. Winsor, *Solvent properties of amphiphilic compounds*, Butterworths Scientific Publications (1954).

[16] Y. Huang and S. Gui, *Factors affecting the structure of lyotropic liquid crystals and the correlation between structure and drug diffusion*, RSC Adv., **8**, pp. 6978–6987 (2018).

[17] O. Muraza, E. Rebrov, T. Khimyak, B. Johnson, P. Kooyman, U. Lafont, M. Decroon, and J. Schouten, *Mesoporous silica films as catalyst support for microstructured reactors: Preparation and characterization*, Chem. Eng. J., **135**, pp. S99–S103 (2008).

[18] C. M. Crudden, M. Sateesh, and R. Lewis, *Mercaptopropyl-modified mesoporous silica: A remarkable support for the preparation of a reusable, heterogeneous palladium catalyst for coupling reactions*, J. Am. Chem. Soc., **127**, pp. 10045–10050 (2005).

[19] M. ValletReg, F. Balas, and D. Arcos, *Mesoporous materials for drug delivery*, Angew. Chem. Int. Ed., **46**, pp. 7548–7558 (2007).

[20] F. Tang, L. Li, and D. Chen, *Mesoporous silica nanoparticles: synthesis, biocompatibility and drug delivery*, Adv. Mater., **24**, pp. 1504–1534 (2012).

[21] M.-H. Tsai, S.-L. Huang, P.-C. Chiang, and C.-J. Chen, *Morphology, dynamic mechanical properties, and gas separation of crosslinking silica-containing polyimide nanocomposite thin film*, J. Appl. Polym. Sci., **106**, pp. 3185–3192 (2007).

[22] M. C. Duke, J. D. Da Costa, D. D. Do, P. G. Gray, and G. Q. Lu, *Hydrothermally robust molecular sieve silica for wet gas separation*, Adv. Funct. Mater., **16**, pp. 1215–1220 (2006).

[23] B. Platschek, A. Keilbach, and T. Bein, *Mesoporous structures confined in anodic alumina membranes*, Adv. Mater., **23**, pp. 2395–412 (2011).

[24] D. W. Breck, *Zeolite Molecular Sieves*, John Wiley  Sons, New York (1974).

[25] S. W. Blocki, *Hydrophobic zeolite adsorbent: a proven advancement in solvent separation technology*, Environ. Prog., **12**, pp. 226–230 (1993).

[26] J. Kim, M. Choi, and R. Ryoo, *Effect of mesoporosity against the deactivation of MFI zeolite catalyst during the methanol-to-hydrocarbon conversion process*, J. Catal., **269**, pp. 219–228 (2010).

[27] J. E. Wijnhoven and W. L. Vos, *Preparation of photonic crystals made of air spheres in titania*, Science, **281**, pp. 802–804 (1998).

[28] J. Schilling, R. Wehrspohn, A. Birner, F. Mller, R. Hillebrand, U. Gsele, S. Leonard, J. Mondia, F. Genereux, and H. Van Driel, *A model system for two-dimensional and three-dimensional photonic crystals: macroporous silicon*, J. Opt. A-Pure Appli. Op., **3**, p. S121 (2001).

[29] Y. Xia, B. Gates, Y. Yin, and Y. Lu, *Monodispersed colloidal spheres: old materials with new applications*, Adv. Mater., **12**, pp. 693–713 (2000).

[30] R. D. Miller, *In search of low-k dielectrics*, Science, **286**, pp. 421–423 (1999).

[31] D. Zhao, P. Yang, N. Melosh, J. Feng, B. F. Chmelka, and G. D. Stucky, *Continuous mesoporous silica films with highly ordered large pore structures*, Adv. Mater., **10**, pp. 1380–1385 (1998).

[32] W. Van Rhijn, D. De Vos, B. Sels, and W. Bossaert, *Sulfonic acid functionalised ordered mesoporous materials as catalysts for condensation and esterification reactions*, Chem. Commun., pp. 317–318 (1998).

[33] M. ValletReg, *Ordered mesoporous materials in the context of drug delivery systems and bone tissue engineering*, Chem. Eur. J., **12**, pp. 5934–5943 (2006).

[34] K. J. Edler and S. J. Roser, *Growth and characterization of mesoporous silica films*, Int. Rev. Phys. Chem., **20**, pp. 387–466 (2001).

[35] C. Kresge and M. Leonowicz, *Ordered mesoporous molecular sieves synthesized by a liquid crystal template mechanism*, Nature, **359**, pp. 710–712 (1992).

[36] S. Shen, Y. Li, Z. Zhang, J. Fan, B. Tu, W. Zhou, and D. Zhao, *A novel ordered cubic mesoporous silica templated with tri-head group quaternary ammonium surfactant*, Chem. Commun., pp. 2212–2213 (2002).

[37] D. Lootens, C. Vautrin, H. Van Damme, and T. Zemb, *Facetted hollow silica vesicles made by templating catanionic surfactant vesicles*, J. Mater. Chem., **13**, pp. 2072–2074 (2003).

[38] S. Shen, A. E. Garcia-Bennett, Z. Liu, Q. Lu, Y. Shi, Y. Yan, C. Yu, W. Liu, Y. Cai, and O. Terasaki, *Three-dimensional low symmetry mesoporous silica structures templated from tetra-headgroup rigid bolaform quaternary ammonium surfactant*, J. Am. Chem. Soc., **127**, pp. 6780–6787 (2005).

[39] L. A. Estroff and A. D. Hamilton, *At interface of Organic and Inorganic Chemistry: Bioinspired Sythesis of Composite Materials*, Chem. Mater., **13**, pp. 3227–3235 (2001).

[40] H.-P. Lin and C.-Y. Mou, *Structural and morphological control of cationic surfactant-templated mesoporous silica*, Acc. Chem. Res., **35**, pp. 927–935 (2002).

[41] K. R. Iler, *The chemistry of silica*, Solubility, Polymerization, Colloid and Surface Properties and Biochemistry of Silica, John Wiley  Sons, New York (1979).

[42] Y. Liu, A. Karkamkar, and T. J. Pinnavaia, *Redirecting the assembly of hexagonal MCM-41 into cubic MCM-48 from sodium silicate without the use of an organic structure modifier*, Chem. Commun., pp. 1822–1823 (2001).

[43] S. Santra, R. Tapec, N. Theodoropoulou, J. Dobson, A. Hebard, and W. Tan, *Synthesis and characterization of silica-coated iron oxide nanoparticles in microemulsion: the effect of nonionic surfactants*, Langmuir, **17**, pp. 2900–2906 (2001).

[44] S. Che, A. E. Garcia-Bennett, T. Yokoi, K. Sakamoto, H. Kunieda, O. Terasaki, and T. Tatsumi, *A novel anionic surfactant templating route for synthesizing mesoporous silica with unique structure*, Nat. Mater., **2**, pp. 801–805 (2003).

[45] G. S. Attard, J. C. Glyde, and C. G. Goltner, *Liquid-crystalline phases as templates for the synthesis of mesoporous silica*, Nature, **378**, pp. 366–368 (1995).

[46] C. Glinka, M. Nicol, G. Stucky, E. Ramli, D. Margolese, Q. Huo, J. Higgins, and M. Leonowicz, *Small angle neutron scattering study of the structure and formation of MCM-41 mesoporous molecular sieves*, J. Por. Mater., **3**, pp. 93–98 (1996).

[47] O. Regev, *Nucleation events during the synthesis of mesoporous materials using liquid crystalline templating*, Langmuir, **12**, pp. 4940–4944 (1996).

[48] C.-F. Cheng, H. He, W. Zhou, and J. Klinowski, *Crystal morphology supports the liquid crystal formation mechanism for the mesoporous molecular sieve MCM-41*, Chem. Phys. Lett., **244**, pp. 117–120 (1995).

[49] H. B. Chan and P. M. Budd, *Control of mesostructured silica particle morphology*, J. Mater. Chem., **11**, pp. 951–957 (2001).

[50] J. Frasch, B. Lebeau, M. Soulard, J. Patarin, and R. Zana, *In situ investigations on cetyltrimethylammonium surfactant/silicate systems, precursors of organized mesoporous MCM-41-type siliceous materials*, Langmuir, **16**, pp. 9049–9057 (2000).

[51] K. Yu, A. J. Hurd, and A. Eisenberg, *Syntheses of Silica/Polystyrene-block-Poly(ethylene oxide) Films with Regular and Reverse Mesostructures of Large Characteristic Length Scales by Solvent Evaporation-Induced Self-Assembly*, Langmuir, **17**, pp. 7961–7965 (2001).

[52] C. J. Brinker, Y. Lu, and A. Sellinger, *Evaporation-Induced Self-Assembly: Nanostructures Made Easy*, Adv. Mater., **11**, pp. 579–585 (1999).

[53] Y. Lu, R. Ganguli, and C. A. Drewien, *Continuous formation of supported cubic and hexagonal mesoporous films by solgel dip-coating*, Nature, **389**, pp. 364–368 (1997).

[54] U. H. Lee, J.-H. Yang, H.-j. Lee, J.-Y. Park, K.-R. Lee, and Y.-U. Kwon, *Facile and adaptable synthesis method of mesostructured silica thin films*, J. Mater. Chem., **18**, pp. 1881–1888 (2008).

[55] T. Dabadie, A. Ayral, C. Guizard, L. Cot, and P. Lacan, *Synthesis and characterization of inorganic gels in a lyotropic liquid crystal medium. Part 2.Synthesis of silica gels in lyotropic crystal phases obtained from cationic surfactants*, J. Mater. Chem., **6**, pp. 1789–1794 (1996).

[56] H. Yang, N. Coombs, I. Sokolov, and G. A. Ozin, *Freestanding and Oriented Mesoporous Silica Films Grown at the Air-Water-Interface*, Nature, **381**, pp. 589–592 (1996).

[57] B. Yang and K. J. Edler, *Free-Standing Ordered Mesoporous Silica Films Synthesized with Surfactant-Polyelectrolyte Complexes at the Air/Water Interface*, Chem. Mater., **21**, pp. 1221–1231 (2009).

[58] B. Yang, R. Jaber, and K. J. Edler, *SilicaSurfactantPolyelectrolyte Film Formation: Evolution in the Subphase*, Langmuir, **28**, pp. 8337–8347 (2012).

[59] B. Yang, J. A. Holdaway, and K. J. Edler, *Robust ordered cubic mesostructured polymer/silica composite films grown at the air/water interface*, Langmuir, **29**, pp. 4148–4158 (2013).

[60] H. Yang, N. Coombs, . Dag, I. Sokolov, and G. A. Ozin, *Free-standing mesoporous silica films; morphogenesis of channel andsurface patterns*, J. Mater. Chem., **7**, pp. 1755–1761 (1997).

[61] K. E. Shopsowitz, H. Qi, W. Y. Hamad, and M. J. MacLachlan, *Free-standing mesoporous silica films with tunable chiral nematic structures*, Nature, **468**, pp. 422–426 (2010).

[62] K. Edler, T. Brennan, S. Roser, S. Mann, and R. Richardson, *Formation of CTAB-templated mesophase silicate films from acidic solutions*, Micropor. Mesopor. Mater., **62**, pp. 165–175 (2003).

[63] K. J. Edler, A. Goldar, T. Brennan, and S. J. Roser, *Spontaneous free-standing nanostructured film growth in polyelectrolyte-surfactant systems*, Chem. Commun., pp. 1724–1725 (2003).

[64] G. B. Kolesar, W. H. Siddiqui, R. G. Geil, R. M. Malczewski, and E. J. Hobbs, *Subchronic inhalation toxicity of tetramethoxysilane in rats*, Toxicol. Sci., **13**, pp. 285–295 (1989).

[65] C. Baes and R. Mesmer, *The Hydrolysis of Cations*, New York, John Wiley  Sons (1976).

[66] J. Šefčík and A. V. McCormick, *Thermochemistry of aqueous silicate solution precursors to ceramics*, AIChE Journal, **43**, pp. 2773–2784 (1997).

[67] C. T. Knight, R. J. Balec, and S. D. Kinrade, *The structure of silicate anions in aqueous alkaline solutions*, Angew. Chem. Int. Ed., **46**, pp. 8148–8152 (2007).

[68] J. L. Bass and G. L. Turner, *Anion distributions in sodium silicate solutions. Characterization by 29Si NMR and infrared spectroscopies, and vapor phase osmometry*, J. Phys. Chem. B, **101**, pp. 10638–10644 (1997).

[69] D. Dimas, I. Giannopoulou, and D. Panias, *Polymerization in sodium silicate solutions: a fundamental process in geopolymerization technology*, J. Mater. Sci., **44**, pp. 3719–3730 (2009).

[70] K. Edler and J. White, *Further improvements in the long-range order of MCM-41 materials*, Chem. Mater., **9**, pp. 1226–1233 (1997).

[71] D. Zhao and D. Goldfarb, *Synthesis of mesoporous manganosilicates: Mn-MCM-41, Mn-MCM-48 and Mn-MCM-L*, J. Chem. Soc., Chem. Commun., pp. 875–876 (1995).

[72] K. W. Gallis and C. C. Landry, *Synthesis of MCM-48 by a phase transformation process*, Chem. Mater., **9**, pp. 2035–2038 (1997).

[73] H.-P. Lin, Y.-R. Cheng, and C.-Y. Mou, *Hierarchical order in hollow spheres of mesoporous silicates*, Chem. Mater., **10**, pp. 3772–3776 (1998).

[74] J. M. Clemente-Juan, E. Coronado, and A. Gaita-Ariño, *Magnetic polyoxometalates: from molecular magnetism to molecular spintronics and quantum computing*, Chem. Soc. Rev., **41**, pp. 7464–7478 (2012).

[75] M. T. Pope, *Heteropoly and isopoly oxometalates*, Springer-Verlag, Springer-Verlag Berlin Heidelberg (1983).

[76] B. S. Bassil, M. Ibrahim, R. AlOweini, M. Asano, Z. Wang, J. van Tol, N. S. Dalal, K. Choi, R. Ngo Biboum, and B. Keita, *A Planar Mn19 (OH) 12 26+ Unit Incorporated in a 60Tungsto6Silicate Polyanion*, Angew. Chem. Int. Ed., **50**, pp. 5961–5964 (2011).

[77] C. Lydon, C. Busche, H. N. Miras, A. Delf, D. Long, L. Yellowlees, and L. Cronin, *Nanoscale growth of molecular oxides: assembly of a V6 double cubane between two lacunary P2W15 polyoxometalates*, Angew. Chem. Int. Ed., **51**, pp. 2115–2118 (2012).

[78] S. G. Mitchell, P. I. Molina, S. Khanra, H. N. Miras, A. Prescimone, G. J. Cooper, R. S. Winter, E. K. Brechin, D. Long, and R. J. Cogdell, *A MixedValence Manganese Cubane Trapped by Inequivalent Trilacunary Polyoxometalate Ligands*, Angew. Chem. Int. Ed., **50**, pp. 9154–9157 (2011).

[79] R. G. Bates, *Polyanions et Polycations*, J. Am. Chem. Soc., **86**, pp. 1653–1654 (1964).

[80] J. J. Borrs-Almenar, E. Coronado, A. Mller, and M. Pope, *Polyoxometalate Molecular Science*, Polyoxometalate Molecular Science, Springer (2003).

[81] D. Long, P. Kgerler, L. J. Farrugia, and L. Cronin, *Restraining Symmetry in the Formation of Small Polyoxomolybdates: Building Blocks of Unprecedented Topology Resulting From ShrinkWrapping[H2Mo16O52] 10Type Clusters*, Angew. Chem. Int. Ed., **42**, pp. 4180–4183 (2003).

[82] M. Sarma, T. Chatterjee, and S. K. Das, *Bringing an important macrocycle into a polyoxometalate matrix: synthesis, crystal structure, spectroscopy and electrochemistry of [Co III (transdiene)(Cl) 2] 2 [Mo 6 O 19],[Ni II (transdiene)][W 6 O 19]· DMSO· DCM and [Zn II (transdsiene)(Cl)] 2 [W 6 O 19]*, Dalton Trans., **40**, pp. 2954–2966 (2011).

[83] D. Long, R. Tsunashima, and L. Cronin, *Polyoxometalates: building blocks for functional nanoscale systems*, Angew. Chem. Int. Ed., **49**, pp. 1736–1758 (2010).

[84] G. Liu, T. Liu, S. S. Mal, and U. Kortz, *Wheel-shaped polyoxotungstate [Cu20Cl (OH) 24 (H2O) 12 (P8W48O184)] 25-macroanions form supramolecular blackberry structure in aqueous solution*, J. Am. Chem. Soc., **128**, pp. 10103–10110 (2006).

[85] T. Liu, E. Diemann, H. Li, A. W. Dress, and A. Mller, *Self-assembly in aqueous solution of wheel-shaped Mo 154 oxide clusters into vesicles*, Nature, **426**, p. 59 (2003).

[86] B. Chen, H. Jiang, Y. Zhu, A. Cammers, and J. P. Selegue, *Monitoring the growth of polyoxomolybdate nanoparticles in suspension by flow field-flow fractionation*, J. Am. Chem. Soc., **127**, pp. 4166–4167 (2005).

[87] A. Mller, E. Krickemeyer, H. Bgge, M. Schmidtmann, and F. Peters, *Organizational forms of matter: an inorganic super fullerene and keplerate based on molybdenum oxide*, Angew. Chem. Int. Ed., **37**, pp. 3359–3363 (1998).

[88] A. Mller, M. Koop, H. Bgge, M. Schmidtmann, and C. Beugholt, *Exchanged ligands on the surface of a giant cluster:[(MoO 3) 176 (H 2 O) 63 (CH 3 OH) 17 H n](32n)*, Chem. Commun., pp. 1501–1502 (1998).

[89] G. Liu and T. Liu, *Strong attraction among the fully hydrophilic Mo72Fe30 macroanions*, J. Am. Chem. Soc., **127**, pp. 6942–6943 (2005).

[90] M. L. Kistler, A. Bhatt, G. Liu, D. Casa, and T. Liu, *A complete macroionblackberry assembly macroion transition with continuously adjustable assembly sizes in Mo132 water/acetone systems*, J. Am. Chem. Soc., **129**, pp. 6453–6460 (2007).

[91] K. Suzuki, M. Sugawa, Y. Kikukawa, K. Kamata, K. Yamaguchi, and N. Mizuno, *Strategic design and refinement of Lewis acidbase catalysis by rare-earth-metal-containing polyoxometalates*, Inorg. Chem., **51**, pp. 6953–6961 (2012).

[92] X. López, J. A. Fernández, and J. M. Poblet, *Redox properties of polyoxometalates: new insights on the anion charge effect*, Dalton Transactions, pp. 1162–1167 (2006).

[93] E. Dempsey, A. Kennedy, N. Fay, and T. McCormac, *Investigations into heteropolyanions as electrocatalysts for the oxidation of adrenaline*, Electroanalysis, **15**, pp. 1835–1842 (2003).

[94] K. Essaadi, B. Keita, L. Nadjo, and R. Contant, *Oxidation of NADH by oxometalates*, J. Electroanal. Chem., **367**, pp. 275–278 (1994).

[95] B. Keita, K. Essaadi, L. Nadjo, and M. Desmadril, *Rate-limiting one-electron transfer in the oxidation of NADH by polyoxometalates*, Chem. Phys. Lett., **237**, pp. 411–418 (1995).

[96] C. Rong and M. T. Pope, *Lacunary polyoxometalate anions are. pi.-acceptor ligands. Characterization of some tungstoruthenate (II, III, IV, V) heteropolyanions and their atom-transfer reactivity*, J. Am. Chem. Soc., **114**, pp. 2932–2938 (1992).

[97] J. M. Poblet, X. Lpez, and C. Bo, *Ab initio and DFT modelling of complex materials: towards the understanding of electronic and magnetic properties of polyoxometalates*, Chem. Soc. Rev., **32**, pp. 297–308 (2003).

[98] Y. Guo and C. Hu, *Heterogeneous photocatalysis by solid polyoxometalates*, J. Mol. Catal. A: Chem., **262**, pp. 136–148 (2007).

[99] R. R. Ozer and J. L. Ferry, *Photocatalytic oxidation of aqueous 1, 2-dichlorobenzene by polyoxometalates supported on the NaY zeolite*, J. Phys. Chem. B, **106**, pp. 4336–4342 (2002).

[100] S. Gao, R. Cao, J. L, G. Li, Y. Li, and H. Yang, *Photocatalytic properties of polyoxometalatethionine composite films immobilized onto microspheres under sunlight irradiation*, J. Mater. Chem., **19**, pp. 4157–4163 (2009).

[101] Y. Guo, Y. Wang, C. Hu, Y. Wang, E. Wang, Y. Zhou, and S. Feng, *Microporous polyoxometalates POMs/SiO2: synthesis and photocatalytic degradation of aqueous organocholorine pesticides*, Chem. Mater., **12**, pp. 3501–3508 (2000).

[102] H. Yang, T. Liu, M. Cao, H. Li, S. Gao, and R. Cao, *A water-insoluble and visible light induced polyoxometalate-based photocatalyst*, Chem. Commun., **46**, pp. 2429–2431 (2010).

[103] A. Dolbecq, P. Mialane, B. Keita, and L. Nadjo, *Polyoxometalate-based materials for efficient solar and visible light harvesting: application to the photocatalytic degradation of azo dyes*, J. Mater. Chem., **22**, pp. 24509–24521 (2012).

[104] A. Troupis, A. Hiskia, and E. Papaconstantinou, *Photocatalytic reduction and recovery of copper by polyoxometalates*, Environ. Sci. Technol., **36**, pp. 5355–5362 (2002).

[105] W. Qi and L. Wu, *Polyoxometalate/polymer hybrid materials: fabrication and properties*, Polym. Int., **58**, pp. 1217–1225 (2009).

[106] Y.-F. Song and R. Tsunashima, *Recent advances on polyoxometalate-based molecular and composite materials*, Chem. Soc. Rev., **41**, pp. 7384–7402 (2012).

[107] A. Dolbecq, E. Dumas, C. R. Mayer, and P. Mialane, *Hybrid organic inorganic polyoxometalate compounds: from structural diversity to applications*, Chem. Rev., **110**, pp. 6009–6048 (2010).

[108] C. F. Faul and M. Antonietti, *Ionic selfassembly: Facile synthesis of supramolecular materials*, Adv. Mater., **15**, pp. 673–683 (2003).

[109] W. Bu, H. Li, H. Sun, S. Yin, and L. Wu, *Polyoxometalate-based vesicle and its honeycomb architectures on solid surfaces*, J. Am. Chem. Soc., **127**, pp. 8016–8017 (2005).

[110] H. Li, H. Sun, W. Qi, M. Xu, and L. Wu, *Onionlike Hybrid Assemblies Based on SurfactantEncapsulated Polyoxometalates*, Angew. Chem. Int. Ed., **46**, pp. 1300–1303 (2007).

[111] M. Nyman, D. Ingersoll, S. Singh, F. Bonhomme, T. M. Alam, C. J. Brinker, and M. A. Rodriguez, *Comparative Study of Inorganic Cluster Surfactant Arrays*, Chem. Mater., **17**, pp. 2885–2895 (2005).

[112] H. Zhang, X. Lin, Y. Yan, and L. Wu, *Luminescent logic function of a surfactant-encapsulated polyoxometalate complex*, Chem. Commun., pp. 4575–4577 (2006).

[113] H. Li, W. Qi, W. Li, H. Sun, W. Bu, and L. Wu, *A Highly Transparent and Luminescent Hybrid Based on the Copolymerization of SurfactantEncapsulated Polyoxometalate and Methyl Methacrylate*, Adv. Mater., **17**, pp. 2688–2692 (2005).

[114] A. Haimov and R. Neumann, *An Example of Lipophiloselectivity: The Preferred Oxidation, in Water, of Hydrophobic 2-Alkanols Catalyzed by a Cross-Linked Polyethyleneimine Polyoxometalate Catalyst Assembly*, J. Am. Chem. Soc., **128**, pp. 15697–15700 (2006).

[115] X. Lin, Y. Wang, and L. Wu, *Hexagonal mesostructure and its disassembly into nanofibers of a diblock molecule/polyoxometalate hybrid*, Langmuir, **25**, pp. 6081–6087 (2009).

[116] Y. Yang, B. Zhang, Y. Wang, L. Yue, W. Li, and L. Wu, *A photo-driven polyoxometalate complex shuttle and its homogeneous catalysis and heterogeneous separation*, J. Am. Chem. Soc., **135**, pp. 14500–14503 (2013).

[117] S. Yin, H. Sun, Y. Yan, W. Li, and L. Wu, *Hydrogen-bonding-induced supramolecular liquid crystals and luminescent properties of europium-substituted polyoxometalate hybrids*, J. Phys. Chem. B, **113**, pp. 2355–2364 (2009).

[118] S. Liu, D. Volkmer, and D. G. Kurth, *Functional polyoxometalate thin films via electrostatic layer-by-layer self-assembly*, J. Cluster Sci., **14**, pp. 405–419 (2003).

[119] H. Li, S. Pang, S. Wu, X. Feng, K. Mullen, and C. Bubeck, *Layer-by-layer assembly and UV photoreduction of graphenepolyoxometalate composite films for electronics*, J. Am. Chem. Soc., **133**, pp. 9423–9429 (2011).

[120] Y. Shen, J. Liu, J. Jiang, B. Liu, and S. Dong, *Fabrication of a metalloporphyrin polyoxometalate hybrid film by a layer-by-layer method and its catalysis for hydrogen evolution and dioxygen reduction*, J. Phys. Chem. B, **107**, pp. 9744–9748 (2003).

[121] B. Ding, C. Li, S. Fujita, and S. Shiratori, *Layer-by-layer self-assembled tubular films containing polyoxometalate on electrospun nanofibers*, Colloids Surf., A, **284**, pp. 257–262 (2006).

[122] H. Ma, J. Peng, B. Zhou, Z. Han, and Y. Feng, *Luminescent multilayer film based on mixed-addenda polyoxometalates and polyethyleneimine by layer-by-layer assembly*, Appl. Surf. Sci., **233**, pp. 14–19 (2004).

[123] H. Ma, J. Peng, Z. Han, Y. Feng, and E. Wang, *Preparation and characterization of luminescent nanocomposite film containing polyoxometalate*, Thin Solid Films, **446**, pp. 161–166 (2004).

[124] M. Jiang, E. Wang, G. Wei, L. Xu, and Z. Li, *Photochromic inorganicorganic multilayer films based on polyoxometalates and poly (ethylenimine)*, J. Colloid Interface Sci., **275**, pp. 596–600 (2004).

[125] D. M. Fernandes, C. M. Brett, and A. M. Cavaleiro, *Layer-by-layer self-assembly and electrocatalytic properties of poly (ethylenimine)-silicotungstate multilayer composite films*, J. Solid State Electrochem., **15**, pp. 811–819 (2011).

[126] M. Clemente-Leon, B. Agricole, C. Mingotaud, C. Gomez-Garcia, E. Coronado, and P. Delhaes, *Toward new organic/inorganic superlattices: Keggin polyoxometalates in Langmuir and Langmuir Blodgett films*, Langmuir, **13**, pp. 2340–2347 (1997).

[127] M. ClementeLen, C. Mingotaud, B. Agricole, C. J. GmezGarcia, E. Coronado, and P. Delhas, *Application of the LangmuirBlodgett technique to polyoxometalates: towards New Magnetic Films*, Angew. Chem. Int. Ed., **36**, pp. 1114–1116 (1997).

[128] M. Clemente-Len, T. Ito, H. Yashiro, and T. Yamase, *Two-Dimensional Array of Polyoxomolybdate Nanoball Constructed by Langmuir Blodgett Semiamphiphilic Method*, Chem. Mater., **19**, pp. 2589–2594 (2007).

[129] P. Yin, C. P. Pradeep, B. Zhang, F. Li, C. Lydon, M. H. Rosnes, D. Li, E. Bitterlich, L. Xu, and L. Cronin, *Controllable SelfAssembly of OrganicInorganic Amphiphiles Containing Dawson Polyoxometalate Clusters*, Chem. Eur. J., **18**, pp. 8157–8162 (2012).

[130] Y. Song, N. McMillan, D. Long, J. Thiel, Y. Ding, H. Chen, N. Gadegaard, and L. Cronin, *Design of hydrophobic polyoxometalate hybrid assemblies beyond surfactant encapsulation*, Chem. Eur. J., **14**, pp. 2349–2354 (2008).

[131] C. Sanchez, J. Livage, M. Henry, and F. Babonneau, *Chemical modification of alkoxide precursors*, J. Non-Cryst. Solids, **100**, pp. 65–76 (1988).

[132] C. R. Mayer, R. Thouvenot, and T. Lalot, *New hybrid covalent networks based on polyoxometalates: Part 1. Hybrid networks based on poly (ethyl methacrylate) chains covalently cross-linked by heteropolyanions: Synthesis and swelling properties*, Chem. Mater., **12**, pp. 257–260 (2000).

[133] D. Agustin, C. Coelho, A. Mazeaud, P. Herson, A. Proust, and R. Thouvenot, *OrganicInorganic Hybrids based on Polyoxometalates. Part 8 Synthesis and Spectroscopic Characterization of the Heterosilylated Anions [PW9O34 (tBuSiO) 3 (SiR)] 3(R=CH3,CH= CH2,CH2CH= CH2,(CH2) 4CH= CH2)Xray Crystal Structure of [nBu4N] 3 [PW9O34 (tBuSiO) 3 (SiCH2CH= CH2)]*, Zeitschrift fr anorganische und allgemeine Chemie, **630**, pp. 2049–2053 (2004).

[134] C. R. Mayer, V. Cabuil, T. Lalot, and R. Thouvenot, *Incorporation of magnetic nanoparticles in new hybrid networks based on heteropolyanions and polyacrylamide*, Angew. Chem. Int. Ed., **38**, pp. 3672–3675 (1999).

[135] S. Landsmann, C. Lizandara-Pueyo, and S. Polarz, *A new class of surfactants with multinuclear, inorganic head groups*, J. Am. Chem. Soc., **132**, pp. 5315–5321 (2010).

[136] P. Yin, P. Wu, Z. Xiao, D. Li, E. Bitterlich, J. Zhang, P. Cheng, D. V. Vezenov, T. Liu, and Y. Wei, *A doubletailed fluorescent surfactant with a hexavanadate cluster as the head group*, Angew. Chem. Int. Ed., **50**, pp. 2521–2525 (2011).

[137] J. J. Giner-Casares, G. Brezesinski, H. Mohwald, S. Landsmann, and S. Polarz, *Polyoxometalate surfactants as unique molecules for interfacial self-assembly*, J. Phys. Chem. Lett., **3**, pp. 322–326 (2012).

[138] Y. Han, Y. Xiao, Z. Zhang, B. Liu, P. Zheng, S. He, and W. Wang, *Synthesis of polyoxometalate polymer hybrid polymers and their hybrid vesicular assembly*, Macromolecules, **42**, pp. 6543–6548 (2009).

[139] S. Landsmann, M. Luka, and S. Polarz, *Bolaform surfactants with polyoxometalate head groups and their assembly into ultra-small monolayer membrane vesicles*, Nat. Commun., **3**, pp. 1–6 (2012).

[140] D. Li, J. Song, P. Yin, S. Simotwo, A. J. Bassler, Y. Aung, J. E. Roberts, K. I. Hardcastle, C. L. Hill, and T. Liu, *Inorganicorganic hybrid vesicles with counterion-and pH-controlled fluorescent properties*, J. Am. Chem. Soc., **133**, pp. 14010–14016 (2011).

[141] C. P. Pradeep, M. F. Misdrahi, F. Li, J. Zhang, L. Xu, D. Long, T. Liu, and L. Cronin, *Synthesis of modular inorganicorganicinorganic polyoxometalates and their assembly into vesicles*, Angew. Chem. Int. Ed., **48**, pp. 8309–8313 (2009).

[142] R. Nagarajan, *Molecular packing parameter and surfactant self-assembly: the neglected role of the surfactant tail*, Langmuir, **18**, pp. 31–38 (2002).

[143] C. Yvon, A. J. Surman, M. Hutin, J. Alex, B. O. Smith, D. Long, and L. Cronin, *Polyoxometalate Clusters Integrated into Peptide Chains and as Inorganic Amino Acids: Solutionand SolidPhase Approaches*, Angew. Chem. Int. Ed., **53**, pp. 3336–3341 (2014).

[144] J. Luo, B. Zhang, C. Yvon, M. Hutin, S. Gerislioglu, C. Wesdemiotis, L. Cronin, and T. Liu, *SelfAssembly of PolyoxometalatePeptide Hybrids in Solution: Elucidating the Contributions of Multiple Possible Driving Forces*, Eur. J. Inorg. Chem., **2019**, pp. 380–386 (2019).

[145] D. A. Dougherty, *The cation  interaction*, Acc. Chem. Res., **46**, pp. 885–893 (2012).

[146] D. Li, Z. Liu, J. Song, H. Li, B. Zhang, P. Yin, Z. N. Zheng, J. E. Roberts, M. Tsige, and C. L. Hill, *Cation Translocation around Single PolyoxometalateOrganic Hybrid Cluster Regulated by Electrostatic and Cation Interactions*, Angew. Chem. Int. Ed., **129**, pp. 3342–3346 (2017).

[147] S. Seiffert, E. Kumacheva, O. Okay, M. Anthamatten, M. Chau, P. Y. Dankers, B. W. Greenland, W. Hayes, P. Li, and R. Liu, *Supramolecular Polymer Networks and Gels*, volume 268, Springer (2015).

[148] P. Terech and R. G. Weiss, *Low molecular mass gelators of organic liquids and the properties of their gels*, Chem. Rev., **97**, pp. 3133–3160 (1997).

[149] J. H. Van Esch and B. L. Feringa, *New functional materials based on selfassembling organogels: from serendipity towards design*, Angew. Chem. Int. Ed., **39**, pp. 2263–2266 (2000).

[150] T. Yi, K. Sada, K. Sugiyasu, T. Hatano, and S. Shinkai, *Photo-induced colour generation and colour erasing switched by the solgel phase transition*, Chem. Commun., pp. 344–345 (2003).

[151] B. Zambrano, E. Caizalez, P. Silva, and A. Briceo, *A bottom-up route for the preparation of novel hierarchical nanostructured hybrid molybdenum oxidehydrogel composites*, New J. Chem., **35**, pp. 288–291 (2011).

[152] Z. He, H. Wang, Y. Wang, Y. Wu, H. Li, L. Bi, and L. Wu, *Instantaneous and reversible gelation of organically grafted polyoxometalate complexes with dicarboxylic acids*, Soft Matter, **8**, pp. 3315–3321 (2012).

[153] Z. He, H. Ai, B. Li, and L. Wu, *A supramolecular gel based on an adenine symmetrically grafted Anderson-type polyoxometalate complex*, Chin. Sci. Bull., **57**, pp. 4304–4309 (2012).

[154] M. Carraro, A. Sartorel, G. Scorrano, C. Maccato, M. H. Dickman, U. Kortz, and M. Bonchio, *Chiral StrandbergType Molybdates [(RPO3) 2Mo5O15] 2 as Molecular Gelators: Self-Assembled Fibrillar Nanostructures with Enhanced Optical Activity*, Angew. Chem. Int. Ed., **47**, pp. 7275–7279 (2008).

[155] Y. Yan, H. Wang, B. Li, G. Hou, Z. Yin, L. Wu, and V. W. Yam, *Smart SelfAssemblies Based on a SurfactantEncapsulated Photoresponsive Polyoxometalate Complex*, Angew. Chem. Int. Ed., **49**, pp. 9233–9236 (2010).

[156] R. C. Schroden, C. F. Blanford, B. J. Melde, B. J. Johnson, and A. Stein, *Direct synthesis of ordered macroporous silica materials functionalized with polyoxometalate clusters*, Chem. Mater., **13**, pp. 1074–1081 (2001).

[157] B. J. Johnson and A. Stein, *Surface modification of mesoporous, macroporous, and amorphous silica with catalytically active polyoxometalate clusters*, Inorg. Chem., **40**, pp. 801–808 (2001).

[158] P. Lei, C. Chen, J. Yang, W. Ma, J. Zhao, and L. Zang, *Degradation of dye pollutants by immobilized polyoxometalate with H2O2 under visible-light irradiation*, Environ. Sci. Technol., **39**, pp. 8466–8474 (2005).

[159] Z. Sun, F. Li, M. Zhao, L. Xu, and S. Fang, *A comparative study on photoelectrochemical performance of TiO2 photoanodes enhanced by different polyoxometalates*, Electrochem. Commun., **30**, pp. 38–41 (2013).

[160] S. Ahn, S. L. Nauert, C. T. Buru, M. Rimoldi, H. Choi, N. M. Schweitzer, J. T. Hupp, O. K. Farha, and J. M. Notestein, *Pushing the limits on metalorganic frameworks as a catalyst support: NU-1000 supported tungsten catalysts for o-xylene isomerization and disproportionation*, J. Am. Chem. Soc., **140**, pp. 8535–8543 (2018).

[161] R. R. Ozer and J. L. Ferry, *Investigation of the photocatalytic activity of TiO2 polyoxometalate systems*, Environ. Sci. Technol., **35**, pp. 3242–3246 (2001).

[162] C. Chen, P. Lei, H. Ji, W. Ma, J. Zhao, H. Hidaka, and N. Serpone, *Photocatalysis by titanium dioxide and polyoxometalate/TiO2 cocatalysts. Intermediates and mechanistic study*, Environ. Sci. Technol., **38**, pp. 329–337 (2004).

[163] H. Jin, Q. Wu, and W. Pang, *Photocatalytic degradation of textile dye X-3B using polyoxometalateTiO2 hybrid materials*, J. Hazard. Mater., **141**, pp. 123–127 (2007).

[164] N. Lu, Y. Zhao, H. Liu, Y. Guo, X. Yuan, H. Xu, H. Peng, and H. Qin, *Design of polyoxometallatetitania composite film (H3PW12O40/TiO2) for the degradation of an aqueous dye Rhodamine B under the simulated sunlight irradiation*, J. Hazard. Mater., **199**, pp. 1–8 (2012).

[165] D. Li, C. Gu, C. Guo, and C. Hu, *The effects of ambient gases on the surface resistance of polyoxometalate/TiO2 film*, Chem. Phys. Lett., **385**, pp. 55–59 (2004).

[166] H. Y. Woo, H. So, and M. T. Pope, *Trimetallo derivatives of lacunary 9-tungstosilicate heteropolyanions. 2. Isotropic nmr shifts in pyridine-type ligands coordinated to the paramagnetic 9-tungsto-3-cuprio (II) silicate anion*, J. Am. Chem. Soc., **118**, pp. 621–626 (1996).

[167] L. C. Baker and J. S. Figgis, *New fundamental type of inorganic complex: hybrid between heteropoly and conventional coordination complexes. Possibilities for geometrical isomerisms in 11-, 12-, 17-, and 18-heteropoly derivatives*, J. Am. Chem. Soc., **92**, pp. 3794–3797 (1970).

[168] L. Lu, L. Li, T. Hu, W. Zhang, X. Huang, J. Zhang, and X. Liu, *Preparation, characterization, and photocatalytic activity of three-dimensionally ordered macroporous hybrid monosubstituted polyoxometalate K5 [Co (H2O) PW11O39] amine functionalized titanium catalysts*, J. Mol. Catal. A: Chem., **394**, pp. 283–294 (2014).

[169] Y. Yang, Y. Guo, C. Hu, Y. Wang, and E. Wang, *Preparation of surface modifications of mesoporous titania with monosubstituted Keggin units and their catalytic performance for organochlorine pesticide and dyes under UV irradiation*, Appl. Catal., A, **273**, pp. 201–210 (2004).

[170] A. Pearson, S. K. Bhargava, and V. Bansal, *UV-switchable polyoxometalate sandwiched between TiO2 and metal nanoparticles for enhanced visible and solar light photococatalysis*, Langmuir, **27**, pp. 9245–9252 (2011).

[171] A. Pearson, H. Jani, K. Kalantar-Zadeh, S. K. Bhargava, and V. Bansal, *Gold nanoparticle-decorated keggin ions/TiO2 photococatalyst for improved solar light photocatalysis*, Langmuir, **27**, pp. 6661–6667 (2011).

[172] A. Pearson, H. Zheng, K. Kalantar-Zadeh, S. K. Bhargava, and V. Bansal, *Decoration of TiO2 nanotubes with metal nanoparticles using polyoxometalate as a UV-switchable reducing agent for enhanced visible and solar light photocatalysis*, Langmuir, **28**, pp. 14470–14475 (2012).

[173] A. Pearson, S. Bhosale, S. K. Bhargava, and V. Bansal, *Combining the UV-switchability of Keggin ions with a galvanic replacement process to fabricate TiO2polyoxometalatebimetal nanocomposites for improved surface enhanced Raman scattering and solar light photocatalysis*, ACS Appl. Mater. Interfaces, **5**, pp. 7007–7013 (2013).

[174] Y. Xie, L. Zhou, and H. Huang, *Enhanced photoelectrocatalytic performance of polyoxometalate-titania nanocomposite photoanode*, Appl. Catal., B, **76**, pp. 15–23 (2007).

[175] L. Wang, L. Xu, Z. Mu, C. Wang, and Z. Sun, *Synergistic enhancement of photovoltaic performance of TiO 2 photoanodes by incorporation of Dawson-type polyoxometalate and gold nanoparticles*, J. Mater. Chem., **22**, pp. 23627–23632 (2012).

[176] S. Yanagida, A. Nakajima, T. Sasaki, Y. Kameshima, and K. Okada, *Processing and Photocatalytic Properties of Transparent 12 Tungsto (VI) Phosphoric Acid TiO2 Hybrid Films*, Chem. Mater., **20**, pp. 3757–3764 (2008).

[177] J. C. Lindon, G. E. Tranter, and D. Koppenaal, *Encyclopedia of spectroscopy and spectrometry*, Academic Press (2016).

[178] T. M. Cooper, B. C. Hall, D. G. McLean, J. E. Rogers, A. R. Burke, K. Turnbull, and A. Weisner, *Synthesis and Characterization of Novel Platinum Acetylide Oligomers*, in *MRS Proceedings*, volume 771, p. L4. 21, Cambridge Univ Press.

[179] Y. Sakamoto, M. Kaneda, O. Terasaki, D. Y. Zhao, J. M. Kim, G. Stucky, H. J. Shin, and R. Ryoo, *Direct imaging of the pores and cages of three-dimensional mesoporous materials*, Nature, **408**, pp. 449–453 (2000).

[180] G. Fragneto, R. K. Thomas, A. R. Rennie, and J. Penfold, *Neutron reflection from hexadecyltrimethylammonium bromide adsorbed on smooth and rough silicon surfaces*, Langmuir, **12**, pp. 6036–6043 (1996).

[181] D. Stigter, *On density, hydration, shape, and charge of micelles of sodium dodecyl sulfate and dodecyl ammonium chloride*, J. Colloid Interface Sci., **23**, pp. 379–388 (1967).

[182] D. Caudwell, J. Trusler, V. Vesovic, and W. Wakeham, *The viscosity and density of n-dodecane and n-octadecane at pressures up to 200 MPa and temperatures up to 473 K*, Int. J. Thermophys., **25**, pp. 1339–1352 (2004).

[183] G. Renaud, R. Lazzari, and F. Leroy, *Probing surface and interface morphology with grazing incidence small angle X-ray scattering*, Surf. Sci. Rep., **64**, pp. 255–380 (2009).

[184] V. F. Sears, *Neutron scattering lengths and cross sections*, Neutron news, **3**, pp. 26–37 (1992).

[185] B. Yang, *Surfactant and Polyelectrolytes Templated Mesostructured Inorganic Materials*, Thesis (2010).

[186] B. C. McAlister and B. P. Grady, *Simulation of small-angle X-ray scattering from single-particle systems*, J. Appl. Crystallogr., **31**, pp. 594–599 (1998).

[187] G. Kostorz, *Neutron scattering: treatise on materials science and technology*, NY : Academic Press, New York (1979).

[188] G. Porod, O. Glatter, and O. Kratky, *Small angle X-ray scattering*, Academic Press, London (1982).

[189] A. Guinier, G. Fournet, and K. L. Yudowitch, *Small-angle scattering of X-rays*, Wiley, New York (1955).

[190] M. Kotlarchyk and S.-H. Chen, *Analysis of small angle neutron scattering spectra from polydisperse interacting colloids*, J. Chem. Phys, **79**, pp. 2461–2469 (1983).

[191] M. Kotlarchyk, R. B. Stephens, and J. S. Huang, *Study of Schultz distribution to model polydispersity of microemulsion droplets*, J. Phys. Chem., **92**, pp. 1533–1538 (1988).

[192] A. Guinier, *La diffraction des rayons X aux trs petits angles: application l'tude de phnomnes ultramicroscopiques*, in *Annales de physique*, volume 11, pp. 161–237, EDP Sciences (1939).

[193] B. Hammouda, *SANS from homogeneous polymer mixtures: A unified overview*, pp. 87–133, Springer (1993).

[194] J. K. Percus and G. J. Yevick, *Analysis of classical statistical mechanics by means of collective coordinates*, Phys. Rev., **110**, p. 1 (1958).

[195] J.-P. Hansen and J. B. Hayter, *A rescaled MSA structure factor for dilute charged colloidal dispersions*, Mol. Phys., **46**, pp. 651–656 (1982).

[196] A. J. Jackson, *Introduction to small-angle neutron scattering and neutron reflectometry*, NIST Center for Neutron Research, pp. 1–24 (2008).

[197] P. R. Bevington, D. K. Robinson, J. M. Blair, A. J. Mallinckrodt, and S. McKay, *Data reduction and error analysis for the physical sciences*, Comput. in Phys., **7**, pp. 415–416 (1993).

[198] W. H. Press, S. A. Teukolsky, W. T. Vetterling, and B. P. Flannery, *Numerical Recipes 3rd Edition: The Art of Scientific Computing*, Cambridge university press (2007).

[199] A. Gibaud, D. Grosso, B. Smarsly, A. Baptiste, J. Bardeau, F. Babonneau, D. Doshi, Z. Chen, C. J. Brinker, and C. Sanchez, *Evaporation-controlled self-assembly of silica surfactant mesophases*, J. Phys. Chem. B, **107**, pp. 6114–6118 (2003).

[200] K. Yu, B. Smarsly, and C. J. Brinker, *SelfAssembly and Characterization of Mesostructured Silica Films with a 3D Arrangement of Isolated Spherical Mesopores*, Adv. Funct. Mater., **13**, pp. 47–52 (2003).

[201] D. A. Doshi, A. Gibaud, V. Goletto, M. Lu, H. Gerung, B. Ocko, S. M. Han, and C. J. Brinker, *Peering into the self-assembly of surfactant templated thin-film silica mesophases*, J. Am. Chem. Soc., **125**, pp. 11646–11655 (2003).

[202] C. Broennimann, E. Eikenberry, B. Henrich, R. Horisberger, G. Huelsen, E. Pohl, B. Schmitt, C. Schulze-Briese, M. Suzuki, and T. Tomizaki, *The PILATUS 1M detector*, J. Synchrotron Radiat., **13**, pp. 120–130 (2006).

[203] A. Hexemer, W. Bras, J. Glossinger, E. Schaible, E. Gann, R. Kirian, A. MacDowell, M. Church, B. Rude, and H. Padmore, *A SAXS/WAXS/GISAXS beamline with multilayer monochromator*, in *J. Phys.: Conference Series*, volume 247, p. 012007, IOP Publishing.

[204] J. Daillant and A. Gibaud, *X-ray and neutron reflectivity: principles and applications*, volume 770, Springer (2008).

[205] T. Russell, *X-ray and neutron reflectivity for the investigation of polymers*, Mater. Sci. Rep., **5**, pp. 171–271 (1990).

[206] G. Vignaud, *Ph.D Dissertation*, Thesis (1997).

[207] J. S. Pedersen and I. Hamley, *Analysis of neutron and X-ray reflectivity data. II. Constrained least-squares methods*, J. Appl. Crystallogr., **27**, pp. 36–49 (1994).

[208] P. Mukerjee and K. J. Mysels, *Critical micelle concentrations of aqueous surfactant systems*, Nat. Sand. Ref. Data Ser., Nat. Bur. Sand., 36, Washington D.C. (1971).

[209] A. Dominguez, A. Fernandez, N. Gonzalez, E. Iglesias, and L. Montenegro, *Determination of Critical Micelle Concentration of Some Surfactants by Three Techniques*, J. Chem. Educ., **74**, pp. 1227–1231 (1997).

[210] C. Tanford, *The hydrophobic effect: formation of micelles and biological membranes*, Wiley-Blackwell (1980).

[211] J. Eastoe, *Surfactant chemistry*, Wuhan University Press (2005).

[212] K. Graf and M. Kappl, *Physics and chemistry of interfaces*, John Wiley  Sons (2006).

[213] J. D. Berry, M. J. Neeson, R. R. Dagastine, D. Y. Chan, and R. F. Tabor, *Measurement of surface and interfacial tension using pendant drop tensiometry*, J. Colloid Interface Sci., **454**, pp. 226–237 (2015).

[214] S. Anastasiadis, J.-K. Chen, J. Koberstein, A. Siegel, J. Sohn, and J. Emerson, *The determination of interfacial tension by video image processing of pendant fluid drops*, J. Colloid Interface Sci., **119**, pp. 55–66 (1987).

[215] H. Girault, D. Schiffrin, and B. Smith, *Drop image processing for surface and interfacial tension measurements*, J. Electroanal. Chem. Interfacial Electrochem., **137**, pp. 207–217 (1982).

[216] Q. S. Bhatia, J.-K. Chen, J. T. Koberstein, J. E. Sohn, and J. A. Emerson, *The measurement of polymer surface tension by drop image processing: application to PDMS and comparison with theory*, J. Colloid Interface Sci., **106**, pp. 353–359 (1985).

[217] W. Goldburg, *Dynamic light scattering*, Am. J. Phys., **67**, pp. 1152–1160 (1999).

[218] R. Borsali and R. Pecora, *Soft matter characterization*, volume 725, Springer (2008).

[219] A. Einstein, *Elementare Theorie der Brownschen) Bewegung*, Zeitschrift fr Elektrochemie und angewandte physikalische Chemie, **14**, pp. 235–239 (1908).

[220] S. W. Provencher, *A constrained regularization method for inverting data represented by linear algebraic or integral equations*, Comput. Phys. Commun, **27**, pp. 213–227 (1982).

[221] F. Fontana, *Memorie Mat*, Fis. Soc. Ital Sci, **1**, p. 679 (1777).

[222] S. J. Gregg and K. S. W. Sing, *Adsorption surface area and porosity*, London : Academic press, 1995. (1982).

[223] Z. ALOthman, *A review: fundamental aspects of silicate mesoporous materials*, Materials, **5**, pp. 2874–2902 (2012).

[224] K. S. Sing, *Reporting physisorption data for gas/solid systems with special reference to the determination of surface area and porosity (Recommendations 1984)*, Pure Appl. Chem., **57**, pp. 603–619 (1985).

[225] J. Broekhoff, *Mesopore determination from nitrogen sorption isotherms: Fundamentals, scope, limitations*, volume 3, pp. 663–684, Elsevier (1979).

[226] S. Lowell, J. E. Shields, M. A. Thomas, and M. Thommes, *Characterization of Porous Solids and Powders: Surface area, Pore size and Density*, volume 16, Springer, Netherlands (2012).

[227] S. Brunauer, P. H. Emmett, and E. Teller, *Adsorption of gases in multimolecular layers*, J. Am. Chem. Soc., **60**, pp. 309–319 (1938).

[228] R. von Helmholtz, *Untersuchungen ber Dmpfe und Nebel, besonders ber solche von Lsungen*, Thesis (1886).

[229] E. P. Barrett, L. G. Joyner, and P. P. Halenda, *The determination of pore volume and area distributions in porous substances. I. Computations from nitrogen isotherms*, J. Am. Chem. Soc., **73**, pp. 373–380 (1951).

[230] R. Heenan, J. Penfold, and S. King, *SANS at pulsed neutron sources: present and future prospects*, J. Appl. Crystallogr., **30**, pp. 1140–1147 (1997).

[231] R. Dalgleish and S. King, *LARMORA Proposal for a Multi-Purpose Instrument for SANS, Diffraction and Spectroscopy utilising the Larmor Precession of Polarised Neutrons.*

[232] O. Arnold, J.-C. Bilheux, J. Borreguero, A. Buts, S. I. Campbell, L. Chapon, M. Doucet, N. Draper, R. F. Leal, M. Gigg, et al., *MantidData analysis and visualization package for neutron scattering and $\mu$ SR experiments*, Nuclear Instruments and Methods in Physics Research Section A: Accelerators, Spectrometers, Detectors and Associated Equipment, **764**, pp. 156–166 (2014).

[233] G. T. Wignall and F. S. Bates, *Absolute calibration of small-angle neutron scattering data*, Journal of applied crystallography, **20**, pp. 28–40 (1987).

[234] C. Nicklin, T. Arnold, J. Rawle, and A. Warne, *Diamond beamline I07: a beamline for surface and interface diffraction*, J. Synchrotron Radiat., **23**, pp. 1245–1253 (2016).

[235] M. Basham, J. Filik, M. T. Wharmby, P. C. Chang, B. El Kassaby, M. Gerring, J. Aishima, K. Levik, B. C. Pulford, and I. Sikharulidze, *Data analysis workbench (DAWN)*, J. Synchrotron Radiat., **22**, pp. 853–858 (2015).

[236] M. Bech, O. Bunk, C. David, P. Kraft, C. Brnnimann, E. Eikenberry, and F. Pfeiffer, *X-ray imaging with the PILATUS 100k detector*, Applied Radiation and Isotopes, **66**, pp. 474–478 (2008).

[237] J. Marchal, N. Tartoni, and C. Nave, *Synchrotron applications of pixel and strip detectors at Diamond Light Source*, Nucl. Instrum. Methods Phys. Res., Sect. A, **604**, pp. 123–126 (2009).

[238] F. Hansen and G. Rdsrud, *Surface tension by pendant drop: I. A fast standard instrument using computer image analysis*, J. Colloid Interface Sci., **141**, pp. 1–9 (1991).

[239] M. W. Droege, M.d. ph.d dissertation (1984).

[240] R. G. Finke, M. W. Droege, and P. J. Domaille, *Trivacant heteropolytungstate derivatives. 3. Rational syntheses, characterization, two-dimensional tungsten-183 NMR, and properties of tungstometallophosphates P2W18M4 (H2O) 2O6810-and P4W30M4 (H2O) 2O11216-(M= cobalt, copper, zinc)*, Inorg. Chem., **26**, pp. 3886–3896 (1987).

[241] C. Comuzzi, G. Dolcetti, A. Trovarelli, F. Cavani, F. Trifir, J. Llorca, and R. G. Finke, *The solid-state rearrangement of the Wells-Dawson K 6 P 2 W 18 O 62 10H 2 O to a stable Keggin-type heteropolyanion phase: a catalyst for the selective oxidation of isobutane to isobutene*, Catal. Lett., **36**, pp. 75–79 (1996).

[242] B. Sun, G. Zhou, C. Shao, B. Jiang, J. Pang, and Y. Zhang, *Spherical mesoporous TiO2 fabricated by sodium dodecyl sulfate-assisted hydrothermal treatment and its photocatalytic decomposition of papermaking wastewater*, Powder Technol., **256**, pp. 118–125 (2014).

[243] U. Ciesla and F. Schth, *Ordered mesoporous materials*, Microporous Mesoporous Mater., **27**, pp. 131–149 (1999).

[244] K. Flodstrm, C. V. Teixeira, H. Amenitsch, V. Alfredsson, and M. Lindn, *In Situ Synchrotron Small-Angle X-ray Scattering/X-ray Diffraction Study of the Formation of SBA-15 Mesoporous Silica*, Langmuir, **20**, pp. 4885–4891 (2004), pMID: 15984246.

[245] S. Dourdain, J.-F. Bardeau, M. Colas, B. Smarsly, A. Mehdi, B. M. Ocko, and A. Gibaud, *Determination by x-ray reflectivity and small angle x-ray scattering of the porous properties of mesoporous silica thin films*, Applied Physics Letters, **86**, p. 113108 (2005).

[246] D. Mildner and P. Hall, *Small-angle scattering from porous solids with fractal geometry*, J. Phys. D Appl. Phys., **19**, p. 1535 (1986).

[247] C. J. Brinker, Y. Lu, A. Sellinger, and H. Fan, *Evaporation-induced self-assembly: nanostructures made easy*, Adv. Mater., **11**, pp. 579–585 (1999).

[248] J. J. Borrs-Almenar, E. Coronado, A. Mller, and M. Pope, *Polyoxometalate molecular science*, volume 98, Springer Science  Business Media (2003).

[249] S. Polarz, B. Smarsly, and M. Antonietti, *Colloidal Organization and Clusters: SelfAssembly of PolyoxometalateSurfactant Complexes towards ThreeDimensional Organized Structures*, ChemPhysChem, **2**, pp. 457–461 (2001).

[250] A. Shiloach and D. Blankschtein, *Measurement and prediction of ionic/nonionic mixed micelle formation and growth*, Langmuir, **14**, pp. 7166–7182 (1998).

[251] A. Khan and E. F. Marques, *Synergism and polymorphism in mixed surfactant systems*, Curr. Opin. Colloid Interface Sci., **4**, pp. 402–410 (1999).

[252] L.-R. Dai, T.-W. Wang, L.-T. Bu, and G. Chen, *Mixed surfactant templating route for mesoporous silica*, Colloids Surf., A, **181**, pp. 151–157 (2001).

[253] H. Yang, L. Bai, D. Wei, L. Yang, W. Wang, H. Chen, Y. Niu, and Z. Xue, *Ionic self-assembly of poly (ionic liquid)-polyoxometalate hybrids for selective adsorption of anionic dyes*, Chem. Eng. J., **358**, pp. 850–859 (2019).

[254] C. Xu, Z. Tian, P. Shen, and S. P. Jiang, *Oxide (CeO2, NiO, Co3O4 and Mn3O4)-promoted Pd/C electrocatalysts for alcohol electrooxidation in alkaline media*, Electrochim. Acta, **53**, pp. 2610–2618 (2008).

[255] K. L. Nardi, N. Yang, C. F. Dickens, A. L. Strickler, and S. F. Bent, *Creating highly active atomic layer deposited NiO electrocatalysts for the oxygen evolution reaction*, Adv. Energy Mater., **5**, p. 1500412 (2015).

[256] T. Tu, X. Bao, W. Assenmacher, H. Peterlik, J. Daniels, and K. H. Dtz, *Efficient AirStable Organometallic LowMolecularMass Gelators for Ionic Liquids: Synthesis, Aggregation and Application of PyridineBridged Bis (benzimidazolylidene)Palladium Complexes*, Chem. Eur. J., **15**, pp. 1853–1861 (2009).